UNIVERSITY OF CAPE TOWN
IYUNIVESITHI YASEKAPA • UNIVERSITEIT VAN KAAPSTAD

BLAST IMPACT & SURVIVABILITY RESEARCH UNIT

BISRU

The strain rate dependent mechanical properties and modelling of bovine cortical bone in compression

Anriëtte van der Westhuizen

Thesis Presented for the Degree of

DOCTOR OF PHILOSOPHY

in the Department of Mechanical Engineering

UNIVERSITY OF CAPE TOWN

April 2008

Trust in the Lord with all your heart and lean not on your own understanding; in all your ways acknowledge him, and he will make your paths straight.

PROVERBS 3:5-6 (NIV)

Abstract

THESIS TITLE: The strain rate dependent properties and modelling of bovine cortical bone in compression.

AUTHOR: Anriëtte van der Westhuizen DATE: April 2008

Cortical bone specimens were extracted in three orientations (longitudinal, radial and tangential) from bovine femur bones and compressed at quasi-static strain rates ($10^{-4}\,s^{-1}$, $10^{-3}\,s^{-1}$, $10^{-2}\,s^{-1}$ and $10^{-1}\,s^{-1}$) on conventional compression test machines. Dynamic compression of longitudinal specimens was conducted on the split Hopkinson pressure bar at strain rates of $2.5 \times 10^{2}\,s^{-1}$ and $10^{3}\,s^{-1}$. Conventional Hopkinson bar experiments resulted in a specimen strain rate that decreases beyond reaching a maximum value at the rise time. The variation in dynamic strain rate was rectified by shaping the Hopkinson bar input pulse with a reusable, conical striker bar. The hypothesis investigated was that a varying strain rate history could result in the measurement of a smeared response for materials with significant strain rate sensitivity. Results indicate that non-uniform, dynamic strain rates result in irregular stress-strain curves; however the stress-strain responses comprise the same corridor as the constant strain rate responses. Bovine cortical bone exhibits significant strain rate sensitivity, with distinct corridors of quasi-static and dynamic stress-strain response. Fracture occurs at a higher stress for both increasing strain rate and bone density. A microstructural investigation indicated that longitudinal compression of bovine bone leads to the formation of shear bands and that fracture depends on the orientation of the vascular porosity. Nine viscoelastic models were evaluated for their ability to constitute the stress-strain responses of bovine cortical bone over the tested strain rate regime. A five parameter model, which comprises both a Maxwell element and a Voigt model with a non-linear dependency on strain rate was found to provide the best response approximation. A similar model was implemented by Shim et al. to represent the strain rate sensitivity of cancellous bone from the human cervical spine. The current isotropic 3-D expansion of this model, reported by Shim et al., was found to violate the principle of frame invariance. An alternative approach, which recovers invariance by using the equivalent strain rate, is recommended in this thesis. The isotropic 3-D constitutive relation was implemented in a user material subroutine for finite element models. The subroutine was verified and validated against a quasi-static diaphysis compression experiment and a dynamic split Hopkinson bar experiment.

Declaration

I, Anriëtte van der Westhuizen, hereby:

1. Grant the University of Cape Town free license to reproduce this thesis, entitled: "**The strain rate dependent mechanical properties and modelling of bovine cortical bone in compression**", in whole or in part, for the purpose of research.

2. Declare that:

   (a) This thesis is my own unaided, both in conception and execution, and that apart from the normal guidance of my supervisor, I have received no assistance apart from that stated in the "Acknowledgements" section of the thesis.

   (b) This thesis or any part of this thesis has not been submitted in past, or is being, or is to be submitted in this or any other form for a degree at the University of Cape Town or any other University.

   (c) I am now presenting this thesis for examination for the degree of PhD in Mechanical Engineering.

Anriëtte van der Westhuizen
April 2008

Acknowledgements

I would like to express my gratitude to the following for their contributions to the successful completion of my thesis:

- I am especially indebted to my supervisor, Prof. G. Nurick, for creating the opportunity which allowed the pursuit of this research topic. His professional guidance and continual support, both academically and financially have been instrumental to the completion of this study.
- Mr. T.J. Cloete from the Department of Mechanical Engineering for his keen interest and assistance in many areas, particularly his exceptional expertise in analytical modelling and dynamic material characterisation experiments.
- Prof. S. Kok from the Department of Mechanical and Aeronautical Engineering at the University of Pretoria, for sharing his extreme proficiency in the areas of viscoelasticity and parameter identification.
- Prof. A. Chinsamy-Turan from the Department of Zoology for contributing her passion and expertise on the investigation of bone histology.
- Mr. C. Harris from the Department of Human Biology who has spent hours machining bone specimens to exact tolerances. Mr. L. Watkins, a master of the lathe, for machining the tapered strikers. The staff at the Centre for Materials Engineering, in particular Ms. P. Parks-Ross for her friendly assistance with the operation of equipment in the laboratory. Mr. O. Strijdom from the Structural Laboratory at the University of Stellenbosch for his assistance with the MTS test machine. Dr. S. Chung for his proficient operation of the high-speed camera.
- The members of the Blast Impact and Survivability Research Unit (BISRU), especially to Dr. D. Bonorchis, Dr. M. Theobald and Mr. R. Govender who have honoured me with many discussions and frequent input on all aspects of this study.
- My parents, Wessie and Magdaleen van der Westhuizen, for their ceaseless wisdom, support and inspiration.
- Bernard Bekker for his priceless companionship and love on this exhilarating journey of post-graduate study.

Contents

List of Figures

List of Tables

Nomenclature

Upper Case Symbols

A	area
$\mathbf{B}$	left Cauchy-Green deformation tensor
$\mathbf{C}$	right Cauchy-Green deformation tensor
$\boldsymbol{C}$	damping matrix
E	Young's modulus
$E(t)$	relaxation modulus
$\mathbf{F}$	deformation gradient tensor
F	force
$\boldsymbol{F}$	force matrix
G	shear modulus
G_{amp}	amplifier gain
H	Heaviside step function
$\mathbf{I}$	unit tensor
I	impedance of a material
I_i	invariants of $\mathbf{B}$
I_M	impulse transferred to the input bar
K	calibration factor which relates voltage to bar stress
K_{gf}	gauge factor
$\boldsymbol{K}$	stiffness matrix
L	length
M	momentum
$\boldsymbol{M}$	mass matrix
N	denotes a number
P	power that describes the relationship between the Voigt stress and strain rate
P_R	probability function
R	relaxation function
R_i	modelling parameters
V_{bridge}	bridge voltage

$\mathbf{X}$	initial position vector of a material particle

Lower Case Symbols

c	speed of sound in the material
d	diameter
f_c	modelling parameter
f_d	modelling parameter
f^2	mass scaling factor
k_i	coefficients of elasticity
m	risk function modelling parameter
m_i	element mass
n	number of time increments
$\mathbf{p}$	pressure tensor for a viscoelastic material
r	radius
t	time
u	elongation or contraction
v	particle velocity
$\boldsymbol{x}$	position vector of a material particle
x	position coordinate
$\boldsymbol{y}$	a state space vector

Greek Symbols

α	modelling parameter
β	modelling parameter
δ	*dirac-delta* impulse function
ε	true strain
$\dot{\varepsilon}$	true strain rate
$\boldsymbol{\varepsilon}$	Green deformation tensor
$\dot{\boldsymbol{\varepsilon}}$	strain rate tensor
γ	modelling parameter
η_i	coefficients of viscosity
ν	Poisson's ratio
$\boldsymbol{\Omega}$	constitutive functional
ω	frequency
ψ	strain energy potential
ρ	material density
$\boldsymbol{\sigma}$	Cauchy stress tensor

σ	true stress
σ_c	quasi-static compressive strength
σ_c^d	dynamic compressive strength
σ_{ut}	ultimate stress
τ	integral variable of time
θ_i	relaxation time
ζ	damping ratio

Subscripts

b	bar
f	failure
I	incident wave
R	reflected wave
s	striker
sp	specimen
T	transmitted wave
ut	ultimate

Acronyms

AIS	Abbreviated Injury Scale
BA	bone axis
BISRU	Blast Impact and Survivability Research Unit
BMD	bone mineral density
FDM	finite difference method
FEM	finite element method
FE	finite element
PMHS	post mortem human surrogate
CT	computer tomography
IC	injury criterion
LMM	lumped mass model
PMA	post mortem age
LA	longitudinal axis
RA	radial axis
RP	reference point
SEM	scanning electron microscope
SHPB	split Hopkinson pressure bar
TA	tangential axis

Chapter 1

Introduction

1.1 Background

The foot-ankle complex is the most vulnerable body region of vehicle occupants subjected to anti-vehicular (AV) blast landmines [1]. Although not life-threatening, foot-ankle injuries are associated with a high risk of long-term impairment and ending of a military career [2]. During the war in Afganistan the lower extremity fracture incidence of vehicle occupants as a result of AV-mine explosions is 64% (as reported by Bir et al. [3] from Nechaev et al. [4]).

A cross section of an AV-protected vehicle is presented in Fig.1.1. The diagram was obtained from a finite element model by Giliomee and Van der Walt [5]. The model includes a landmine protected vehicle hull with a single seated passenger. The bones of the lower extremity and possible locations of AV-mine threats are superimposed on the model diagram. The detonation of an AV-landmine anywhere under the vehicle hull results in the deformation of the vehicle floor. The vehicle floor transmits a compressive load to the plantar foot surface [*plantar foot surface:* pertaining to the sole of the foot] of the occupant, which is channelled through the bones of the foot/ankle complex. This ultimately results in the axial compression of the tibia. **The lower extremity injury criterion (IC) for anti-vehicular (AV) landmine resistant vehicles is based on an axial force threshold of** 5400 N, measured in the lower tibia load cell of a Hybrid III crash test dummy during ballistic impact [6]. The IC stems from tests on Post Mortem Human Surrogates (PMHS) (Yoganandan et al.[7]) and represents a 10% risk of simple ankle/foot fracture for dynamic impact to the plantar foot surface. According to the South African Military Standard (RSA-MIL-STD-37 [8]) survivability in landmine protected wheeled vehicles shall be calculated using a 10% probability threshold values for Abbreviated Injury Scale (AIS) 2+ injuries. An injury of AIS 2+ categorically corresponds to *moderate injury*, which includes simple fracture of the tibia, patella or pelvis.

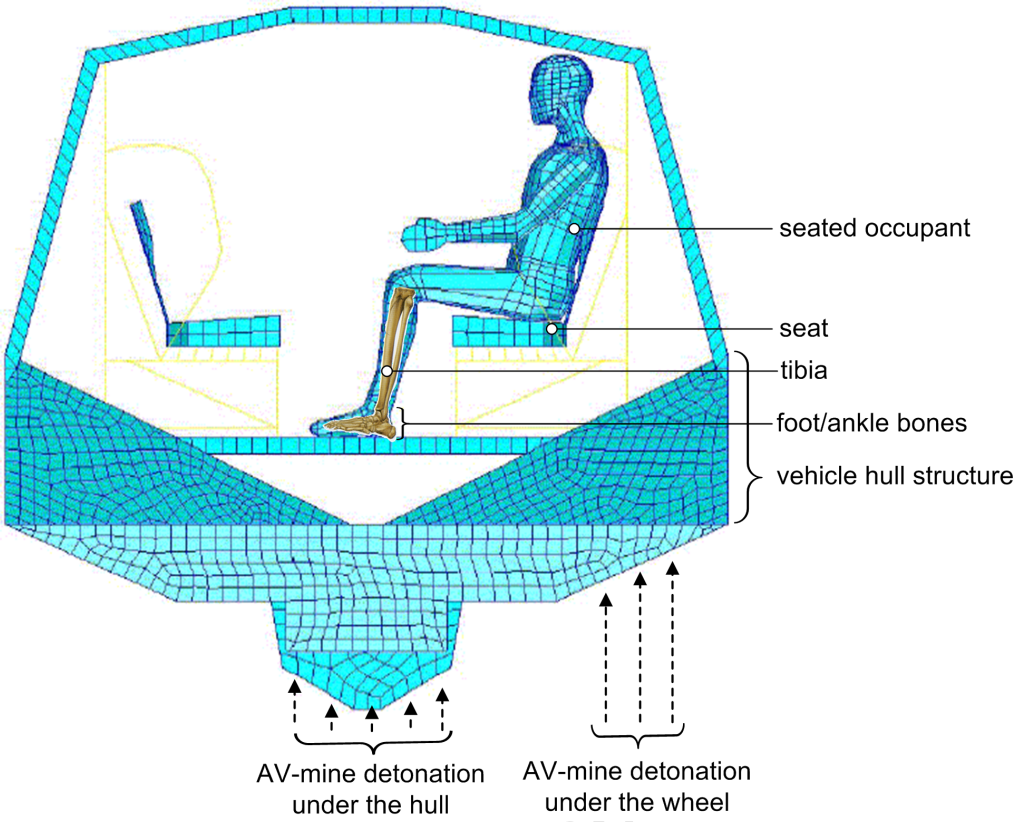

Figure 1.1: A finite element model of a seated occupant in an AV-mine protected vehicle hull by Giliomee and Van der Walt [5]. The bones of the lower extremity and possible AV-mine threats are superimposed.

The PMHS experiments by Yoganandan et al. [7] were designed to simulate lower extremity trauma sustained during frontal vehicular impact. The specific loading conditions of frontal vehicle impact are likely to differ from those due to the dynamic deformation of a vehicle structure that compresses the lower extremity during an AV blast. For one, the occupant lower extremity musculature is expected to be relaxed during an AV-blast, whereas Achilles tension is present in panic braking for frontal automotive crashes [9]. The active musculature pre-loads the tibia in compression and disposes it to injury. Furthermore, the effective load of AV landmine blast on the occupant lower extremity depends on many factors, such as the location of detonation, stand-off distance and hull protection structure. Wang et al. [10] noted that, in a medium sized armoured vehicle with a conventional hull, the average floor acceleration and velocity typically exceed 100 g and 12 ms^{-1}, respectively. The addition of protective structures to the vehicle hull (such as using a false vehicle floor built from energy absorbing materials [10]), potentially attenuates both, the average floor acceleration and velocity. **The injury assessment of occupants of landmine protected wheeled vehicles therefore involves knowledge of the response of the lower extremity at a variety of loading rates.**

Hight [11] conducted an investigation for the Air Force Aerospace Medical Research Laboratory (AFAMRL) which was concerned with the computational modelling of emer-

gency ejections from high-speed aircraft. The injury assessment of occupants in this hazardous environment required the development of an injury criteria for long bones. **Hight [11] concluded that the strength and other properties of bone are time dependent and therefore expressed the need for a bone fracture criterion which includes a loading-rate dependency.** A criterion was consequently developed (expressed in terms of strain rate or load duration) on the basis of data from McElhaney [12] who conducted strain rate dependent compression tests on bone from human and bovine femurs. In the light of the work of Hight [11] **it is deemed necessary to extend the lower extremity injury criterion (IC) for anti-vehicular (AV) landmine resistant vehicles, which only specifies an absolute force threshold at present, to include loading rate or duration.**

A more detailed understanding of lower extremity and bio-material response is necessary to estimate human predisposition to injury due to AV blast landmines. The properties of long bones are of particular interest as the lower extremity IC pertains to the fracture and response of the tibia. The load bearing ability of long bones is ascribed to cortical bone, which is a dense laminar tissue (Vigue [13]). Cortical bone tissue is primarily situated in the diaphysis [*diaphisis:* the middle, shaft region] of long bones (such as the tibia and femur).

1.2 Problem definition

The strain rate dependent dynamic properties of cortical bone have been investigated by several researchers in the last century. The works of McElhaney et al.[12], Crowninshield and Pope [14], Katsamanis and Raftopoulos [15] and Tanabe and Kobayashi [16] **state the strain rate of testing, but do not include the strain rate histories of the reported bone response.** Tennyson et al.[17], Lewis and Goldsmith, [18] and Ferreira et al.[19] observed that conventional dynamic experiments did not result in a constant strain rate test. All the researchers concluded that the response of cortical bone is highly strain rate dependent. **Given the evident sensitivity of bone response to strain rate, Adharapurapu et al. [20] hypothesised that a varying strain rate during a test could result in the measurement of a smeared response.** Adharapurapu et al. [20] subsequently succeeded in conducting a constant strain rate experiment by using the pulse shaping technique on the Split Hopkinson Pressure Bar (SHPB). Although Adharapurapu et al. [20] reported that both constant and non-constant strain rate compression experiments were conducted, no comparison was made between the bone responses measured in the two experiments. **At present it is unclear what the anticipated effect of a *varying strain rate history* is on the responses reported in existing literature.**

The computational simulation of the complex, dynamic interactions of the human body in harsh environments has become an extremely useful and cost-effective research

and development tool (Hight [11]). The evaluation of protection systems for vehicle occupants is greatly aided by computational models which are able to approximate human response under AV mine blast conditions. **The computational representation of the lower extremity in AV blast conditions requires both, an understanding of the thresholds of bone injury, and the response of bones prior to injury.**

Literature concurs that the suitable material models for cortical bone are viscoelastic. Standard finite element (FE) packages facilitate the use of viscoelastic models with parameters that are determined from relaxation or creep experiments. Testing techniques are well developed for these tests at quasi-static load or strain rates. However, no dynamic relaxation test methodology was found in literature to perform what would be a highly challenging experiment. At present an alternative experimental and modelling approach is required to establish a constitutive framework for dynamic viscoelasticity. Tanabe and Kobayashi [16], Tennyson et al.[17] have proposed viscoelastic models to approximate cortical bone response based on quasi-static and dynamic bone compression experiments. **Again, as the exact strain rate histories were not reported the strain rate dependent models developed require further investigation.** Shim et al.[21] presented a viscoelastic constitutive model for the strain rate dependent response of cancellous bone from the human cervical spine. This model results in an excellent approximation of cancellous bone compressive response which was acquired from constant strain rate quasi-static and dynamic experiments. Shim et al.[21] furthermore extended this viscoelastic relation to an isotropic 3-D model such that it contains the 1-D model as a special case. This model for cancellous bone is particularly attractive in that it provides a constitutive framework from which a computational material model can be developed for implementation in FEM.

The hypothesis of this work is therefore to:

- **Establish the strain rate dependent mechanical properties of cortical bone in longitudinal compression and investigate the effect of strain rate history on the resulting dynamic bone response. This involves the development of an experimental technique by which the constant strain rate dynamic response of cortical bone can be determined.**
- **To propose a suitable viscoelastic constitutive model for the strain rate dependent response of cortical bone.**
- **To extend this model to 3-D and implement it in FEM such that it can be used in computational simulations.**

1.3 Thesis outline

1. Literature review
    - The factors that influence bone fracture
    - Measurement of bone response
    - Bone as a viscoelastic material
    - Expressions for bone strength
2. Bone microstructure
    - The preparation of bone for histological examination
    - Histology of bovine cortical bone
3. Bone compression experiments
    - Specimen preparation
    - Quasi-static bone compression tests
    - Dynamic testing of bone on the Split Hopkinson Pressure Bar(SHPB)
4. Experimental results
    - Compression response for specimens with a longitudinal orientation
    - Compression response for specimens with a radial orientation
    - Compression response for specimens with a tangential orientation
5. Constitutive model
    - Development of viscoelastic constitutive relations
    - The constitutive modelling of strain rate dependent bone response in 1-D
    - An isotropic expansion of the 1-D model to 3-D
6. Model verification and validation
    - Verification of an isotropic VUMAT for bovine cortical bone for use in FEM
    - Comparison of FEM model results to quasi-static and dynamic experiments
7. Conclusions and recommendations

Chapter 2

Literature Survey

The biological material of the human body is organised into cells, tissues, organs, and individual organisms. The skeleton is composed of bone and cartilage. Bone is a living, highly specialised, hard form of connective tissue that forms most of the skeleton. This tissue provides protection for vital organs, storage for salts and a continuous supply of new blood cells [22].

The dominant function of bone is to provide support to the body, thus providing a mechanical basis for movement. Movements of the body tend to load the skeletal structure which it supports. External forces, such as impacts between sports players or collisions between vehicles, also load the bone structure that protects vital organs and prevents the excessive deformation of surrounding tissues. The particular interest of the present work is the compressive loading which results in the lower extremity of vehicle occupants which are subjected to an anti-vehicular (AV) landmine blast.

The goals of the literature study are to:

- Describe the physiology of long bones and particularly cortical bone material.
- Report the factors that influence bone fracture.
- Study publications on the experimental methods required to determine the stress-strain relationship of cortical bone.
- Summarise existing stress-strain relations that convey the most important mechanical properties of cortical bone material during the loading process.
- Investigate the existing relations of bone strength and fracture risk.

2.1 The physiology of long bones and cortical bone material

The broader motivation for the present work is the definition of the injury thresholds and response of cortical bone, which provides structural integrity to the foot/ankle complex of occupants of wheeled landmine protected vehicles. As described in Section 1.1, the detonation of an AV-landmine anywhere under a vehicle hull results in the deformation of the vehicle floor. The vehicle floor transmits a compressive load to the plantar foot surface of the occupant, which is channelled through the bones of the foot/ankle complex and the long bones of the lower extremity. The bones of the lower extremity are illustrated in Fig.2.1(a) as presented by Vigue and Martin [13].

Radonic et al. [1] reported on injuries from AV landmines during the war in Croatia. Of the 42 vehicle related occupant injuries, two cases of traumatic amputation of the lower leg was noted with calcaneous fractures of the opposite leg. An additional six calcaneus fractures were reported with two additional incidences of tibia fractures and a single incidence of a femur fracture.

The calcaneus is the largest of the bones of the foot (Fig.2.1(c)) and forms the posterior projection of the heel. This bone comprises of an outer shell of cortical bone (compact) with an inner core of cancellous (spongy) bone. The fibula is a long bone which acts as a stabiliser for the foot/ankle complex. Funk et al. [23] quantified fibula load sharing during dynamic axial loading of the lower extremity (by pendulum impacts at $7\,\mathrm{ms}^{-1}$). The fibula was found to bear significantly less relative load in specimens sustaining foot/ankle fracture. In specimens not suffering foot/ankle injury, it was estimated that 23% of the dynamic axial load was supported by the fibula. The tibia is the primary structural element of the lower extremity below the knee. The large, superior extreme of the tibia forms part of the knee joint, whereas the smaller inferior extreme articulates with the fibula and talus bones to form the ankle joint (Vigue and Martin [13]). The tibia has a long central diaphysis (Fig.2.1(b)) which comprises of a cortex of cortical bone. In humans, the tibia is the most common long bone to fracture (Moore and Dalley [22]). The tibia is at its narrowest at the junction of its middle and inferior thirds, a site that is located on the bone diaphysis and which is the most common site of fracture [22].

A section of the tibia diaphysis is presented in Fig.2.1(d). The inner and outer bone surfaces are respectively covered by the endosteum and periosteum. The cortex of the diaphysis comprises of cortical bone tissue, which is responsible for the load bearing ability of this material. The medullary cavity is a duct which occupies the centre of the diaphysis of long bones and contains the bone marrow.

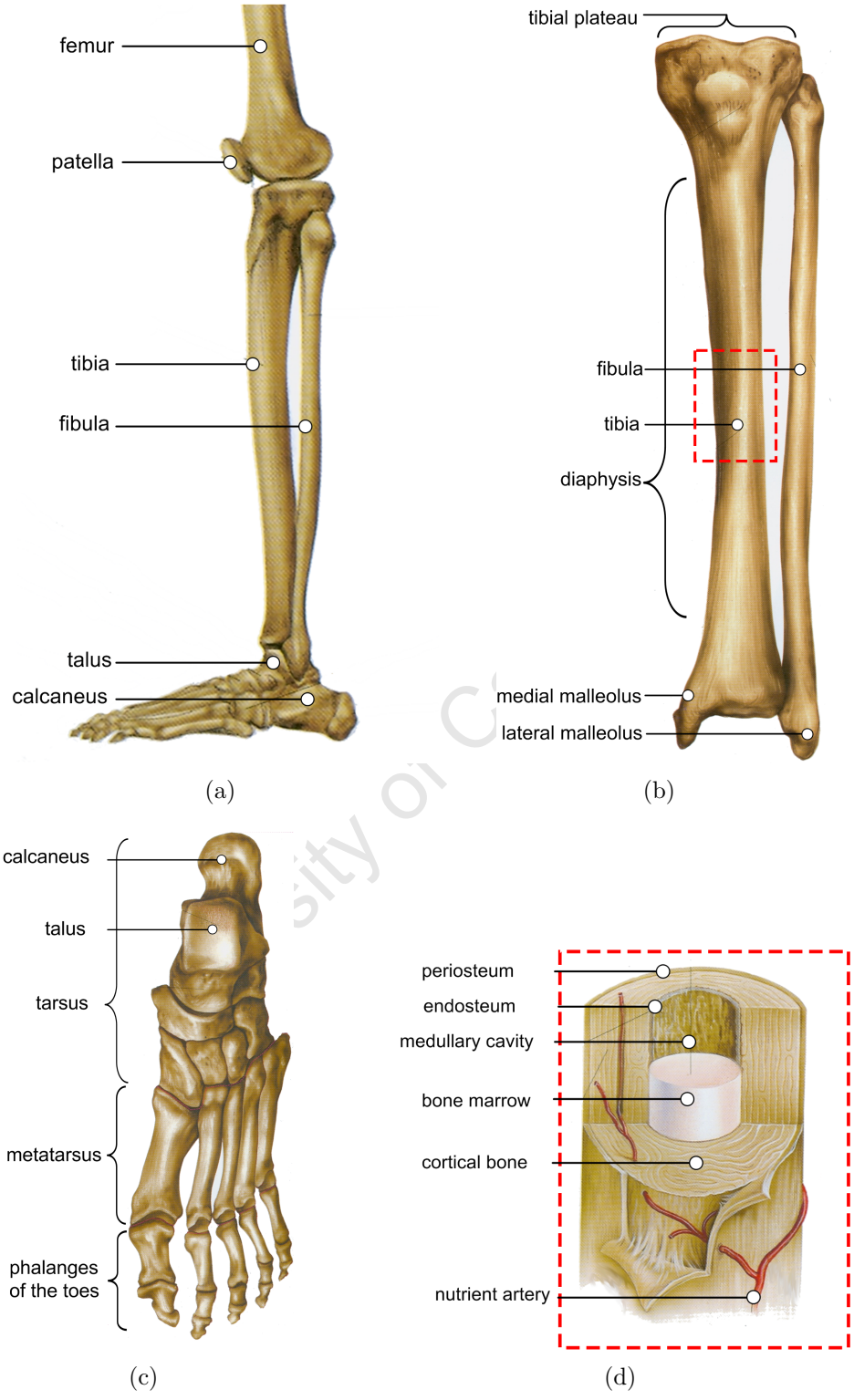

Figure 2.1: Sketches of (a) the bones of the human lower extremity, (b) an anterior view of the tibia and fibula, (c) the bones of the foot and (d) a section of the mid-diaphysis of a long bone as presented by Vigue and Martin [13]

Structurally, bone consists of cortical and trabecular (cancellous) bone. Cortical bone is a dense, laminar tissue bone which is structured as a shell on the outside surface of skeletal bones [13]. Cancellous or spongy bone can be recognised by its lattice structure. The pores of the lattice are filled with marrow, which contains red blood cells and which also has a structural function. Cortical bone has a hierarchical structure, which means that it contains various different structures on various levels of scale. The structures of cortical bone tissue are illustrated in Fig.2.2.

An osteon is the functional unit of osseaous tissue, which is also known as the Haversian system. Osteons are composed of cylinders of osseous laminae arranged around the central canal. The Haversian canal forms the central duct of the osteon. This canal contains cellular fluids as well as vascular and nervous terminations. A Volkmann's canal is a transversal duct that links the Haversian canals of the osteons. Intraosseous capillaries are vascular terminations that occupy the central canal of the osteon and transport arterial blood (Vigue and Martin [13]).

On a further level in the bone hierarchy small spaces are observed in the bone matrix. These spaces are the lacunae (Latin for "lakes") which serve in the place of vessels for the circulation of the fluids of the body. The lacunae are connected to each other through tiny channels or canaliculi which run through the laminae that comprise the osteons (Vigue and Martin [13]). The osteocytes, or cells which form the bone tissue are lodged in the lacunae. Table 2.1 summarises the relevant sizes of the structures in the bone tissue hierarchy.

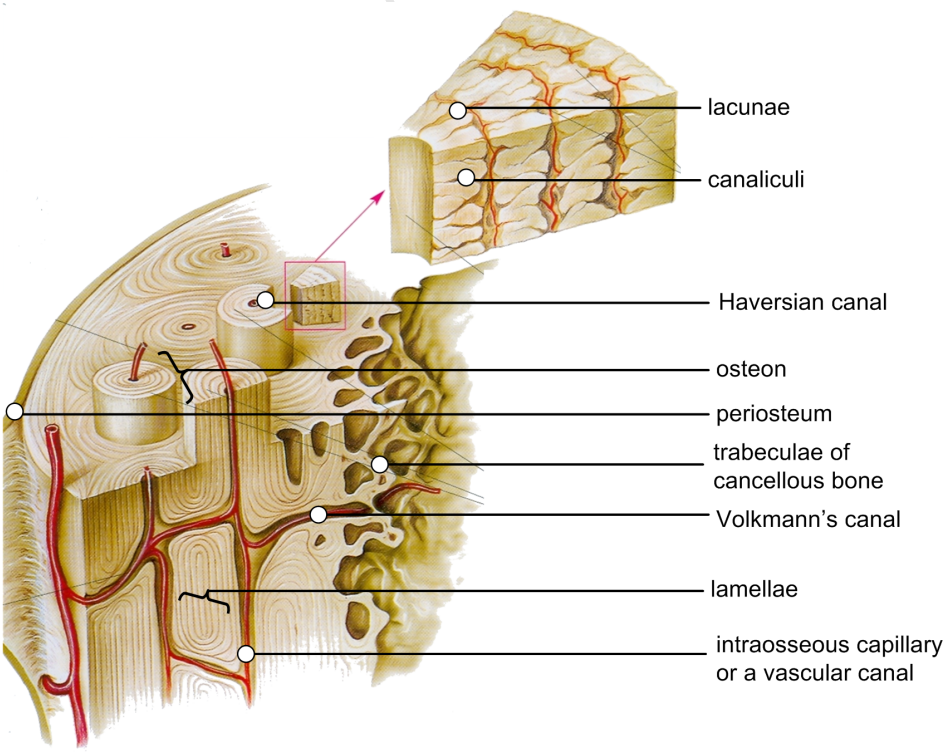

Figure 2.2: A diagram of cortical bone structure as described by Vigue and Martin [13]

Level	Cortical structure	Approximate size
0	Solid material	$\geq 3000\,\mu$m
1	Primary osteons (found in primary lamellar cortical bone) [24] Secondary osteons (found in secondary cortical bone) [24] Plexiform structure (found in plexiform bone) [24] Interstitial bone [24]	100 to $300\,\mu$m
2	Lamellae Lacunae Cement lines (found in secondary cortical bone)[25]	3 to $20\,\mu$m
3	Collagen mineral composite [26]	0.06 to $0.6\,\mu$m

Table 2.1: The hierarchical structure of cortical bone

The present investigation is directed to bovine cortical bone, with ethical approval to perform experiments on animal material in vitro. This structure will be investigated on a macroscopic level. The smallest volume of material that will be considered is solid bone material which comprises of a great number of cells (Level 0, according to Table 2.1). It is therefore convenient to consider bone material as a *continuum*.

Fung [27] states that: "*The classical definition of a material continuum is an isomorphism of the real number system in a 3-D Euclidean space: between any two material particles there is another material particle. Each material particle has a mass. The mass density of a point* $\mathbf{X}$ *is defined by considering a sequence of volumes* $\mathbf{\Delta V}$ *enclosing* $\mathbf{X}$*. If the mass of particle in* $\mathbf{\Delta V}$ *is denoted by* $\mathbf{\Delta M}$*, and if the ratio* $\frac{\mathbf{\Delta M}}{\mathbf{\Delta V}}$ *tends to a limit* $\rho(\mathbf{X})$ *when* $\mathbf{\Delta V}$ *tends to zero, then* $\rho(\mathbf{X})$ *is the mass density of the continuum at* $\mathbf{X}$".

2.2 Factors that influence bone fracture

As with any material, the components of the human body are expected to have a yield point as well as an ultimate stress threshold where it loses its load bearing ability and fracture occurs. For bone, this fracture threshold is subject to certain factors that will be mentioned briefly and discussed in the paragraphs that follow:

- Material orientation
- Bone mineral density (BMD)
- Gender, stature and age
- Location
- Mode of loading
- Strain rate

2.2.1 Material orientation

Cortical bone is considered to be an orthotropic material with a set of material properties in three orthogonal directions. It grows in such a way that its greatest load bearing capacity is structured in the longitudinal direction. Tanabe and Kobayashi [16] investigated anisotropy of bovine femoral cortical bone. A cartesian coordinate system was specified with 3 axes (Fig.2.3(a)): the bone axis (BA), radial axis (RA) and tangential axis (TA). Specimens were cut at 0°, 15°, 30°, 45°, 60°, 75° and 90° to the BA, RA and TA axes. All specimens showed secondary Haversian systems (i.e. cement lines were present). Five specimens, each from different bones, were tested for every different orientation. Fig.2.3(b) shows that the compressive response of bovine cortical bone is clearly anisotropic. The results indicated that bovine femoral cortical bone response is linear in quasi-static compression, but clearly non-linear under impact conditions. Quasi-static stiffness is greater in the BA direction than in the other two directions. Dynamically, bone is the stiffest in the BA direction, followed by the RA and TA directions.

Tables 2.2 and 2.3 show some values that have been published for bone as a 3-D orthotropic material. The 1, 2 and 3 directions correspond to the radial, tangential and axial directions respectively. The values given here were determined from quasi-static tests. **No orthotropic models were found for bone under dynamic loading.**

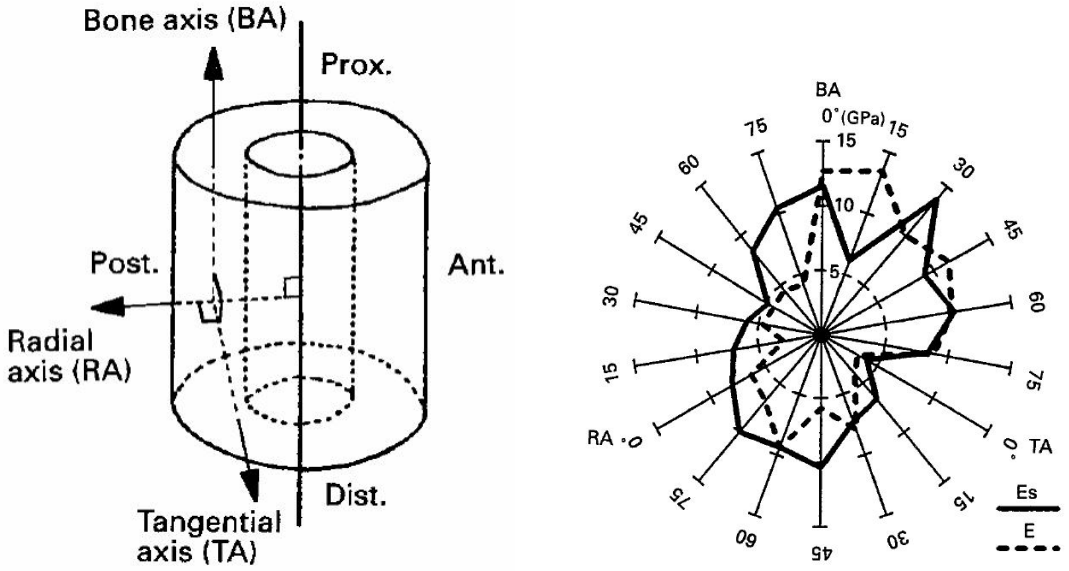

(a) (b)

Figure 2.3: (a) The cartesian bone axis for the anisotropic characterisation of bone and (b) the variation of static and dynamic Young's modulus with bone direction as determined by Tanabe and Kobayashi [16]

Author	Bone details	E_1 [GPa]	E_2 [GPa]	E_3 [GPa]	G_{12} [GPa]	G_{23} [GPa]	G_{13} [GPa]
Krone [28]	Human femur	6.30	6.88	16.00	3.60	3.20	3.30
Lasaygues [29]	Bovine femur 1	20.6	23.4	30.2	3.0	4.6	3.0
	Bovine femur 2	18.8	20	28	2.9	2.8	3.7
Ionescu [30]	Human tibia	6.91	8.51	18.4	2.41	3.56	4.91

Table 2.2: Anisotropic elastic constants and shear moduli for cortical bone

Author	Bone details	ν_{12}	ν_{23}	ν_{13}	ν_{21}	ν_{32}	ν_{31}
Krone [28]	Human femur	0.45	0.30	0.30			
Lasaygues [29]	Bovine femur 1	0.12	0.18	0.2	0.21	0.24	0.29
	Bovine femur 2	0.26	0.17	0.17	0.28	0.25	0.26
Ionescu [30]	Human tibia	0.49	0.14	0.12			

Table 2.3: Anisotropic Poisson's ratios for cortical bone

2.2.2 Bone mineral density (BMD)

During cadaver ankle impact tests, Dubbeldam et al. [31] correlated a resistance to leg injury with a high BMD. Groups sustaining malleolar and soft tissue injuries were shown to have relatively high BMD measurements; whereas structural injuries, such as talar and calcaneal fracture, corresponded to low BMD. In humans BMD decreases with age, which explains why the elderly are more prone to bone fracture injuries. BMD also varies between bones. The calcaneus and talus are more spongy compared to the tibia, and therefore have a lower BMD.

Shim et al. [21] defined *apparent bone density* as the density of the bone mineral without the fat and liquids. **It is most appropriate to find the correlation between bone strength and apparent density because the fat and liquids do not contribute appreciably to the load bearing ability of the structure.** Shim et al.[21] stated that it could be argued that marrow and fat should be removed from specimens before testing to allow for the correlation of apparent density to bone strength. However the removal of fat has proven cumbersome. Sharp et al. [32] remarked that water and air jets are unlikely to remove fat from the intertrabecullar spaces deep within the specimens. The water jets tend to disintegrate compression test specimens and produce loose fragments, while alcohol is not an effective fat solvent. Sharp et al. [32] used the chemical solvent trichloroethylene, to effectively remove the marrow and fat from specimens. Shim et al. [21] defatted cancellous bone specimens by using an ultrasonic bath of trichloroethylene, followed by centrifuging, to remove liquid from the pores in order to obtain apparent bone density. **However, due to the destructive nature of high strain rate testing and the concern that chemical solvents may affect the mechanical properties of bone, Shim et al. [21] correlated compressive bone strength to *fresh bone density* instead.** Fresh bone density is calculated:

$$\rho = \frac{\text{total mass of bone specimen}}{\text{specimen volume}} \tag{2.1}$$

Bone density is dependent on the location from which the specimen is extracted because **the internal structure of bone is not homogeneous. This necessitates the measurement of density for every specimen [21].**

2.2.3 Gender, stature and age

Rittweger et al. [33] proved that females have lower bone fracture thresholds than males of the same age. This is in part due to the smaller cross sectional area of female bones which results in a smaller force carrying capacity. However, the bones of female athletes show greater cortical wall thickness and have been shown to have a similar bone cross sectional area to that of normal men. Women, in general, also have more bone mineral

per muscle tissue than men [33].

Zioupos and Currey [34] report that ageing adversely affects the elastic and ultimate properties of human cortical bone. This observation is consistent in quasi-static loading, high strain rate impact and fatigue. The responses of older bones are generally more brittle than younger ones. Younger bone is more compact and homogeneous in that it has fewer weak interfaces, such as remodelling cavities and secondary osteons (which form in remodelling cavities). Zioupos and Currey [34] observed that the crack patterns in older bone is therefore more deflected or zig-zagged than it is in younger bone. The consensus in literature is that human bone reaches maturity by the age of 30 to 35 years, after which it deteriorates [34]. In their study of 129 healthy female individuals, Saeed et al. [35] found a consistent decrease in the speed of sound in the tibia (cortical bone) of women above the age of 40 years. A decrease in the speed of sound is indicative of deteriorating bone mineral density.

2.2.4 Location

The location on the bone from which samples are extracted should be carefully noted. **According to Morgan and Keaveny [36], the properties of bone and soft tissue materials can depend much on the location in the human body, i.e. it may vary from member to member and within an individual part.** Certain bones of the body are more prone to fracture than others. In humans, the tibia is the most common long bone to fracture. Possible reasons for this include that it is not supported antero-medially throughout its length. The tibia is at its narrowest at the junction of its middle and inferior thirds, a site that is located on the bone diaphysis and which is the most common site of fracture according to Moore and Dalley [22]. The bone on the tibial plateau (where it articulates at the knee) is reported to be twice as dense and therefore stronger than a sample extracted from the mid-shaft region. A thorough study of epidemiologies could highlight the most dominant causes and locations of bone fracture. **Specimens should thus be extracted from these sights and tested at the mode and rate of loading relevant to the epidemiology.**

2.2.5 The mode of loading

Moore and Dalley [22] report that the mode of loading has an effect on the type of fracture that results in a bone. Clinically a diagonal fracture of the tibia could result from severe torsion. A high speed forward fall, such as in skiing where the leg is bent over a rigid ski boot, results in “boot top fractures”. Here the bone fractures into several pieces at the middle and distal thirds. Tibial fractures might also result from direct trauma, such as that inflicted by the bumper of a car. Pedestrians often present with compound (open) fractures where both the tibia and fibula fractured in a transverse fashion [22]. The

conclusions of material scientists such as Mercer et al. [37] and Ebacher et al. [38] seem to agree with clinical observations of Moore and Dalley [22] that the mode of loading affects the type of fracture. Mercer et al. [37] reported a cross-hatching, shear band formation in cortical bone under compression. These bands were observed by investigating fractured microstructure with a combination of bright field and epi-fluorescence optical microscopy, as well as BSE electron microscopy.

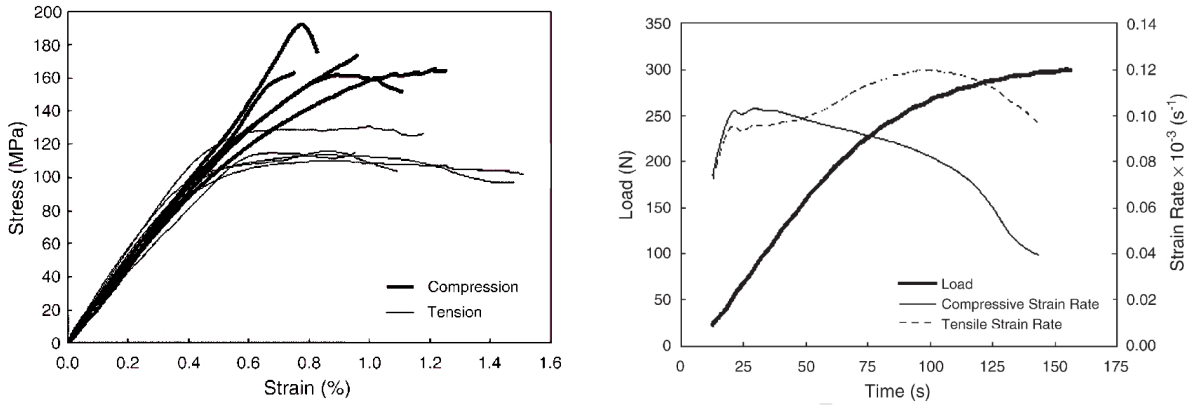

(a) Stress-strain response

(b) Strain rate history

Figure 2.4: Comparison of compressive and tensile bone responses for human tibial cortical bone as reported by Ebacher [38]

Ebacher et al. [38] illustrated that cortical bone exhibits inelastic responses that differ in tension and compression (Fig.2.4). This agrees with the findings of Reilly and Burnstein [39] and Carter and Hayes [40]). Bending of both cortical bone specimens (specimen orientation along the bone axis) and whole tibia mid-diaphysis shafts shows a difference in micro- and macro-damage morphologies. Microdamage of the compression surface shows cross-hatching microdamage far away from the final fracture site (Figs.2.5(a) and 2.5(b)), whereas the tensile surface shows diffuse microdamage at the final fracture site (Figs.2.5(c) and 2.5(d)). On macro scale, whole tibia bone diaphyses (Fig.2.6(b)) in bending failed similarly to standard cortical bone specimens (Fig.2.6(a)) in terms of strain redistribution, microdamage development, and macro-scale fracture patterns. Shear angles formed by individual microcracks ($28.4 \pm 4.5°$) and macro-scale cracks ($27.4 \pm 7.4°$) were very similar. "Butterfly" bending fractures observed clinically in long bones are most probably the result of a compressive failure as well as a tensile failure of bone material starting at the microstructural level.

Even though the failure mechanism differs from tension to compression, the response prior to tensile yield is similar (Ebacher et al. [38] in Fig.2.4(a)). Fig.2.4(b) shows the resulting strain rate response found by Ebacher et al. [38] when bone specimens were subjected to an identical quasi-static load in tension and compression. Notice that the rate at which the specimens strain is initially similar for both load cases ($\dot{\varepsilon} = 10^{-3}\,\mathrm{s}^{-1}$). After about 50 s bone specimens responded differently in tension and compression. The strain

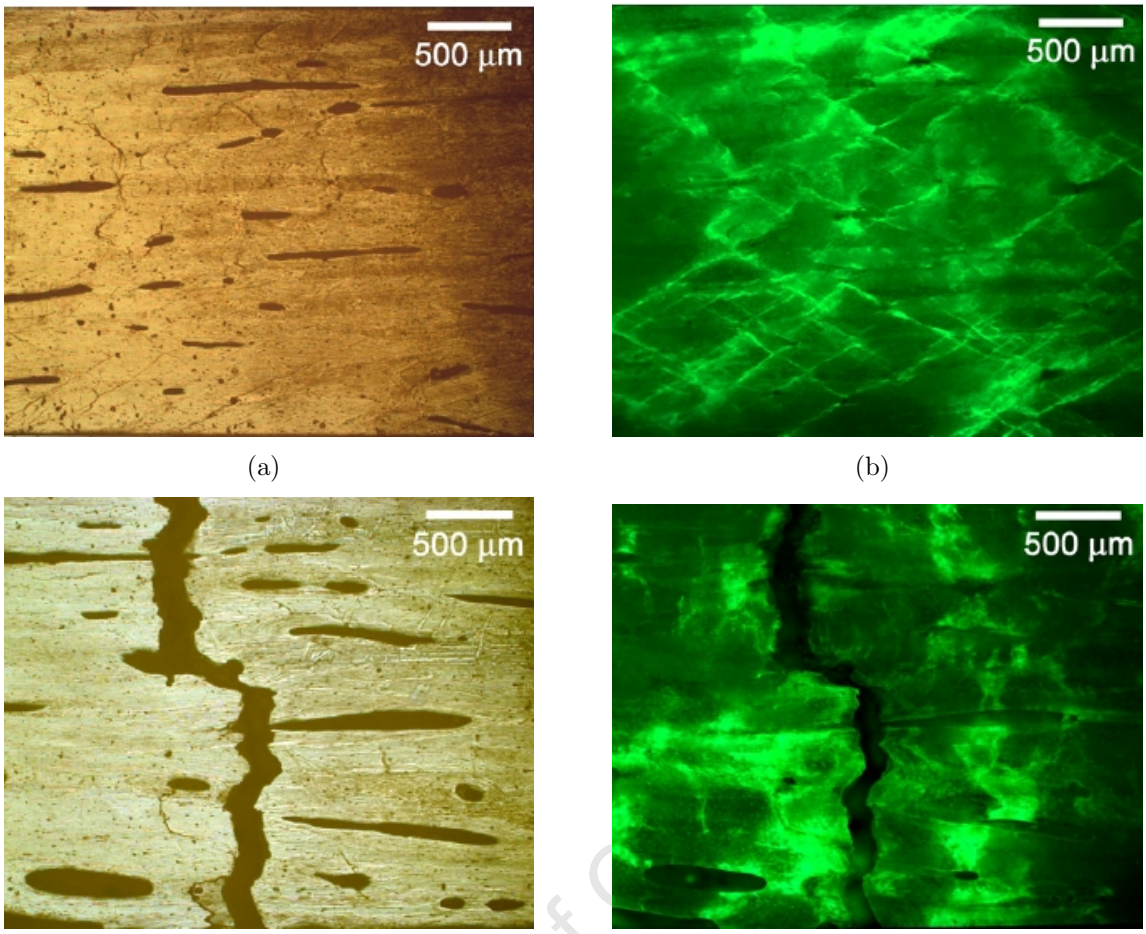

Figure 2.5: Micrographs of the differences in cortical microdamage due to compressive and tensile loads. (a) Compressed cortical bone microstructure and the resulting (b) cross-hatching microdamage far from the crack surface. (c) Cortical bone microstructure as a result of tensile loading shows (d) diffuse microdamage at the fracture site as reported by Ebacher et al. [38]

rate tended to decrease in compression where it tended to increase in tension. The observation that the Young's modulus of bone is similar in tension and compression at quasi-static strain rates is also reported at dynamic strain rates. Katsamanis and Raftopoulos [15] reported no significant difference in the dynamic Young's modulus between tension and compression. The Poisson's ratio remained constant at 0.36 regardless of dynamic or static loading conditions. These findings are in agreement with those reported by Reilly et al. [41] and Bargren et al. [42]. The results of McElhaney et al. [12] do not agree with this in that the Youngs modulus was found to be 35% higher in compression than it was in tension.

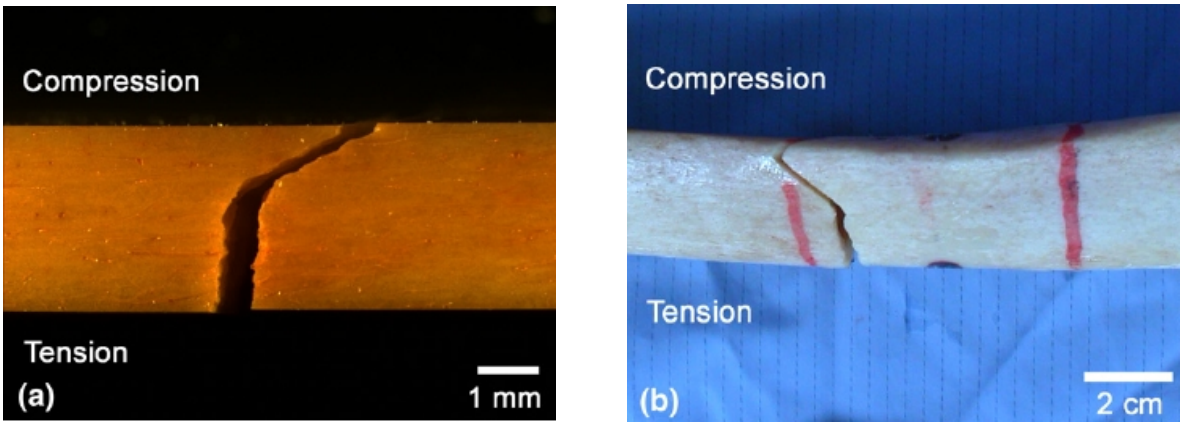

(a) (b)

Figure 2.6: The different fracture mechanisms are visible in the "butterfly" bending fractures which were observed in both (a) bovine bone specimens and (b) whole bovine bone shafts [38]

2.2.6 Strain rate

Strain is defined as the deformation per unit length, therefore strain rate is the rate of deformation per unit length [43]. The stress-strain behaviour of both, cortical and cancellous bone are strain rate dependent [16, 21, 12, 20, 14].

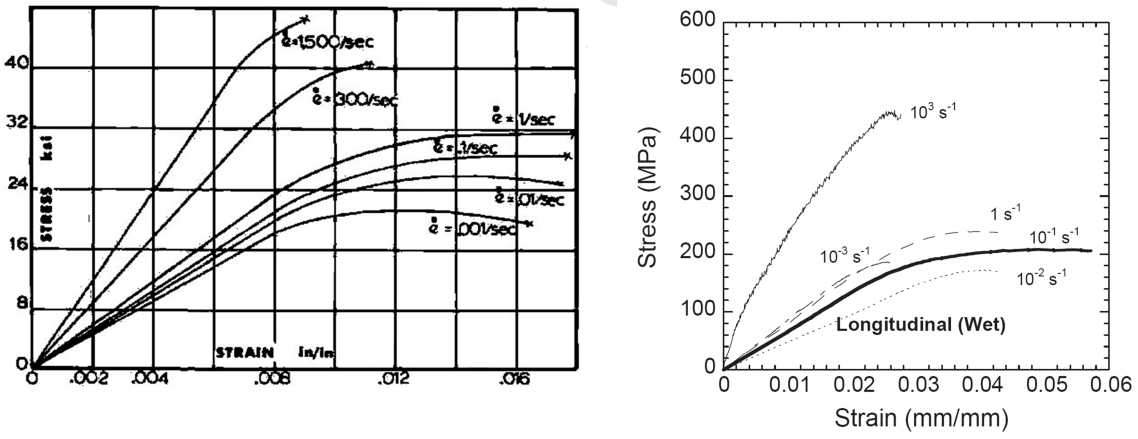

(a) (b)

Figure 2.7: The strain rate dependent response of (a) human femoral cortical bone in compression as determined by McElhaney [12] and (b) bovine cortical bone in compression as determined by Adharapurapu et al. [20]

The effect of strain rate on cortical bone response is characterised by the following observations:

- **Bone fracture is strain rate sensitive in that it occurs at a higher stress and lower strain with increased loading rate (Fig.2.7). This behaviour is relevant to cortical bone response in both tension (Crowninshield and Pope [14]) and compression (McElhaney [12]).**

- **The strain rate sensitivity in bone response is evident for small changes in both quasi-static and dynamic strain rates.**

The exact strain rate histories were not reported along with the stress-strain curves determined for cortical bone by McElhaney [12] or Crowninshield and Pope [14]. The dynamic properties of cortical bone have been investigated using the Split Hopkinson Pressure Bar (SHPB); however the strain rate was not constant throughout the testing period (Katsamanis and Raftopoulos [15] and Lewis and Goldsmith [18]). **Given the evident sensitivity of bone response to strain rate, Adharapurapu et al. [20] hypothesised that a varying strain rate during a test could result in the measurement of a smeared response.** Adharapurapu et al. [20] subsequently succeeded in conducting a constant dynamic strain rate compression experiment on the SHPB (at $10^3\,s^{-1}$) using sacrificial high work hardening alloy pulse shapers. **Although Adharapurapu et al. [20] reported that both constant and non-constant strain rate compression experiments were conducted, no comparison was made between the bone responses measured in the two experiments. At present it is unclear what the anticipated effect of varying strain rate is on the responses reported in existing literature by McElhaney[12], Crowninshield[14], Katsamanis and Raftopoulos [15], and Lewis and Goldsmith [18].** The remainder of this chapter is dedicated to the discussion of the measurement and modelling of the strain rate dependent properties of cortical bone.

2.3 The measurement of bone response

The following discussion considers specimen preparation and storage to facilitate successful experimentation. Subsequent sections summarise the approaches described in literature for the strain rate dependent characterisation of bone by quasi-static and dynamic compression and tension tests.

2.3.1 Specimen preparation

The use of animal tissue to approximate human tissue response

As mentioned earlier, the properties of bone and soft tissue materials depend much on the location in the human body, i.e. it varies vary from member to member and within an individual part [36]. The sensitivity of bone properties to location of specimen extraction therefore imply that bone specimens should ideally be extracted from the exact bone and location of a species with the age for which fracture epidemiology is being studied. The ideal specimens for the characterisation of human bone material should therefore be extracted from the appropriate human bones. However, ethics often require experiments to be developed on the appropriate animal material first.

In literature, human bone properties are mostly obtained from cadaver tests and their behaviour in living bodies [44] can only be approximated. It is important to establish that the cadaver bones do not originate from people who suffered illness, such as osteoporosis, that would have affected bone strength. Mechanical properties of cadaver bones often originate from older individuals and therefore have a predisposition to lower bone density (as previously explained in Section 2.2). McElhaney [12] obtained human bone specimens from the right femur of a 24-year-old white male who died of acute cardiac failure. The sample had been embalmed with a mixture of formalin, phenol, alcohol, and glycerine, and was typical dissecting room material. Currey [45] reported that embalming degenerates the stiffness and strength properties of bone.

Evans et al. [46] reported that **various types of bone can be compared provided, that it is of the same histological type and has a similar number of osteons and osteon fragments per unit area.** Haversian bone [*Haversian bone:* is a bone structure which comprises of both primary and secondary osteons and is often found in adult human long bones] was used with the aim of extrapolating these results from bovine to human bone. This approach is supported by Ascenzi and Bonucci [47], who reported that bone osteons from different species behave similarly at the microstructural level.

Bovine cortical bone has often been used to do experimental development work for later testing on human cortical bone. Slaughter age cattle is usually obtained from the butchery. Some researchers were able to secure bones immediately following slaughter at a local abattoir [20, 14]. Specimens are mostly extracted from the bone mid-diaphysis

[16, 12, 20, 14, 19, 17]. The middle third of the shaft of both the beef and human femora is most often used [12]. Cortical bone properties have mostly been characterised along the bone axis. In these cases care was taken to maintain the axis of the specimens parallel with the axis of the shaft [12, 20, 19].

Specimen machining, hydration and post-mortem age

Some emphasis is also afforded to the surface finishing of specimens. This avoids localisation of the load during compression on the protruding parts of the uneven top surface. Wet sanding produces a surface finish that is smooth and free from defects, with no heating of the material or moisture loss [20]. Since drying causes significant changes in the mechanical properties of bone, the samples are kept either wet or submerged in water at all times. A small bench miller is employed for the final machining operation. Specimens are stored in a frozen condition, except during specimen preparation [20].

Subsequent to extraction, the time and preparation of bone samples should be noted even though good experimental practice has proved that these effects on material properties can be minimised (Shim et al. [21]). Tennyson et al. [17] conducted compression tests on bone for a range of post mortem ages (PMA) from 1 to 38 days, including a set at 240 days in which the bones were allowed to dehydrate in a refrigerated environment. Tennyson et al. [17] found that bone viscosity decayed by more than 50% within at a PMA of 6 days, whereas the effect of PMA on bone elasticity was only apparent at a PMA of 10 days (Fig.2.8). Compressive bovine cortical bone response is indicative of a viscoelastic material with a strain rate dependent modulus. The effect of dehydration on the material is evident from tests conducted at a PMA of 240 days. Crowninshield and Pope [14] stored freshly machined specimens at -10° C and tested them within 48 hours in accordance with the recommendations by Sedlin and Hirsch [48].

The beef bone specimens used by McElhaney [12] were all extracted from the right femur of a 3-year-old steer. Less than 5 days elapsed from the time the animal was slaughtered to the completion of all tests, except the highest strain-rate test. This test was performed approximately 30 days later. During this period, the material was kept submerged in water and refrigerated. Cutting and machining operations were performed with specimens in a wet condition to minimise temperature effects. Tennyson et al. [17] immersed his specimens in water and refrigerated them at 1.7 °C, using the same approach as McElhaney [12].

Adharapurapu et al. [20] dried all samples in air for 15 days. Two sets of specimens were prepared for testing: the first set was comprised essentially of the dry samples, whereas the second set of samples were hydrated by soaking in Hanks balanced salt solution (HBSS) for at least 30 hours prior to testing. Typically, the difference in mass between the dry and hydrated (or wet) specimen was 4 to 5%. Adharapurapu et al. [20] reported that an earlier investigation by Currey [49] had shown that the effects of drying and re-wetting

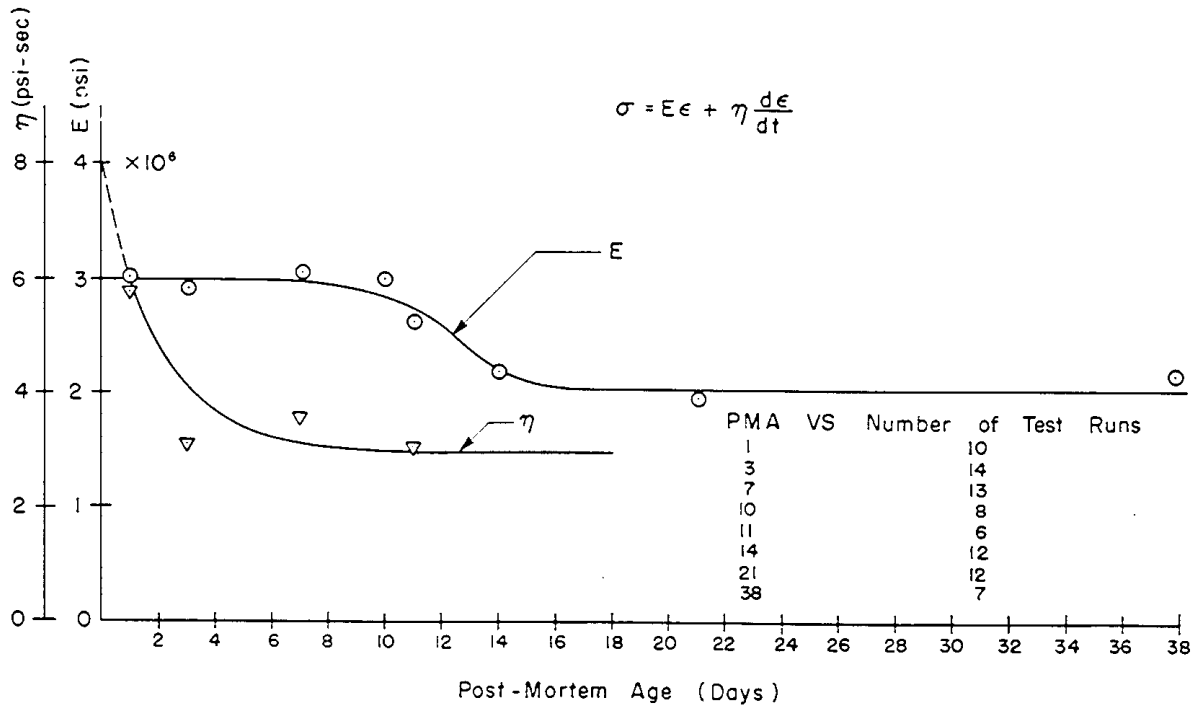

Figure 2.8: The effect of post-mortem age on the mechanical properties of bone specimens as shown by Tennyson et al. [17]

on the mechanical properties of cortical bone is minimal. Therefore, this procedure ensures that the hydrated samples are sufficiently saturated with the salt solution without causing damage to the original bone.

Specimen geometry

McElhaney [12] reported two distinct advantages in using short specimens in dynamic testing:

- The shorter the specimen, the shorter the transit time for stress waves. This means that more reflections will occur in a given test time (the specimen ring-up time will become shorter) and uniform stress will be more closely realised.
- Assuming uniform straining, the strain rate is the velocity of the piston (or compression device) divided by the length. Therefore, short specimens allow for higher strain rates to be obtained with lower striking velocities.

Crowninshield and Pope [14] machined tensile specimens from the mid-diaphyses of bovine tibiae, obtained within 10 minutes after slaughter. Care was taken to machine strips out of bone regions that contained Haversian bone. A total of 46 bone specimens were cut with the gauge length oriented in the direction of the longitudinal axis of the bone (and therefore the average direction of the osteons). A further 25 were machined at an orientation of 90° to the longitudinal axis. The specimen dimensions are shown in

Fig.2.9, which shows that it is possible to machine specimens with a complex geometry from cortical bone.

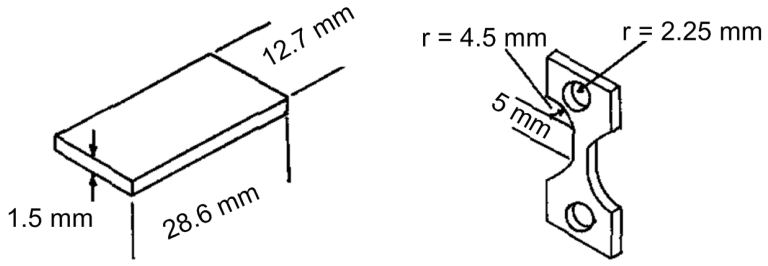

Figure 2.9: Bone specimens used in tensile tests by Crowninshield and Pope [14]

2.3.2 Determination of quasi-static strain rate dependent response

Bone is considered to be viscoelastic material which is expected to display phenomena of both relaxation and creep. Viscoelasticity is further discussed in Section 2.5. Conventionally, viscoelastic materials can be fully characterised by determining their bulk and shear modulus from creep and relaxation tests.

The American Society for Metals [50] states that creep behaviour of a material is usually determined by uniaxial loading of specimens, heated to some temperature in some environment. The load is controlled so that it remains constant and the strain-time response of the specimen is measured. If the test is stopped before failure, the experiment is termed an "interrupted creep experiment". A creep rupture test is an experiment where the creep test is continued up to the point of failure. A single rupture test may extend over many months.

Creep tests determine the material response in terms of strain rate, stress and temperature. The development of these tests can be time intensive and expensive because a successful test could require the use of many test stands, specimens and thousands of hours of testing. A relaxation test eliminates these difficulties [50] because a range of strain rate vs. stress data can be generated from a single specimen.

A stress relaxation test involves loading or straining a specimen to a predetermined load and halting the cross-head, thereby keeping the strain constant. The load is now measured as a function of time. The load will change as a function of time because the elastic strain of the deformed specimen will convert to plastic strain. The permanent deformation of the material implies that the load required to keep the specimen at its deformed length will decrease over time or "relax" [50]. A disadvantage of relaxation testing is that the load-measuring equipment must be capable of measuring very small changes in load over time. The effect of loading rate on relaxation rate should be evident. Furthermore, the surrounding temperature should be precisely controlled and monitored

as changes in temperature could lead to thermal expansion or contraction that could mask the relaxation effect. An inconvenience of relaxation and creep tests are that they are time consuming.

The early stage of stress relaxation, up to 10 seconds after strain application, was studied by Sasaki et al [51]. The relaxation modulus was expressed as a combination of the Kohlrausch-Williams-Watts (KWW) function and an exponential decay function, or Debye function:

$$E(t) = E_0 \left[R_1 e^{-\left(\frac{t}{\theta_1}\right)^{\beta}} + R_2 e^{-\frac{t}{\theta_2}} \right] \tag{2.2}$$

Where $R_1 + R_2 = 1$ and $0 \leq \beta \leq 1$.
E_0 is the relaxation modulus value at $t = 0$, R_1 and R_2 are portions of the first term (the KWW relaxation) and the second term (the Debaye relaxation) respectively, and θ_1 and θ_2 are relaxation times of the respective relaxation processes. β is a parameter that describes the shape of the relaxation function. The relaxation times, θ_1 and θ_2 have respective values of 10^3 and 10^{5-6} s [51]. The early stage of relaxation was characterised by the KWW function and shown to be applicable to data of Lugassy and Korostof (1969) [52]. Goto et al. [53] indicated the existence of a new relaxation in the short time response region at $t \leq 2$ to 3 s that is not described by Eq.2.2. The relaxation fit underestimates the relaxation modulus in the short time relaxation response before approximately 3 s. It was concluded that this short time relaxation is not attributed to overshoot, but to material properties. No alternative relaxation function was suggested.

Iyo et al. [54] suggested a description of the relaxation modulus that is a function of a fast KWW process and a slow KWW process. Bovine femur cortical bone samples were strained to 0.23% within 0.03 s. That is a strain lower than the yield strain of bone at a strain rate of roughly 0.08 s^{-1}. The relaxation modulus was measured for a time of 1×10^5 s^{-1}. The specimen was immersed in saline solution with anti-bacterial agent during testing. Furthermore, the temperature was maintained at 37 °C. In a subsequent study, Iyo et al. [55] increased the time of relaxation testing to 6×10^5 s to develop a relaxation modulus curve with a high level of completeness. The new data showed that the almost linear portion, corresponding to the slow KWW process, was in fact a curve with a large radius of curvature. Iyo et al. [54] describes the relaxation modulus with Eq.2.3, which gives a good description of both the early stage and slow relaxation responses. The second study of Iyo et al. [55] led to the addition of the power γ to the second KWW term (i.e. the same relation was used in [54] but with $\gamma = 1$):

$$E(t) = E_0 \left[R_1 e^{-\left(\frac{t}{\theta_1}\right)^{\beta}} + (1 - R_1) e^{-\left(\frac{t}{\theta_2}\right)^{\gamma}} \right] \tag{2.3}$$

Where $0 \leq R_1, \beta, \gamma \leq 1$.

Long term relaxation response is highly relevant when considering permanent fixations in patients who have to undergo hip or knee replacements or who have to be fitted with pins for fracture setting. **For the purposes of this study, however, the short term relaxation response is more relevant. The techniques and testing machines are well developed for these tests at quasi-static load or strain rates. However, no dynamic relaxation test methodology was found in literature for strain rates of** $10^2\,s^{-1}$ **and above.** The challenge here is that the strain (relaxation test) or load (creep test) must be applied dynamically and halted at a constant level for a long time while the load or strain is measured respectively.

Thus, when dynamic material models are required, an alternative experimental approach is needed. **Most existing studies on the strain rate dependency of bone characterise the material by tensile or compression tests at quasi-static and dynamic strain rates [16, 21, 12, 20, 14].** Quasi-static tests are performed on conventional quasi-static test machines. Adharapurapu et al. [20] conducted quasi-static compression tests ($10^{-3}\,s^{-1}$) on a standard servo-hydraulic testing machine under displacement control. Tanabe and Kobayashi [16] investigated the compressive response of bovine bone prior to yield and conducted quasi-static tests at a strain rate of $10^{-3}\,s^{-1}$ on a Shimadzu AG-25TD materials testing machine.

2.4 Determination of dynamic bone response

Recently, the dynamic characterisation of bone material is mostly performed on the Split Hopkinson Pressure bar (SHPB) by which the material pre-fracture stress-strain response and ultimate properties are obtained. However, the classical studies on the dynamic response of cortical bone were preformed by means of other methods. The following sections will discuss the other methods of dynamic material characterisation and SHPB tests.

2.4.1 Classical studies of dynamic bone response

McElhaney [12]

In 1966, McElhaney [12] investigated the compressive properties of bone at strain rates which ranged from $0.001\,s^{-1}$ (the region of so-called static tests) to $1500\,s^{-1}$. A custom made testing machine was designed to apply compressive loads on small samples at varying rates. The machine was air-operated with a reservoir to store air and a honed cylinder into which a piston was carefully fit. A quick release mechanism was used to hold and release the piston. The piston would compress the specimen onto an instrumented platform, supported by butyl rubber. The load platform was shimmed to control specimen compres-

sion at a level of 0.065 inches ($\approx 1.65\,\text{mm}$). Beyond this point of compression the piston impacts a fibreglass stop, moves the entire platform and compresses the butyl rubber until it is fully decelerated. A piezoelectric quartz load cell was mounted underneath the specimen to record the load-time history. An aluminium ring was placed around the specimen. The capacitance between the ring and the piston was related to the distance between the ring and piston bottom surface. This enabled the measurement of the displacement-time history of the specimens during the test.

McElhaney [12] determined the instantaneous area for bone by calculating the instantaneous cross-section dimensions from Poisson's ratio (the ratio of the strain in the direction of the load to the strain perpendicular to the load) measurements. These measurements were made on dry bovine bone using high-elongation-resistance foil strain gauges. The grid of the strain gauges covered approximately one fourth of the lateral surface area. Two gauges were placed on opposing sides of the specimen and their output connected in series. Thus, an electrical averaging occurred and flexure strain due to non-uniform loading and response of the specimen tended to cancel.

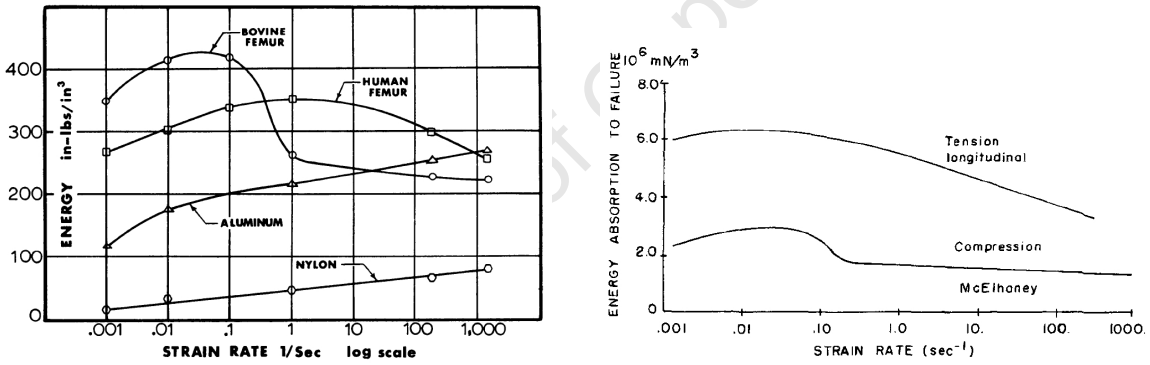

(a) Energy to fracture vs. strain rate

(b) Ultimate stress vs. strain rate

Figure 2.10: The phenomenon of critical velocity as shown by McElhaney[12] and Crowninshield and Pope [14]

A very interesting result by McElhaney is shown in Fig.2.10(a). **The figure illustrates that the properties of both human and bovine cortical bone exhibit a large variation in properties over a small range of strain rates. This indicates that a critical velocity exists for bone where there is a large change in the energy absorption capacity to failure.** McElhaney's results show that the critical bovine femur bones have a maximum ability to absorb strain energy at $\dot{\varepsilon} = 0.1\,\text{s}^{-1}$. If the rate of loading is increased by one order of magnitude to $\dot{\varepsilon} = 1\,\text{s}^{-1}$, the energy absorption capacity drops rapidly. Human femur bone displays a greater ability to absorb dynamic strain energy than bovine cortical bone. The existence of a critical velocity is also supported by the work of Panjabi et al. [56], which shows that the energy absorption capacity of bone first increases and then decreases with increasing strain rate. Crowninshield and

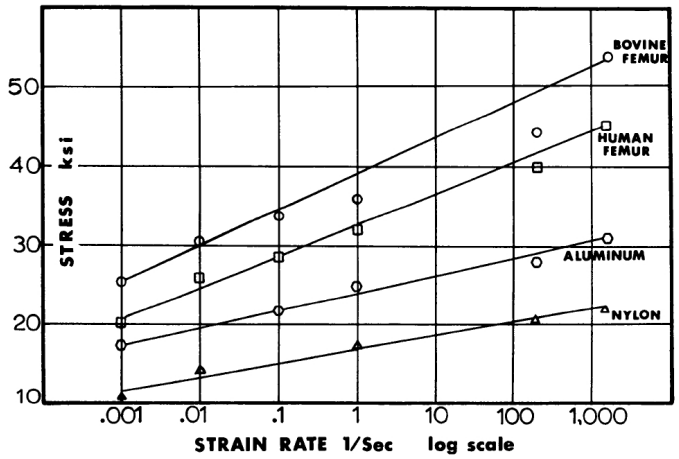

Figure 2.11: Stress as a function of strain rate as shown by McElhaney [12]

Pope [14] found that bovine tibia bone has a maximum energy absorption capacity at a strain rate of $0.1\,s^{-1}$ in tension. This is the same strain rate at which McElhaney found a critical velocity for bovine bone in compression even though his work was conducted on a femur. The energy absorption capacity in tension is much higher than it is in compression. This is ascribed to the presence of plastic deformation on the post-yield region of tensile bone response.

Fig.2.11 shows that bovine specimens fracture at a higher stress than human femur specimens throughout the strain rate regime. The exact strain rate histories of McElhaney's work are not reported. Furthermore the compression experiments were conducted on only one human femur bone (24 tests) and a single steer femur (45 tests).

Crowninshield and Pope [14]

Crowninshield and Pope [14] investigated anisotropic behaviour of bovine compact bone in tension at strain rates of between $10^{-2}\,s^{-1}$ and $2 \times 10^{1}\,s^{-1}$. The study was motivated by the fact that bones other than the talus, calcaneus and vertebral bodies normally break in bending or torsion, which results in tensile failure. Bone exhibited considerable plasticity throughout the range, except when tested in a direction normal to the long axis.

Crowninshield and Pope [14] conducted higher strain rate tests with a drop hammer device capable of impact velocities of up to $8\,ms^{-1}$. The drop hammer was assumed to have a constant velocity over the loading distance (5 mm) because the energy to failure was more than an order of magnitude smaller than the energy of the drop hammer. The exact strain rate histories for the stress-strain curves shown in Fig.2.12 were not reported.

Katsamanis and Raftopoulos [15]

Katsamanis and Raftapoulos [15] used the Hopkinson bar stress technique to investigate the dynamic and mechanical properties of cortical bone from the human femur (44 to 55

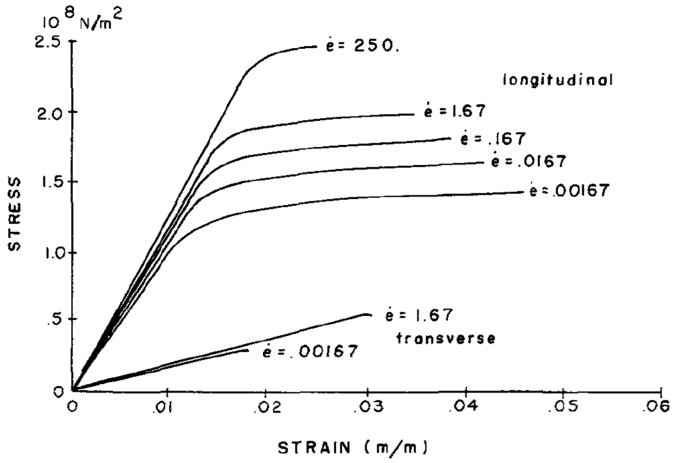

Figure 2.12: Stress-strain curves for bovine compact bone in tension [14]

year old male cadaver). These properties were compared to static properties determined with an Instron 1125 universal testing machine. The Hopkinson bar technique was implemented in a unique way when compared to other approaches in literature. A gas gun fired metal spheres at a long human femur bone shaft specimen ($220 \times 10.5 \times 4\,\text{mm}$), which was suspended by two strings. Four strain gauges (two on opposing sides) were attached at three intervals along the specimen length, and strain was measured in the axial and transverse directions. The time intervals between the arrival of the strain waves at the different gauge stations allowed the calculation of the wave speed. The dynamic Young's modulus then directly follows from:

$$c = \sqrt{\frac{E_d}{\rho}} \tag{2.4}$$

On average, the dynamic Young's modulus ($E_d = 19.9\,\text{GPa}$) was 23% higher than the static Young's modulus ($E_s = 16.2\,\text{GPa}$). No difference was found between the average Young's modulus in tension and compression. The exact strain rate history is not reported here. The dynamic Poisson's ratio could be calculated by the ratio of the amplitudes of the transverse and longitudinal strains. No difference found between the dynamic and quasi-static Poisson's ratio, which was determined in both loading regimes as $\nu = 0.36$.

Katsamanis and Raftopoulos [15] report that the fresh femur specimens were left for several days to dry out in order to mount strain gauges. The results therefore represent the characteristics of dry bone. McElhaney [12] also mounted strain gauges directly on the specimens, using conventional techniques. The responses for cortical bone by Bernstein et al. [57] display significant plastic deformation in bone after yielding. Additionally, the specimens fractured at greater strains than those measured by McElhaney [12]. This is attributed to the effect of drying on specimen response. Bernstein [57] proposes an indirect method of strain measurement for the following reasons:

- The fact that a dry surface is needed for proper strain gauge bonding is problematic.
- Electrical conductivity must be maintained despite attempts to prevent the drying of the specimen.

Crowninshield and Pope [14] implemented such an indirect method by measurement of the relative displacement of the two specimen gripping devices with a resistive displacement transducer. The validity of this measurement was checked by observing the specimen during the test with a measuring microscope.

A summary of cortical bone properties

A summary of cortical bone properties, reported by Katsamanis and Raftopoulous [15] is extended in Table 2.4 to include the more recent works from literature. The cortical bone properties, which are listed were obtained from experiments which tested bone response in the direction of the bone axis.

- There is agreement in literature (by Ko [58], McElhaney [12], Reilly and Burnstein [39] and Katsamanis and Raftopoulos [15]) that the quasi-static Youngs modulus of cortical bone is between 15.1 GPa and 17.3 GPa as determined by compression and tension tests.
- Dynamic Youngs moduli vary between 9.3 GPa and 29.5 GPa. With the exception Fereira et al. [19] who determined the dynamic Youngs modulus for bone to be between 9.3 and 19.4 GPa the works of McElhaney [12], Katsamanis and Raftopoulos [15] and Ebacher et al. [38] record a Youngs modulus at dynamic loading rates of between 19.9 and 29.5 GPa. The Youngs moduli at dynamic strain rates have a greater magnitude than the range of values reported for quasi-static loading rates.
- With the exception of the works by Reilly and Burnstein [39] and Lappi et al. [59] literature concurs that the Poisson's ratio of cortical bone is between 0.34 and 0.36. This ratio is independent of loading rate.

Authors	E [GPa]	ν	Comments
Ko (1953) [58]	17.3	–	Very low strain rate (wet bone)
Sedlin (1965) [48]	15.8	–	Bending unknown strain (wet bone)
McElhaney (1966) [12]	15.1	–	Low strain rate ($1 \times 10^{-3}\,s^{-1}$)(wet bone)
	29.5		High strain rate ($3 \times 10^{2}\,s^{-1}$)(wet bone)
Abendschein and Hyatt (1970) [60]	24.5	–	Ultrasonics (wet bone)
Bargren et al. (1974) [42]	15.8	–	Hydrated (5.2 Hz)
	18.7	–	Air dried (5.2 Hz)
Reilly and Burnstein (1975) [39]	17.0	0.46	Low strain rate (wet bone)
Lappi et al. (1979) [59]	5.5	0.39	Ultrasonics (wet bone)
Ashman et al. (1984) [61]	20	0.36	Ultrasonics (wet bone)
Katsamanis and Raftopoulos (1990) [15]	16.2	0.36	Low strain rate ($2 \times 10^{-5}\,s^{-1}$)(dry bone)
	19.9	0.36	High strain rate ($1 \times 10^{2}\,s^{-1}$)(dry bone)
Ferreira et al. (2006) [19]	9.3 to 19.4	–	Varying dynamic strain rate (≈ 3.6 to $8 \times 10^{2}\,s^{-1}$)(wet bovine bone compression)
Ebacher et al. (2007) [38]	23 ± 3	0.35 ± 0.03	Dynamic strain rate ($1.5 \times 10^{2}\,s^{-1}$)(wet human tibia bone tension)
	23 ± 2	0.34 ± 0.01	Dynamic strain rate ($1.5 \times 10^{2}\,s^{-1}$)(wet human tibia bone compression)

Table 2.4: Previous studies on cortical bone

2.4.2 Dynamic characterisation of bone on the SHPB

The history of the Split Hopkinson Pressure Bar (SHPB)

In 1914, Hopkinson [62] introduced a technique for determining the pressure time relations pertaining to an impact produced by a bullet or explosive. The apparatus consisted of a long steel rod, a short steel billet, and a ballistic pendulum. When one end of the rod is impacted, a compressive pressure wave of finite length is generated inside the rod. A short steel billet is placed in contact with the far end surface of the rod. A layer of grease is smeared at the interface. The compressive wave will move down the bar, through the greased joint, and into the billet. It will reflect at the far end as a pulse of tension. The grease can not withstand any appreciable tensile loads, therefore the billet would fly off with a definite momentum, measured with a ballistic pendulum. The time over which this momentum acts is the time of the longitudinal wave in the billet.

Although the maximum pressure and total duration of these impact events could always be measured with a Hopkinson pressure bar, the exact pressure-time curves remained unclear until Davies (1948) [63] developed a technique using condensers to measure the strains. The output from the condenser is proportional to the displacement-time relations, that are proportional to the pressure-time relations assuming the pressures in the bars are under the elastic limit of the material. Using condensers to measure strains greatly improved the accuracy of Hopkinson's original apparatus, which relied on measuring the momentum of a steel billet flying off the end of the pressure bar.

In 1949, Kolsky [64] added a second pressure bar to the original apparatus of Hopkinson, hence the name *split* Hopkinson bar. Kolsky impacted the first of the two bars with a striker bar. A specimen was sandwiched between the second and third bars. Kolsky presented expressions by which specimen properties could be calculated, based on the bar strain histories.

Bar strains were measured by condensers until 1966, when Hauser [65] added strain gauges to the SHPB to measure bar surface displacements.

The two bar technique proposed by Kolsky [64] is the most widely used dynamic material testing procedure today. In some literature, the split Hopkinson bar may be referred to as the Kolsky bar. **Fig.2.13 shows a diagram of a SHPB system. It is composed of long input and output bars with a short specimen placed between them. A striker is fired at the input bar at a velocity, v_0, which is recorded by the speed trap. The impact of the projectile at the free end of the input bar develops a compressive longitudinal wave, called the *incident wave* (ε_I), which is transmitted along the bar to the specimen interface. When the incident wave reaches the input bar-specimen interface, a part of it, the *reflected wave* (ε_R), is reflected back along the input bar as a tensile wave. The remaining part is transmitted to the output bar and is termed the *transmitted wave* [66].**

These three basic waves are recorded by the strain gauges cemented on the input and output bars. According to the wave propagation theory, the stress and the particle velocity associated with a single wave can be calculated from the associated strain measured by the strain gauges. The calculation of the specimen stress and strain from the incident, reflected and transmitted waves is discussed in Section 4.3.3.

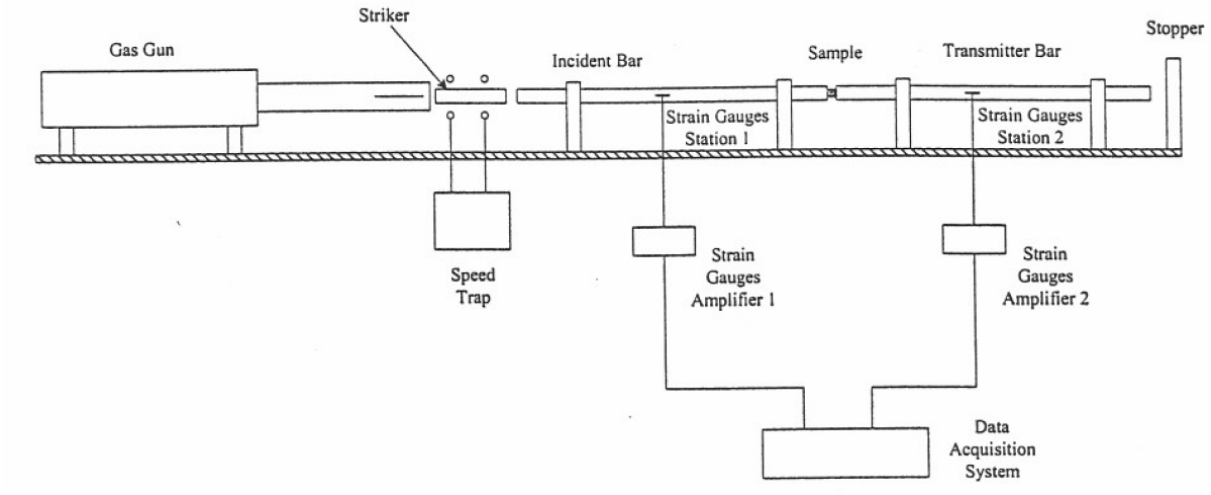

Figure 2.13: A SHPB system [67]

2.4.3 Strain rate dependent investigations of bone on the SHPB

Tanabe and Kobayashi [16] investigated the compressive response of bovine bone prior to yield. Impact compression tests were carried out on the same specimens as tested in quasi-static compression at a strain rate of approximately $100\,s^{-1}$, using the SHPB (bar diameter 10 mm, length 2000 mm and striker diameter 11 mm and length 200 mm). Foil strain gauges were used to detect the incident and reflected stress waves and the signals of these waves were stored in a digital oscilloscope with a sampling frequency of 4 MHz.

Ferreira et al. [19] investigated the dynamic properties of bovine cortical bone by using the SHPB technique (bar diameter 18 mm, sampling rate 2 MHz). The strain rate histories of the tests were not reported. The maximum strain rate varied between $368\,s^{-1}$ and $795\,s^{-1}$, and the strain rate at fracture between $41\,s^{-1}$ and $386\,s^{-1}$. The elastic modulus was found to be between 9.3 GPa to 19.4 GPa. The ultimate strength ranged from 223 MPa to 310 MPa, and the strain at fracture from 1.49% to 3.2%.

Tennyson et al. [17] investigated the dynamic characteristics of bovine cortical bone as a function of elapsed post-mortem time. Specimens from the dense posterior section of the femoral midshaft were exposed to a wide range of strain rates ($\dot{\varepsilon} = 10$ to $450\,s^{-1}$) by direct compression on the split Hopkinson pressure bar. The specimen-bar interfaces were coated with silicon lubricant to reduce the frictional forces and ensure contact to permit stress

wave transmission. The specimens were compressed but not allowed to fracture, with a resulting stress rate of 1×10^8 psi. s^{-1} to 6×10^8 psi. s^{-1} (6.9×10^2 to 4.1×10^3 MPa. s^{-1}).

Shim et al. [21] characterised cancellous bone from the human cervical spine in compression. Tests were performed at strain rates in the region of about 10^2 to $10^3\,s^{-1}$, using a SHPB arrangement with magnesium bars. The strain rate was constant throughout the test period and no pulse shaping was required to achieve this with cancellous bone.

Adharapurapu et al. [20] compressed bovine bone specimens at various strain rates (10^{-3} to $10^3\,s^{-1}$) in both longitudinal (parallel to the axis of the bone) and transverse (perpendicular) direction. Adharapurapu et al. [20] observed that it was difficult to achieve constant strain rate compression of bovine cortical bone samples with conventional AHPB experiments. Fig.2.14(a) presents the input, reflected and transmitted pulses obtained from the conventional SHPB experiment. The associated stress vs. strain and strain rate vs. strain responses are shown in Fig.2.14(b)). Notice that the strain rate reaches a peak of about $1600\,s^{-1}$ and then decreases in an oscillatory fashion in the course of the compression test.

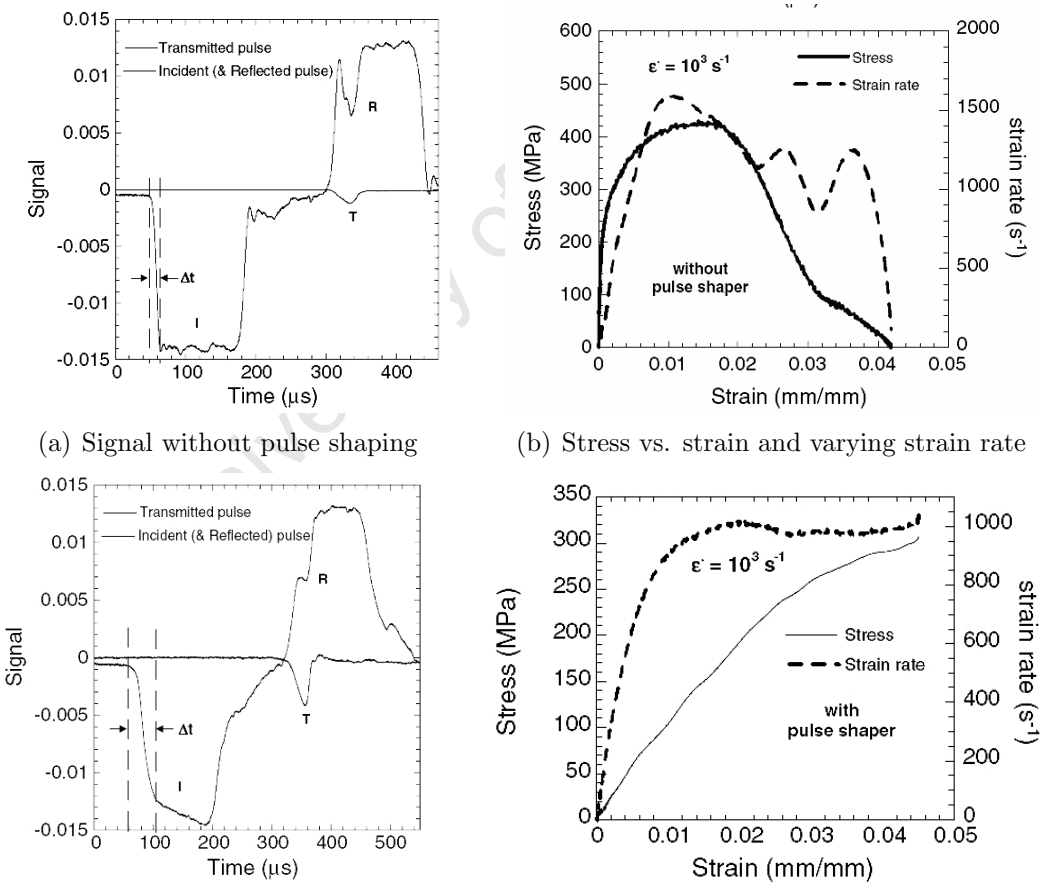

(a) Signal without pulse shaping

(b) Stress vs. strain and varying strain rate

(c) Signal with pulse shaping

(d) Stress vs. strain with constant strain rate

Figure 2.14: Pulse shaping used by Adharapurapu et al. [20] to correct the strain rate variation during a SHPB compression test

The researchers hypothesised that a considerable variation in strain rate

may significantly influence the mechanical properties of materials that are sensitive to strain rate, which is especially true in the case of bone. Additionally, for some brittle and soft materials, such as ceramic (composites), polymer and rubber, **an incident pulse with relatively long rise time is required to yield dynamic stress equilibrium in the sample for obtaining reliable data for the materials.**

Adharapurapu et al. [20] used a pulse shaping technique to achieve a constant strain rate and a relatively long pulse rise time. The conventional pulse shaping technique involves placing a deformable metal disk on the impact surface of the incident bar to gradually transfer the impact. A 3 mm cylindrical disk out of a high work hardening alloy was used as the pulse shaper. The work hardening properties of the pulse shaper material was used to increase the slope of the input stress wave as shown n Fig.2.14(c). This resulted in an accelerator pulse in the input bar which counteracted the tendency of the material to decelerate the rate of deformation. Additionally pulse shaping resulted in a signal with a relatively long rise time, which allowed force equilibrium to be achieved. Fig.2.14(d) presents the stress vs. strain and strain rate vs. strain histories which were recorded as a result of pulse shaping on the SHPB. Notice that pulse shaping rectified the variation in strain rate. The rate of deformation rises to approximately $10^3\ s^{-1}$ and remains constant for the remainder of the test.

2.4.4 Pulse shaping

Conventional pulse shaping

In conventional Hopkinson bar techniques, it could prove difficult to achieve a constant strain rate during the sample deformation. A considerable variation in strain rate may significantly influence the mechanical properties of materials that are sensitive to strain rate, which is especially true in the case of bone.

Conventionally, a constant strain rate is achieved by the compression of a dummy specimen to tailor the shape of the incident pulse. Ellwood et al. [68] proposed the use of a pre-loading bar (placed between the striker and input bar), together with a pulse-shaping dummy specimen of the same material, as the test specimen. This allowed SHPB compression tests to be conducted at virtually constant rates of strain.

Subsequent pulse-shaping techniques employ a pulse shaper at the impact end of the incident bar, which is directly struck by the striker. These techniques are not only used to tailor the shape of the input pulse to achieve a constant strain rate, but also to generate an initially slow loading profile in the incident pulse [69]. A slow rising incident pulse facilitates early dynamic stress equilibrium. Early stress equilibrium is particularly important when testing brittle materials, where test durations tend to be shorter. Furthermore, an increasingly high loading rate causes increasingly severe initial non-equilibrium

in the specimen. To lengthen the input pulse, Frew et al. [70] placed a thin disk of metal (annealed copper) on the impact surface of the incident bar. After impact by the striker bar, the copper disk deformed plastically and spread the pulse in the incident bar.

Through proper combination of material and dimensions of the pulse shaper and striking speed of the striker, an appropriate pulse-shaping design is capable of modifying the profile of the incident pulse to facilitate not only dynamic stress equilibrium, but also a nearly constant strain-rate deformation in specimen. The choice of materials and dimension for this pulse shaper is strongly dependent on the desired strain rate and the material to be tested.

Shaped strikers

Kobayashi et al. [71] implemented a tapered striker tube to achieve accelerator and decelerator loading pulses during dynamic tensile tests on 0.45%C steel on the SHPB. It was undoubtedly found that an acceleration or deceleration incident pulse is created by the collision of a tapered tube. An acceleration pulse ensues when the smaller end of the striker tube collides with the input bar. In this instance, the acceleration and deceleration pulses were used to vary the strain rate in a specific way throughout the test duration.

Lok et al. [72] tested the dynamic compressive strength of fibre-reinforced concrete on a large diameter SHPB (75 mm). The rapid rise time produced by a conventional cylindrical striker fractured the brittle specimen well before a uniform stress-strain state was established. Two shaped striker bars (Fig.2.15) were developed to achieve uniformity of the stress and strain.

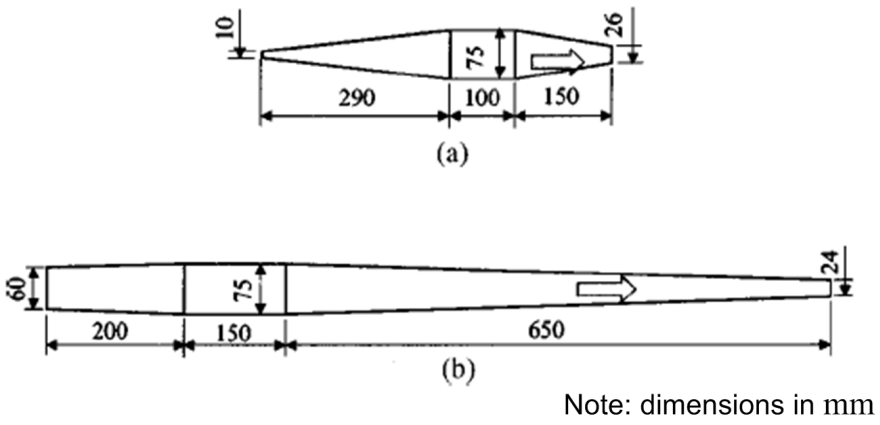

Figure 2.15: Dimensions for the shaped striker bars developed by Lok et al. [72] (a) short striker bar (b) long striker bar

Kumar et al. [73] expanded the work of Lok et al. [72] by developing a striker that enables a lengthened test duration of non-homogeneous brittle materials on a large diameter SHPB. The shape of the striker ensures that the magnitude of the stress in the specimen does not rise abruptly. This enables a uniform stress to be achieved across the specimen.

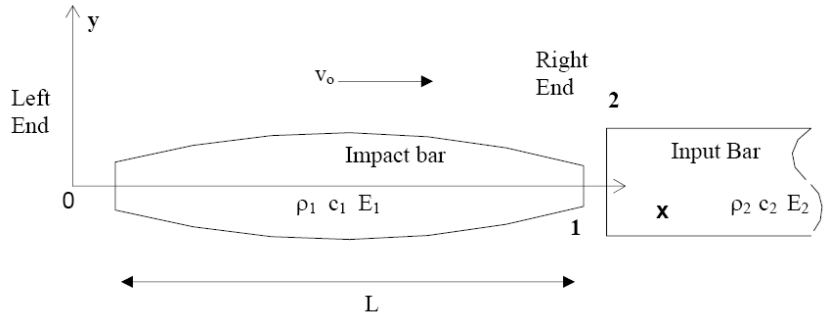

Figure 2.16: Impact of an arbitrary shape striker bar on an incident bar [73]

Kumar et al. [73] proposed governing differential equations as well as boundary and initial conditions (Eqs.2.5 and Fig.2.16) by which the waveform in the input bar (due to impact with a shaped striker) can be predicted.

$$\begin{cases} \frac{\partial}{\partial x}\left(A\frac{\partial u}{\partial x}\right) = \frac{A}{c^2}\frac{\partial^2 u}{\partial t^2} & \\ \frac{\partial u}{\partial x} = 0 & \text{at x= 0} \\ EA_1\frac{\partial u}{\partial x} + \rho_2 c_2 A_2 \frac{\partial u}{\partial t} = -\rho_2 c_2 A_2 v_0 & \text{at } x = L \\ u = 0 & \text{at } t = 0 \\ \frac{\partial u}{\partial t} = 0 & \text{at } t = 0 \end{cases} \tag{2.5}$$

Kumar et al. [73] implemented Eqs. 2.5 in a finite difference scheme and showed that the predicted waveform correlated well with the stress measured in the input bar during experiments. Fig.2.17 shows an example of the measured and predicted pulse shape in a Hopkinson bar as a result of impact with the long striker bar shown in Fig.2.15(b).

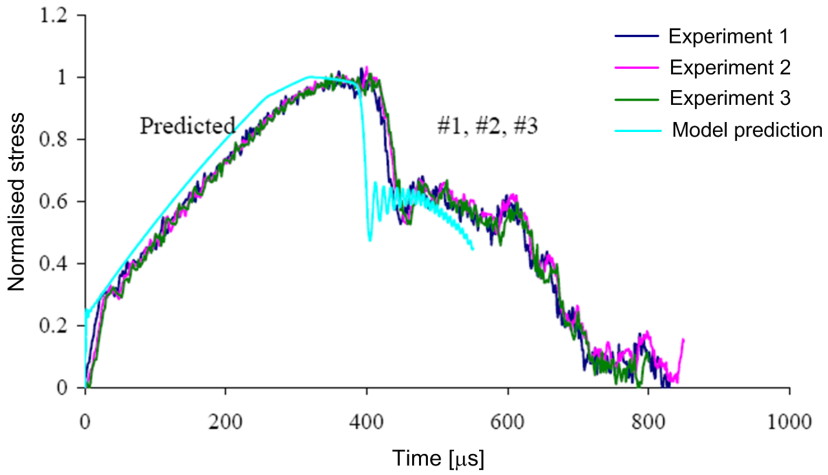

Figure 2.17: Input bar pulses as a result of impact with a shaped striker, as measured in three experiments and predicted by the finite difference scheme by Kumar et al. [73]

2.4.5 SHPB testing on low impedance materials

A measure of the amplitude of wave propagation is the impedance (Z), which is given by the product of the speed of sound in the material (c), the material density (ρ) and the area (A):

$$Z = IA = \rho cA \tag{2.6}$$

The acoustic impedance ($I = pc$) values for some cortical and cancellous bone and SHPB materials are reported in Table 2.5. **The acoustic impedance of cortical bone is comparable to that of magnesium and approximately six times smaller than the acoustic impedance of steel.** Hopkinson bar analysis requires that a transmitted pulse can be measured [74]. **The impedance (Z, i.e. the combination of acoustic impedance and area) of the specimen should be similar to that of the bars if full transmission of the stress wave between two dissimilar materials is required.** There are possible limitations to the application of the SHPB technique when testing the compressive strength of low-strength, low-impedance materials such as bone. The low mechanical impedance of a specimen allows the bar-specimen interface to move almost freely under stress wave loading. A very small pulse is therefore transmitted to the transmitter bar [75]. The small magnitude of the transmitted signal could approach the level of noise in the measurement and therefore result in a bad measurement. According to Shim et al. [21], a greater transmitted signal can be assured by choosing a material for the transmitter bar so that the specimen and bar impedances match as closely as possible (by varying the area or material of the Hopkinson bars).

Material	Density [kg. m^{-3}]	Speed of sound [ms^{-1}]	Impedance [kg. m^{-2}s^{-1}]
Aluminium	2710	5082	13.8×10^6
Magnesium	1810	4759	8.6×10^6
Low density poly-ethylene	952	917	0.8×10^6
Steel	7850	5047	39.6×10^6
Human tibia cortical bone (Saeed et al. [35])		$3959 - 3795$	
Cortical bone (Hosokawa and Otani [76])	1960	$3400 - 4200$	$6.7 - 8.2 \times 10^6$

Table 2.5: Properties of possible bar materials and cortical bone

Lee and Yoon [77] and Williams [78] investigated the speed of sound in cancellous and cortical bone. Biot's theory [79] was implemented during both these studies to predict the speed of acoustic wave propagation in porous cancellous bone. The theory initially proposed a general theory of elastic wave propagation in a system composed of a porous elastic solid saturated by a viscous fluid. In Biot's theory it is predicted that two longitudinal

waves should exist in the material:

- A fast speed wave, corresponding to the solid and fluid moving in phase
- A slow speed wave, where the solid and fluid are moving out of phase

For cortical bone, where the solid phase comprises of almost the full volume fraction, the fluid interaction has a negligible effect on opposing the solid wave speed (Fig.2.18). Hosokawa and Otani [76] list the model parameters used for Biot's theory as a Young's modulus of $E = 22\,\text{GPa}$, and a density of $\rho = 1960\,\text{kg.m}^{-3}$, for solid bone material (considered equivalent to cortical bone). If the speed of sound is calculated from the elastic wave speed definition (following the approach of Katsamanis and Raftopoulos [15]) $c = \sqrt{\frac{E}{\rho}}$ the calculated speed of sound is $c = 3350\,\text{ms}^{-1}$. This results in an acoustic impedance of $I = c\rho = 6.6 \times 10^6\,\text{kg.m}^{-2}\text{s}^{-1}$.

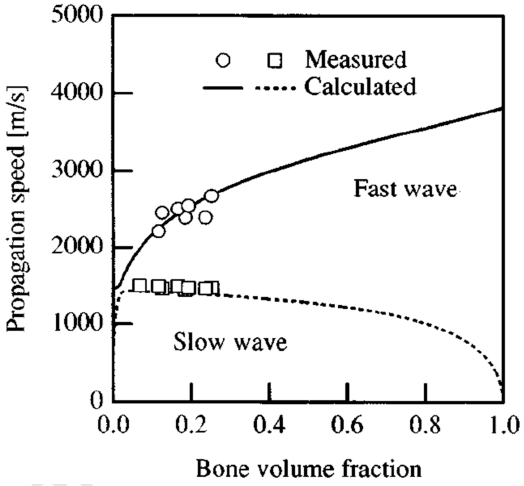

Figure 2.18: Fast and slow wave speed predictions by Biot's theory at 1 MHz compared to experimental results for porous and solid bone (Hosokawa et al. [76])

2.5 Bone as a viscoelastic material

Viscoelasticity has long been deemed the appropriate approach for bone modelling. Viscoelasticity incorporates aspects of both fluid behaviour (viscous) and solid behaviour (elastic). Elastic materials store 100% of their energy due to deformation, whereas viscoelastic materials actually lose or dissipate some of this energy. This dissipation is also known as hysteresis. Viscoelastic materials are associated with two other characteristics: *stress relaxation* and *creep*. Stress relaxation refers to the behaviour of stress as it reaches a peak and then decreases or relaxes over time under a fixed level of strain. Creep is the slow deformation of a material under a stress that results in a permanent change of shape [50]. The material exhibits an increased deformation under a constant stress, until an asymptotic level of strain is reached. **Any material that exhibits hysteresis, creep and stress relaxation is considered to be a viscoelastic material.**

2.5.1 Reasons for viscoelasticity in bone

Garner et al. [80] attributes the viscoelastic response of bone to multiple processes at different scales in the hierarchichal structure of this material:

- On a molecular level, Sasaki et al. [81] proved that the *collagen fibres* (Fig.2.2) in the concentric lamellae of Harvesian systems can give rise to significant viscoelasticity. This major role of collagen is suggested by the similarity in *shape* of the relaxation curves of mineralised and demineralised bone. The mineral phase of bone is crystalline hydroxyapatite, which provides the stiffness to bone and which is virtually elastic.
- *Interfaces* such as the cement lines between osteons and the boundaries of the lamellae within the osteons give rise to a portion of viscoelasticity in bone, particularly for long loading times. A thin layer of compliant protein polysaccharide substance occurs at cement line interfaces.
- Viscoelasticity can also arise from *fluid flow* in porous media.

2.5.2 Spring-damper systems for viscoelastic modelling

Spring-damper models are often used to gain a physical understanding of viscoelastic response. Fung [27] explains the responses of springs and dampers in the context of viscoelasticity as follows: a linear *spring* is used to model an instantaneous *deformation*, proportional to the load. A *dashpot* produces a *velocity*, proportional to the load at any instant. **The *Kelvin* or *Voigt* model (hence referred to as the Voigt model) is a parallel arrangement of a spring and dashpot** (shown in Fig.2.19(a)). **The**

***Maxwell* model in viscoelasticity is the combination of a spring and dashpot in series** as shown in Fig.2.19(b) [82]. This model is often used to model viscous fluid behaviour. The simple Maxwell and Voigt models do not always suffice to describe the behaviour of a viscoelastic material, but are often used in multiples and combinations to model real materials (such as the models by Shim et al. [21] and Funk et al. [83]). **The**

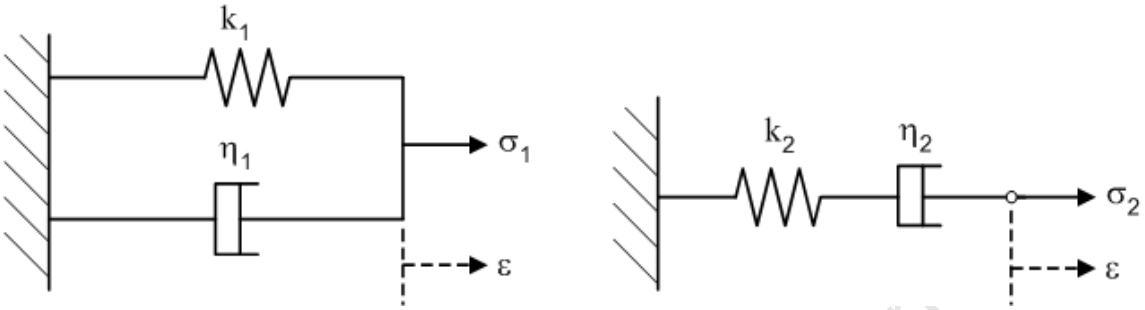

(a) (b)

Figure 2.19: Models of linear viscoelasticity (a) Voigt (b) Maxwell

creep and relaxation responses of the Maxwell and Voigt models are discussed subsequently. The relaxation response describes the stress a material experiences when a unit strain is applied to it, whereas the creep response describes the deformation history when the material is exposed to a unit stress. The loads, which are applied to obtain creep and relaxation responses are shown in Fig.2.20.

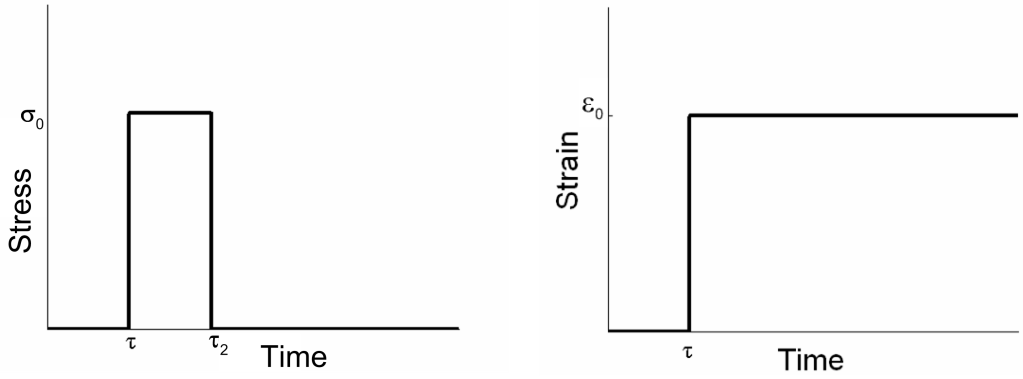

(a)

Figure 2.20: (a) Creep load and release and a (b) relaxation load as shown by Fung [27]

Step loadings are mathematically represented by the *Heaviside function. It is a discontinuous function, defined as:*

$$H(t) = \begin{cases} 0, & t < 0 \\ \frac{1}{2}, & t = 0 \\ 1, & t > 0 \end{cases}$$

The derivative of the Heaviside function is the dirac-delta function: $\frac{d}{dt}H(t) = \delta(x)$.

Voigt model relaxation and creep response

The stress-strain relation for the Voigt model (Fig.2.19(a)) is described by:

$$\sigma_1(t) = k_1\varepsilon(t) + \eta_1\frac{d\varepsilon(t)}{dt} \tag{2.7}$$

The Voigt creep and relaxation responses are shown in Fig.2.21(a) and Fig.2.21(b) respectively. A constant instantaneous stress, σ_0 is applied at $t = \tau$, where $t < \tau_2$ to determine the creep response (Fig.2.20(a)), i.e. the change in strain over time. If the initial strain is assumed to have a value of ε_0, Eq.2.7 reduces to:

$$\sigma_0 = k_1\varepsilon + \eta_1\frac{d\varepsilon}{dt} \tag{2.8}$$

By rearranging Eq.2.8 and dividing by k_1 it follows that:

$$\int_{\varepsilon_0}^{\varepsilon}\frac{1}{\varepsilon - \frac{\sigma_0}{k_1}}d\varepsilon = \int_{\tau}^{t} -\frac{k_1}{\eta_1}dt \tag{2.9}$$

It follows that:

$$\left[\ln\left(\varepsilon - \frac{\sigma_0}{k_1}\right)\right]_{\varepsilon_0}^{\varepsilon} = \left[-\frac{k_1}{\eta_1}t\right]_{\tau}^{t} \tag{2.10}$$

If Eq.2.10 is solved for ε and if the *relaxation time* is defined as $\theta_1 = \frac{\eta_1}{k_1}$ then:

$$\varepsilon(t) = \frac{\sigma_0}{k_1}\left[1 - e^{\left(-\frac{t-\tau}{\theta_1}\right)}\right] + \varepsilon_0 e^{\left(-\frac{t-\tau}{\theta_1}\right)} \tag{2.11}$$

If the initial strain, ε_0, is zero, only the first term of Eq.2.11 remains. This is the creep response conventionally stated as the creep response for the Voigt model.

To determine the relaxation response the change in stress is monitored over time, when an instantaneous deformation of ε_0 is applied at $t = \tau$ (as shown in Fig.2.20(b)). Under these conditions, the strain rate is infinite at $t = \tau$ and zero elsewhere. The relaxation load conditions are substituted into the stress-strain relation for the Voigt model (Eq.2.7) to obtain the relaxation response:

$$\sigma_1(t) = k_1\varepsilon_0 + \delta(\tau) \tag{2.12}$$

The relaxation response of the Voigt model increases linearly with strain and is time independent. The stress at the instant of deformation will be infinite, because the damping stress is directly proportional to the rate of deformation (which is infinite, see Fig.2.21(b)).

Mathematically, this is represented with the *dirac-delta* function, $\delta(\tau)$ which has an infinite amplitude at $t = \tau$ and an area of 1.

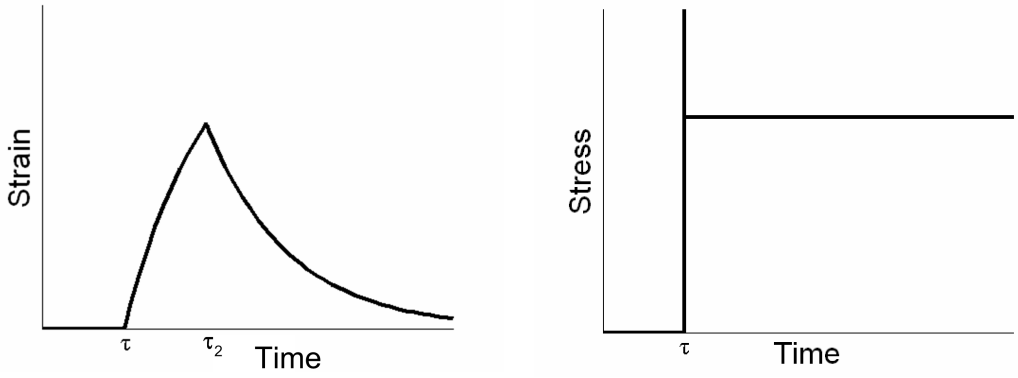

(a) (b)

Figure 2.21: Voigt model (a) Creep and release and (b) relaxation response

Maxwell model creep and relaxation response

The stress state of the Maxwell model (Fig.2.19(b)) is described by:

$$\frac{d\sigma_2(t)}{dt} = k_2\frac{d\varepsilon(t)}{dt} - \frac{k_2}{\eta_2}\sigma_2(t) \tag{2.13}$$

The creep response is determined by applying a constant, instantaneous stress, σ_0 to the system at $t = \tau$ (Fig.2.20(a)) and solving for the change in strain over time. If $t < \tau_2$, the conditions of the creep load are $\sigma_2(0) = \sigma_0$, $\varepsilon(0) = \frac{\sigma_0}{k_2}$ and $\frac{d\sigma_2}{dt}(t) = 0$. Under these conditions Eq.2.13 reduces to:

$$0 = k_2\frac{d\varepsilon}{dt} - \frac{k_2}{\eta_2}\sigma_0 \tag{2.14}$$

In order to obtain the strain as a function of time, Eq.2.14 is integrated such that:

$$\int_{\varepsilon_0}^{\varepsilon} d\varepsilon = \int_{\tau}^{t} \frac{\sigma_0}{\eta_2} dt \tag{2.15}$$

The resulting creep response for the Maxwell model is:

$$\varepsilon(t) = \sigma_0\left(\frac{t-\tau}{\eta_2} + \frac{1}{k_2}\right) \tag{2.16}$$

To determine the relaxation response of the Maxwell model the relaxation load (Fig.2.20(b)) with an amplitude of $\varepsilon(\tau) = \varepsilon_0$ is applied at $t = \tau$. The stress response of the model is consequently determined, subject to the following conditions: $\frac{d\varepsilon}{dt}(t) = 0$ and $\sigma(0) = k_2\varepsilon_0$.

Substitution of these conditions into Eq.2.13 results in:

$$\int_{\sigma_0}^{\sigma_2} \frac{1}{\sigma_2} d\sigma_2 = \int_{\tau}^{t} -\frac{k_2}{\eta_2} dt \tag{2.17}$$

By defining the *relaxation time* as $\theta_2 = \frac{\eta_2}{k_2}$ and integrating:

$$\sigma_2(t) = k_2 \varepsilon_0 e^{-\left(\frac{t-\tau}{\theta_2}\right)} \tag{2.18}$$

The relaxation response of the Maxwell model is plotted in Fig.2.22(b).

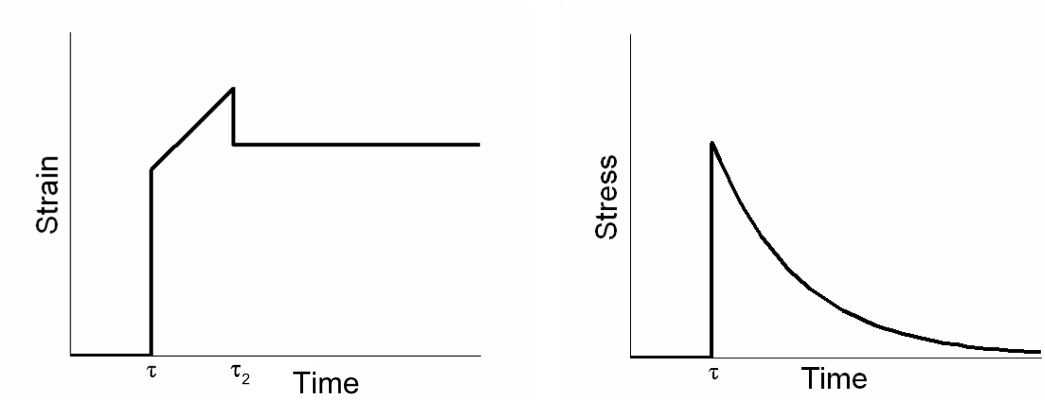

(a) (b)

Figure 2.22: Maxwell model (a) Creep and release and (b) relaxation responses

Viscoelastic models that represent bone response

Tennyson et al. [17] observed only a small degree of non-linearity in the response curves of bovine cortical bone for the range of strain rates ($\dot{\varepsilon} = 10$ to $450\,s^{-1}$) tested on the split Hopkinson bar. A first-order linear viscoelastic model was used to model experimental data. The model is equivalent to a three-element model, composed of a spring in series with a parallel arrangement of another spring and dashpot which can be expressed as:

$$p_1 \frac{d\sigma}{dt} + p_2 \sigma = q_1 \frac{d\varepsilon}{dt} + q_2 \varepsilon \tag{2.19}$$

The model was simplified by assuming a constant stress rate. Furthermore, a comparison between the static and dynamic modulus tests led to the conclusion that the constant p_1 is very small and was hence assumed to be zero. The simplified model is identical to a Voigt viscoelastic model:

$$\sigma(t) = E\varepsilon(t) + \eta_1 \dot{\varepsilon}(t) \tag{2.20}$$

This model by Tennyson et al. [17] was also implemented by Katsamanis and Raftopoulos [15] to approximate strain rate dependent bone response.

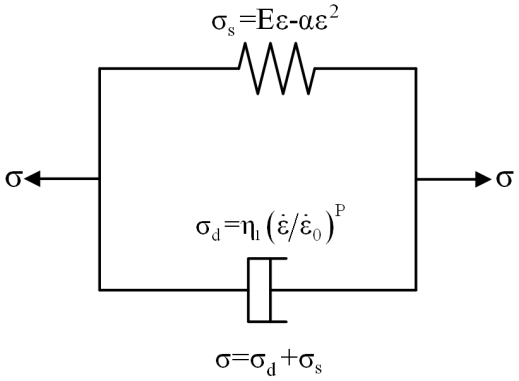

Figure 2.23: The non-linear viscoelastic model used by Tanabe [16] to model strain rate dependent bone properties

Tanabe and Kobayashi [16] investigated the compressive response of bovine femoral cortical bone prior to yield. The results indicate that bovine femoral cortical bone response is linear in quasi-static compression. However, the response is clearly non-linear under impact conditions. In order to represent both responses with a single constitutive relation, a non-linear viscoelastic model was adopted to represent the mechanical behaviour of bone. The constitutive model consists of a non-linear spring and dashpot in parallel (Fig.2.23) and is described by:

$$\sigma(t) = E\varepsilon(t) - \alpha\varepsilon(t)^2 + \eta_1 \left(\frac{\dot{\varepsilon}(t)}{\dot{\varepsilon}_0}\right)^P \tag{2.21}$$

Where: E, α, η_1, P are viscoelastic constants and $\dot{\varepsilon}_0 = 0.1\,\mathrm{s}^{-1}$. The second term of this equation could possibly be interpreted as a parameter that introduces the effect of damage to the model, because the growth of the elastic stress contribution is limited as the strain increases. The model was validated by plotting the experimental bone compression curves and the theoretical curves computed by Eq.2.21 with the identified parameter values (E, α, η_1 and P). Tanabe and Kobayashi [16] identified the model parameters for each of the tested bone orientations. These values were used to examine the change in behaviour and viscoelastic characteristics of bone in different orientations.

The Shim viscoelastic model for cancellous bone

Shim et al. [21] developed a 1-D viscoelastic model that successfully characterised the behaviour of human cancellous bone from the cervical spine. The model is attractive in that it includes the effects of both density and strain rate.
The viscoelastic model by Shim et al. [21] is subject to the following assumptions:

- Deformation prior to the attainment of dynamic strength is recoverable.
- Static stress response follows the laws of density dependent linear elasticity (σ^e).
- Rate sensitivity can be modelled by density independent non-linear viscoelasticity (σ^v).
- Total stress is a sum of static and dynamic components $\sigma = \sigma^e + \sigma^v$.

It was assumed that the rate-dependent mechanical behaviour observed in bone material can be described by viscoelasticity, which is the classic material model for time dependent effects. As the smallest sample of material comprised of a great number of cells, the material was approached as a continuum (Section 2.1). Consider a point initially located at some position $\mathbf{X}$ in a material. Displacement to a new position $\mathbf{x}$ after deformation, results in a deformation gradient $\mathbf{F}$ defined by; $\mathbf{F} = \frac{\partial \mathbf{x}}{\partial \mathbf{X}}$. Deformation of the material can be described by the left Cauchy-Green deformation tensor $\mathbf{B} = \mathbf{F} \cdot \mathbf{F^T}$, or by the right Cauchy-Green deformation tensor $\mathbf{C} = \mathbf{F^T} \cdot \mathbf{F}$. The deformation tensor is related to the Green strain tensor by $\dot{\boldsymbol{\varepsilon}} = \frac{1}{2}[\mathbf{C} - \mathbf{I}]$. The three invariants of $\mathbf{B}$ are defined by: $I_1 = \mathrm{tr}(\mathbf{B})$, $I_2 = \frac{1}{2}[(\mathrm{tr}(\mathbf{B}))^2 - \mathrm{tr}(\mathbf{B}^2)]$ and $I_3 = \det(\mathbf{B})$. If the material is incompressible, it is reasonable to assume that $I_3 = 1$.

Yang et al. [84] considered viscoelasticity in their development of a visco-hyperelastic constitutive model for rubber. The form of the frame-independent finite strain viscoelastic model for incompressible materials proposed by Yang et al. [84] was implemented with great success by Shim et al. [21] for the viscoelastic modelling of cancellous bone. The development of this model is summarised by Yang et al. [84]. The constitutive relationship for a homogeneous, isotropic and compressible material can be expressed in the following form:

$$\boldsymbol{\sigma}^v(t) = \boldsymbol{p}^v(t) + \mathbf{F}(t) \cdot \overset{\mathbf{t}}{\underset{\tau=-\infty}{\boldsymbol{\Omega}}} \{\mathbf{C}(\tau)\} \cdot \mathbf{F^T}(t) \tag{2.22}$$

where $\boldsymbol{\sigma}^v$ is the Cauchy stress tensor, $\boldsymbol{p}^v$ the pressure for a viscoelastic material, and $\boldsymbol{\Omega}$ is a matrix functional that describes the effect of strain history on stress. Studies by Lockett [85] and Carreau et al. [86] show that relatively few parameters are needed to model finite strain viscoelastic material behaviour. The BKZ (Bernstein-Kearsly-Zapas) model [57]

proposes a simple form of the functional Ω (Eq.2.22).

$$\overset{t}{\underset{\tau=-\infty}{\Omega}}\{\mathbf{C}(\tau)\} = \int_{-\infty}^{t} \phi(I_1, I_2) r(t-\tau)\dot{\boldsymbol{\varepsilon}}(\tau) d\tau \tag{2.23}$$

where the strain rate tensor is defined by

$$\dot{\boldsymbol{\varepsilon}} = \frac{1}{2}(\dot{\mathbf{F}}^{\mathbf{T}} \cdot \mathbf{F} + \mathbf{F}^{\mathbf{T}} \cdot \dot{\mathbf{F}}) \tag{2.24}$$

and the relaxation function $r(t)$ decreases with t; in general, $R(t)$ is assumed to be an exponential series described by

$$R(t-\tau) = \sum_{i=1}^{N} e^{\left(-\frac{t-\tau}{\theta_i}\right)} \tag{2.25}$$

The relaxation time, θ_i is the time at which the stress would reach zero if the material continued relaxing at its initial rate [87]. To minimise the number of parameters, the strain energy potential, $\psi(I_1, I_2)$, which is assumed to be representable by a polynomial series, involving $(I_1 - 3)$ and $(I_2 - 3)$, and model parameters (R_i) as follows:

$$\psi(I_1, I_2) = R_1 + R_2(I_2(\tau) - 3) \tag{2.26}$$

If only a single relaxation time is considered $(i = 1)$ the generalised form of the frame-independent finite strain viscoelastic model for incompressible materials is:

$$\boldsymbol{\sigma}^v(t) = -\boldsymbol{p}^v(t)\mathbf{I} + \mathbf{F}(t) \cdot \left[\int_0^t [R_1 + R_2(I_2 - 3)] e^{\left(-\frac{t-\tau}{\theta_1}\right)} \dot{\boldsymbol{\varepsilon}}(\tau) d\tau\right] \cdot [\mathbf{F}(t)]^{\mathbf{T}} \tag{2.27}$$

Notice that the model in Eq.2.27 is capable of representing finite strain response as is expected from a material such as rubber. Shim et al. [21] applied this generalised approach to model the rate dependent dynamic and quasi-static behaviour of cancellous bone. Cancellous bone, and especially cortical bone, are expected to fail in regimes where small strain assumptions are valid. The finite strain modelling ability of Eq.2.27 will not be utilised in the modelling of bone. Furthermore, the finite strain capability of the model does not have adverse effects on the results for small strains.

The 1-D viscoelastic relationship implemented by Shim et al. [21] depends non-linearly on strain rate:

$$\sigma^v(t) = \int_0^t k_2 \dot{\varepsilon}(\tau) e^{-\frac{t-\tau}{\theta_2}} d\tau + \eta_1 \dot{\varepsilon}(t)^{\frac{1}{2}}$$

where k_2, θ_2 and η_1 are material parameters, where k_2 is a stiffness modulus and $\theta_2 = \frac{\eta_2}{k_2}$ the relaxation time of the Maxwell model. Shim et al. [21] explained the addition of non-

linearity of the viscous term ($\dot{\varepsilon}^{\frac{1}{2}}$) by referring to the work of Yang et al. [84]. **Yang et al. [84] concluded that a Maxwell model, whereby the relationship between stress and strain rate associated with the dashpot is assumed to be proportional to the n^{th} root of the strain rate ($\sigma_\eta \propto \dot{\varepsilon}^{\frac{1}{n}}$), can be used to capture a larger range of rate-sensitive behaviour. Non-linear strain rate dependency is therefore implemented to extend the equation's coverage of strain rates without a need to add more parameters.**

The stress in the specimen with viscous and elastic attributes can thus be described as:

$$\sigma(t) = E_0\rho^\beta\varepsilon(t) + \eta_1\dot{\varepsilon}(t)^{\frac{1}{2}} + \int_0^t k_2\dot{\varepsilon}(\tau)e^{-\frac{t-\tau}{\theta_2}}d\tau \tag{2.28}$$

Shim et al. [21] found that the Young's modulus of the quasi-static response depended on fresh bone density (Section 2.2.2) according to the relationship given in Eq.2.29. For the sake of uniformity throughout the discussion, the quasi-static Young's modulus will be referred to as k_1 in the remainder of the document.

$$E = E_0\rho^\beta = k_1 \tag{2.29}$$

Therefore

$$\sigma(t) = k_1\varepsilon(t) + \eta_1\dot{\varepsilon}(t)^{\frac{1}{2}} + \int_0^t k_2\dot{\varepsilon}(\tau)e^{-\frac{t-\tau}{\theta_2}}d\tau \tag{2.30}$$

The Shim model is represented by a spring-dashpot system as shown in Fig.2.24. The model consists of a Voigt and Maxwell model in parallel. The Voigt dashpot response is non-linear with respect to strain rate. Shim et al [21] determined the quasi-static and

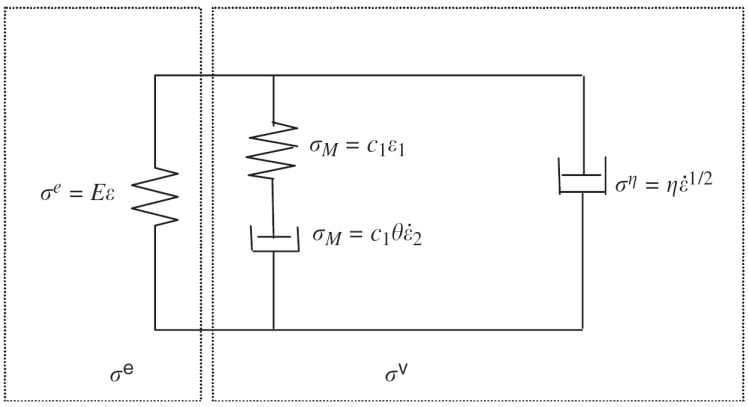

Figure 2.24: The non-linear viscoelastic model used by Shim et al. [21] to model strain rate dependent cancellous bone from the human cervical spine

dynamic stress-strain curves through experiments. The five parameters from Eq.2.28, E_0, β, c_1, θ and η were identified with least squares fitting and are listed in Table 2.6.

E_0 [MPa]	β	k_2 [MPa]	η_1 [MPa. $s^{\frac{1}{2}}$]	θ_2 [s]
242	1.95	0.122	354	5.5×10^{-5}

Table 2.6: Model parameters for Eq.2.28 as determined by Shim et al. [21]

Shim et al. [21] achieved an excellent fit of experimental data (Fig.2.25). The model is capable of simulating prefracture response at strain rates between 10^{-2} and $10^{3}\,s^{-1}$.

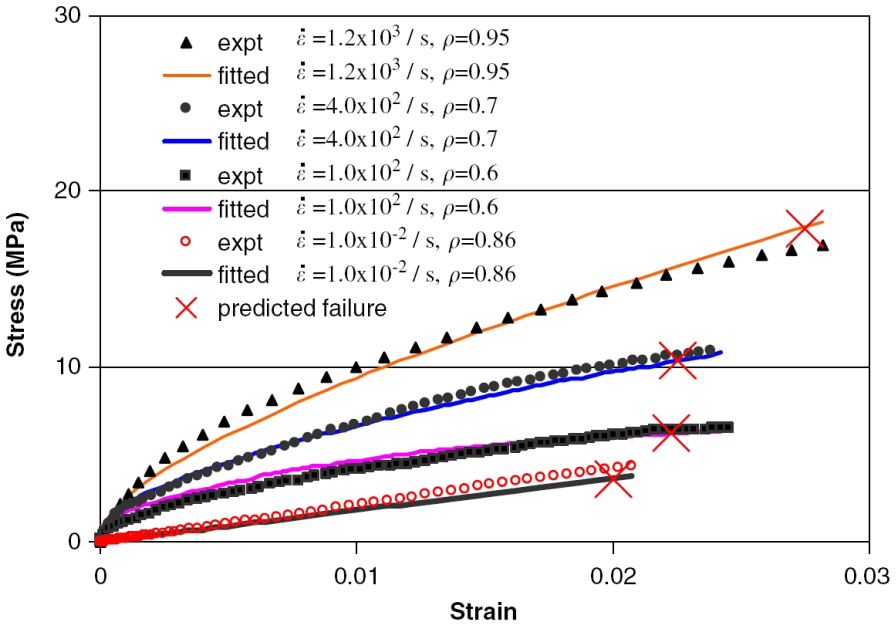

Figure 2.25: A comparison between experimental and viscoelastic model stress-strain response by Shim et al. [21] to model strain rate dependent cancellous bone from the human cervical spine

The establishment of a 3-D constitutive equation is required to facilitate the utilisation of computational simulation of bone material. Assumptions were made in order to formulate a constitutive model, based on the 1-D experimental data obtained. Shim et al. [21] proposed an isotropic model to provide initial estimates of cancellous bone response. A 3-D elastic relationship was derived for the static, strain rate dependent, behaviour of cancellous bone:

$$\boldsymbol{\sigma^e} = \frac{k_1}{1+\nu}\left(\frac{\nu}{1-2\nu}\mathrm{tr}(\boldsymbol{\varepsilon})\mathbf{I} + \boldsymbol{\varepsilon}\right) \tag{2.31}$$

Where $\boldsymbol{\sigma^e}$ and $\boldsymbol{\varepsilon}$ are the elastic stress and strain tensors and ν is the isotropic Poisson's ratio. The viscoelastic elements were expanded to three dimensions by replacing the 1-D

strain rate variable, $\dot{\varepsilon}$, by a function of the strain rate tensor $\dot{\boldsymbol{\varepsilon}}$, thus:

$$\dot{\varepsilon} \Rightarrow \frac{1}{1+\nu}\left(\frac{\nu}{1-2\nu}\mathrm{tr}(\dot{\boldsymbol{\varepsilon}})\mathbf{I} + \dot{\boldsymbol{\varepsilon}}\right) \tag{2.32}$$

The isotropic 3-D expansion of the 1-D results in a relation that describes the stress tensor, $\boldsymbol{\sigma}$ as follows:

$$\begin{aligned}\boldsymbol{\sigma}(t) &= \frac{k_1}{1+\nu}\left(\frac{\nu}{1-2\nu}\mathrm{tr}(\boldsymbol{\varepsilon}(t))\mathbf{I} + \boldsymbol{\varepsilon}(t)\right) + \frac{\eta_1}{(1+\nu)^{\frac{1}{2}}}\left(\frac{\nu}{1-2\nu}\mathrm{tr}(\dot{\boldsymbol{\varepsilon}}(t))\mathbf{I} + \dot{\boldsymbol{\varepsilon}}(t)\right)^{\frac{1}{2}} \\ &\quad + \int_0^t \frac{k_2}{1+\nu}\left(\frac{\nu}{1-2\nu}\mathrm{tr}(\dot{\boldsymbol{\varepsilon}}(\tau))\mathbf{I} + \dot{\boldsymbol{\varepsilon}}(\tau)\right) e^{-\frac{t-\tau}{\theta_2}}\, d\tau \end{aligned} \tag{2.33}$$

The model by Shim et al. [21] is implemented in future chapters to simulate the compressive response of bovine bone in axial compression.

2.6 Expressions for bone strength

Carter and Hayes [88] explored the hypothesis that porous trabecular bone and cortical bone can be viewed as a single material. This suggests that the 3-D lattice of trabecular bone consists of material with similar microscopic mechanical properties to that of cortical bone. The authors sought to express the ultimate compressive strength of this single bone material as a function of apparent density and strain rate, whilst additionally investigating the effect of bone marrow in situ. Cylindrical (length, 5 mm, radius 10.3 mm) trabecular specimens were machined under continuous irrigation from human tibial plateaus (100 specimens) and bovine femoral condyles (24 specimens). The two species provided specimens that span a large range of densities and were orientated with their axes parallel to the long axis of the bone. The specimens were stored at $-20\,^{\circ}\mathrm{C}$ until the time of testing.

Specimens were tested in uniaxial strain by confining them in a rigid cylindrical cavity and compressing them by more than 50% of their original length in an electro-hydraulic materials testing machine (MTS Systems). Half of the specimens were tested with marrow, whereas the marrow from the other half was removed with an air jet and running water. During compression the marrow was allowed to escape by using porous compression platens (pore size $165\,\mu$m). The marrow was extracted from the specimens that had undegone experiments with marrow in situ. All specimens were then degreased with ethanol and degassed in a vacuum. They were immersed in distilled water and, subsequently, their submerged mass was measured. The volume of bone tissue (without pores) was calculated from the difference between the wet and submerged mass. Bone tissue density was determined by dividing the wet specimen mass by the bone tissue volume. The apparent density is the wet specimen mass divided by the initial specimen volume as measured by a micrometer. Apparent densities varied from $0.07\,\mathrm{g.\,cm^{-3}}$ and $0.97\,\mathrm{g.\,cm^{-3}}$. The tissue densities were approximately equal to that of cortical bone (1.6 to $2.0\,\mathrm{g.\,cm^{-3}}$).

The response of the bone specimens with marrow in situ only varied from those with the marrow removed at the highest tested loading rate ($\dot{\varepsilon} = 10\,\mathrm{s^{-1}}$). Viscous flow of the marrow out of the pores had a strengthening effect at this loading rate. Results show that the compressive strength of bone tissue is proportional to the strain rate raised to the 0.06_{th} power.

The investigation of Carter and Hayes [88] suggests that the longitudinal compressive strength of bone is proportional to the square of the apparent density. The authors attribute the squared relationship to failure of the bone struts in buckling. Bone strength is described by the equation:

$$\sigma_{ut} = \sigma_c \dot{\varepsilon}^{0.06} \left(\frac{\rho}{\rho_c}\right)^2 \tag{2.34}$$

Where σ_{ut} is the ultimate compressive strength [MPa] of compact bone with an apparent density of ρ [g. cm^{-3}] and σ_c[MPa] is a the ultimate strength of compact bone, with a density of ρ_c[g. cm^{-3}] tested at a strain rate of 1.0 s^{-1}. Carter and Hayes [88] further derived a strain rate and density dependent strength relation for human bone by substituting an ultimate strength value of 221 MPa and an approximate density of 1.8 g. cm^3 into Eq.2.34:

$$\sigma_{ut} = 68\dot{\varepsilon}^{0.06}\rho^2 \tag{2.35}$$

This expression shows that compressive strength is a strong function of apparent density and a weak function of the imposed strain rate. This equation is most useful in describing strength changes when large density variations are present.

Shim et al. [21] observed that the quasi-static stress-strain curves (measured for human cancellous bone in axial compression) are linear elastic up to a point B, which is indicated in Fig.2.26(a). The stress at point B was found to be about 5% smaller than the stress at point A (the ultimate stress). Shim et al. [21] therefore defined the failure stress by a value 5% below the ultimate stress. The compressive strength, σ_c was also found to increase as a non-linear function of density (Fig.2.27(a)), which was obtained by a least squares fit with experimental data. The power law function that Shim et al. [21] related to the quasi-static failure stress to density is given by Eq. 2.36:

$$\sigma_c = f_c\rho^{\alpha} \tag{2.36}$$

Shim et al. [21] followed a similar approach for the dynamic failure stress by defining it at a level 5% below the ultimate dynamic compressive stress. The dynamic failure stresses are indicated by red markers in Fig.2.26(b). It was observed that dynamic compressive cancellous bone strength increased with both bone density and strain rate. Shim et al. [21] elected to isolate the contribution of strain rate to dynamic strength by assuming that the contribution of density to bone strength would be the same, regardless regardless of whetheher the strain rate is quasi-static or dynamic. The dynamic strength could therefore be expressed by the summation of two terms, one depending on density and one depending on strain rate. The contribution of density to strength is expressed in Eq.2.36. The effect of strain rate was found by subtracting the strength variation attributed to density (assumed to be the same as the static contribution) from the experimentally determined dynamic compressive strengths (σ_c^d). The difference is shown in Fig.2.27(b) and expressed in Eq.2.37:

$$f_d\dot{\varepsilon}^{\gamma} = \sigma_c^d - \sigma_c = \sigma_c^d - f_c\rho^{\alpha} \tag{2.37}$$

The parameter values, f_d and γ were determined from a least squares fit. The total

dynamic compressive strength is therefore expressed as:

$$\sigma_c^d = f_c \rho^\alpha + f_d \dot{\varepsilon}^\gamma \tag{2.38}$$

It can be concluded from the strength relations published by Carter and Hayes [88] and Shim et al. [21] that bone strength is a non-linear function of density and strain rate.

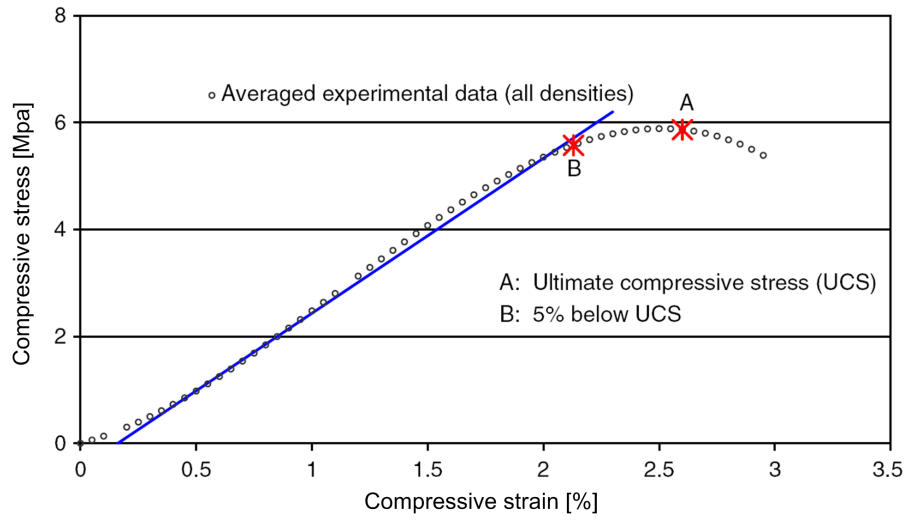

(a)

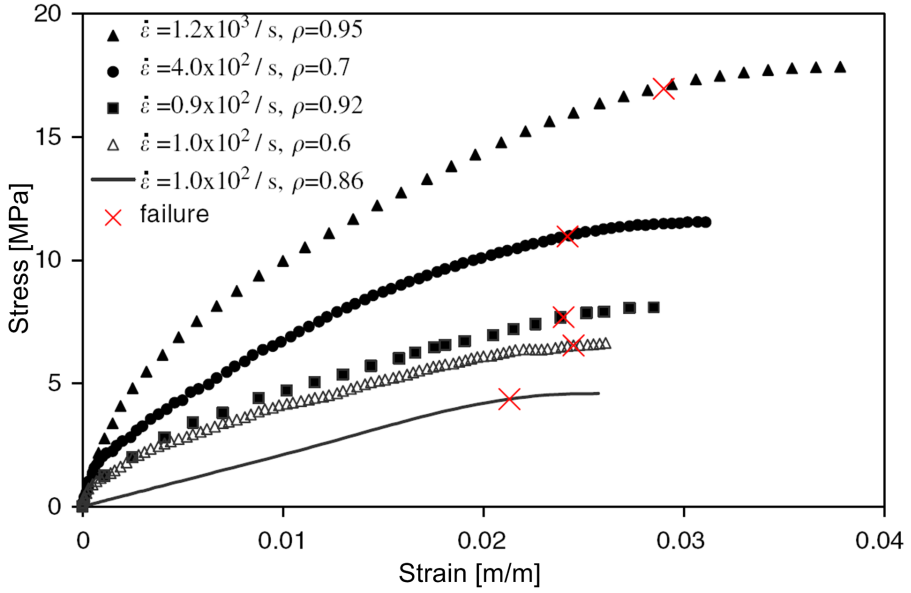

(b)

Figure 2.26: (a) The quasi-static and (b) dynamic failure stress of cancellous bone from the human cervical spine as defined by Shim et al. [21]

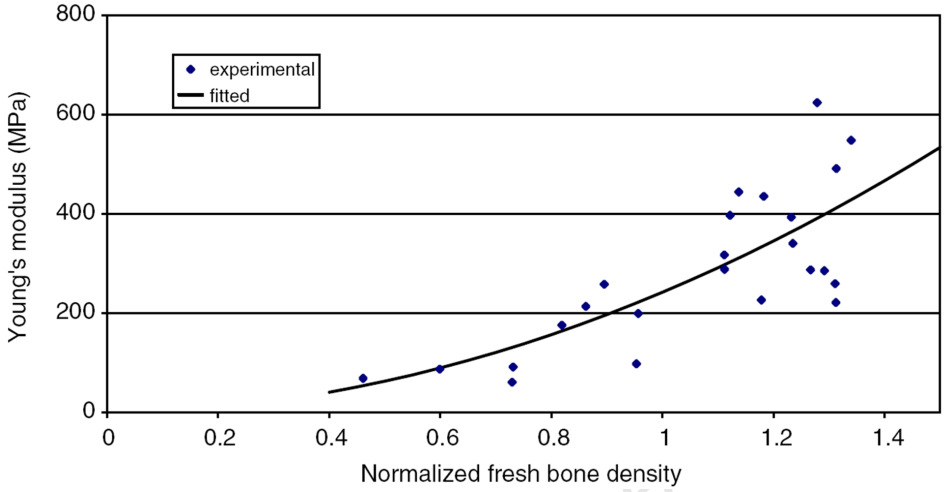

(a)

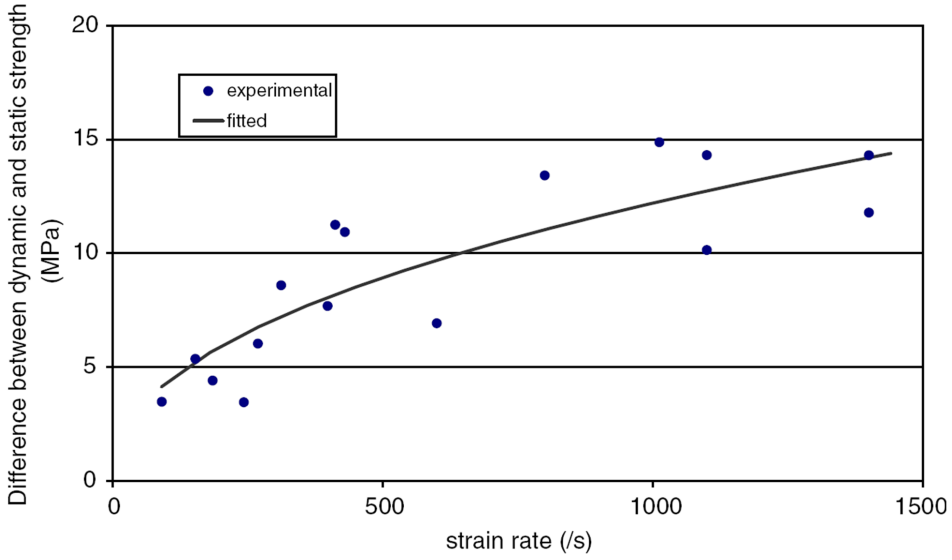

(b)

Figure 2.27: (a) Quasi-static failure stress as a function of specimen density and (d) the difference between dynamic and static strength as a function of strain rate as determined by Shim et al. [21]

2.7 The risk of injury

Injury criteria, such as the criterion related to AV impact (Section 1.1), is related to the *risk of injury.* According to the South African Military Standard (RSA-MIL-STD-37 [8]) survivability in landmine protected wheeled vehicles shall be calculated using a 10% probability threshold values for Abbreviated Injury Scale (AIS) 2+ injuries. An injury of AIS 2+ categorically corresponds to *moderate injury*, which includes simple fracture of the tibia, patella or pelvis when considering the lower extremity. The lower extremity injury criterion (IC) for anti-vehicular (AV) landmine resistant vehicles is based on an axial force threshold of 5400 N, measured in the lower tibia load cell of a Hybrid III crash test dummy during ballistic impact [6]. The IC stems from tests on post mortem human surrogates (PMHS) (Yoganandan et al. [7]) and represents a 10% risk of ankle/foot fracture as measured by the Abbreviated Injury Scale 2+ (AIS 2+) for dynamic impact to the plantar foot surface.

The work of Yoganandan et al. [7] was aimed at understanding the biomechanical response of the human foot/ankle complex under axial loading. The research program involved component testing of human cadaver lower extremities exposed to plantar foot surface impacts. Combined fracture probability distributions were developed from dynamic impact tests at the Medical College of Wisconsin (MCW) (26 tests) and similar tests at Wayne State University (17 tests) and Calspan Corporation (10 tests). The total available sample size was 52. The dynamic force-time histories of the impact loads are not reported, however, the plantar surface impact velocity of the MCW experiments ranged between 2.2 ms^{-1} and 7.6 ms^{-1}, and those for Calspan are all reported to be 4.6 ms^{-1}. Dynamic data indicated that the fracture forces ranged between 7.8 kN and 13.0 kN. Yoganandan et al. [7] determined a closed form equation for the probability of fracture (of any of the bones of the lower extremity) if axial tibia load force is the only discriminant:

$$P_R(F) = 1 - exp\left\{ - exp\left\{ \frac{\ln(F\ (\text{kN})) - 2.036057}{0.3323456} \right\} \right\} \tag{2.39}$$

This risk function does not include the conditions of active lower extremity musculature. These conditions are well suited to the loading of occupants in AV-mine protected vehicles as occupants do not usually anticipate an AV-mine detonation.

Funk et al. [9] developed an empirical model for the axial load tolerance of the foot/ankle complex for the which includes lower extremity muscle tension. Experiments were conducted on 43 isolated lower extremities from post mortem human surrogates. The experimental apparatus is presented in Fig.2.28. Blunt axial impacts were delivered to the plantar foot surface by a padded transfer piston, which was accelerated by a pneumatic impactor. The axial force history in the tibia was measured with a tibia load cell. The

precise time of fracture was determined by acoustic sensors which monitored the onset of cracking. The apparatus was equipped with the ability to include Achilles tension in order to simulate the effect of pre-impact bracing or panic braking which impose additional loads on the lower extremity bone structure.

The effect of muscle tension was investigated by testing a two groups of extremities: the first, *with*, and the second *without* without experimentally simulated Achilles tension. The primary fracture mode with no Achilles tension was calcaneal fracture. However, fracture initiated at the distal tibia more frequently with the addition of Achilles tension.

Funk et al. [9] implemented a multivariate Weibull model using age, gender, body mass, and peak Achilles force as predictor variables to represent the peak axial tibial force data. Funk et al. [9] correlated the risk of fracture of any of the bones of the foot-ankle complex, with axial tibial force in a closed form survivor function:

$$\begin{aligned} P_R(F|x_i) \;=\; \exp\Big\{ -\exp\Big\{ & 4.99\ln(F\ \text{(kN)}) - 43.7 - 0.964\cdot\ \text{gender (male)} \\ & + 0.0793\cdot\ \text{age (years)} \;- 0.552\cdot\ \text{mass (kg)} \\ & - 0.437\cdot\ \text{Achilles tension (kN)} \Big\}\Big\} \end{aligned} \tag{2.40}$$

Where $P_R(f|x_i)$ is the probability that the fracture force in the tibia is greater than F, given the vector x_i of predictors. The survivor function presented by Funk et al. [9] can be used to estimate the risk of foot/ankle fracture that a blunt axial impact would pose to a human based on the peak tibial axial force measured by an anthropomorphic test device.

Notice that both Yoganandan et al.[7] and Funk et al. [9] correlated the risk of fracture of *any* of the bones of the foot-ankle complex, with the corresponding axial force measured in the tibia.

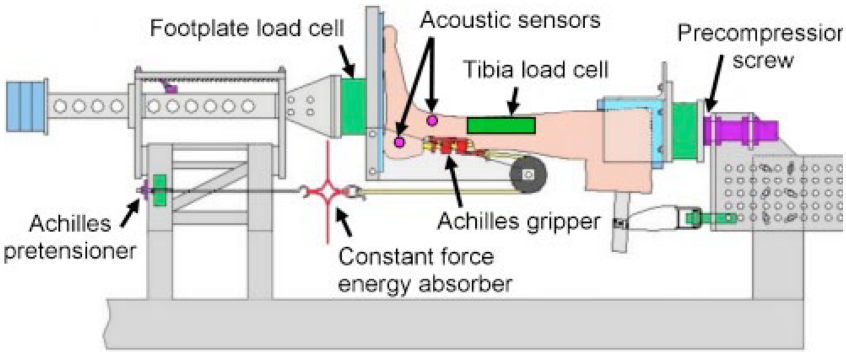

Figure 2.28: A schematic of the test apparatus used to determine the response of PMHS lower extremities to impacts to the plantar foot surface. The Achilles gripper, pretensioner, and energy absorber were used to experimentally simulate active muscle tension in the study of Funk et al. [9]

In cases where PMHS tests are not possible, the computational simulation of the complex, dynamic interactions of the human body in harsh environments is an extremely useful and cost-effective research and development tool (Hight [11]). Representative computational modelling of the lower extremity requires accurate models of the constitutive behaviour and failure of biomaterials such as bone and muscle tissue.

It is possible to determine the stress, which corresponds to the desired probability of fracture from appropriate material tests on biomaterials. Pithioux et al. [89] investigated the tensile ultimate stress of bovine cortical bone and expressed the probability of failure with a Weibull cumulative distribution function:

$$P_R(\sigma_{ut}) = 1 - exp\left\{ -\frac{\sigma_{ut}}{\sigma_0} \right\}^m \Bigg\} = 1 - e^{-\left(\frac{\sigma_{ut}}{\sigma_0}\right)^m} \tag{2.41}$$

Where $P_R(\sigma_{ut})$ is the probability of reaching the ultimate stress, σ_{ut} [MPa] is the ultimate stress and σ_0[MPa] and m are parameters that are identified through a curve fitting process. The dynamic and quasi-static fracture risk curves by Pithioux et al. [89] are

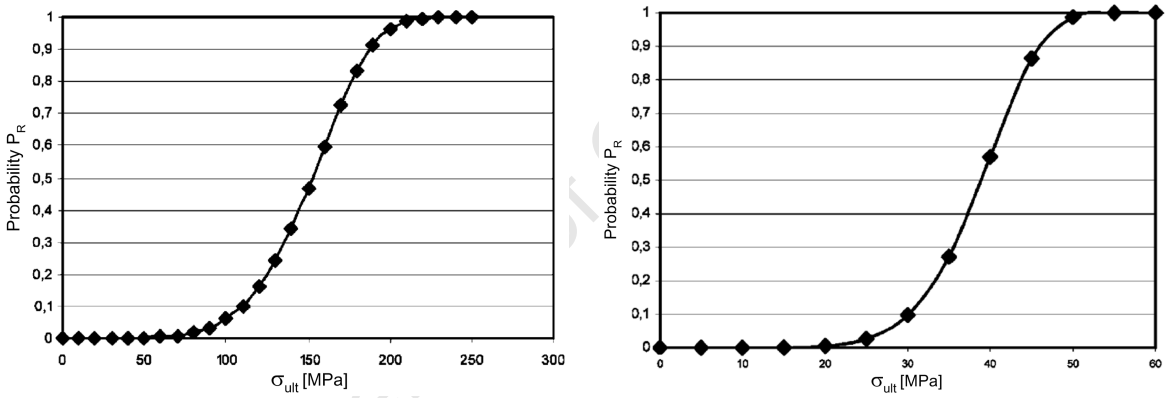

(a) (b)

Figure 2.29: Failure probability laws for compact bones under (a)quasi-static and (b) dynamic tension loads [89]

shown in Fig.2.29. The quasi-static failure stresses reported by Pithioux [89] correlate very well with the work of other researchers such as Adharapurapu et al. [20]. However, the dynamic risk curve (Fig.2.29(b)) is located at stresses that are uncharacteristically low in comparison with other values found in literature, where bone is expected to fracture at higher stresses [12, 14]. Such a failure model enables the determination of injury criteria, where a stress threshold for a certain probability of injury is desired.

Chapter 3

Bovine bone structure

One of the requirements for ethical clearance to conduct experiments on human materials is preparatory studies on the related animal material. The animal material chosen here, must therefore reflect the properties of human bone as accurately as possible to ensure the relevance of the techniques developed. Table 3.1 compares some mechanical properties of human cortical bone with those of bovine and equine bones in tension as determined by Currey [45, 90]. Both bovine and equine bones have higher Youngs moduli than human bone. It is not clear from Table 3.1 if equine and bovine bones have a comparable or superior strength and ability to sustain deformation in relation to human bone. The work of McElhaney [12] indicated that bovine bone has a greater compressive strength than human bone over the dynamic and quasi-static strain rate regimes (as previously shown in Fig.2.11).

	Young's modulus [GPa]	Strength [MPa]	Ultimate strain [m/m]
Man (Currey [45])	17.5	148	0.0031
Man (Currey [90])	16.7	122	0.0072
Bovine (Currey [45])	26.5	167	0.0033
Bovine (Currey [90])	24.3	142	0.0056
Equine (Currey [90])	23.7	155	0.0065

Table 3.1: Comparison of mechanical bone properties of human, equine and bovine bone in tension

Evans et al. [46] reported that **various types of bone can be compared provided, that it is of the same histological type and has a similar number of osteons and osteon fragments per unit area. This approach is supported by Ascenzi and Bonucci [47], who reported that bone osteons from different species behave similarly at the microstructural level.**

It was decided that bovine femur bones would be used in the present study. The choice of this material is motivated by the following reasons:

- The development of experimental testing techniques for bone requires an ample supply of specimens. Bovine femur bones are readily purchased from the local butchery.
- A letter describing the intended experimental procedures for this study was submitted to the Animal Research Ethics Committee at the Faculty of Health Science of the University of Cape Town. No further ethical clearance was required to conduct experiments of bovine cortical bone in vitro.
- There are no special or expensive storage requirements for bovine bones. The material is hygienic as it was originally intended for the purposes of human consumption.
- There is sufficient literature available on bovine bone which gives a good indication of mechanical properties. An experimental result from a new method can be verified with greater confidence.
- Bovine femurs have a thick cortical wall which supplies ample material for specimen extraction.

3.1 Preparation of a bovine diaphysis specimen

Bovine femurs were purchased after being transported in a refrigeration truck from the abattoir in Grabouw (about 60 km) to the local butchery in Cape Town. Fig.3.1 shows the bones of the bovine skeleton. The femur is located at the upper part of the rear limbs of bovine species. All meat and most of the bone facia were already removed when the bones were in their purchased state. It is estimated that the bones were received from the butchery between 3 to 7 days after slaughtering.

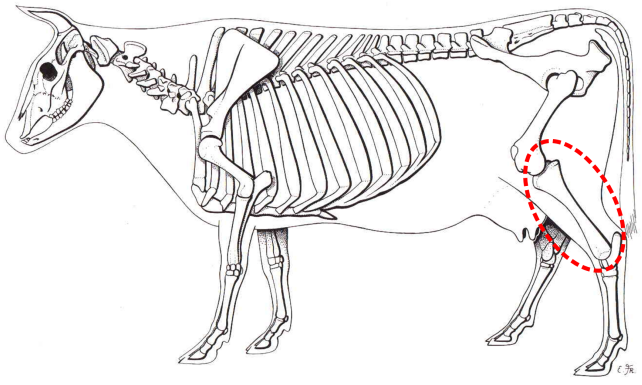

Figure 3.1: A diagram of a bovine skeleton [91]

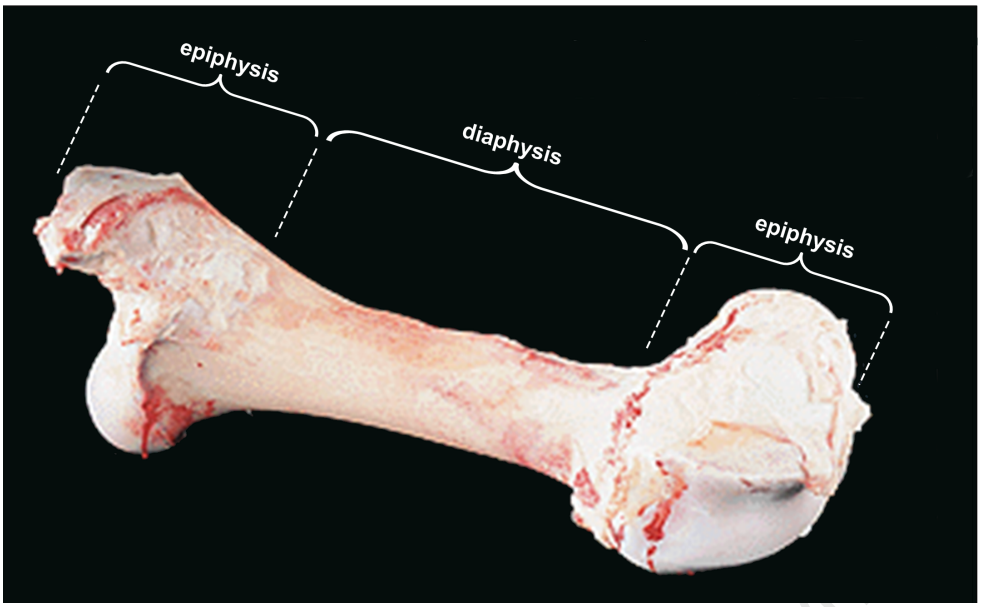

Figure 3.2: A photograph of a bovine femur bone

A photograph of a bovine femur bone is presented in Fig.3.2. The femur bones were taken to the Department of Human Biology machining facility on the Medical Campus of the University of Cape Town where they were thoroughly thawed in water before starting the machining process. The mid-diaphysis was cleaned by removing the articulating ends of the bone with a band saw, leaving only an approximately 150 mm section.

This section was frequently split in half to increase the ease of handling. The remaining soft tissue and bone marrow was scraped off with a scalpel or pulled off with small pliers. Fig.3.3 shows a cross sectional view of the mid-diaphysis after cleaning.

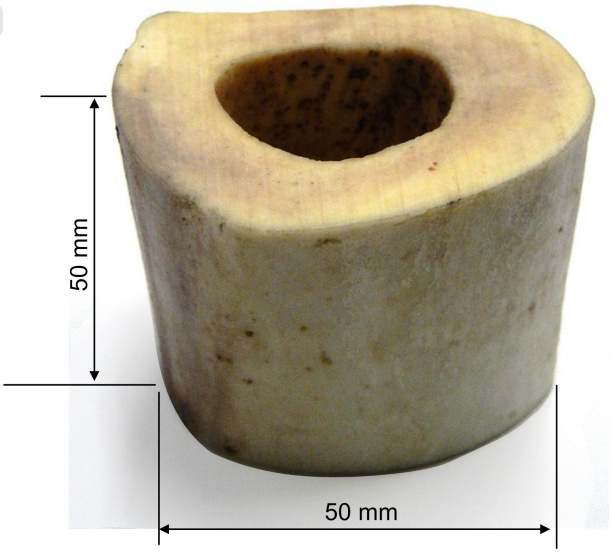

Figure 3.3: A photograph of a bovine femur mid-diaphysis section after cleaning

3.2 Bovine bone histology

Bone strength is influenced by many factors, including location in the body and direction of the load (Tanabe and Kobayashi [16]). Furthermore the failure mechanisms of bone differ depending on the type of load that is exerted on the material (i.e. compression or tension as shown by Ebacher et al. [38]). These loads are channelled through the material by the bone microstructure. The remainder of this chapter is dedicated to the study of the microstructure of the bovine mid-diaphysis. The goals of the microstructural investigation are:

- To describe the nature of the microstructure that is encountered in test specimens extracted from the bovine mid-diaphysis. This would enable future researchers to compare not only their stress-strain results, but also the underlying microstructure with the work presented here.
- To illustrate the presence of shear zones in the fractures of bone specimens that were compressed at quasi-static strain rates in the direction of the bone axis.
- To visualise bone microstructure to facilitate the development of an anisotropic bone model in future work.
- To supplement macroscopic observations of bone compression on a microstructural level.

The preparation of bone for histological examination is subsequently described. The results of the histological examination are discussed under two topics. The first describes the types of histology encountered in the study of bone specimens. The unloaded and therefore undistorted forms of the bone histology are reported and discussed. The second topic demonstrates significant observations made during the investigation of specimens that were exposed to quasi-static loading. These observations are discussed in Chapter 5. No histological investigations were possible for bone specimens exposed to dynamic loading because the specimens were completely destroyed during the SHPB tests.

3.2.1 Preparation of bovine bone for histological examination

Chinsamy and Raath [92] describe a method of thin sectioning specifically intended for studying the microscopic structure of fossil bone. Chinsamy [93] states that this method of thin sectioning can be used on fresh bone specimens, provided that they have dried sufficiently. This method is chosen because the equipment is readily available in a laboratory at the Department of Zoology at the University of Cape Town. The technique described here is fully described by Chinsamy and Raath [92] and is specific to the one used in the

thin sectioning laboratory at the Department of Zoology. It is summarised here as applied to fresh bovine bone specimens.

The procedures used for preparing thin sections of bovine bone is divided into seven processes:

- Measurement and recording data
- Photography
- Embedding specimens for sectioning
- Sectioning embedded bone
- Grinding one surface to affix to a slide
- Mounting and labelling the specimen
- Finishing

Measurement and recording of data

Thin sectioning of bone is a destructive process. For this reason the mechanical properties of bovine bone in compression are determined from the specimens before the histology can be examined. Some bovine bone specimens were reserved for histological investigation and did not undergo compression testing. The purpose of this was to observe and classify the undamaged bovine microstructure. Compressed specimens were also studied to make a preliminary assessment of damage for future work. All specimens were dried by placing them in containers at room temperature for two weeks prior to thin sectioning.

Photography

Chinsamy and Raath [92] recommend the photography of specimens to create two sets of records:

- Record an unambiguous record of the bone morphology before sectioning.
- Compile a photographic record of the end result of sectioning

These steps were not of such great importance for the present study because no attempt was made to study the variation of bone properties or microstructure with location. However, an exact photographic record could be of greater importance if ethical clearance is obtained to conduct an investigation of human bone material. An extract from a photographic record is shown in Fig.3.4. This record will enable specimens to be traced back to the exact bone and location from which they originate.

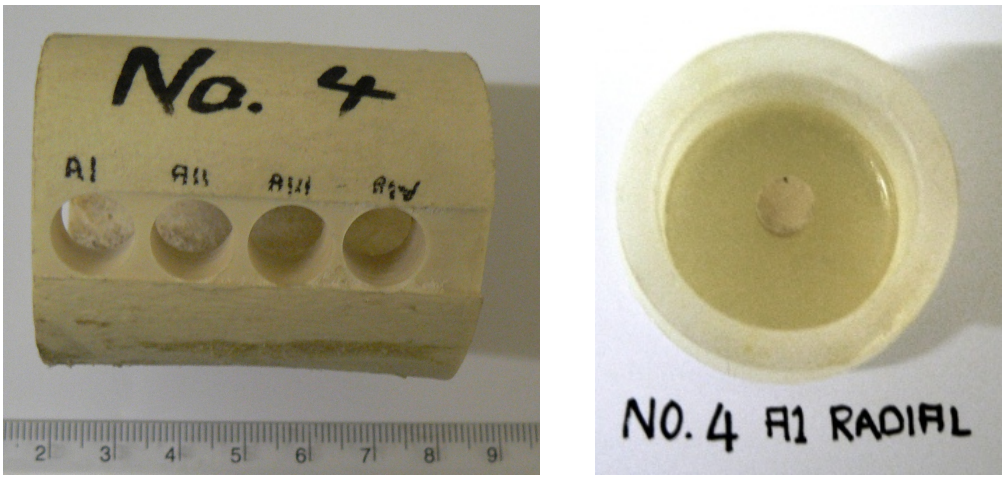

(a) (b)

Figure 3.4: Photographs of (a) a bone shaft with a bone number, nominal dimensions and locations and numbers of specimen extraction and (b) a specimen inside a container, ready for embedding. The specimen is clearly marked throughout the thin sectioning process with the bone number, specimen number and machining direction.

Embedding specimens for sectioning

Specimens are embedded in a mounting medium or resin to reinforce fragile tissue structures and prevent the relatively brittle specimen from shattering or disintegrating during sectioning and grinding. As compression tests were conducted on cylindrical specimens that are 6 mm in length and diameter, the mounting medium also enlarges the dimensions of the piece to increase the ease of handling.

A clear, cold-curing epoxy resin was used (Epofix). This medium was chosen because it does not interfere with the optical properties or tissue structure. The resin was prepared according to the product instructions.

Suitable containers are required for the embedding process. Custom designed moulds of latex or silicone rubber can be used in cases where the size of the specimen is predictable. Fig.3.5(a) shows such containers with removable bases that were custom made for embedding specimens. Other disposable containers such as empty yoghurt cups and pill or film containers were also found to work well. Containers should have sufficient room for the specimen, but should not be too large to avoid wastage of the mounting resin. Containers are prepared by smearing the inner surface with petroleum jelly (Vaseline) to facilitate removal of the embedded piece.

To ensure that the bottom of the specimen is well embedded a 5 mm layer of resin is poured into the container and allowed to harden. The specimen is placed in the required position and the resin is poured until it covers the specimen completely (Fig.3.5). The specimen is allowed to cure and harden for 24 hours and then removed from the container.

(a) (b)

Figure 3.5: Photographs of (a) suitable containers for specimen embedding: custom moulds with removable bases and a yoghurt container and (b) a bone diaphysis specimen embedded in resin inside a container of the right size.

Sectioning embedded bone

The specimen is sectioned at the site where the bone histology is to be investigated. This task proved challenging because of the small specimen size. Excess resin is removed with a grinder, fitted with a ceramic cutting blade.

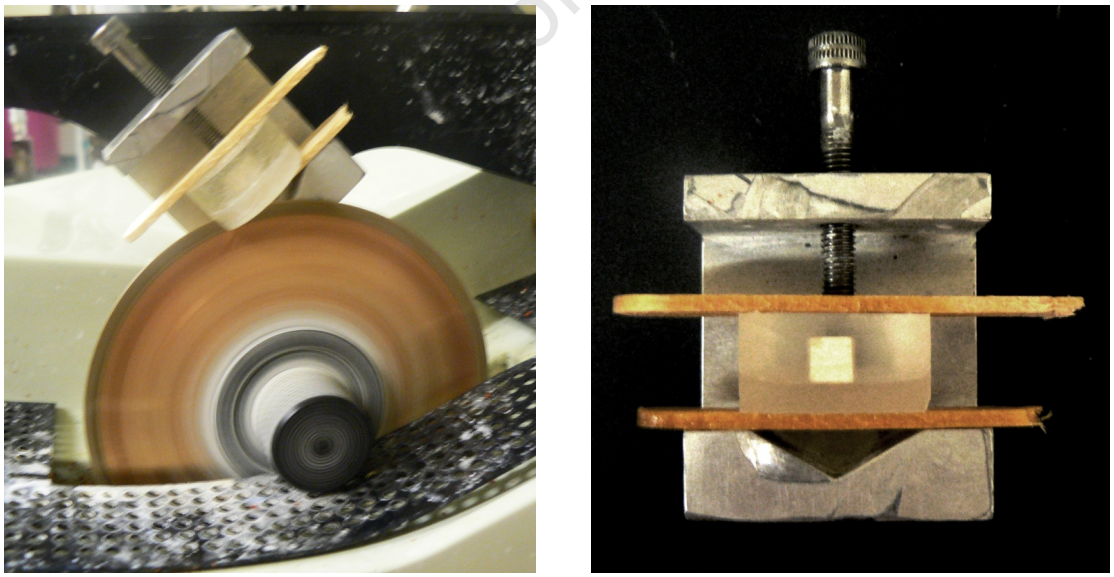

(a) (b)

Figure 3.6: In this photograph (a) an embedded specimen is gripped firmly in a holding mount and sectioned with a rock cutter with a water-cooled-diamond studded blade. (b) A photograph of a holding mount with an embedded specimen sectioned at the desired location.

The embedded specimen is gripped firmly in a holding mount and sectioned with a rock cutter with a water-cooled-diamond studded blade which rotated at 120 rpm (Fig.3.6).

The smoothest cuts were achieved with a fast blade rotation and a slow cutting speed. It is important to realise that a small amount of material will be lost due to the thickness of the cutting blade. The specimen will also be polished in subsequent steps, which means that some more of the material will be ground down and lost. It is therefore important to allow a little excess thickness to ensure that the histology can be studied in the desired location.

The purpose of this microstructural investigation was simply to observe bovine bone histology and some crack patterns as a result of quasi-static loading. The knowledge of bone microstructure was therefore to attribute the compression data to a possible series of classified bovine bone microstructures and not to study fracture and crack propagation.

Grinding one surface to affix to a slide

The cut surface was ground down on a series of abrasive grinding discs until the surface is smooth and completely free of scratch marks. Mechanical grinding involves the use of a rotating lap wheel onto which waterproof abrasive grinding disks are placed. The rough cut surface is smoothed by rubbing it in small circular motions on a sequence of grinding discs with decreasing coarseness. Hand pressure is applied to the specimen, whilst continually changing the direction of the circular motions. The sequence of discs were 400, 600, 800, 1000 and finally 1200 grit (the finest).

Care was taken not to wedge the specimens. Final polishing is done with an Op-Chem polishing cloth with colloidal silica suspension (OP-U Suspension) on the lap wheel (Fig.3.7). After final polishing the specimen is washed with water and dried. The drying process is sped up by placing the specimen onto filter paper towels, whilst taking care not to scratch the surface.

Figure 3.7: A photograph of the final polishing of a specimen with an Op-Chem polishing cloth on a lap wheel

Mounting and labelling the specimen

The polished surface of the specimen is mounted onto a petrographic glass slide. Frosted slides were found [92] to provide better optical resolution as well as a better adhesive surface for the mounting medium. Clear petrographic slides can be frosted by rubbing them gently on a glass plate with an abrasive paste of 600 grit silicon carbide powder. The slides were labelled by engraving with a diamond tipped stylus to ensure that the specimens remain identifiable. Chinsamy and Raath [92] suggested that this is done before the specimen is mounted onto the slide as engraving occasionally causes the slides to break or crack. Care must be taken to stick the correct specimen onto the correct slide. The slides are placed on a flat surface and paired up with the correct specimens. Epotek resin adhesive is used to fix the polished end of the specimen to the frosted side of the petrographic slide. The adhesive is allowed to cure for 24 hours or until it is completely dry.

The next step is to remove the excess material from the glass slide by making a section of approximately 1 mm thick (Fig.3.8). A "Micro-Trim" section-cutting machine was used for this purpose. The slide is placed into a fixture that frames it and holds it in position by vacuum suction. The frame is bolted onto the rock cutter with a water-cooled, rotating, diamond-encrusted blade. The blade is positioned to leave about 1 mm thickness of the polished, embedded specimen on the glass slide. Again account must be taken for material losses due to the thickness of the blade.

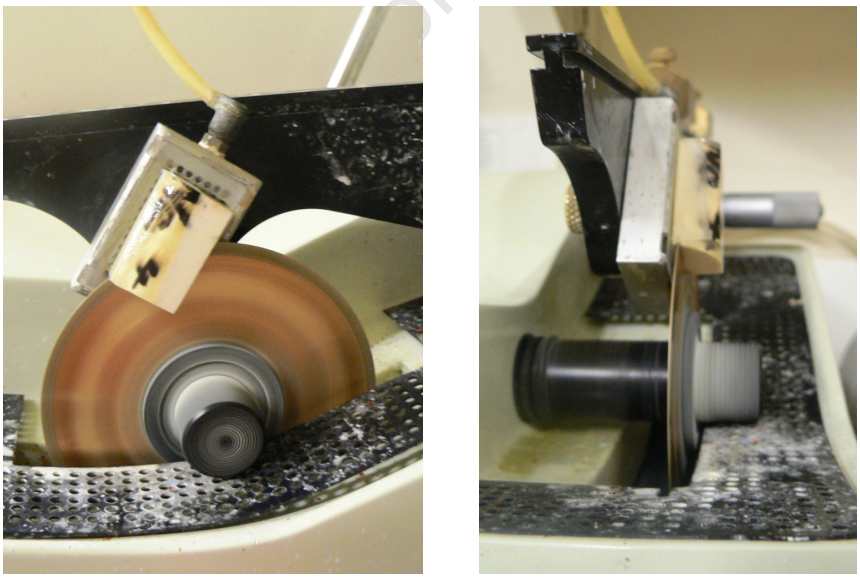

(a) (b)

Figure 3.8: Photographs showing how (a) the slide is held in position by vacuum suction and (b) a rock cutter with a diamond encrusted blade is used to remove excess material, leaving about 1 mm thickness of the polished, embedded specimen on the glass slide.

Finishing

The resulting thin sections will bear distinct cutting marks on the free surface. These scratches must be removed by carefully grinding the slide down as outlined in Section 3.2.1. Slides are very thin and could be difficult to handle during grinding on a lap wheel. Handling can be facilitated by making a slide holder (from i.e. teflon) in the form of a rectangular block, with a slot of the exact size (loose fit) and depth of the glass slides (Fig.3.9). A hole through the holder can allow for the removal of the slide by pushing on the slide.

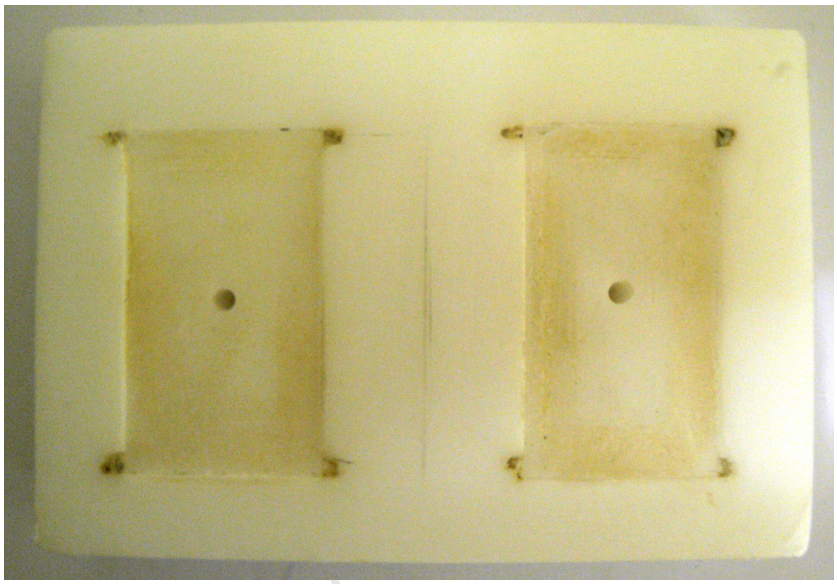

Figure 3.9: A photograph of a custom made double slide holder with slots at the corners and holes to facilitate the removal of slides

The slide is progressively ground down until all scratch marks are removed and it is thin enough for light to shine through. The slide is then ready for final polishing. Progress is continually assessed on a low power dissecting stereomicroscope to ensure that the specimen is not wedged or ground down too far. The process ends when the bone microstructure is clearly visible. A more detailed examination is carried out under higher magnification on a more powerful microscope.

3.2.2 Histology of bovine bone specimens

The histology of unloaded bovine bone is undertaken here to describe the nature of the microstructure that was encountered in the test specimens. Knowledge of bone histology also enables the visualisation of bone structure to facilitate the future development of an anisotropic bone model. Microstructural classification would additionally enable future researchers to compare not only their stress-strain results, but also the underlying microstructure with the work presented here.

The thin sections in this study were conducted in two planes:

- Transverse sections cut through the bone in a plane that is perpendicular to the bone axis. These sections show the bone histology that is circumferentially arranged around the central bone axis as shown in Fig.3.10(a).
- Longitudinal sections are made in any plane that contains the bone axis. These sections show the structure of the bone histology that runs down the bone cortex in the direction of the bone axis (Fig.3.10(b)).

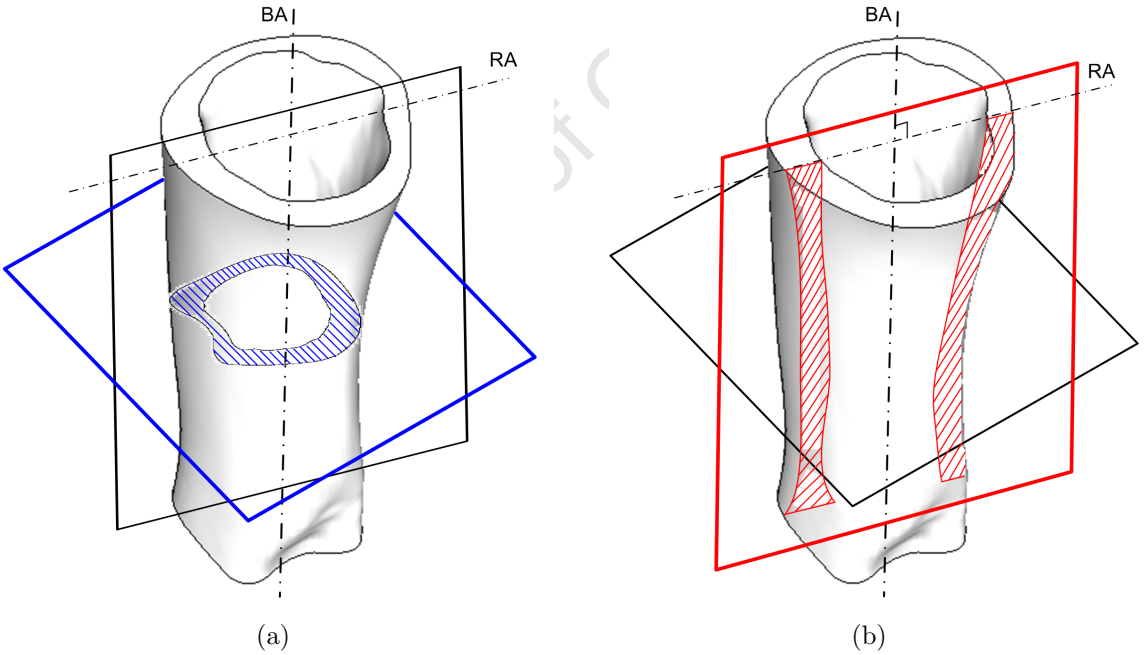

Figure 3.10: A (a) transverse section and a (b) longitudinal section of a femur diaphysis. The bone axis (BA) and radial axis (RA) of the bone coordinate system are indicated

Transverse sections

Both whole bovine femur shafts and test specimens were sectioned to investigate undamaged bone histology. A transverse section of a whole bovine mid-diaphysis is shown in Fig.3.11. The endo-osteal (inside) and peri-osteal (outside) bone surfaces are indicated in

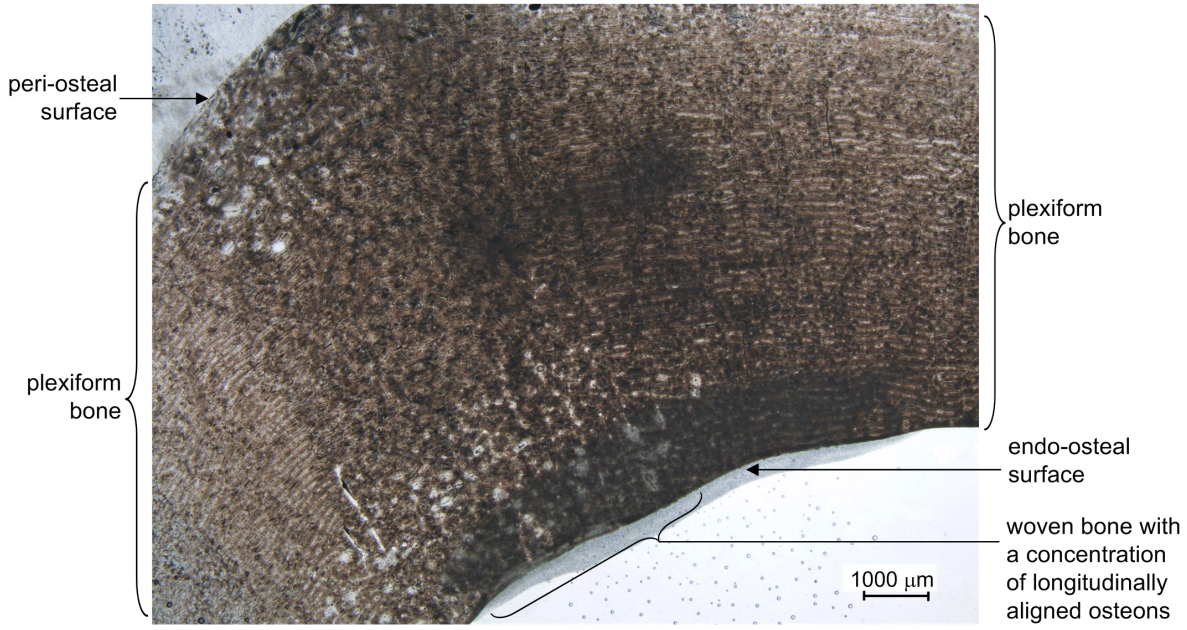

Figure 3.11: A micrograph which shows the bone histology in the transverse section of a bovine femur diaphysis

the figure. **The bone histology is arranged in roughly concentric rings between the inner and outer bone surfaces. The transverse microstructure is predominated by two microstructural arrangements: a plexiform microtructure and woven bone with a concentration of longitudinally aligned osteons. This slide illustrates that the arrangement of bone histology can vary from location to location within an individual bone. This could possibly explain observations by Morgan and Keaveny [36] that bone tissue properties (such as density and strength) vary from member to member and within an individual part.**

The woven bone microstructure is magnified in Figs.3.12(a) and 3.12(b). The figure shows a concentration of longitudinally aligned primary osteons within the woven bone matrix. No secondary osteons are discernible from the present section. Secondary osteons form in the cavities that originate as a result of bone growth. Secondary osteons therefore occur in increased numbers in more aged bone specimens. They are distinguished by the presence of a cement line that marks the boundary between the secondary osteon and the old cavity wall. Sasaki et al. [81] stated that the compliant protein polysaccharide material of cement lines is one of the structural reasons for viscoelasticity in bone.

The canal that runs down the centre of the osteon contains blood vessels, nerves and many other cellular structures. **The mineral matrix between the central canal and outer boundary of both primary and secondary osteons is arranged in concentric lamellae. This is evident from the concentric arrangement of the osteocytes**

or bone cells. Sasaki et al. [81] attributes another reason for viscoelasticity to the collagen fibres that comprise these lamellae.

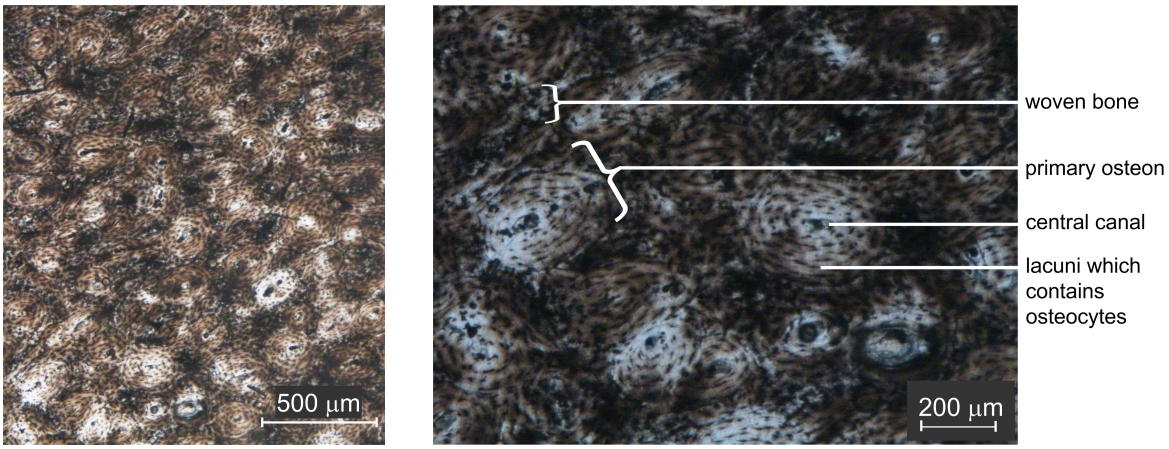

(a) (b)

Figure 3.12: Micrographs of woven bone with a concentration of longitudinally aligned primary osteons in a transverse section of a bovine femur mid-diaphysis. (a) 5× magnification (b) 11.25× magnification

Fig.3.13 shows magnifications of a classic plexiform microstructure with radial anastamosis (branching network). Plexiform bone is formed more rapidly than primary or secondary bone tissue. The structure must offer increased mechanical support for longer periods of time and is primarily found in large rapidly growing animals such as cows or sheep and is rarely seen in young, growing, human individuals. Mineral buds grow first perpendicular and then parallel to the outer bone surface, which produces the brick like structure characteristic of plexiform bone. Each "brick" in plexiform bone is about 125 μm across. Plexiform bone, like primary and secondary bone, must be formed on existing bone or cartilage surfaces and cannot be formed de novo. Because of its organization, plexiform bone offers much more surface area compared to primary or secondary bone upon which bone can be formed [45]. This increases the amount of bone which can be formed in a given time frame and provided a way to more rapidly increase bone stiffness and strength in a short period of time. Structurally, plexiform bone has a greater stiffness than primary or secondary cortical bone. However, it lacks the superior crack arresting properties of primary and secondary cortical bone tissue which is encountered in more active species such as canines (dogs) and humans. Martin and Burr [24] hypothesized that primary osteonal cortical bone may be mechanically stronger than secondary osteonal cortical bone because the vascular canals within primary osteons tend to be smaller than those of secondary osteons.

The specimens used for the experimental investigation of bovine bone response were cylindrical with a length and diameter of 6 mm (as discussed in Section 4.1). A thin section was prepared of a longitudinally orientated specimen cross section which is located in the transverse femur plane (Fig.3.14). **The central bone axis is located towards**

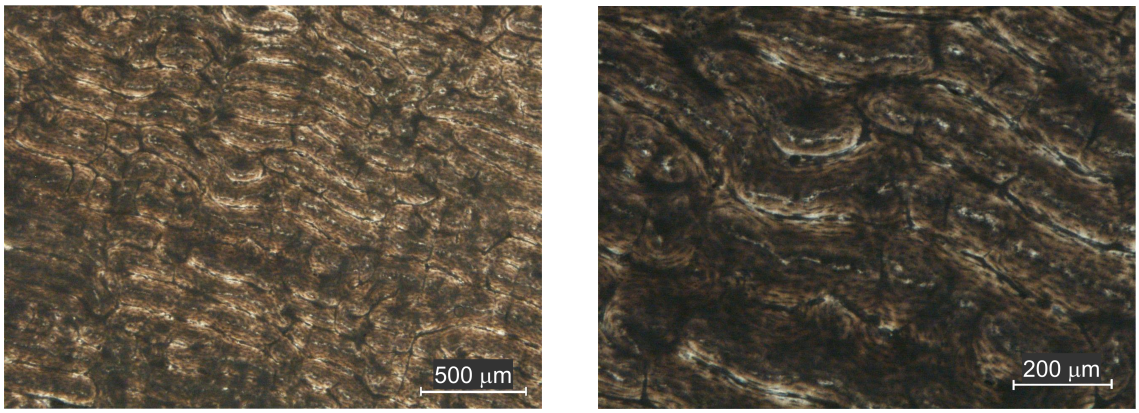

(a) (b)

Figure 3.13: Plexiform bone is visible in a micrograph of the transverse section of a bovine femur mid-diaphysis. (a) 5× magnification (b) 8× magnification

the centre of curvature of the vascular canals which are primarily orientated in circumferential rings around the bone wall. The majority of the osteons are aligned tangentially to the inner and outer bone surfaces. Fig.3.15 shows a greater magnification of the plexiform microstructure of the specimen. Porosity in cortical bone is not only attributed to the vascular canals. The osteons themselves are porous in that they are riddled with cavities called lacunae which contain the osteocytes. These cavities are interconnected by tiny channels called canaliculi. Both the lacunae and canaliculi contribute to bone porosity. The shape and orientation of the lacunae are therefore instrumental in the identification of compaction damage as a result of compression.

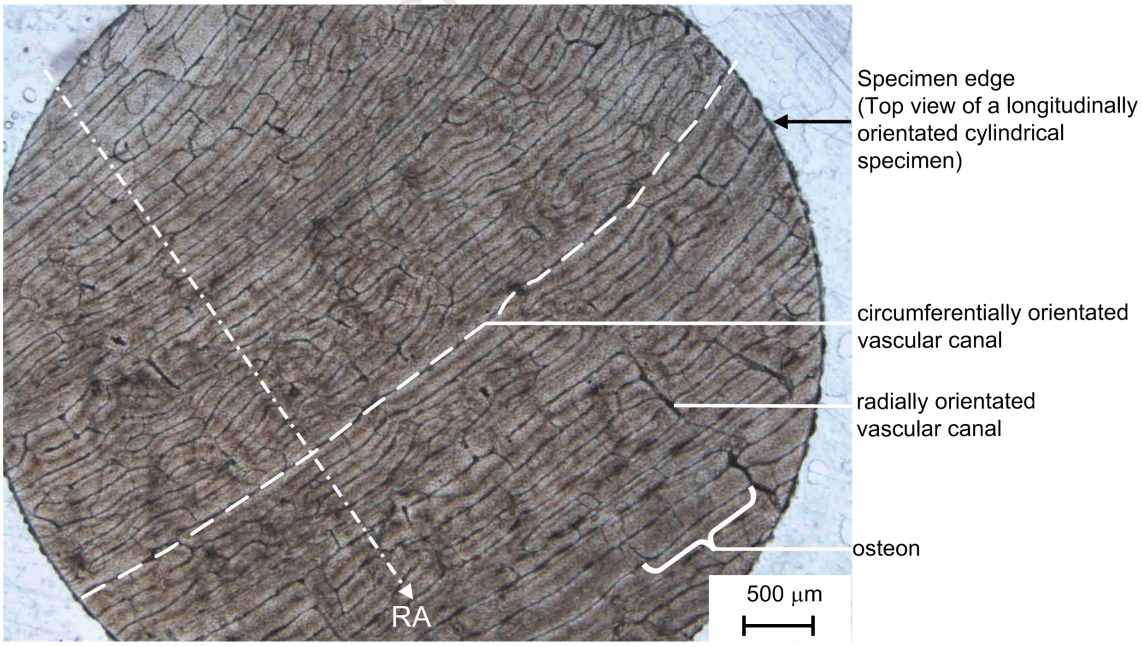

Figure 3.14: A micrograph of the transverse section of a longitudinally orientated plexiform cortical bone specimen showing a radial anastomosis (branching network)

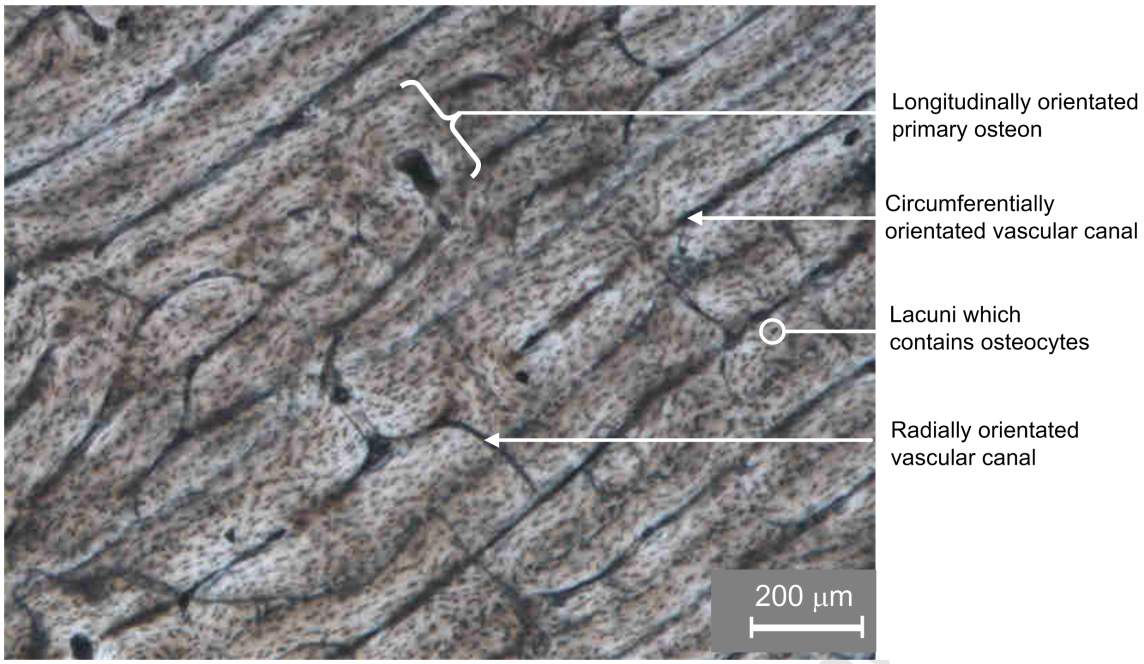

Figure 3.15: A micrograph which shows the magnification (8×) of the plexiform microstructure. A primary osteon directed in the longitudinal bone direction

Kim et al. [94] studied transverse sections of bovine femurs and humeri. This study reports a the presence of plexiform and secondary (Haversian) microstructural arrangements in the transverse sections of bovine cortical bone (Fig.3.16). The microstructural investigation was conducted on a scanning electron microscope (SEM), by immersing specimens in acetone for 30 seconds and coating the fracture surfaces with white gold. Notice the clear cement line boundaries of the secondary osteons in the Haversian microstructure (Fig.3.16(b)).

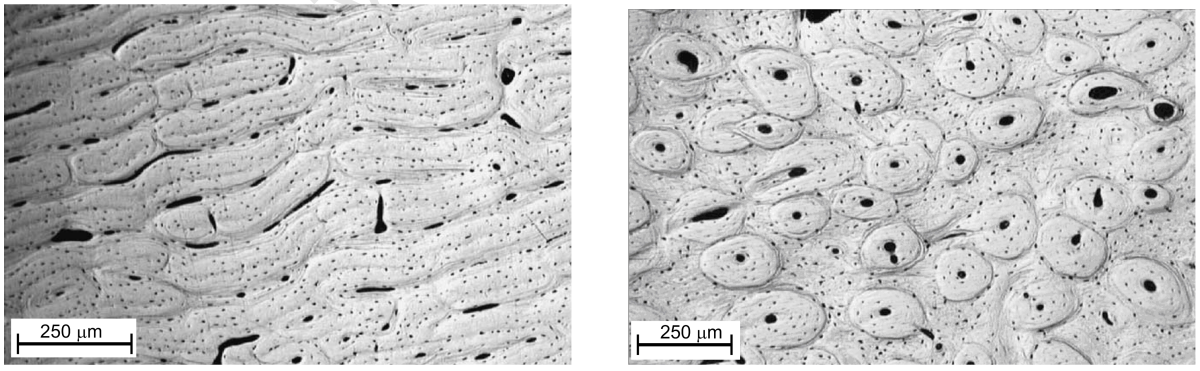

(a) (b)

Figure 3.16: Micrographs from an SEM which show the transverse sections of bovine cortical bone as reported by Kim et al. [94]

Longitudinal sections

A longitudinal section of a bovine femur diaphysis is shown in Fig.3.17. The orientation of the bone axis (BA) is indicated as well as the peri-osteal surface. The endo-osteal surface is not visible but is located towards the right hand side of the slide. The central section of the bone wall comprises of a plexiform microstructure, whereas the microstructure closer to the periosteum has a reticular arrangement. The dominant orientation of the vascular canals of the plexiform structure is more or less aligned with the bone axis. Plexiform microstructure was described in Section 3.2.2.

Figure 3.17: A micrograph of a longitudinal section of a bovine femur diaphysis

Reticular bone tissue is an amorphous younger tissue comprising of a fine network of cells. Enlarged views of this structure are shown in Fig.3.18. The vascular canals observed in this microstructure appear unorganised in the bone compacta and vary greatly in orientation. The lacunae in the bone matrix are aligned in some regions and orientated randomly in others.

Fig.3.19 presents a reticular microstructure from the bovine femur diaphysis as viewed

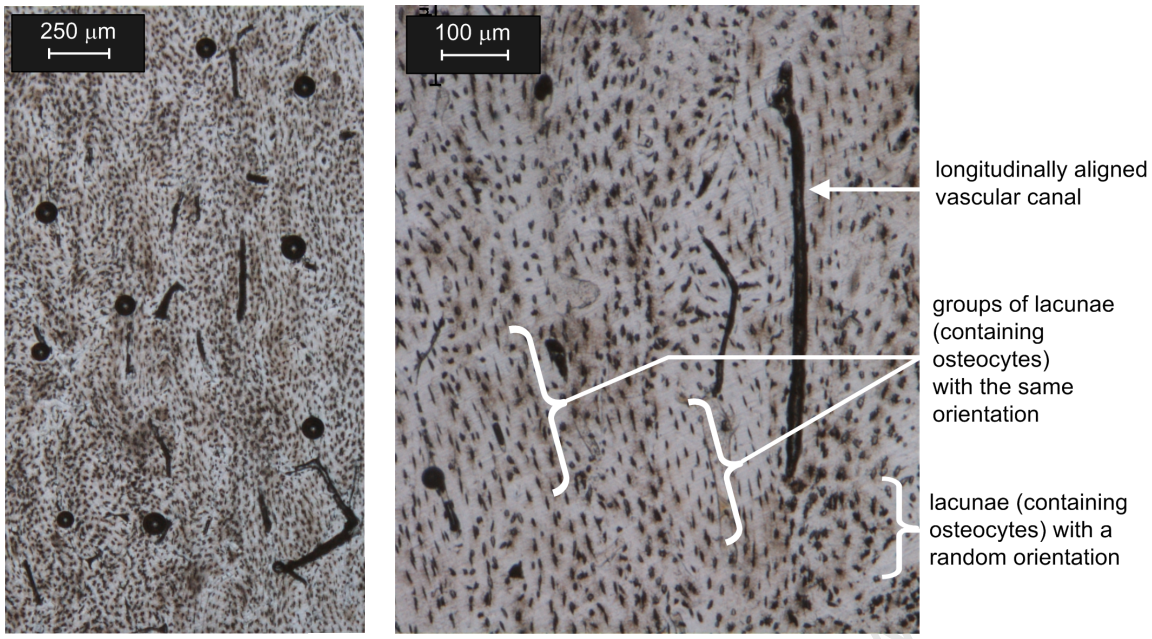

Figure 3.18: Micrographs showing the (a) 5× and 11.25× magnifications of a reticular microstructural arrangement in the longitudinal section plane of the bovine femur diaphysis

through a polarizing filter. The filter causes all the lacunae with the same orientation to be displayed in the same colour. It is clear that the lacunae in the reticular structure do not have a uniform orientation.

Longitudinal sections of longitudinally orientated test specimens presented with one of three microstructural arrangements: laminar, reticular or plexiform. The microstructure of some specimens consisted of more than one microstructural arrangement. The majority of investigated specimens comprised of laminar or plexiform arrangements.

A laminar microstructural arrangement (indicated in Fig.3.20) occurs as part of a plexiform bone microstructure. The specimen assumes a laminar longitudinal structure with a transition to a reticular arrangement. The vascular canals are visible, as well as the lacunae which contain the osteocytes, or bone cells. The vascular porosity of laminar bone is clearly aligned with the direction of the bone axis.

The longitudinal sections of the bovine femur diaphysis show that both laminar and plexiform cortical bone have a vascular porosity that is more or less aligned with the orientation of the bone axis. The reticular vasculature appears unorganised in the bone matrix. It is anticipated that the laminar, plexiform and reticular bone structures could have different mechanisms of microstructural failure because of the variation in their respective arrangement of bone porosity (such as vascular canals and canaliculi).

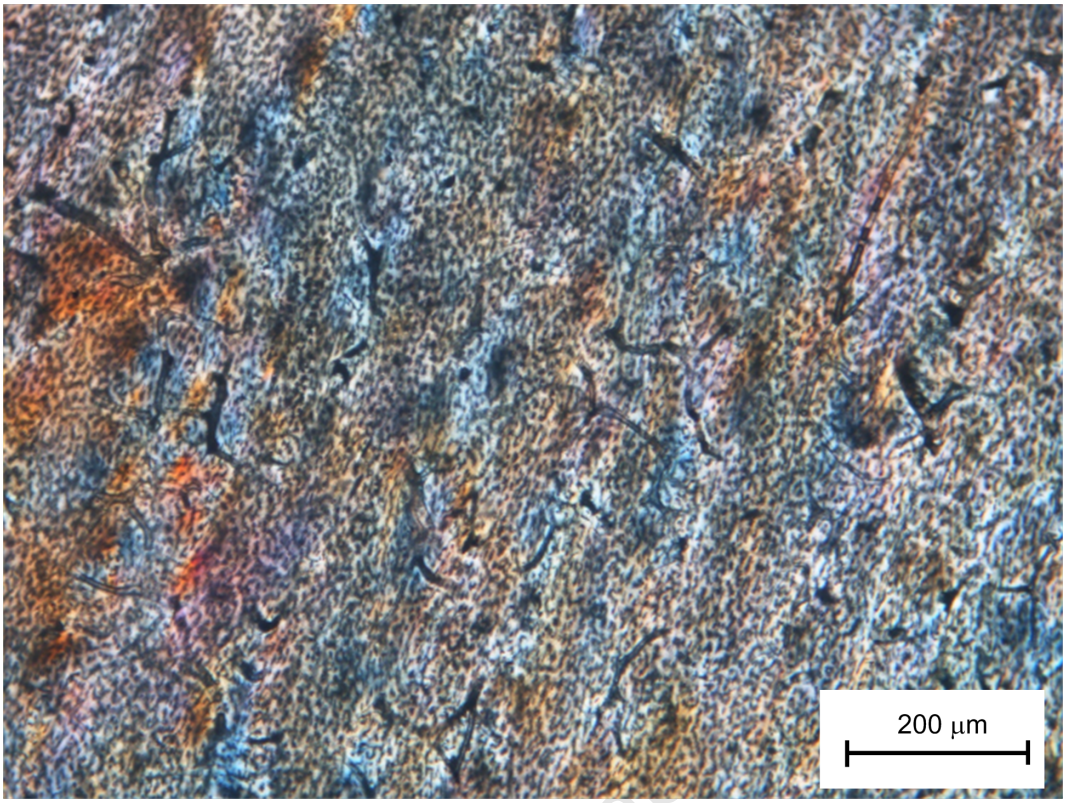

Figure 3.19: A micrograph of a reticular microstructure (longitudinal section) which was taken through a polarization filter

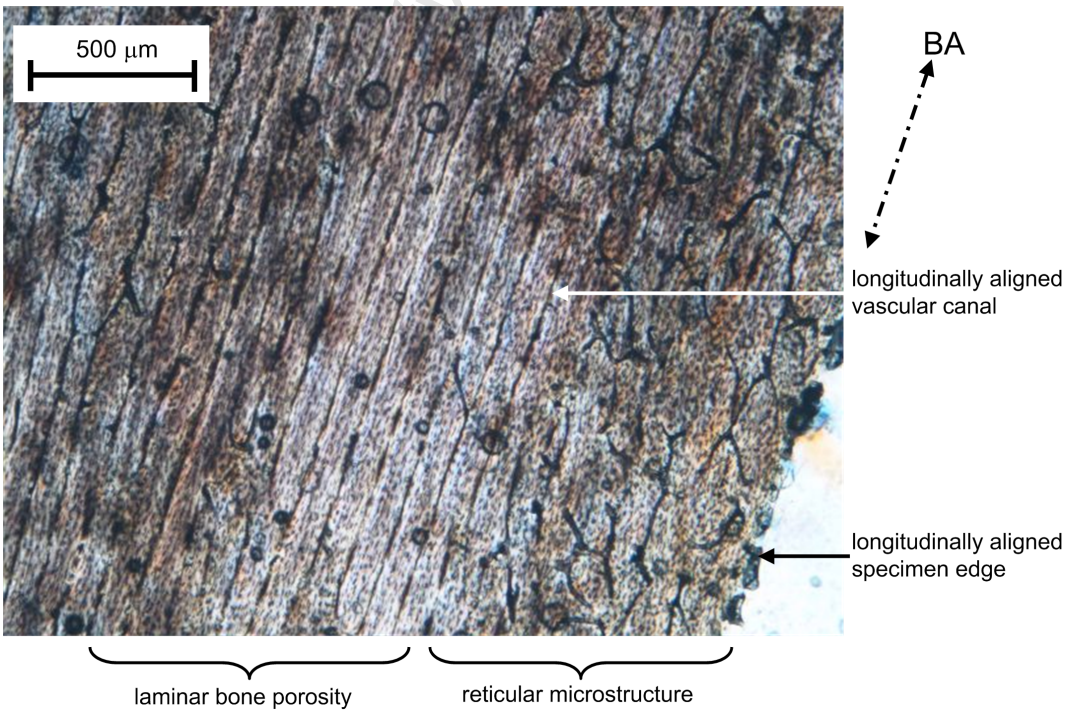

Figure 3.20: A micrograph of a longitudinal section of a bovine bone specimen. The specimen presents with a transition between laminar and reticular bone structure

3.3 An approximation of bovine bone microstructure

The great complexity and variation in bone microstructure is evident from the discussions in this chapter. As thin sectioning is a destructive process, the microstructure of fractured specimens will be investigated subsequent to the discussions on compression testing (Section 5.1.2). It is therefore highly likely that specimens with different microstructural arrangements are considered in the current investigation of bone compressive strength. No attempt will be made to differentiate between the response of cortical bones with specific microstructures. For the purposes of this study, the microstructure of the bovine femur diaphysis is simplified to facilitate the future description of this bone as an orthotropic material with unique properties in three orthogonal orientations (Fig.3.21). The simplification of bone structure is based on two characteristics which are observed in the investigated microstructural arrangements:

- Both laminar and plexiform cortical bone structure have a preferred orientation of the bone porosity which is more or less aligned with the longitudinal bone axis (when considering longitudinal sections). Whereas the reticular bone arrangement is characterised by random orientations of vascular canals and osteocytes. The majority of investigated specimens comprised of plexiform or laminar microstructural arrangements. **The simplified bone microstructure of the bovine mid-diaphysis is therefore assumed to have a longitudinal porosity.**

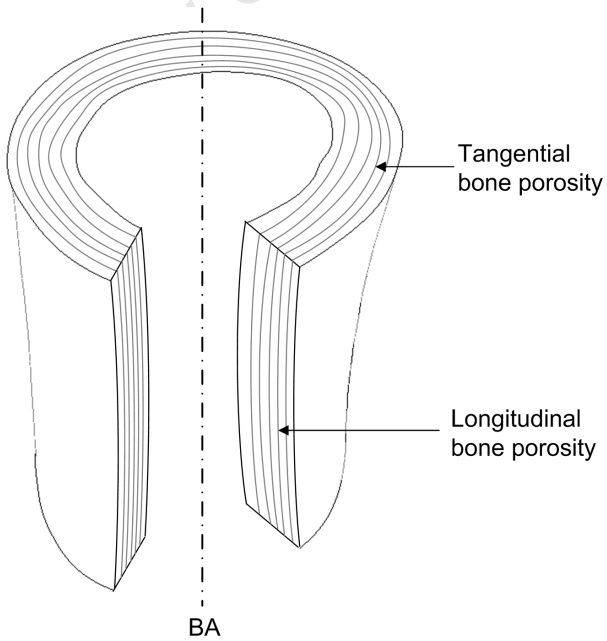

Figure 3.21: A simplification of bone microstructure

- The transverse sections of the bovine femur diaphysis are dominated by plexiform bone microstructure, which is arranged in roughly concentric rings between the inner

and outer bone surfaces. **For this reason the simplified bone microstructure of the bovine mid-diaphysis is assumed to have a tangentially oriented porosity which is arranged concentrically between the inner and outer bone surfaces.**

Chapter 4

Bone Compression Experiments

This chapter discusses the techniques required to conduct an experimental study on the response of bovine cortical bone to different rates of compression up to the event of fracture. The initial experimental programme was aimed at determining bone response for compression along the bone axis. However, the techniques developed in the initial programme facilitate a preliminary study of specimens in the radial and tangential orientations. The first section describes the preparation of bone specimens for compression tests. The following discussion describes the testing of these specimens at as wide a range of strain rates as could be achieved with two available experimental techniques:

- Quasi-static compression on the Zwick test machine.
- Dynamic compression with the SHPB.

Great emphasis is placed on strain rate control and determination of the effects of strain rate variation in the course of dynamic compression experiments.

4.1 The preparation of specimens for compression experiments

Specimens were only extracted from the middle third of the mid-diaphysis as the osteons are well aligned with the longitudinal bone axis in this location:

- The bone diaphysis specimens, which were investigated in Section 3.2.2, were found to have predominantly laminar and plexiform cortical bone microstructural arrangements. The preferred orientation of the bone porosity in these structures was found to be more or less aligned with the longitudinal bone axis.
- The findings of the present study agree with the work of Adharapurapu et al. [20], who showed that the osteons are well aligned with the longitudinal bone axis in the middle third of the bovine femur diaphysis.

The extraction of specimens from the middle third of the mid-diaphysis therefore enlarges the probability of a specimen sample with less variability in fibre direction, despite likely variations in density and microstructure of individual bones.

The machining of bovine femur bones was conducted at the Department of Human Biology machining facility on the Medical Campus of the University of Cape Town. Diaphysis specimens were prepared according to the procedure discussed in Section 3.1. The cleaned mid-diphysis sections were thawed in water (for 1 to 2 hours) whilst awaiting further machining.

The dimensions for specimens used in compression experiments were chosen such that the quasi-static and dynamic tests could be conducted on specimens with the same dimensions. Cylindrical (length 6 mm, diameter 6 mm) specimens were extracted. A cylindrical specimen shape was chosen above cubical for two reasons:

- Cubic specimens require that three pairs of sides be machined perfectly parallel, whereas cylindrical specimens require the turning or coring of a cylindrical bone rod and the cutting of one pair of parallel sides. The choice of cylindrical shape greatly reduced the amount of specimens damaged during machining and demanded only a third of the machining time required for cubic specimens. Bone machining is a laborious process, an experienced machinist required two hours to machine 10 (6 mm $\times$6 mm) cylindrical specimens from one bone.

- As bone is believed to be potentially anisotropic, a cylindrical specimen shape reduces the bias of results if the compressive strength of cortical femur bone varies through the cross section.

Cylindrical specimens were extracted from three orthogonal orientations. The longitudinal axis (LA), radial axis (RA) and tangential axis (TA) are indicated in Fig.4.1. The longitudinal axis (LA) is parallel to the bone axis (BA) which is located at the centre of the medullary cavity of the femur diaphysis. **The orientation of the bone axis (BA) is synonymous with the *axial direction* which is often referred to in literature.** The selection of the present axis system is motivated by the histological examination of bovine cortical bone which is concluded in Section 3.3. The microstructural arrangement of bovine femur bone in the mid-diaphysis is such that the material could potentially be described as an orthotropic structure with unique properties in three orthogonal orientations (Fig.3.21).

Specimens from individual bones were marked clearly with a number and machining date (i.e. Bone 8, 2007/08/13). A separate container was used for each bone. The bone samples were submerged in water and frozen until 32 hours before testing, at which time they were allowed to thaw and rehydrate.

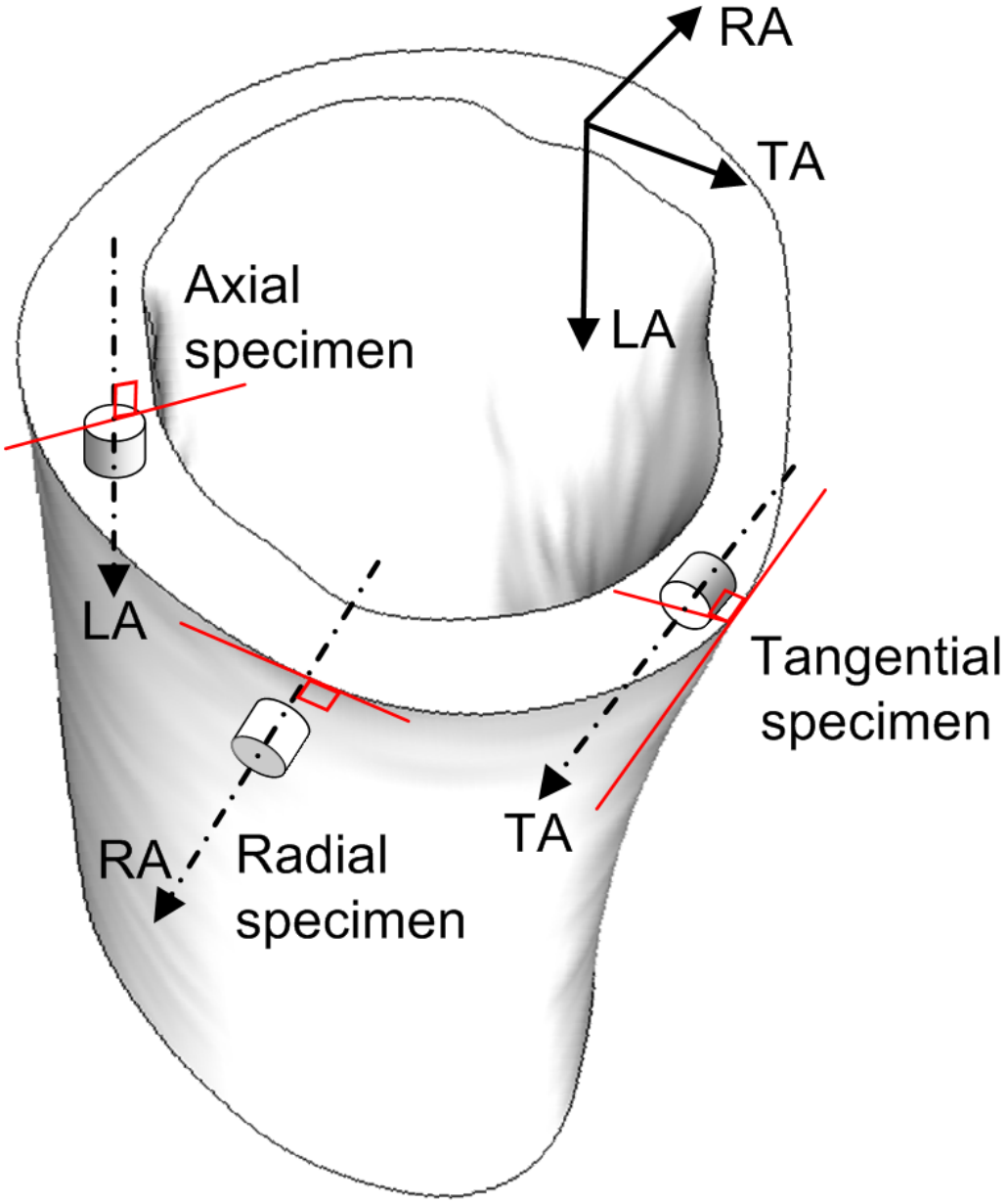

Figure 4.1: Orientation of the longitudinal, radial and tangential specimens within the bone cortex

Longitudinal specimens

Cylindrical (6 mm ×6 mm) specimens were turned from 23 bones (see Table 4.1 for the test programme) for the dynamic and quasi-static compression tests. The mid-diaphysis was sectioned perpendicular to the outer surface. Strips were cut longitudinally in the direction of the bone axis (as shown in Figs.4.1 and 4.2(a)) and turned to cylindrical rods. The material was well lubricated during machining. The rods were sectioned at the required length and faced off to ensure that their surfaces are flat.

Radial specimens

Cylindrical specimens were machined from the mid-diaphyses of five additional bovine femurs (Bones $24-28$). This time, the axis of the specimen was orientated perpendicular to the outer surface of the bone as shown in Fig.4.2(b). A core drill was used to extract cylindrical pieces of material from the bone cortex. The drill was positioned such that all the teeth were in contact with the bone surface prior to machining. The rods were faced off at the desired length.

(a) (b)

Figure 4.2: Photographs of (a) a bone cross section with markers for longitudinal specimen extraction and (b) a bone shaft where radial specimens were extracted with a core drill

Tangential specimens

Tangential specimens were machined from yet another five bovine femurs (Bones $29-33$). The mid-diaphysis was inspected to find a location where the inner and outer surface of the cortex is roughly concentric and where the outer surface is more flat.

The mid-diaphysis was sectioned perpendicular to the bone surface, leaving the flat surface section to one side. It was hoped that the microstructure of the bone is as homogeneously aligned as possible due to these precautions. The surface was machined flat and

finished off smoothly. The bone was clamped and the core drill surface teeth were placed in contact with the smoothed surface to determine the machining direction. Cylindrical specimens were cored from the cortex of the flat surface section.

4.1.1 Bone compression test programme

As cortical bone is a strain rate sensitive material [12, 20] the aim of the experimental programme is to isolate the effects of loading rate and therefore strain rate on the compressive response of bone. Great emphasis is placed on the time vs. strain rate history of the compressive tests. The questions that need to be answered are twofold:

- **Firstly, what are the properties of cortical bone at a variety of quasi-static and dynamic strain rates that are controlled to be constant throughout the test?**
- **Secondly, does the variation of strain rate result in properties that vary significantly from those obtained during constant strain rate tests?**

The bone compression test matrix is given in Table 4.1. Thirty five bovine femurs are considered in this study. Each of the femur bones originate from different animals.

1. Bones 1 - 23 were used to develop experimental techniques and determine mechanical properties of bovine cortical bone in the direction of the longitudinal bone axis. Specimens from Bones 1 - 10 were used for experiments at the quasi-static strain rates and dynamic compression at rates in the order of $10^2\,s^{-1}$.

2. Dynamic compression at higher strain rates proved more challenging. Specimens from Bones 11 - 13 were used to develop the appropriate experimental technique at a strain rate in the order of $10^3\,s^{-1}$. Specimens from the bones in question were additionally tested at the other strain rates to ensure that mechanical properties from these femurs do not vary drastically from the properties of Bones 1 - 10.

3. Fresh specimens were machined from Bones 14 - 23 in order to conduct high strain rate compression tests at $10^3\,s^{-1}$. A small sample of quasi-static and dynamic test were additionally preformed to confirm that these bones respond similarly to Bones 1 - 13.

4. Experiments were conducted on specimens from Bones 24 - 28 in the radial direction to establish if the techniques used for bone in the longitudinal direction also prove effective for bone in the other directions.

5. Specimens from Bones 29 - 33 were machined in the tangential orientation. The experimental techniques developed for longitudinal compression were evaluated for their ability to determine the mechanical properties of cortical bone in the tangential orientation.

6. An isotropic constitutive bone model, which is based on longitudinal compression data, is developed in this study. This model is evaluated by simulating the quasi-static compression of a femur diaphysis section which was extracted from Bone 34.

7. Finally, a fresh longitudinal specimen was machined from Bone 35. The dynamic compression of this specimen was simulated to evaluate the constitutive bone model performance at high strain rates.

	Quasi-static				Dynamic	
	$10^{-4}\,s^{-1}$	$10^{-3}\,s^{-1}$	$10^{-2}\,s^{-1}$	$10^{-1}\,s^{-1}$	$10^{2}\,s^{-1}$	$10^{3}\,s^{-1}$
A. Longitudinal						
1. Bones 1 - 10	x	x	x	x	x	
2. Bones 11 - 13	x	x	x	x	x	x
3. Bones 14 - 23	x				x	x
B. Radial						
4. Bones 24 - 28	x	x	x		x	
C. Tangential						
5. Bones 29 - 33	x	x	x		x	
D. Model validation						
6. Bone 34		x				
7. Bone 35					x	

Table 4.1: Experimental test programme

4.2 Quasi-static compression tests

Quasi-static compression tests were conducted on the Zwick Universal Test Machine at the Centre for Materials Engineering at the department of Mechanical Engineering of the University of Cape Town. The displacement of the screw driven machine head was controlled to compress 6 mm specimens on a rigid platform. The axial force and head displacement were continually monitored and measured at a sampling rate of 20 Hz. The compression test was terminated when the specimen lost its load bearing ability. This was signified by an instantaneous drop in the axial force measurement as the specimen does not resist the displacement of the machine head beyond failure.

A limitation of these tests is that neither a small extensometer nor an LVDT was available to monitor the exact length of specimens. This implies that the only measure of the change of length of the specimen is the head displacement of the machine. The danger is that the machine compliance is included in the deformation attributed to the specimen. The internal compliance of the machine is a function of the force applied to fracture the specimen as well as the stiffness of the test machine. The Zwick is rated to a maximum force of 200 kN. Bones fracture at about 7 kN which is a very small fraction of the maximum range of the machine. Additionally, the machine stiffness is much greater than the stiffness of the specimens. To minimise any possible effects of compliance, the specimens were placed in a way such that the displacement head of the machine pushed directly onto them. No mounting jigs were used in order to eliminate any further sources of deformation that did not belong to the specimen. This study assumes with caution that the change in length of the specimen is equal to the displacement differential between the stationary base and the machine head. This implies that the deformation is assumed to be uniform along the specimen length (6 mm), i.e. strain calculations will exclude localised strain effects.

The instantaneous length of the specimen is thus calculated by the differential between the original specimen length, l_0 and the instantaneous head displacement, $u(t)$:

$$l_{sp}(t) = l_0 - u(t) \tag{4.1}$$

The true strain, ε of the specimen is:

$$\varepsilon(t) = \ln\left(l_{sp}(t)\right) - \ln\left(l_0\right) \tag{4.2}$$

Note that all measures of strain in the present document refer to true strain or logarithmic strain, which is denoted by ε. The true strain rate is the time derivative of the strain which is given by:

$$\dot{\varepsilon}(t) = \frac{\varepsilon(t)}{dt} = \frac{\varepsilon(t) - \varepsilon(t - \Delta t)}{\Delta t} \tag{4.3}$$

In order to calculate the true stress, the instantaneous area of the specimen must be known. It is elected to follow the approach of McElhaney [12] who accounted for the change in area by using Poisson's effects. For the purposes for this study the instantaneous specimen area will be calculated by assuming that bone is isotropic and has a Poisson's ratio of 0.36. This assumption seems reasonable because:

- Cortical bone structure is riddled with blood vessels and canaliculi which causes it to be porous. It is thus unlikely that the compression of this material is entirely volume conserving.
- The value for Poisson's ratio of 0.36 is in agreement with the works of Ashman et al. [61], Katsamanis and Raftopoulos [15] and Ebacher et al. [38]. The values reported by Reilly and Burnstein [39] and Lappi et al. [59] are even higher. This indicates that bone certainly does not compress in accordance with a constant area assumption.
- Poisson's ratio seems unaffected by strain rate as reported by Katsamanis and Raftopoulos [15], Reilly et al. [39] and Bargren et al. [42]. This assumption can therefore be extended to instantaneous area calculations for dynamic tests.

For an instantaneous compression of the specimen by a length, $-u(t)$, the specimen diameter will expand with $\nu u(t)$. The instantaneous area is thus:

$$A_{sp}(t) = \frac{\pi}{4}\left[d_0 + \nu u(t)\right]^2 \tag{4.4}$$

The stress is assumed to be uniform in the specimen and is thus expressed as the ratio of the instantaneous transducer force, F, and the instantaneous specimen area, A_{sp}.

$$\sigma(t) = \frac{F}{A_{sp}(t)} \tag{4.5}$$

Care was taken to keep the strain rate of loading constant. The Zwick Universal Test Machine allowed the successful testing of bovine cortical bone at strain rates of $10^{-4}\,\mathrm{s}^{-1}$, $10^{-3}\,\mathrm{s}^{-1}$ and $10^{-2}\,\mathrm{s}^{-1}$. The specimens fractured at strains of about 3% to 4% (thus a machine head displacement of $0.18 - 0.24\,\mathrm{mm}$) and 200 MPa. At strain rates higher than $10^{-2}\,\mathrm{s}^{-1}$ the strain rate ceased to be constant. The reason for this is that the bone specimens fracture before the machine head is able to achieve a constant head velocity as explained in the following section.

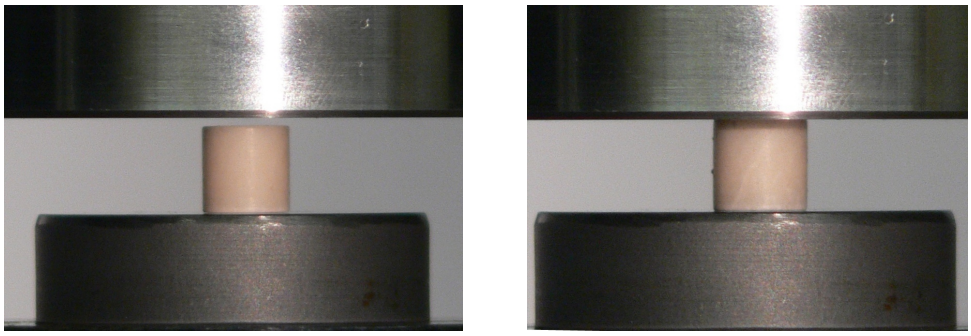

(a) (b)

Figure 4.3: Photographs of a bovine bone specimen (a) before and (b) after cracking in the course of a quasi-static compression test

4.2.1 Limits of quasi-static compression

Compression on the Zwick Universal Test Machine (Fig.4.3) could only be conducted at constant rates between $10^{-4}\,s^{-1}$ and $10^{-2}\,s^{-1}$. Testing at higher rates resulted in a strain rate that never increases to the target strain rate.

Note that **it is essential to calculate the strain rate (with Eq.4.3) from the displacement-time histories measured during compression tests:** Fig.4.4 shows an example where the displacement of the Zwick machine was controlled at $0.6\,mm.\,s^{-1}$ which should result in a strain rate of about $0.1\,s^{-1}$. It seems that the machine head is still accelerating by the time the specimen breaks. This observation would be missed if the machine was simply assumed to test bone material at a strain rate of $0.1\,s^{-1}$. Calculation of the true strain rate shows that the rate of deformation increases almost linearly in the course of the compression experiment. The specimen fractures before the machine head has accelerated to the desired speed. Thus, the machine head never achieves constant velocity compression and the specimen does not deform at a constant strain rate before.

It could be argued that a constant velocity experiment at a strain rate of $0.1\,s^{-1}$ could be achieved if the machine head was accelerated to the required speed before impacting the specimen. The machine head could therefore achieve a constant velocity before impacting the specimen. The machine would still slow down when it impacts the specimen, but perhaps the acceleration needed to achieve the desired constant velocity would be small enough to overcome before the specimen breaks. This approach was unsuccessful on the Zwick Universal Test Machine (as indicated in Fig.4.4). The compression head of the machine slowed down upon impact and was still in the process of accelerating (to the desired speed) at the time of specimen fracture. Pre-acceleration of the machine head did, however result in a more accelerated strain rate in comparison with a conventional test.

Further attempts were made on the MTS testing machine in the Structural Laboratory at the Department of Mechanical Engineering of the University of Stellenbosch. The machine head was accelerated to about 10% faster than $0.6\,mm.\,s^{-1}$ and allowed to impact

the specimen. Fig.4.4 shows a typical strain rate history from an pre-accelerated head test. The head impacts the specimen at speed and slows down slightly. The strain rate increases again either due to the shortening of the specimen or due to the acceleration of the machine head (which is still controlled to move at 10% faster than the required 0.6 mm. s^{-1}). The strain rate is much more constant, but slightly lower (between 0.08 s^{-1} −0.095 s^{-1}) than the desired level of 0.1 s^{-1} (Fig.4.4). This was the highest semi-constant strain rate that could be achieved with the MTS testing machine on the 6 mm specimens.

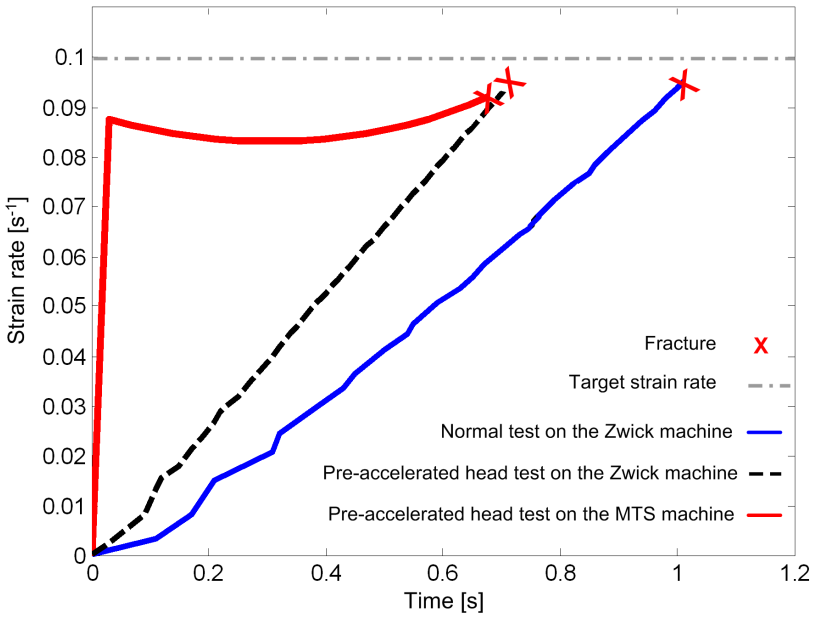

Figure 4.4: The insufficient strain rate that results from a 0.1 s^{-1} compression test on the Zwick machine and the rectification of this strain rate by pre-acceleration of the MTS machine displacement head

The strain rate could be increased by shortening the specimen. If the specimen area was decreased accordingly, the amount by which the specimen is pushing back on the machine, which would possibly allow the machine head to accelerate with greater ease. However, the distance in which the machine is required to achieve a constant velocity will also decrease to 3%−4% of the shorter length. The tests were reattempted on 4 mm(length and diameter) cylindrical specimens without an improvement in the discussed results.

Most of the works on bone compression do not include data at the problematic middle strain rates [21, 16, 19]. The studies that do, do not report the strain rate histories [12, 20], which are associated with measured responses. It is unclear if the strain rates mentioned refer to the maximum, average or constant strain rates.

- McElhaney [12] presented compression results for both human and bovine cortical bone at strain rates of 0.1 s^{-1} and 1 s^{-1}).

- Crowninshield [14] characterised the strain rate dependent response of bovine cortical bone in tension at strain rates of $0.167\,s^{-1}$ and $1.67\,s^{-1}$).
- Adharapurapu et al. [20] achieved a strain rate of $1\,s^{-1}$ on a standard servo-hydraulic test machine, which is possibly superior to the machines that are available for the present work.

Compression tests on bovine bones in the middle strain rate region require a test machine that is able to accelerate to and retain the desired speed before the relatively brittle specimen breaks. Furthermore, the specimen offers increasing resistance to the movement of the compressive device, which results in a decreasing strain rate. A constant velocity test requires velocity control rather than displacement control. It is beyond the means of the present study to pursue bovine cortical bone compression at constant rates in the middle strain rate region. Quirion and Lesaffre [95] propose the combination of a fast hydraulic machine and high-speed photography to achieve compression experiments in the middle strain rates. The specimen is compressed by the machine head via a bar-like anvil rod which is instrumented with strain gauges at two places along its length. This anvil acts as a load cell for low impact velocities and an "output bar" for medium impact velocities. The current system experiences difficulties with respect to the measurement of specimen length and the occurrence of strain rate jumps. The future pursuit of such an investigation would complete the perspective of the strain rate dependent response of bovine cortical bone.

4.3 High strain rate testing on the Split Hopkinson Pressure Bar (SHPB)

The dynamic compression of bovine cortical bone specimens was conducted on a SHPB. The experimental rig and methodology is described with regard to the following aspects:

- The apparatus and calibration
- Bone compression at $\dot{\varepsilon} = 2.5 \times 10^2\,\mathrm{s}^{-1}$ with 20 mm diameter bars and a conventional aluminium striker (diameter 12 mm).
- Bone compression at $\dot{\varepsilon} = 1 \times 10^3\,\mathrm{s}^{-1}$ on smaller, 12 mm diameter bars and a 10 mm steel striker.
- Pulse shaping with tapered strikers to achieve bone compression at a constant strain rate.
- Simulation of striker-input bar impacts to enable striker design.

4.3.1 The SHPB apparatus

The SHPB system at the University of Cape Town (Fig.4.5) was developed by Cloete and reported by Marais [67], who described the components of the SHPB system.

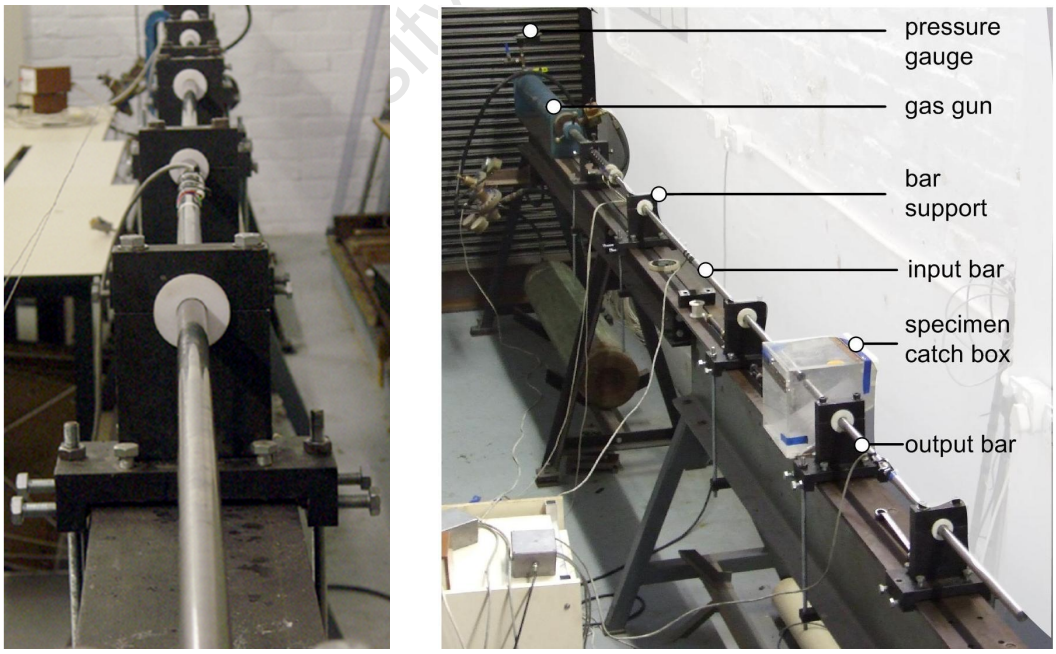

(a) Front view (b) Isometric view

Figure 4.5: The SHPB system at the University of Cape Town

The SHPB system comprises of:

- A gas gun and the associated valves that can launch a striker to produce a controlled pulse in the incident bar.
- A light trap to measure the striker velocity before impact. This facilitates the calibration of the system.
- Two long homogeneous bars, the incident bar and the transmitter bar.
- Bearing and alignment fixtures to allow the bars to move freely, but impact each other in an aligned manner.
- Four strain gauges mounted centrally on opposing sides (to cancel bending effects) of each of the bars to measure the stress wave propagation.
- Amplifiers and a data acquisition system to record the stress wave. The data acquisition card has a sampling frequency of 10 MHz.

4.3.2 System calibration

The system can be calibrated by three methods:

- The theoretical calibration factor
- The momentum balance calibration factor
- The stress calculation calibration factor

Each of these methods will be discussed briefly in the paragraphs that follow. The calibration factors and system parameters will subsequently be summarised for the two SHPB bar systems that were utilized in this study.

Theoretical calibration factor

The stress in a Hopkinson bar can be calculated directly from the product of the theoretical calibration factor, K, and V_{read}, which is the voltage output signal that is recorded from the strain gauges as a result of striker impact.

$$\sigma = KV_{read} = \frac{4E_b}{G_{amp}K_{gf}NV_{bridge}}V_{read} \tag{4.6}$$

Where E_b is the Youngs modulus of the bars (determined from $E_b = c_b^2\rho_b$ by measuring the time and distance of wave propagation by a simple experiment). G_{amp} is the gain of the amplifier. For the current system this is 1000. The gauge factor, K_{gf}, is 2.11 on the

20 mm steel bars and 2.10 for the 12 mm bars. $N = 4$ is the number of active arms in the Wheatstone bridge and V_{bridge} is the bridge voltage. The theoretical calibration factor is thus described by:

$$K = \frac{4E_b}{G_{amp}K_{gf}NV_{bridge}} \tag{4.7}$$

The parameters of the two SHPB systems, which were used in this study are listed in Table 4.2. Here d_b and l_b is the respective diameter and length of the bars, whereas c_b is the acoustic wave speed in the bar material.

SHPB rig	d_b [mm]	l_b [m]	K_{gf}	V_{bridge} [V]	ρ_b [kgm^{-3}]	c_b [ms^{-1}]	E_b [GPa]
ϕ20 mm bars for $\dot{\varepsilon} \approx 2.5 \times 10^2\,\mathrm{s}^{-1}$	19.94	2.007	2.11	2.53	7941.7	5143.4	210.1
ϕ12 mm bars for $\dot{\varepsilon} \approx 10^3\,\mathrm{s}^{-1}$	12.00	1.001	2.10	1.52	7948.9	5128.2	209.0

Table 4.2: Parameters for the two SHPB systems

Momentum balance calibration factor

The total impulse transferred to the input bar, I_M, is obtained from the momentum balance of the striker before and after impact. The momentum of the striker before and after impact is denoted by M^0 and M^{reb} respectively.

$$M^0 = m_s v_s^0 \qquad M^{reb} = m_s v_s^{reb} \tag{4.8}$$

Where m_s is the mass of the striker and v_s^{reb} is the rebound velocity of the striker after impact with the Hopkinson bar. This velocity can be calculated (Eq. 4.9) if the striker area (A_s) and bar area (A_b) is determined and the striker velocity prior to impact, v_s^0, is measured with a light trap.

$$v_s^{reb} = \frac{v_s^0\left(\frac{A_s}{A_b} - 1\right)}{\left(\frac{A_s}{A_b} + 1\right)} \tag{4.9}$$

The impulse transferred to the input bar is therefore:

$$I_M = m_s(v_s^0 - v_s^{reb}) \tag{4.10}$$

The impulse transferred is calculated by assuming a uniform stress distribution through the bar cross-section:

$$I_M = \int_0^t F dt = K A_b \int_0^t V_{read} dt \tag{4.11}$$

The momentum calibration factor can thus be found by numerical integration of the voltage output, V_{read} through Eq.4.12:

$$K = \frac{I_M}{A_b \int_0^t V_{read} dt} \tag{4.12}$$

The strikers used to calibrate the rigs were chosen such that a signal without noise was measured in the bars. A striker with an equal cross-section to the SHPB could impact the input bar under imperfect conditions due to slight misalignment of the bars or lack of contact at the bar edges. Therefore, it was generally found that impact with a striker with a smaller diameter than the input bar resulted in a clear stress signal. The diameter (d_s), length (l_s) and mass (m_s) of the strikers used for bar calibration purposes are listed in Table 4.3.

	d_s [mm]	l_s [mm]	m_s [g]
ϕ20 mm bars for $\dot{\varepsilon} \approx 2.5 \times 10^2\,\mathrm{s}^{-1}$	11.9	350.0	313.5
ϕ12 mm bars for $\dot{\varepsilon} \approx 10^3\,\mathrm{s}^{-1}$	9.6	250.0	139.6

Table 4.3: Strikers used for SHPB calibration

Maximum stress calculation calibration factor

The stress in the bar can be calculated from:

$$\sigma_b = \rho_b c_b v_b \qquad \text{where} \qquad \sigma_b = \frac{\rho_b c_b v_s^0 \frac{A_s}{A_b}}{1 + \frac{A_s}{A_b}} \tag{4.13}$$

The maximum stress in the bar can be calculated because the striker impact velocity, the elastic wave speed and bar density are known. The average maximum voltage output from the amplifier is known, therefore the calibration factor can be found from:

$$K = \frac{\sigma_b^{max}}{V_{read}^{max}} \tag{4.14}$$

Summary of SHPB parameters and calibration factors

Two sets of Hopkinson bars were used to conduct dynamic compression of bovine cortical bone:

- 20 mm diameter bars for compression at $\dot{\varepsilon} = 2.5 \times 10^3\,\mathrm{s}^{-1}$.
- 12 mm bars for compression at $\dot{\varepsilon} = 10^3\,\mathrm{s}^{-1}$.

The calibration factors for the two sets of bars were calculated by the theoretical, momentum balance and maximum stress calculation methods. The input and output bars for both the 20 mm and 12 mm bars were calibrated separately. The three calibration factors for each bar and the striker velocities are presented in Tables 4.4 and 4.5.

	ϕ20 mm input bar	ϕ20 mm output bar
Striker velocity for calibration tests	v_s^0 [m. s^{-1}]	v_s^0 [m. s^{-1}]
	10.4	7.0
Calibration factors	K[Pa. V^{-1}]	K[Pa. V^{-1}]
Theoretical	3.936×10^7	3.936×10^7
Momentum balance	$\mathbf{3.673 \times 10^7}$	$\mathbf{3.737 \times 10^7}$
Maximum stress calculation	3.353×10^7	3.573×10^7

Table 4.4: Calibration factors for the ϕ20 mm bars which were used for dynamic compression experiments at $\dot{\varepsilon} = 2.5 \times 10^2\,\mathrm{s}^{-1}$

	ϕ12 mm input bar	ϕ12 mm ouput bar
Striker velocity for calibration tests	v_s^0 [m. s^{-1}]	v_s^0 [m. s^{-1}]
	17.0	14.0
Calibration factors	K[Pa. V^{-1}]	K[Pa. V^{-1}]
Theoretical	6.549×10^7	6.549×10^7
Momentum balance	$\mathbf{6.024 \times 10^7}$	$\mathbf{6.025 \times 10^7}$
Maximum stress calculation	6.266×10^7	6.237×10^7

Table 4.5: Calibration factors for the ϕ12 mm bars which were used for dynamic compression experiments at $\dot{\varepsilon} = 10^3\,\mathrm{s}^{-1}$

The theoretical calibration factor originates from strain gauge theory, whereas both the momentum and maximum stress calculation calibration factors rely on actual measurements from the SHPB apparatus. The difference between the calibration factors is

an indication of how close the alignment and positioning of the strain gauges are to the theoretical ideal. The use of either the momentum or maximum stress calibration factor is therefore recommended as the actual alignment of strain gauges is usually imperfect. **For the purposes of this study, the momentum balance calibration factor was used** because it relies on the integration of the entire strain gauge voltage signal as opposed to the maximum stress calibration factor that only takes the maximum stress value into consideration.

The SHPB systems are now calibrated such that the strain gauge measurements can be correlated to bar stress. The subsequent section discusses how the specimen stress and strain can be calculated from the stress waves in the bars using 1-D wave propagation theory.

4.3.3 One dimensional wave propagation theory

Spotts [96] explains the travelling of stress waves in a bar as follows: assume that a stress, σ, is suddenly applied to the end of a uniform bar (such as by the impact of a striker). An infinitely thin layer of material will be compressed at the first instant. This layer presses against the adjacent layer of material and so the compressive wave is transferred along the bar, for as long as the stress is being applied. The compressive wave front which is thus produced, travels along the bar with a velocity, c_b. After a time, t, a length of bar, $c_b t$, will be compressed, leaving the remainder of the bar at rest in the unstressed condition. An elastic wave, which is assumed to be fully developed (uniform throughout the cross section), can be described by the 1-D wave equation in terms of displacement, u, spatial coordinate, x, and time, t:

$$\frac{\partial^2 u}{\partial x^2} = \frac{1}{c_b^2}\frac{\partial^2 u}{\partial t^2} \tag{4.15}$$

The elastic wave speed or fundamental longitudinal wave velocity, c_b, is expressed as:

$$c_b = \sqrt{\frac{E_b}{\rho_b}} \tag{4.16}$$

Here E_b is the Youngs modulus and ρ_b is the density of the bar material. The general solution of the wave equation gives the bar displacement, $u(x,t)$ at any point, x at time, t and can be written as the superposition of two waves moving in opposite directions as described in Eq.4.17.

$$u(x,t) = f(x - c_b t) + g(x + c_b t) \tag{4.17}$$

The wave under consideration is moving in one direction along the Hopkinson bar, in the positive x-direction, the general solution becomes:

$$u(x,t) = f(x - c_b t) \tag{4.18}$$

The 1-D strain in the bar is found by differentiating Eq.4.18 with respect to x:

$$\varepsilon = \frac{\partial u}{\partial x} = f' \tag{4.19}$$

The differentiation of Eq.4.18 with respect to time gives the change in bar particle displacement in time, and thus results in an expression for particle velocity:

$$v = \frac{\partial u}{\partial t} = -c_b f' \tag{4.20}$$

Here the ($'$) refers to differentiation with respect to the argument $(x - c_b t)$. The unknown functional, f', can be eliminated by substitution Eq.4.19 into Eq.4.20, which gives:

$$\frac{\partial u}{\partial t} = -c_b \frac{\partial u}{\partial x} \qquad \text{or} \qquad v = -c_b \varepsilon \tag{4.21}$$

Because the Hopkinson bars are assumed to operate within their elastic limit: $\sigma_b = E_b \varepsilon$, which is combined with the elastic wave speed definition Eq.4.21 to give:

$$\sigma_b = -\rho_b c_b v \tag{4.22}$$

The negative sign indicates that a compressive wave is moving in the positive x-direction in the bar. Conventionally compressive waves in Hopkinson bars are considered to be positive. *For the remainder of this document a positive sign convention is adopted for a compressive stress wave in the SHPB*, therefore:

$$\sigma_b = \rho_b c_b v \tag{4.23}$$

If this knowledge is now applied to the incident (σ_I), reflected (σ_R) and transmitted (σ_T) stress waves in the bars (discussed in Section 2.4.2) the resultant particle velocities due to each of these three waves can be expressed as:

$$\Delta v_I = \frac{\sigma_I}{\rho_b c_b} \qquad \Delta v_R = -\frac{\sigma_R}{\rho_b c_b} \qquad \Delta v_T = \frac{\sigma_T}{\rho_b c_b} \tag{4.24}$$

Notice the negative sign of the reflected wave, which will reflect back from the input bar-specimen interface as a tensile wave. By the principle of superposition [66] the total

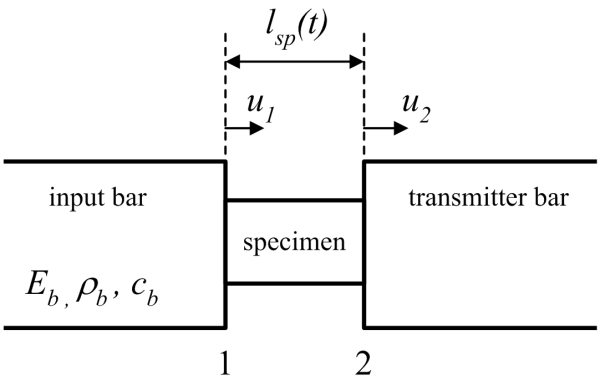

Figure 4.6: The instantaneous specimen length is dictated by the input- and transmitter bar end displacements

particle velocities at the specimen interfaces of the input bar and output bar are:

$$v_1 = \Delta v_I + \Delta v_R = \frac{1}{\rho_b c_b}(\sigma_I - \sigma_R) \tag{4.25}$$

and

$$v_2 = \Delta v_T = \frac{1}{\rho_b c_b}\sigma_T \tag{4.26}$$

The velocity is integrated to find the specimen-bar interface displacements:

$$u_1 = \int_0^t v_1 dt = \frac{1}{\rho_b c_b}\int_0^t (\sigma_I - \sigma_R)dt \tag{4.27}$$

and

$$u_2 = \int_0^t v_2 dt = \frac{1}{\rho_b c_b}\int_0^t \sigma_T dt \tag{4.28}$$

The true strain experienced by the specimen is described in terms of the instantaneous ($l_{sp}(t)$) and original specimen length:

$$\varepsilon = \int_{l_0}^{l} \frac{dl}{l} = \ln\left(l_{sp}(t)\right) - \ln\left(l_0\right) \tag{4.29}$$

The specimen ends are in contact with the input and output bars. Therefore, the instantaneous specimen length will be dictated by the movement of the bar ends at these interfaces as shown in Fig.4.6. The instantaneous length of the specimen is expressed in terms of the original specimen length, l_0 and the input bar end displacement, u_1, and the output bar end displacement, u_2:

$$l_{sp}(t) = l_0 - u_1(t) + u_2(t) \tag{4.30}$$

Therefore, the true strain of the specimen with respect to time is:

$$\varepsilon(t) = \ln\left(\frac{l_0 - u_1(t) + u_2(t)}{l_0}\right) = \ln\left(1 + \frac{u_2(t) - u_1(t)}{l_0}\right) \tag{4.31}$$

The instantaneous strain rate is found by differentiating the strain with respect to time:

$$\frac{d\varepsilon}{dt} = \frac{d}{dt}\left(\ln\left(\frac{l_{sp}(t)}{l_0}\right)\right) = \frac{1}{\left(\frac{l_{sp}(t)}{l_0}\right)}\frac{d}{dt}\left(\frac{l_{sp}(t)}{l_0}\right) \tag{4.32}$$

Thus

$$\dot{\varepsilon} = \frac{v_1(t) - v_2(t)}{l_{sp}(t)} \tag{4.33}$$

The true stress can be obtained by assuming that the instantaneous area changes according to the Poisson's ratio [12] (as discussed in Section 4.2). In this case:

$$A_{sp}(t) = \frac{\pi}{4}\left[d_0 + \nu(l_0 - l_{sp}(t))\right]^2 \tag{4.34}$$

Where $A_{sp}(t)$ is the instantaneous cross-sectional area of the specimen and d_0 is the initial specimen diameter, $\nu = 0.36$ is the Poisson's ratio and $(l_0 - l_{sp}(t))$ is the instantaneous change in specimen length. The stress at the incident bar-specimen interface is therefore:

$$\sigma_{sp1} = \frac{(\sigma_I - \sigma_R)A_b}{A_{sp}(t)} \tag{4.35}$$

and the stress at the specimen-transmitter bar interface is

$$\sigma_{sp2} = \frac{\sigma_T A_b}{A_{sp}(t)} \tag{4.36}$$

Davies [63] described the assumptions that form the basis of the Hopkinson bar equation. These assumptions are listed here along with assumptions by other researchers and conclusions from the present study:

- The Hopkinson bars must remain elastic throughout the test. The maximum allowable impact velocity (v_s^{max}) of the striker for the bars to remain is given by Reid et al [97]:

$$v_s^{max} = \frac{2c_b\sigma_{yield_b}}{E_b} \tag{4.37}$$

- No attenuation or dispersion occurs.

- The pulse is uniform through the cross section of the bar. The wave is fully developed

in four (Davies [63]) to ten (Follansbee [98]) bar diameters from the interface.

- The specimen remains in equilibrium throughout the test. Note that equilibrium is achieved once the ringing up of the specimen is complete and $\sigma_{sp1} = \sigma_{sp2}$ (as reported by Marais [67]).
- The specimen inertia effect is negligible (Zhao and Gary [66]).
- The friction effect in the compression test is negligible [66].
- The instantaneous specimen area is calculated by assuming that it changes according to Poisson's ratio ($\nu = 0.36$ which is taken from the works of Ashman et al. [61], Katsamanis and Raftopoulos [15] and Ebacher et al. [38]). This assumes that there is no difference between the quasi-static and dynamic Poisson's ratios, which seems reasonable from literature (by Katsamanis and Raftopoulos [15], Reilly and Burnstein [39] and Bargren et al. [42]). Bone fractures at very small strains ($\varepsilon_{ut} \approx 3\% - 7\%$ as reported by McElhaney [12]) in compression and therefore the associated area change is also anticipated to be very small and does not have an appreciable effect on specimen stress.

4.3.4 SHPB experiments at an average strain rate of 250 s^{-1}

Dynamic tests were performed on a 20 mm elastic steel SHPB with bar parameters given in Table 4.2. To ensure contact between the bone specimen and bar interfaces, the bar contact surfaces were smeared with a thin layer of grease. A uniform area aluminium striker (diameter 11.95 mm, length 653 mm, mass 0.202 kg) was fired at the SHPB. The velocity of the striker (around 3.5 ms^{-1}) was measured with a light trap just before impact. The resulting stress waves in the bars are shown in Fig.4.7(a). Notice that the sign convention is positive for compression. Impact of a uniform area striker with the SHPB results in a square compressive stress wave in the incident bar. The duration of the stress wave is determined by the length of the striker. The incident wave reaches the bar-specimen interface where some of the incident stress is transferred to the specimen and the residual stress is reflected back along the input bar. The stress wave in the specimen causes it to press against the output bar. Again, some of the stress is transferred to the output bar and the remainder is reflected back along the specimen. Therefore there exists an instant between the arrivals of the stress wave at the input bar-specimen interface and output bar-specimen interface where the stress in the specimen faces is not equal. This time is known as the specimen ring-up time (which is in the order of 20 μs for this particular experiment). As the specimen is progressively loaded it reaches its ultimate capacity and fracture occurs. At this point the specimen is unable to transfer any more stress to the output bar and all the incident stress that arrives at the specimen is reflected back along the input bar. Specimen fracture is evident from the signals reported in Fig.4.7(a). When the specimen fractures the transmitted signal drops to zero and the tensile reflected signal jumps to the level of the originally applied incident stress.

The resulting stress-strain curve and strain rate history are indicated in Fig.4.7(b). It is clear that **the strain rate rises to a maximum value (of about** 400 s^{-1}**) and then decreases *in an almost linear fashion* (to a value of** 190 s^{-1}**) in the course of the dynamic compression test.** As bone is a strain rate sensitive material a possible concern is that the stress vs. strain curve reports properties that are smeared across a range of strain rates (as suspected by Adharapurapu et al.[20]). To establish if this is in fact the case the experiment will be remedied such that the strain rate remains constant beyond the rise time in later sections of this chapter (Section 4.3.7).

One of the assumptions in the derivation of the specimen stress (Section 4.3.3) and strain during a SHPB experiment is that the stress and strain are distributed uniformly throughout the specimen. For this to be true there must be force equilibrium between the input- and output bar interfaces of the specimen. As previously discussed there exists a finite ring-up time before the two faces of the specimen reach the same stress. In this time there will not be force equilibrium between the specimen interfaces. It is therefore desirable that

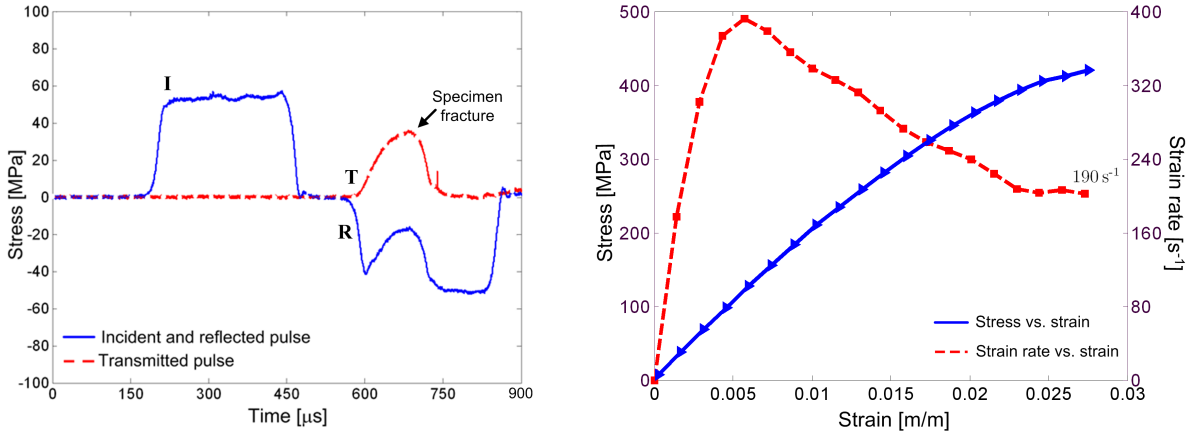

(a) (b)

Figure 4.7: (a) Incident (**I**), reflected (**R**) and transmitted (**T**) pulses and (b) stress and strain rate vs. strain data with a uniform area striker and no pulse shaping

the ring-up time be as short as possible. The equilibrium between the specimen input- and output bar interfaces is shown in Fig.4.8. The specimen interfaces are in force equilibrium beyond the ring-up time. The lack of equilibrium in the initial part of the test is the reason that researchers are reluctant to report a dynamic Young's modulus from SHPB experiments. It is possible to improve the initial test equilibrium by shaping the rise-time of the input stress signal such that it is more gradual. Both Adharapurapu et al. [20] and Lok et al. [72] report that this measure results in good equilibrium in the early stages of a SHPB compression test.

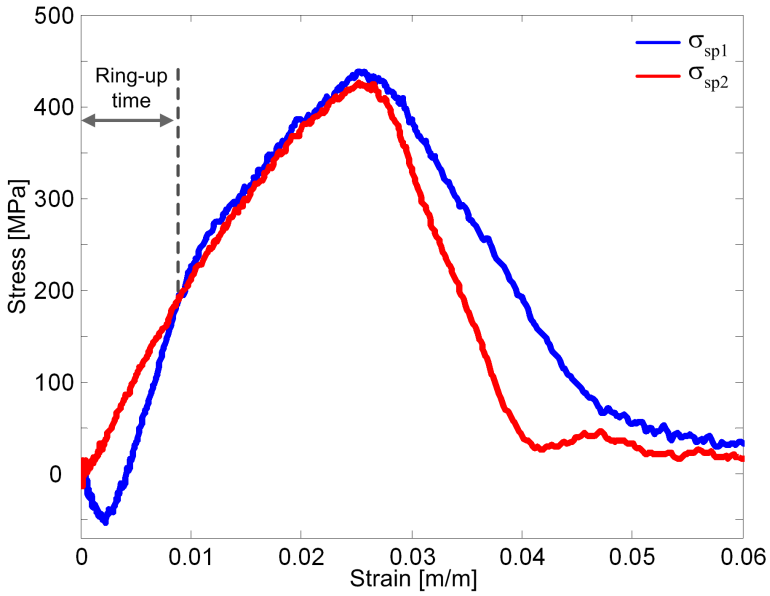

Figure 4.8: The equilibrium between the specimen interfaces during SHPB testing at $\dot{\varepsilon} \approx 2.5 \times 10^2\,\mathrm{s}^{-1}$ with a uniform area striker

However, the lengthening of the test rise time implies that a shorter total test duration is available for constant strain rate compression. For the purposes of this study, a signal with a rapid rise time was used as the primary objective of this work is to achieve constant strain rate compression for a significant portion of the test duration.

4.3.5 SHPB experiments at an average strain rate of 1000 s^{-1}

The impact velocity of the striker is increased to obtain a higher strain rate of compression on the SHPB system. The magnitude of the incident stress wave increases as a result of the increased striker impact velocity (v_s^0). Assuming that the bar and striker are of the same material, the stress can be quantified in terms of the bar area (A_b), acoustic wave speed (c_b), density (ρ_b) and striker area (A_s):

$$\sigma_b = \frac{A_s}{A_s + A_b} c_b \rho_b v_s^0 \tag{4.38}$$

A shorter pulse duration is needed at higher strain rates. The length of the striker was therefore decreased. This also facilitated its acceleration by the pressure of the gas gun that fires it. The striker needs to be accelerated to a velocity of at least 6 $\mathrm{ms^{-1}}$ in order to realise a strain rate of 1000 $\mathrm{s^{-1}}$ on a bone specimen with a length of 6 mm.

Dynamic testing at higher strain rates, i.e. $\dot{\varepsilon} \approx 10^3\,\mathrm{s^{-1}}$ were unsuccessful on the 20 mm bars for the following reason: **The input wave on the SHPB experienced dispersion on** 20 mm **SHPB system when the striker impact velocity was increased to obtain a strain rate of** $\dot{\varepsilon} \approx 10^3\,\mathrm{s^{-1}}$**.** The resulting rounded signals affected the ability to control the strain rate experienced by the specimen in the course of the experiment.

It is believed that the dispersion in the shorter signal only poses problems for the 1000 $\mathrm{s^{-1}}$ **experiments as the ratio of the signal duration (which effects the compressed bar length) to bar diameter becomes more significant with the decrease in pulse which is required to achieve higher strain rate dynamic tests.** Merle and Zhao [99] reported that the pulse shape in Hopkinson bars become increasingly rounded with an increase in bar diameter as a result of a radially non-uniform distribution of stress.

A bone compression experiment at 1000 $\mathrm{s^{-1}}$ requires a stress wave with a duration of approximately 100 μs. The length of the wave in the bar is thus approximately:

$$L_{wave} = c_b \Delta t \approx 5000 \times 100 \times 10^{-6} = 0.5\,\mathrm{m} \tag{4.39}$$

In order to further decrease dispersion shorter Hopkinson bars with a length of 1 m were used instead of the previous 2 m long bar length. The bar diameter was also decreased from 20 mm to 12 mm in accordance with the study by Adharapurapu et al. [20] which successful SHPB experiments at this strain rate on 12.5 mm (half inch) steel bars. The use of smaller

diameter bars would increase the strain experienced by the 12 mm compared to the 20 mm bars if the same 6 mm cylindrical specimen, which was used in other experiments, were to be loaded to fracture. The net dispersive effect would be smaller on the larger magnitude signal in the 12 mm bars.

Furthermore it is concluded that the use of thinner bars could possibly result in better experiments at the lower dynamic strain rates (such as the experiments conducted at 2.5 s^{-1}) with less dispersive effects. However, longer bars ($than$1 m) would be required to accommodate a longer pulse duration. In order to prevent flexure of these long slender bars, more supports along the bar length would be essential to such a SHPB setup.

The method of strain gauge adhesion on smaller diameter Hopkinson bars

During the calibration phase some difficulties were encountered with the measurement of a clear stress signal in the 12 mm bars. Fig.4.9(a) shows the stress wave measured in a single bar when impacted with a uniform diameter steel striker (diameter, 9.6 mm). Two undesirable effects are visible: Firstly, the incident stress does not return to zero immediately after the passing of the incident wave. Secondly, the reflected signal does not have a flat plateau and only reflects the incident wave amplitude after 70 μs.

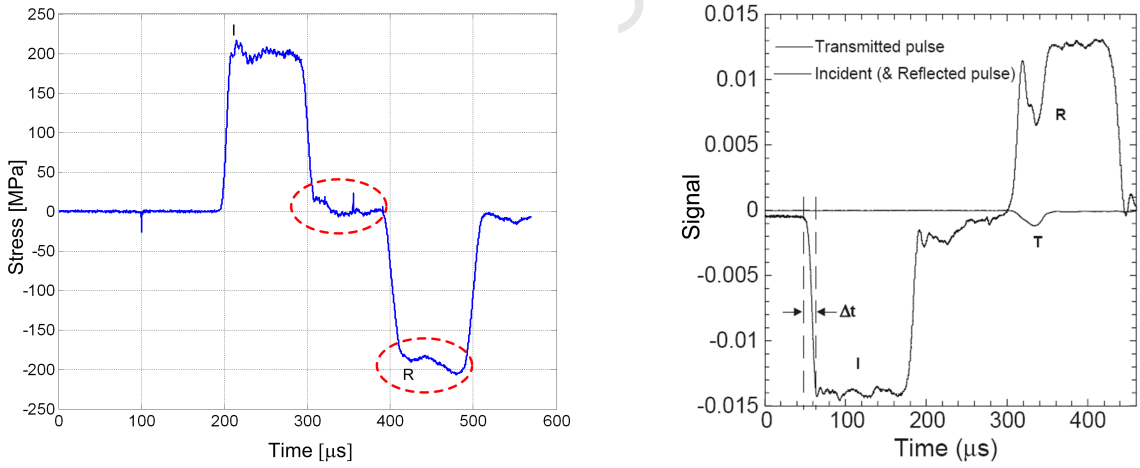

(a) (b)

Figure 4.9: (a) A graph of the undesirable effects of the stress wave signal in a 12 mm bar with conventional strain gauge attachment. (b) Identical phenomena occurring in the work of Adharapurapu et al. [20] who worked on 12.5 mm steel bars

The first phenomena also presents itself in a study by Adharapurapu et al. [20] (Fig.4.9(b)). The incident wave does not return to zero. The stress waves reflected in this figure result from a compression test, which conducted on a bovine cortical bone specimen on 12.5 mm bars. The first part of the reflected wave is not reported and it is not possible to tell if the second of the before mentioned undesirable effects is present.

The strain gauges on the SHPB were investigated to identify the source responsible for the poor quality of the SHPB signal. The strain gauges were checked for loose attachments of discontinuity. The bars were removed from the teflon sleeves in which they normally rest and slide. A tight sleeve could lead to radial constraint of the bar and subsequent attenuation of the stress wave. The convention at the Blast Impact and Survivability Research Unit at the University of Cape Town is that strain gauges and strain gauge pads are stuck onto directly opposing sides of the bars. The pads provide a connection platform to which the strain gauge leader wires and strain gauge cables are soldered (as indicated in Fig.4.10). The strain gauge cable is loosely secured to the bar by three bands of isolation tape around the bar circumference. Isolation tape was chosen for its ability to stretch. The cable is prevented from tugging at the strain gauge by loosely securing it with three cable ties that fit over the isolation tape (Fig.4.10(a)).

In a further attempt to improve the stress measurement the cable-ties as well as the stretch isolation tape was removed. Even though neither the tape, nor the cable ties were fit tightly around the bars, their presence seem to have a significant effect on the measured stress wave in the smaller diameter Hopkinson bars.

Fig.4.11 shows the improvement in the measured signal after the isolation tape and cable-ties were removed. Note that the bar stress still does not return to exactly zero. It is suspected that the undesirable effect of the signal is related to the strain gauge leader cable. The weight of the leader, cable ties and isolation tape would be insignificant compared to the weight of the 20 mm bars, but would be much greater in relation to the smaller diameter bars.

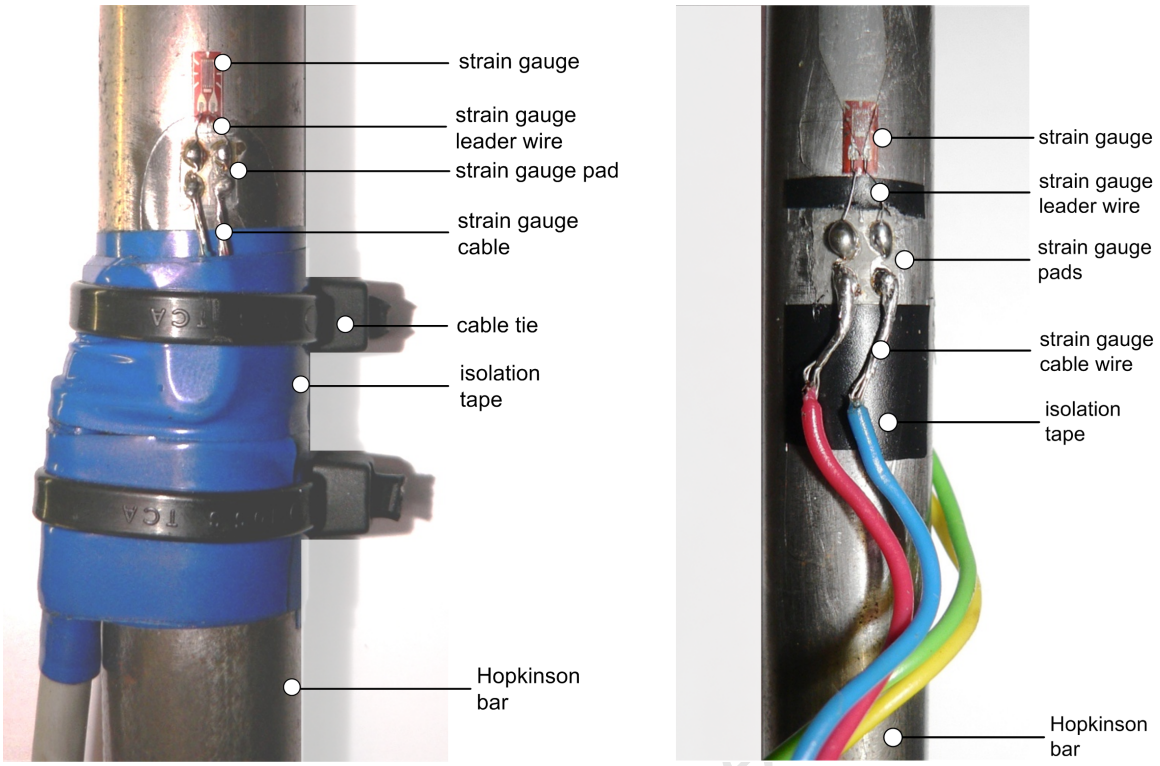

(a) Conventional strain gauge cable fastening with isolation tape and loose fitting cable ties

(b) All excess isolation tape, cable ties and wire shielding removed

Figure 4.10: Photographs of (a) conventional and (b) improved strain gauge cable attachments to a Hopkinson bar

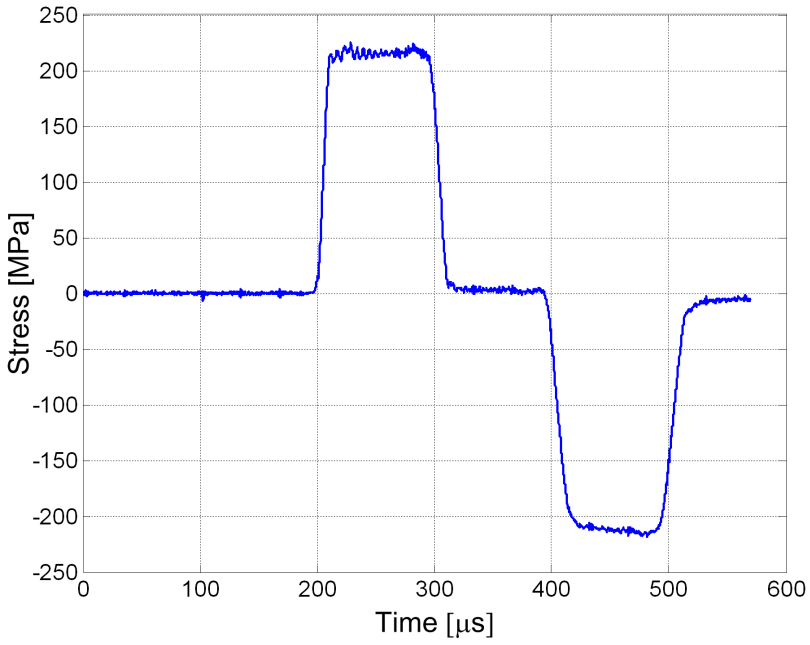

Figure 4.11: A graph which shows how removal of the cable ties and isolation tape from the strain gauge cables results in the improvement of the stress wave measurement in the ϕ12 mm bars.

Compression at $\dot{\varepsilon} = 10^3\,\mathrm{s}^{-1}$ with a uniform diameter striker

Conventional bone compression tests were preformed on the 12 mm bars with a 9.6 mm steel striker. The stress signals in the bars are shown in Fig.4.12(a). The fracture of the specimen is apparent from the fact that the transmitted stress signal in the output bar drops to zero in the course of loading by the input stress wave. The reflected signal rises to the level of the original incident stress at the corresponding time. As with the $\dot{\varepsilon} = 2.5\times10^2\,\mathrm{s}^{-1}$ test the strain rate does not remain constant beyond the rise time, but decreases (from $1100\,\mathrm{s}^{-1}$ to $850\,\mathrm{s}^{-1}$) as the specimen is progressively compressed (Fig.4.12(b)).

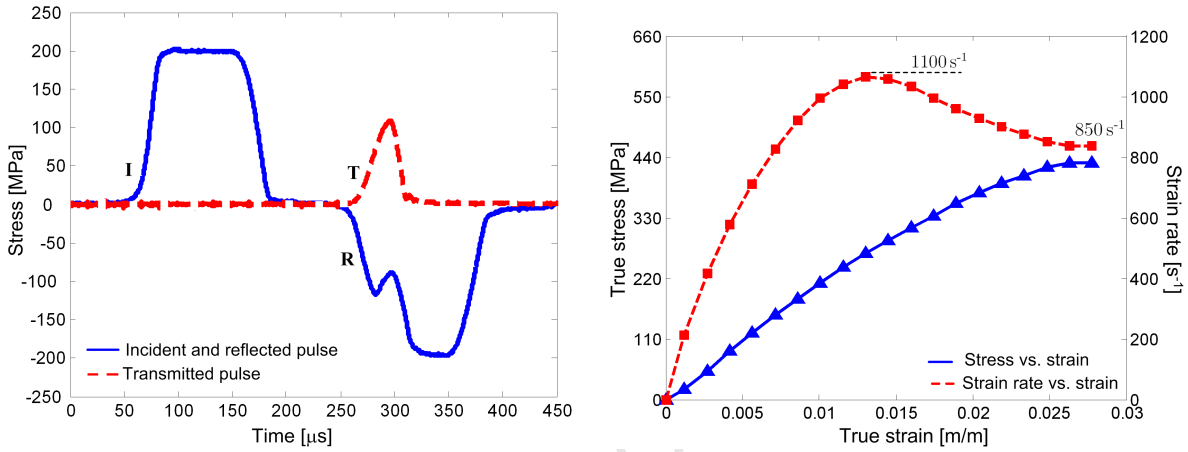

(a) (b)

Figure 4.12: (a) Incident (**I**), reflected (**R**) and transmitted (**T**) pulses and (b) stress and strain rate vs. strain data for a uniform area striker and no pulse shaping on the 12 mm bars

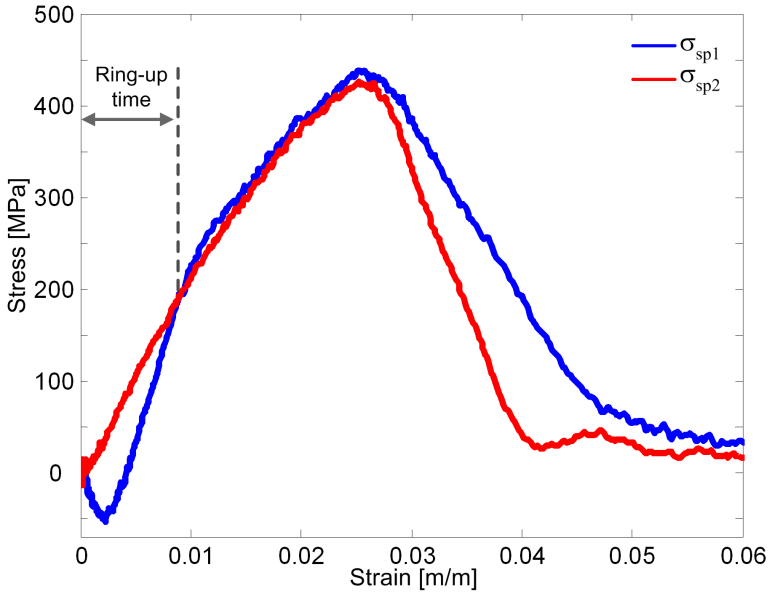

Figure 4.13: The equilibrium between the specimen interfaces during SHPB testing at $\dot{\varepsilon} \approx 10^3\,\mathrm{s}^{-1}$ with a uniform area striker

Pulse shaping is therefore required to achieve the constant strain rate compression of cortical bone beyond the rise time. The stress equilibrium between the specimen input- and output bar interfaces are shown in Fig.4.13. The stresses at the input and output bar interfaces with the specimen match beyond the rise time.

The conventional SHPB experiments at $\dot{\varepsilon} \approx 2.5 \times 10^2\,\mathrm{s}^{-1}$ and $\dot{\varepsilon} \approx 10^3\,\mathrm{s}^{-1}$ both result in a decrease in specimen strain rate. **It is established that pulse shaping is required to achieve a constant strain rate response.** The discussion in subsequent sections focusses on the required shape and method of shaping the incident stress signal.

4.3.6 Pulse shape required to achieve a constant strain rate

The strain rate in the specimen is determined by the velocity at which the specimen is changing in length, which is given by:

$$\dot{\varepsilon}(t) = \frac{v_2(t) - v_1(t)}{l_{sp}(t)} \tag{4.40}$$

Eq.4.41 shows that the strain rate is influenced by the instantaneous length of the specimen and the velocity differential between the specimen end of the input and out bars. The decrease in specimen length during compression causes a slight increase in strain rate as the test progresses. **Because bone fracture occurs at a small strain of roughly** 3% **the change in length has a relatively small effect on strain rate. The dominant factor that influences strain rate is therefore the velocity differential.**

Fig.4.14(a) shows the velocity at the specimen ends of the input, v_1, and output bars, v_2, as well as the velocity differential during a dynamic bone compression test on the SHPB with a striker with a uniform area (during a $\varepsilon = 2.5 \times 10^2\,\mathrm{s}^{-1}$ experiment). The resulting velocity differential decreases dramatically during the specimen loading phase. This implies that the specimen interaction causes the input bar to slow down. It follows that **if a constant strain rate is required, the velocity differential between the input and output bar sides of the specimen must be constant.** This implies that either the input- or output bar velocities should be manipulated in order to achieve this goal. The output bar velocity is a result of loading due to the input bar and is therefore not a controllable parameter. The only remaining option is to accelerate the input bar during the test to compensate for the deceleration that the specimen interaction inflicts to the input bar during loading. An initial estimate of the desired pulse shape can therefore be calculated from:

$$v_1(t) = v_2(t) - l_{sp}(t)\dot{\varepsilon}(t) \tag{4.41}$$

The output bar velocity at the specimen interface, v_2 was determined from the conventional SHPB compression experiment. For example, to determine the pulse shape for a nominally

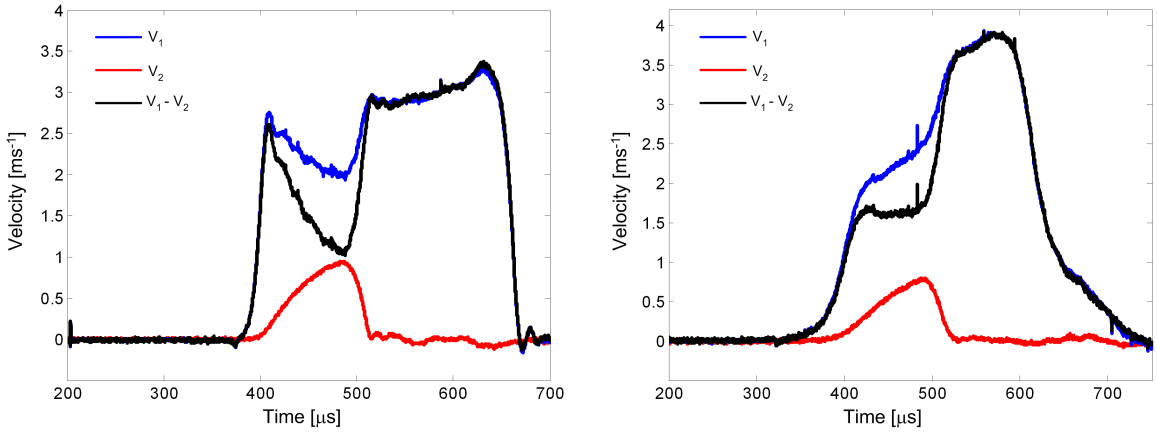

Figure 4.14: Graphs of bar velocities at the specimen interfaces and the velocity differential which results in a (a) decreasing strain rate and (b) a nominally constant strain rate

constant strain rate of $2.5\times10^2\,\mathrm{s}^{-1}$ it is assumed that $\dot{\varepsilon}(t) = 2.5\times10^2\,\mathrm{s}^{-1}$ and $l_{sp}(t) = 6\,\mathrm{mm}$. An example of the signal, which results from such a calculation, is shown in Fig.4.14(b). **The input bar velocity should thus be shaped such that it has the same slope as (or is parallel to) the output bar velocity, which would result in a constant velocity differential.**

4.3.7 Pulse shaping with conical strikers

Pulse shaping is conventionally achieved by placing a small dummy specimen at the striker-input bar interface [20]. The material properties and or the geometry of the pulse shaper is chosen such that the compression of the shaper by the striker results in the desired shaped pulse in the input bar.

An alternative to this approach was found by a novel application of shaped strikers as reported by Kumar et al.[73], who used them to vary the strain rate of concrete during SHPB tests. **It was found that if a conical striker (such as the one in Fig.4.15), impacts a SHPB with its small end first, this will result in an accelerator pulse in the bar that increases in steepness as a function of the cone angle.**

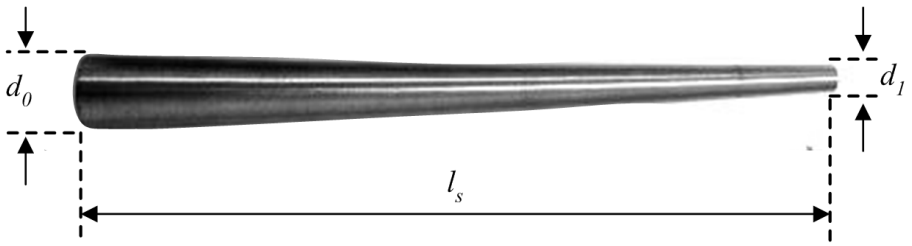

Figure 4.15: An example of a tapered striker

The SHPB experiments at strain rates of $2.5 \times 10^2\,s^{-1}$ and $10^3\,s^{-1}$ each required the design of a tapered striker. The striker angles were determined by a trial-and-error process where a new striker with a steeper or shallower taper angle was turned depending on the dynamic strain rate response. In the present study 4 iterations were required to achieve the $2.5 \times 10^2\,s^{-1}$ constant strain rate experiment and 6 iterations to achieve the experiment at $10^3\,s^{-1}$. The greater amount of iterations to achieve the latter experiment is attributed to buckling of the striker tip. The parameters of the suitable strikers for the two experiments are reported in Table 4.6.

Strain rate [s^{-1}]	d_0 [mm]	d_1 [mm]	l_s [mm]	ρ_s [kg. m^{-3}]	c_s [ms^{-1}]
$\approx 2.5 \times 10^2$	19.02	10.11	550	7937	5143
$\approx 10^3$	11.88	6.52	169	7937	5143

Table 4.6: Tapered striker dimensions for constant dynamic strain rate compression of cortical bone on the SHPB

These strikers successfully shaped the input pulse to achieve a nominally constant strain rate of $\dot{\varepsilon} = 2.5 \times 10^2\,s^{-1}$ (Figs.4.16(a) and 4.16(b)) and $\dot{\varepsilon} = 10^3\,s^{-1}$ (Figs.4.17(a) and 4.17(b)).

Advantages of conical strikers over sacrificial pulse shapers include:

- **Test repeatability because the same striker is used in every test.**
- **Improved control of the pulse shape [73] because of the possible variations in striker geometry.**
- **Tapered strikers are reusable, therefore a single striker is used to conduct an entire series of tests if inter-specimen variation is not significant (as was the case for the cortical bone investigated in the present study).**

The challenges of the use of tapered strikers are:

- **Buckling of the striker tip as a result of excessive stress or bad alignment with the input bar.**
- **Shortening of the possible test duration in a given length of bar, because of the 'tail' that occurs in the signal. This phenomena can be explained as follows: When the striker impacts the input bar, stress waves originate at the impact surfaces. The stress wave in a uniform area striker would run to the end of the striker and back to the interface. At this point the striker will lose contact with the bar if it has a smaller diameter than the bar. This is not the case with a non-uniform striker, impacting with**

the small end first. The diameter increase across the length implies that there is a residual mass that must be decelerated and this accounts for the "tail".

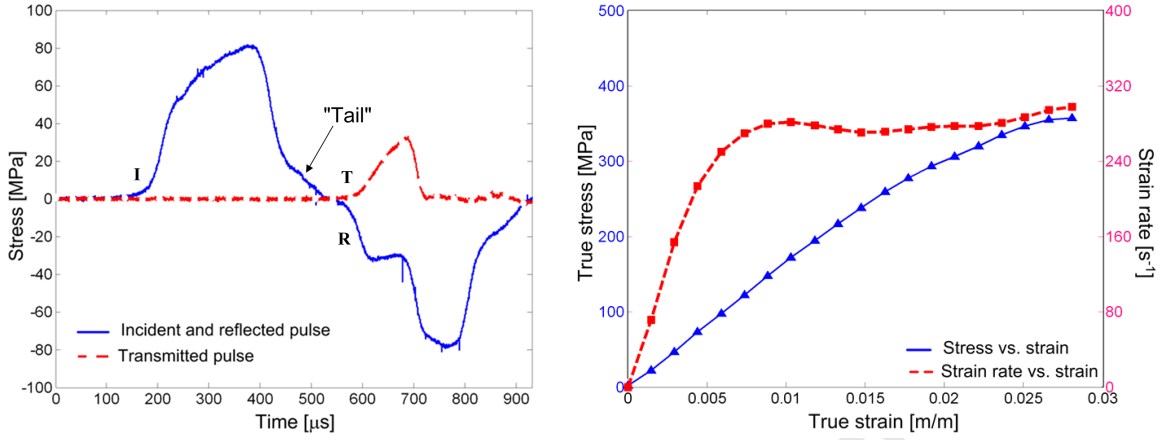

(a) (b)

Figure 4.16: (a) Incident (**I**), reflected (**R**) and transmitted (**T**) pulses and (b) stress and strain rate ($\dot{\varepsilon} \approx 3 \times 10^2\,\mathrm{s}^{-1}$) vs. strain data with a conical striker

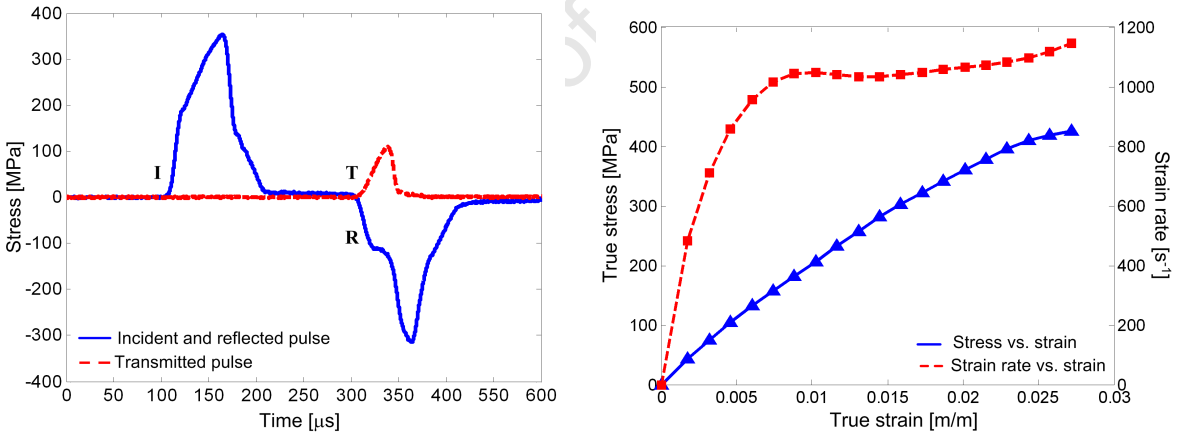

(a) (b)

Figure 4.17: (a) Incident (**I**), reflected (**R**) and transmitted (**T**) pulses and (b) stress and strain rate ($\dot{\varepsilon} \approx 1.1 \times 10^3\,\mathrm{s}^{-1}$) vs. strain data with a conical striker

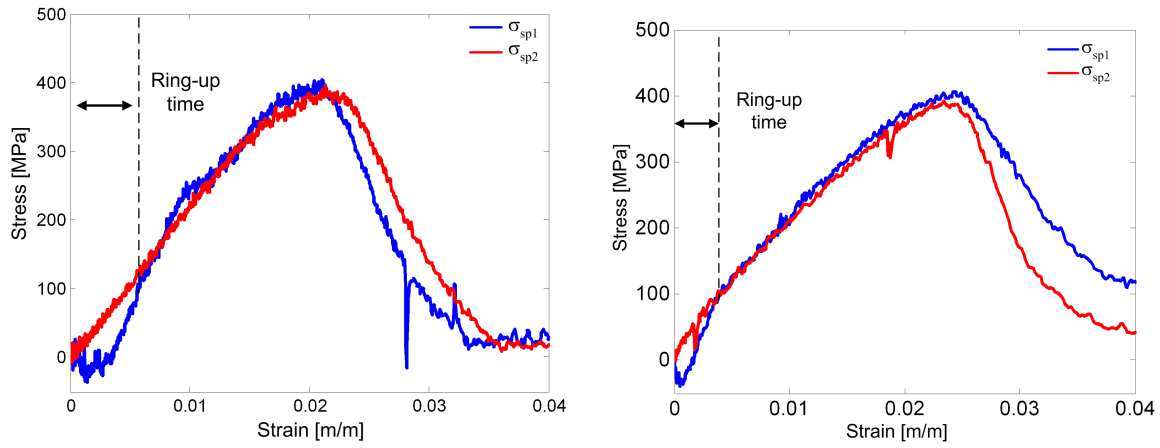

Figure 4.18: The equilibrium between the specimen interfaces during SHPB testing with tapered strikers at (a) $\dot{\varepsilon} \approx 2.5 \times 10^2\,\mathrm{s}^{-1}$ and (b) $\dot{\varepsilon} \approx 10^3\,\mathrm{s}^{-1}$

Recall that the relations for specimen stress and strain in the SHPB were derived by assuming equilibrium between the input bar and output bar interfaces (uniform deformation of the specimen). The equilibrium for SHPB tests with tapered strikers are shown in Fig.4.18 for the two strain rates. The rise time for the $2.5 \times 10^2\,\mathrm{s}^{-1}$ and $10^3\,\mathrm{s}^{-1}$ experiments are around $22\,\mu$s and $5\,\mu$s respectively.

Conical striker simulation

To achieve efficient experimental design and avoid unnecessary trail-and-error iterations in future the bar and striker were modelled with spring-damper systems as shown in Fig.4.19. This enables the prediction of the stress wave in a bar as a result of impact with a given striker. The area differential between the striker ends results in a tail in the input signal which effects the length of the incident stress pulse which in turn influences the required length of the Hopkinson bars. The prediction of the duration of this 'tail' can additionally aid in choosing the appropriate striker length for a given set of Hopkinson bars and *vice versa* .

The application of Newton's second law to every mass in the system results in an array of second order differential equations which can be written as:

$$\boldsymbol{M}\ddot{\boldsymbol{x}} + \boldsymbol{C}\dot{\boldsymbol{x}} + \boldsymbol{K}\boldsymbol{x} = \boldsymbol{F}(t) \tag{4.42}$$

Damping is included to reduce the oscillations which result when modelling the impact between bars.

If the bar is represented by N_b lumped mass nodes, the force equilibrium at each node, i, of the uniform area elastic Hopkinson bar with uniform material damping can be

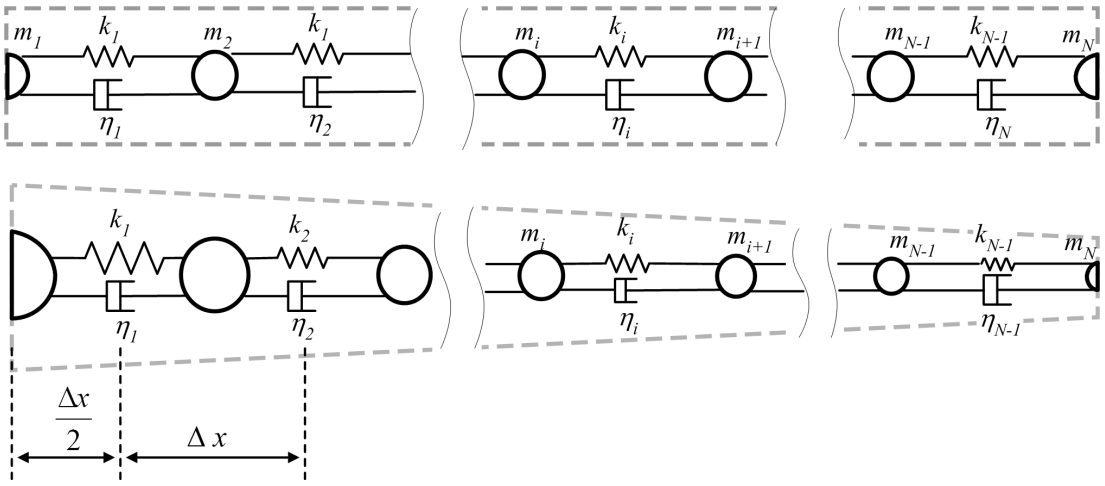

Figure 4.19: A schematic of the analytical model used to represent a conical striker impacting a SHPB

expressed as:

$$\rho_b A_b \Delta x \begin{bmatrix} 0 & 1 & 0 \end{bmatrix} \begin{bmatrix} \ddot{x}_{i-1} \\ \ddot{x}_i \\ \ddot{x}_{i+1} \end{bmatrix} + \eta_b \begin{bmatrix} -1 & 2 & -1 \end{bmatrix} \begin{bmatrix} \dot{x}_{i-1} \\ \dot{x}_i \\ \dot{x}_{i+1} \end{bmatrix} + \frac{A_b E_b}{\Delta x} \begin{bmatrix} -1 & 2 & -1 \end{bmatrix} \begin{bmatrix} x_{i-1} \\ x_i \\ x_{i+1} \end{bmatrix} = \begin{bmatrix} 0 \\ 0 \\ 0 \end{bmatrix} \tag{4.43}$$

Where $i = 1, 2 \ldots N_b$

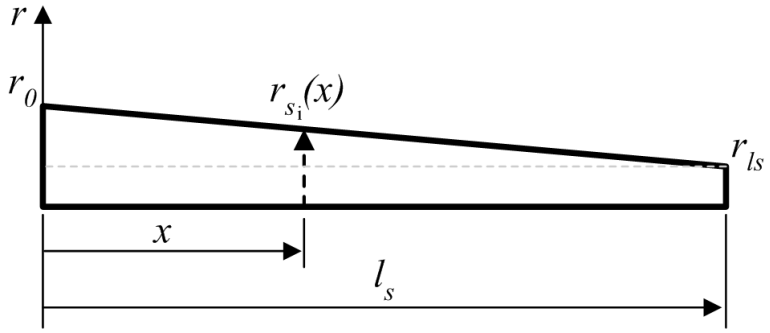

Figure 4.20: A schematic of the parameters used to model the shaped striker

The varying area of the tapered striker affects the mass of each element and the stiffness of the springs that act on either side of it. For a tapered striker (Fig.4.20) of length, l_s, with a free end radius, r_0 and impact end radius, r_{l_s} the area, A_{s_i}, at node i, a distance x along its length is given by $A_{s_i} = \pi r_{s_i}^2$.

Where:

$$r_{s_i}(x) = r_{l_s} + (r_0 - r_{l_s}) \frac{l_s - i\Delta x}{l_s} \tag{4.44}$$

Thus for $i = 1, 2 \ldots N_s$

$$\rho_s \Delta x \begin{bmatrix} 0 & A_{s_i} & 0 \end{bmatrix} \begin{bmatrix} \ddot{x}_{i-1} \\ \ddot{x}_i \\ \ddot{x}_{i+1} \end{bmatrix} + \eta_s \begin{bmatrix} -1 & 2 & -1 \end{bmatrix} \begin{bmatrix} \dot{x}_{i-1} \\ \dot{x}_i \\ \dot{x}_{i+1} \end{bmatrix}$$

$$+ \frac{E_s}{\Delta x} \begin{bmatrix} -\frac{1}{2}(A_{s_{i-1}} + A_{s_i}) & \frac{1}{2}(A_{s_{i-1}} + 2A_{s_i} + A_{s_{i+1}}) & -\frac{1}{2}(A_{s_i} + A_{s_{i+1}}) \end{bmatrix} \begin{bmatrix} x_{i-1} \\ x_i \\ x_{i+1} \end{bmatrix} = \begin{bmatrix} 0 \\ 0 \\ 0 \end{bmatrix} \tag{4.45}$$

The end nodes of the both, the striker and the bars have half the mass because the element length at the end points was chosen as $\frac{\Delta x}{2}$. **To simulate striker and bar impact the end node of the striker was merged with the first node of the bar to simulate contact.** The first node of the striker and last node of the bar therefore have free boundary conditions. For the last node of the bar:

$$\sigma_{N_s+N_b-1}(t) = E_b[x_{N_s+N_b-1}(t) - x_{N_s+N_b-2}(t)] = 0$$

Therefore

$$x_{N_s+N_b-1}(t) = x_{N_s+N_b-2}(t) \tag{4.46}$$

Similarly, for the first node of the striker:

$$\sigma_{s_1}(t) = E_s[x_{1_s}(t) - x_{2_s}(t)] = 0$$

Thus

$$x_{1_s}(t) = x_{2_s}(t) \tag{4.47}$$

Because the solution of $x_{s_2}(t)$ follows from $x_{s_1}(t)$ it is convenient to take a first guess of $x_{s1}(t + \Delta t) = x_{s_2}(t)$. All the nodes belonging to the striker are given an initial velocity of v_s^0:

$$\dot{x}_{s_{1\ldots N_s}}(0) = v_s^0 \tag{4.48}$$

It is useful to rewrite this expression in a first-order or state-space form by defining the two $(N_s + N_b - 1) \times 1$ vectors $\boldsymbol{y}_1 = \boldsymbol{x}$ and $\boldsymbol{y}_2 = \dot{\boldsymbol{x}}$.

$$\dot{\boldsymbol{y_1}} = \boldsymbol{y_2} \tag{4.49}$$

$$\dot{\boldsymbol{y_2}} = -\boldsymbol{M}^{-1}\boldsymbol{K}\boldsymbol{y_1} - \boldsymbol{M}^{-1}\boldsymbol{C}\boldsymbol{y_2} + \boldsymbol{M}^{-1}\boldsymbol{F}(t) \tag{4.50}$$

Which can be expressed in a single equation as

$$\dot{\boldsymbol{y}} = \boldsymbol{A}\boldsymbol{y}(t) + \boldsymbol{f}(t) \tag{4.51}$$

Where

$$\boldsymbol{A} = \begin{bmatrix} 0 & \boldsymbol{I} \\ -\boldsymbol{M}^{-1}\boldsymbol{K} & -\boldsymbol{M}^{-1}\boldsymbol{C} \end{bmatrix} \tag{4.52}$$

$$\dot{\boldsymbol{y}}(t) = \begin{bmatrix} \boldsymbol{y_1}(t) \\ \boldsymbol{y_2}(t) \end{bmatrix} \qquad \boldsymbol{f}(t) = \begin{bmatrix} 0 \\ \boldsymbol{M}^{-1}\boldsymbol{F}(t) \end{bmatrix} \qquad \text{and} \qquad \dot{\boldsymbol{y_0}}(t) = \begin{bmatrix} \boldsymbol{y_1}(0) \\ \boldsymbol{y_2}(0) \end{bmatrix} \tag{4.53}$$

A Runge-Kutta method was used to solve the system of first order differential equations. The solution vector contains the displacement and velocity of each node for each point in time. The stress in the bar as a result of a striker impact is calculated from:

$$\sigma_{b_i} = E_b \frac{x_{i+1} - x_i}{\Delta x} \tag{4.54}$$

An experiment was conducted and simulated with the numerical model presented here to evaluate the lumped mass model (LMM) for impact with a tapered striker. The experimental stress signal was measured when a steel striker ($d_0 = 11.88\,\text{mm}$, $d_1 = 6.52\,\text{mm}$, $\rho_s = 7937\,\text{kg.m}^{-3}$, $c_s = 5143\,\text{ms}^{-1}$) impacted a steel Hopkinson bar ($d_b = 12.00\,\text{mm}$) at $v_s^0 = 9.24\,\text{ms}^{-1}$. The striker and bar were simulated with $N_s = 75$ and $N_b = 300$ nodes respectively and a time step of $\Delta t = 1 \times 10^{-7}\,\text{s}$ (chosen to correspond to the experimental sampling frequency of 10 MHz). An arbitrary material damping value of $\eta_b = \eta_s = 0.001\,\text{MPa.s}^{-1}$, was chosen for the striker and bar material.

The correlation of the LMM and experimental mid-bar stresses are plotted in Fig.4.21 and compare as follows:

- The stress and the wave slope is slightly over-estimated by the finite difference model.
- The wave rise- and fall time is more idealistic (or "sharper") when predicted with the LMM. The model would therefore be over-optimistic in its prediction of the possible test duration with a tapered striker in a given length of bar.
- No attempt was made to simulate the decoupling of the striker and the bar.

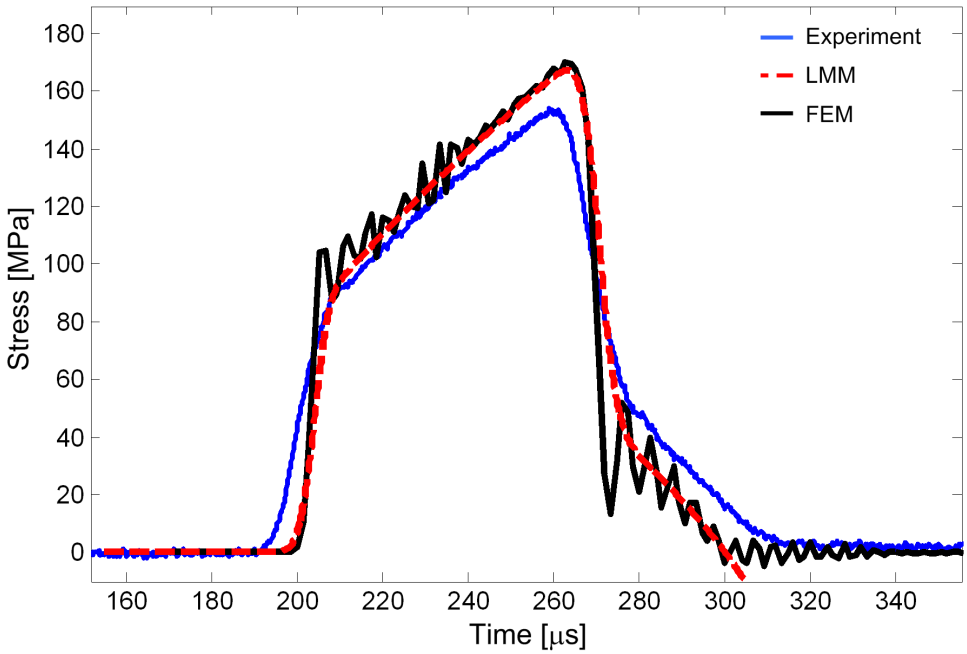

Figure 4.21: A graph of the comparison between experimental and simulated Hopkinson bar stresses resulting from impact with a tapered striker

The model LMM predictions were supplemented by a finite element model (FEM) prediction. The FEM result matches the LMM very closely. The slight disparity in the rise- and fall times of the FEM and LMM stress waves is attributed to the addition of material damping to the LMM. Material damping facilitates the prediction of a stress wave without oscillations.

Importantly, the ability of the model to approximate the stress wave slope enables a good first approximation of the striker dimensions required to achieve the desired wave slope. The wave shape as a result of more complex geometry could also be facilitated in future.

The future design of tapered strikers will therefore require:

- The calculation of a desired pulse shape from a uniform striker experiment on the SHPB.
- Estimation of the approximate striker dimensions with the developed simulation model.
- Manufacturing of the striker with the initial estimate of dimensions and testing on the SHPB.
- Interrogation of the specimen strain rate and further iteration if required.

Chapter 5

Experimental Results

The experimental programme was designed to investigate the response of bovine cortical bone to different rates of compression up to the event of fracture. The experiments were aimed at testing these specimens at as wide a range of strain rates as could be achieved with two available experimental techniques: **Quasi-static compression in the Zwick test machine and dynamic compression with the SHPB. Furthermore, experiments were controlled such the strain rate of compression remained as constant as possible throughout the test.**

The results of the experimental programme are subsequently presented. The material response prior to fracture will be discussed in terms of the stress and strain that arises in bone as a result of different strain rates of loading. **The primary focus of this work is to characterise the response of bovine cortical bone in the longitudinal direction.** However, the techniques developed for the characterisation of longitudinally orientated specimens facilitate the testing of specimens in other orientations. **Additional specimens were extracted from 5 bones in the radial and tangential directions.** Some preliminary quasi-static and dynamic results are presented to give an indication of the applicability of the experimental techniques and the three dimensional nature of bone material.

The longitudinal quasi-static compressive response is discussed with regard to stress and strain, density and microstructure. **Given the evident sensitivity of bone response to strain rate, Adharapurapu et al. [20] hypothesised that a varying strain rate during a test could result in the measurement of a smeared response.** Adharapurapu et al. [20] subsequently succeeded on conducting a constant dynamic strain rate compression experiment on the SHPB (at $10^3\,s^{-1}$) using sacrificial high work hardening alloy pulse shapers. **Although Adharapurapu et al. [20] reported that both constant and non-constant strain rate compression experiments were conducted, no comparison was made between the bone responses measured in the two experiments. At present it is unclear what the anticipated effect of varying strain rate is on the responses reported in existing literature by McElhaney[12],**

Crowninshield[14], Katsamanis and Raftopoulos [15] and Lewis and Goldsmith [18]. The results presented in this chapter will compare the responses of bovine cortical bone that resulted from constant and varying strain rate experiments.

Furthermore, the quasi-static and dynamic response corridors are summarised together to analyse their relative contexts. The discussion ends with an investigation into the ultimate properties and fracture risk of bovine cortical bone under different strain rates of compression.

5.1 Bone compression results for specimens with a longitudinal orientation

5.1.1 Quasi-static compression tests

Longitudinally orientated specimens were compressed in the direction of the bone axis at strain rates ranging over four orders of magnitude. The test procedure is briefly summarised in the following steps:

- The Zwick Universal Test Machine was used to compress specimens (with displacement control) at strain rates of $10^{-4}\,s^{-1}$, $10^{-3}\,s^{-1}$ and $10^{-2}\,s^{-1}$.
- A further test series was performed at $10^{-1}\,s^{-1}$ on a MTS testing machine with displacement control.
- Ten compression tests were conducted at each strain rate. Each specimen in a test series originated from a different bone and was compressed to failure. To clarify, batches of specimens were machined from Bone 1 to Bone 10. For example at a strain rate of $10^{-4}\,s^{-1}$, one specimen was taken from the sample batches of each of Bones 1 to 10 and compressed at the desired strain rate.
- The time, displacement and force histories were measured. This allows the true stress, true strain and true strain rate to be calculated as described in Section 4.2. All measures of stress and strain discussed in this study refer to the true stress and true strain.
- Great emphasis was placed on keeping the strain rate as constant as possible throughout the duration of the test.

The strain rate vs. time and stress vs. strain histories of the four test series are summarised in Appendix A. The stress vs. strain rate curves at $10^{-4}\,s^{-1}$, $10^{-3}\,s^{-1}$ and $10^{-2}\,s^{-1}$ show that constant strain rates were achieved at the desired levels. The true strain rate increases slightly as the specimen is shortened by the compression.

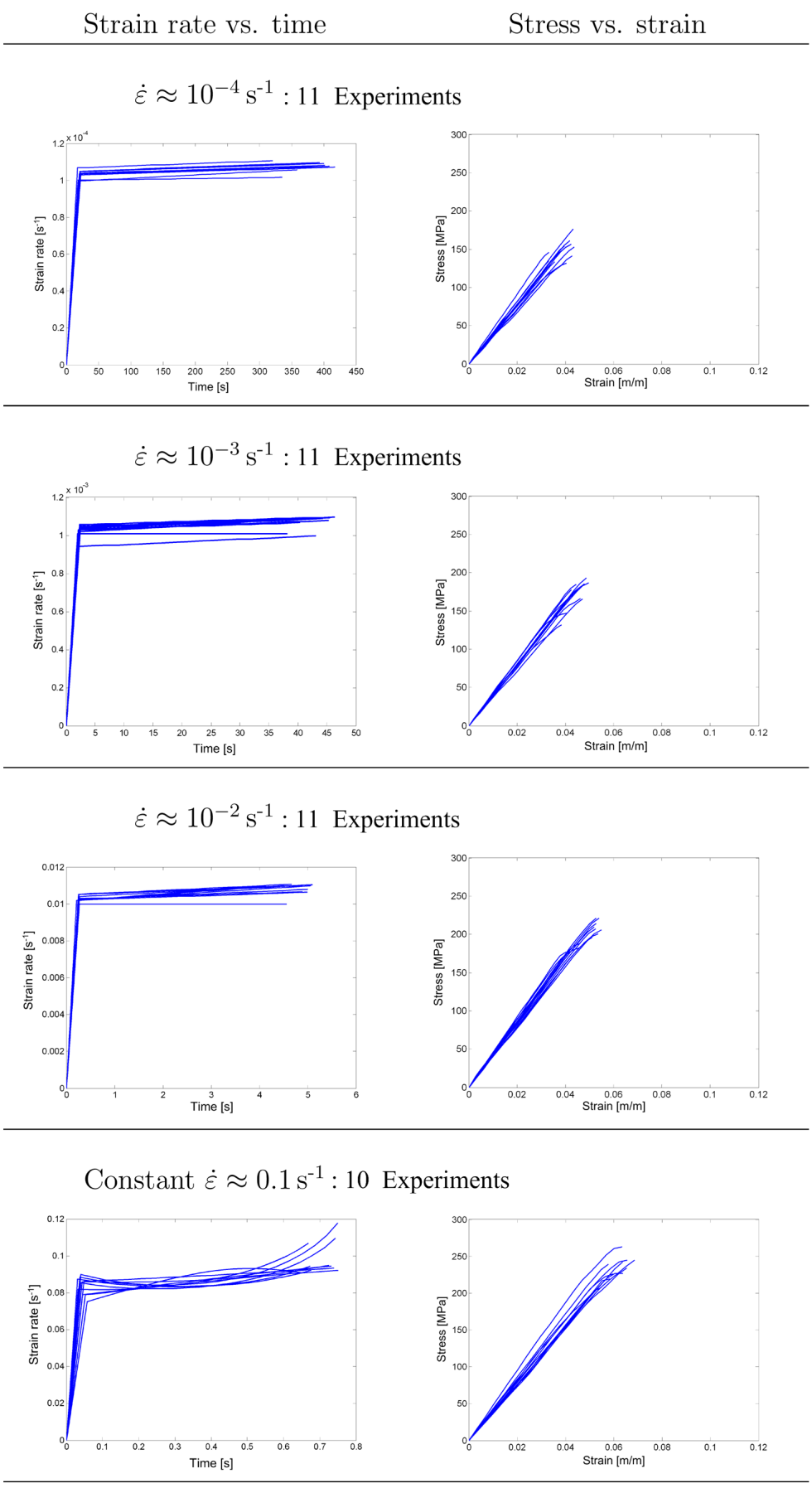

Figure 5.1: Quasi-static compression test results for longitudinally orientated specimens

The test series at $\dot{\varepsilon} = 10^{-1}\,\mathrm{s}^{-1}$ shows a less repeatable strain rate which only really reaches a strain rate of about $\dot{\varepsilon} = 0.9 \times 10^{-1}\,\mathrm{s}^{-1}$. In most instances of this test series the strain rate initially decelerates before increasing towards the end of the test. Recall that the MTS machine head was pre-accelerated to the desired speed before impacting the specimens. This explains the initial decrease in strain rate.

The stress-strain curves for the longitudinal specimens at different quasi-static strain rates of compression are combined in Fig.5.2. It is clear that bone material displays significant inter-specimen variation and that experiments can only hope to identify a **corridor of response**. Inter-specimen response variation can be explained by variations in bone density, microstructural type and possibly microstructural orientation (as discussed in Chapter 3).

Pithioux et al.[89] stated that three phases are evident from the quasi-static stress-strain response curves of bovine bone in compression:

- When bone specimens are compressed the stress initially increases linearly with strain.
- At some point, the slope of the curve softens and the strain in the material increases more rapidly than the stress. This softening is attributed to the formation of microcracks and shear zones. The crack growth and propagation will determine when the specimen will finally fail. This point has been described by Shim et al. [21] as the point of material failure. The association of the onset of non-linearity in the originally linear response with damage or the formation of micro-cracks is further confirmed by Zioupos and Currey [34].
- In the final stage, failure occurs suddenly. In the present study it was found that most specimens failed immediately after reaching a *maximum stress* value. A small minority of the specimen stress responses reach a maximum value beyond which the stress decreases slightly before final fracture at the *ultimate stress*. Strictly speaking, there is a slight difference between the *maximum stress* and *ultimate stress* . However, in the present study the difference was found to be 0.8% for the specimens which did not fail at the *maximum stress* . *For this reason the ultimate stress is considered to be synonymous to the maximum stress in the present study* .

The average ultimate stress and strain at fracture is summarised in Table 5.1 for each stain rate. The standard deviations of these metrics are indicated after the $\pm$ signs. Bovine cortical bone fractures at small strains ranging between 4.0% to 6.2%, that is a deformation of 0.24 mm to 0.36 mm for quasi-static compression of a 6 mm specimen. The ultimate stress at fracture ranges between 149 MPa and 235 MPa. There is a progressive trend in the ultimate stress and strain at fracture with an increase in strain rate.

The average Young's moduli (slope of the linear part of the stress vs. strain curves) are listed with the appropriate strain rate in Table 5.1. Youngs' modulus increases consistently

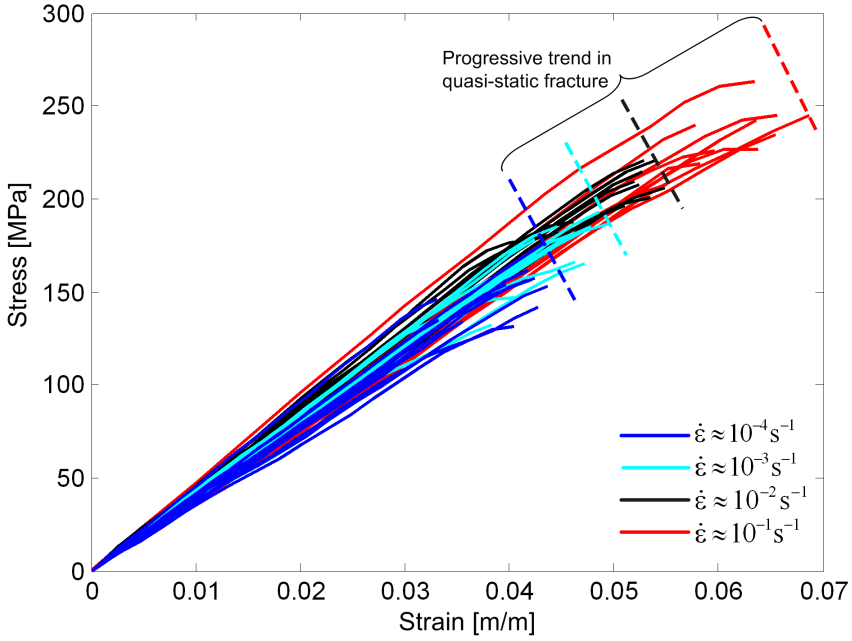

Figure 5.2: Stress-strain curves for longitudinal specimens at different quasi-static strain rates of compression

from 3.88 GPa at $\dot{\varepsilon} \approx 10^{-4}\,\text{s}^{-1}$ to 4.23 GPa at $\dot{\varepsilon} \approx 10^{-2}\,\text{s}^{-1}$. When the material is compressed a little faster at $\dot{\varepsilon} \approx 10^{-1}\,\text{s}^{-1}$ the modulus decreases slightly to 4.05 GPa.

The effect of strain rate is apparent in quasi-static compression. Bovine cortical bone is the least resistant to fracture when a slow load is applied for a long time. Both the ultimate stress and strain increase consistently with strain rate. This observation agrees with the analysis of McElhaney [12] concerning the effect of strain rate on the fracture of cortical bone from the human femur.

$\dot{\varepsilon}$ [s^{-1}]	σ_{ut} [MPa]	ε_{ut} [m. m^{-1}]	E[GPa]
$\dot{\varepsilon} \approx 10^{-4}$	149.6 ± 13.7	0.0398 ± 0.004	3.88
$\dot{\varepsilon} \approx 10^{-3}$	171.9 ± 18.5	0.0451 ± 0.004	3.98
$\dot{\varepsilon} \approx 10^{-2}$	202.1 ± 14.9	0.051 ± 0.004	4.23
$\dot{\varepsilon} \approx 10^{-1}$	234.8 ± 15.5	0.062 ± 0.000	4.05

Table 5.1: Quasi-static compression test results for longitudinally orientated bovine bone specimens

5.1.2 Bone microstructure in longitudinal compression

Two observations are evident from the investigation of bone microstructure that was exposed to quasi-static loading:

- The observation of shear bands in the longitudinal plane

- Preferential cracking along the vascular canals in the transverse plane

Observation of shear bands

Shear bands or **kink zones** were observed in the longitudinal sections of longitudinal specimens that were compressed in the direction of the bone axis. Hull [100] describes kink zones as the phenomena when fibres fracture along two planes and display massive fibre rotation between the planes. In the present study shear bands were observed on different scales: on microstructural level and on whole test specimens. Fig.5.3(a) shows a photograph of a whole 6 mm specimen where shear bands can be observed with the naked eye. The specimen fractured along two roughly parallel planes. The material between the parallel fractures is dislocated by the movement of the shear planes and has rotated to an orientation that is not aligned with the rest of the specimen material. Magnification of the material around a shear plane (Fig.5.3(b)) shows that the movement of the shear planes load the surrounding material in bending.

Currey [49] observed that cortical bone yields in compression, but that the incidence of yield is at a higher stress than in tension. It strain hardens rapidly to a peak, then softens and fails. Currey and Brear [101] attributed this softening to the formation of shear bands. The work presenter here agrees with the observations of Currey and Brear. Observe that the material around the shear planes has failed in tension but is still intact on the compressive side.

Shear bands were also evident in the compressive fractures studied by Mercer et al.[37]. Mercer et al. [37] established that the bands extend across the bone lamellae and are mirror symmetric with respect to the loading axis. Higher resolution images reveal that

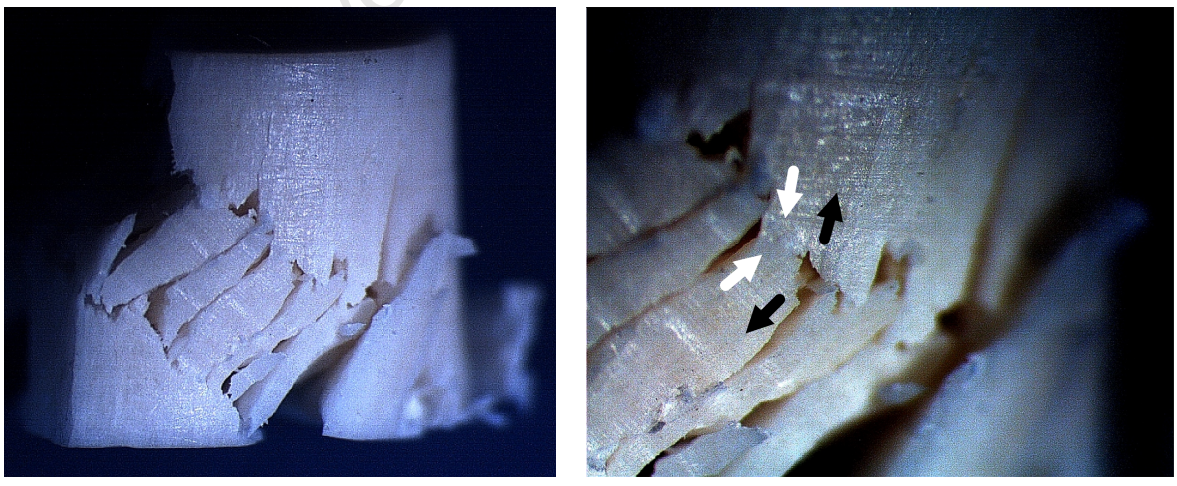

(a) (b)

Figure 5.3: Photographs of a fractured specimen which present with a “kink zone” as a result of the movement of shear planes. (a) A whole specimen. (b) A magnified view of the bending on one side of the kink. Observe that the material has failed in tension but is still intact on the compressive side.

many of the bands nucleate at the blood vessels. Hull [100] reported the development of kink zones during compression in composite materials with longitudinally aligned fibres (Fig.5.4(a)). Similar observations have been made with Kevlar 49 between fibres, where the kinks occur without fibre fracture due to compressive yield in the fibres. Watanabe et al. [102] observed shear bands (i.e. kink zones) in $Gd_2Zr_2O_7$ impressed at 1137°C (Fig.5.4(b)). This material is a thermal barrier oxide (used in engine components) with a columnar microstructure, grown by electron beam evaporation. The study showed that large separations form between the columns in the shear band. Additionally, the columns themselves crack in bending at the boundaries of the band. Mercer et al. [37] suggested that the similarity of the failure mode of bone in compression with the kinking of fibrous oxides at high temperature, provides a possible methodology for the modelling of bone compressive strength.

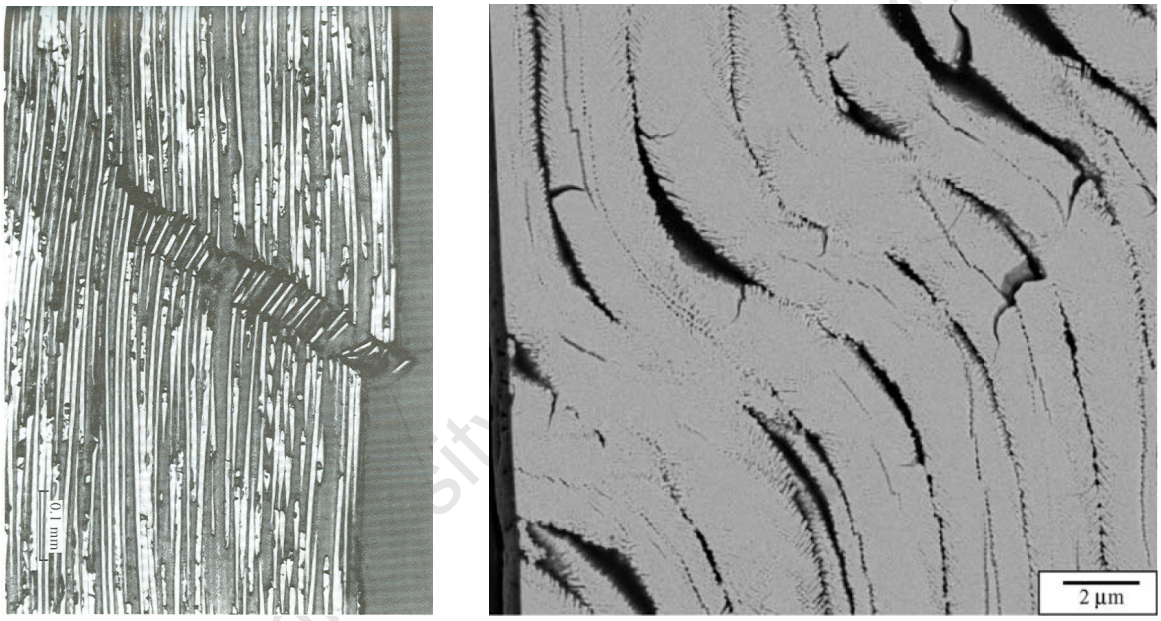

(a) (b)

Figure 5.4: Micrographs of "kink zones" observed in other materials. (a) Hull [100] compressed composite materials with longitudinally aligned fibres (b) Watanabe et al. [102] $Gd_2Zr_2O_7$ impressed at 1137°C

In the present study, shear bands were also observed in compressed bovine bone microstructure which was investigated under a petrographic microscope. The microstructure depicted in Fig.5.5 originates from longitudinal specimens that were compressed quasi-statically in the direction of the bone axis. The load direction is indicted in the figures and is in the same direction as the longitudinal bone axis. Notice the severe rotation of the material in the shear zone which is identified with the help of a polarizing lens. When the specimen is loaded the material weakens in the shear plane. The bone matrix is twisted as these planes slide over each other. The regions where the specimen is not cracked right through are twisted along with this motion. This results in a dislocated region and in

some instances two parallel cracks where the material is bent and eventually fractured.

Figs.5.5(b) and A.9(a) present the microstructure of a fractured specimen. Damage to the structure includes several longitudinal cracks as well as a shear band. The material is twisted between two parallel cracks that run diagonally across the sample. The dislocation of the material between the cracks is apparent if the slide is viewed through a polarizing filter.

Fig.5.6 shows a smaller shear band in another specimen. Again, the orientation of the material in the shear dislocation region varies distinctly from the orientation of the original laminar bone matrix. Notice the deformation of the fractured osteons and the extreme deformation of the osteocytes. Several fine cracks have originated perpendicular to the shear plane. The cracks seem to originate from the lacunae (which contains the osteocytes) which are twisted and squashed with respect to the surrounding bone matrix.

Additional longitudinal sections of longitudinally oriented bone specimens fractured in quasi-static compression are included in Section A.3 of the Appendix.

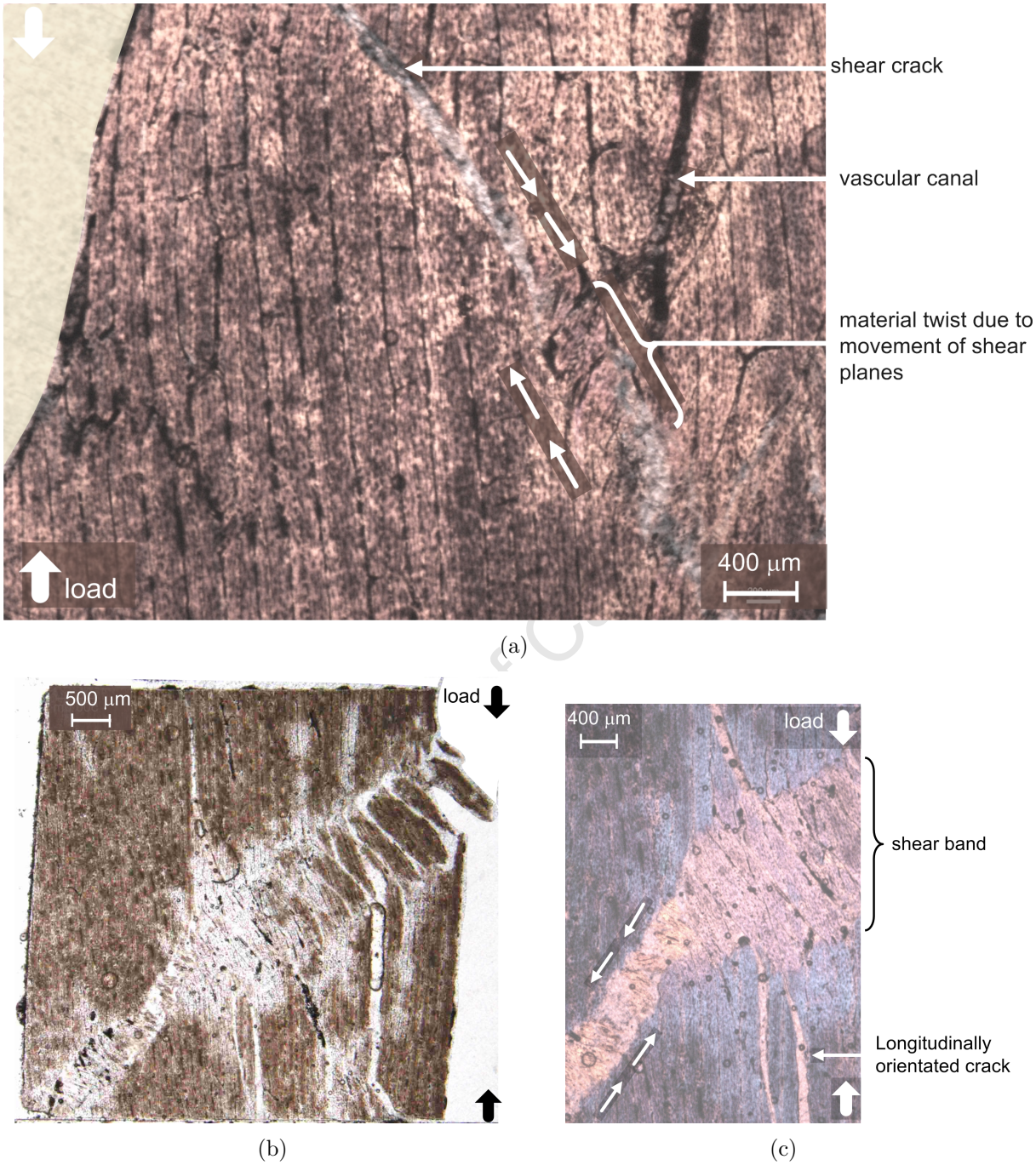

Figure 5.5: Micrographs of (a) the onset of twisting in laminar bone material. (b) A shear band dislocation region that stretches across a longitudinally orientated bone specimen. (c) A magnification of the shear band was recorded through a polarization filter. The colour is indicative of the orientation of the osteocytes in the bone matrix. The material in the shear band is twisted and disorientated by the movement of the shear planes

(a)

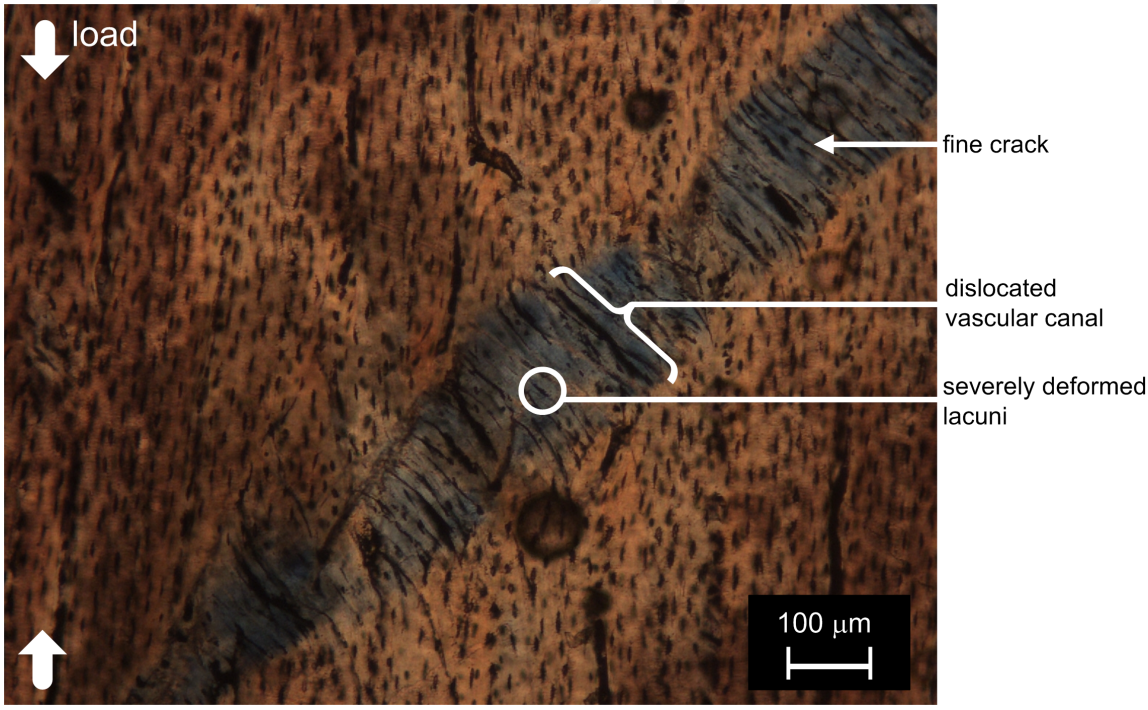

(b)

Figure 5.6: Micrographs of (a) a shear band dislocation zone in a specimen with a laminar microstructure. (b) A magnification of the shear band shows several fine cracks perpendicular to the shear plane and severe distortion of the osteocytes

Preferential cracking along the vascular canals in the transverse plane

The transverse sections of longitudinally orientated specimens were studied subsequent to quasi-static compression in the direction of the bone axis. All investigated specimens were found to have a plexiform arrangement in the transverse plane. The transverse sections show that the preferential direction of cracking is circumferentially around the original bone wall as opposed to radially through it.

Fig.5.7 shows a transverse section (top view) of damage to the compressed specimen microstructure. Several parallel cracks are present. It is clear that the cracks curve with the vascular canals and are orientated circumferentially along the tangential axis. A greater magnification of the specimen in Fig.5.7(b) shows that the cracks actually run along the blood vessels.

The slides seem to be unevenly ground such that certain areas allow the light of the microscope through, whereas others do not. In fact the bone has been compacted and therefore densified in some regions as a result of compression. The middle region of Fig.5.7(b) shows patches on the slide where the thin section of bone histology has been ground down too far.

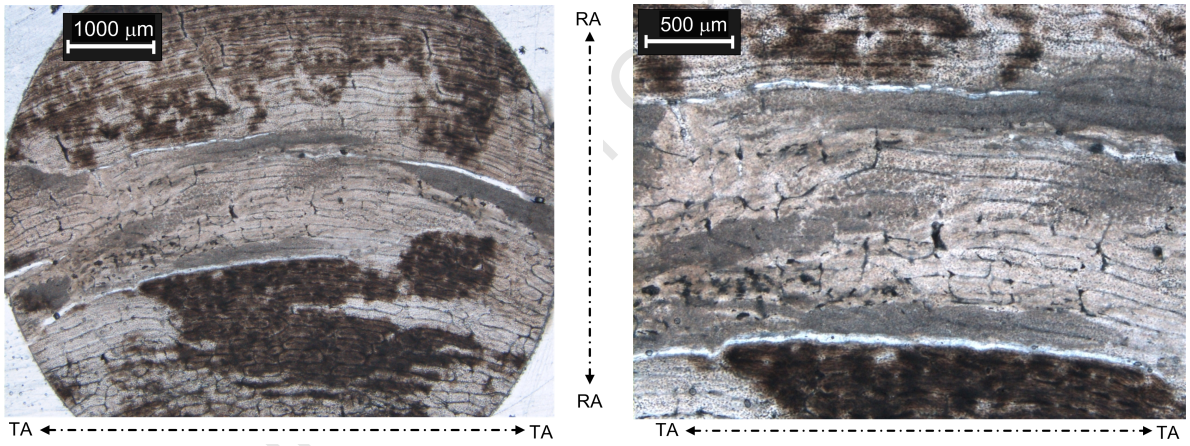

(a) (b)

Figure 5.7: Micrographs of cracks in the transverse plane of a longitudinally orientated specimen loaded in the direction of the bone axis. (a) Cracks develop parallel to each other and run in a direction that lies circumferentially around the original bone wall. (b) Magnification shows that the cracks run along the vascular canals or blood vessels of the plexiform microstructure.

The cracks do not always propagate along the vasculature, but sometimes crack diagonally through the osteons (which are also orientated tangentially). However, the general direction of the cracks remain in the same orientation as the dominant direction of the osteons and vascular canals (shown in Fig.5.8). None of the investigated specimens presented with radially orientated cracks in the transverse plane.

The preferential cracking of bone in one direction could be indicative of anisotropy in the bone structure, where one orientation of the bone matrix is weaker than the other.

Furthermore, it is possible that the tangential porosity of the bone structure (concentric arrangement of the plexiform network) acts as a weakness along which cracks propagate. These observations are supported by the observation of macroscopic bone fracture on which is discussed in Section 5.4.3. Furthermore, circumferential cracks are observed in the transverse plane of a whole femur diaphysis which fractured as a result of quasi-static compression (Section 7.5.2 in particular Fig.7.13). The present observations remain to be confirmed by a more extensive study of bone microstructure as a result of quasi-static compression.

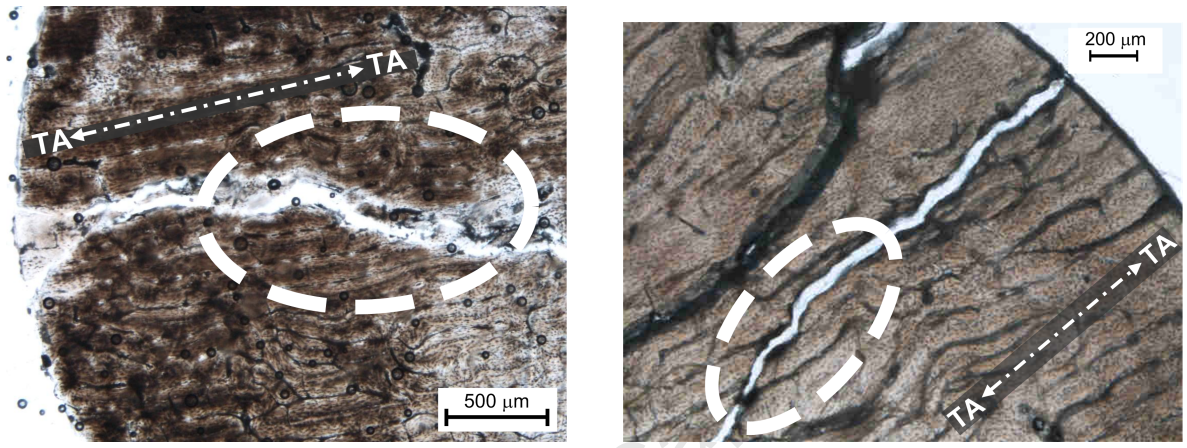

(a) (b)

Figure 5.8: Micrographs of transverse sections of two longitudinal specimens that were compressed in the direction of the bone axis. Cracks develop in the dominant direction of the osteons and vascular canals and sometimes propagate diagonally through the osteons.

5.1.3 Dynamic compression of longitudinally orientated specimens

This section discusses the results of dynamic bovine bone compression on the SHPB where two experimental rigs were used to test at two dynamic strain rates:

- At a strain rate of $2.5 \times 10^2\,\mathrm{s}^{-1}$ on 20 mm diameter, length 2 m bars with a 12 mm diameter, 650 mm uniform cylindrical striker.
- A strain rate of $10^3\,\mathrm{s}^{-1}$ on 12 mm diameter, length 1 m bars and 10 mm diameter, 200 mm uniform cylindrical striker.
- It was found that the use of conventional cylindrical strikers on the SHPB result in a strain rate that decreases during the test. Two conical strikers (one for each SHPB rig) were subsequently designed to shape the input signals in such a way that the strain rate remained constant (Section 4.3.7).
- The focus of these experiments were to determine the dynamic compressive properties of bovine cortical bone and to determine the potential effect that a varying strain rate in the course of the experiment would have on these properties.

Fig.5.9 supplies a summary of all the dynamic compression results obtained from tests on the SHPB. Variation in specimen density, microstructural type and microstructural orientation accounts for the variation in strain rate and stress-strain response. **A single tapered striker seems to be effective to control the strain rate of all tested specimens. Thus, inter-specimen variation does not affect the shape of the striker that is needed to achieve a constant strain rate dynamic compression test.**

The ultimate stress and strain of dynamic bone compression is listed in Table 5.2. On average bovine cortical bone achieves an ultimate stress of 383.9 MPa at a strain rate of $2.5 \times 10^2\,\mathrm{s}^{-1}$. This increases to 413.9 MPa at a strain rate of $10^3\,\mathrm{s}^{-1}$. The average ultimate strains are 2.4% and 2.7% respectively.

$\dot{\varepsilon}$ [s^{-1}]	σ_{ut} [MPa]	ε_{ut} [$\mathrm{m.\,m}^{-1}$]
$\dot{\varepsilon} \approx 2.5 \times 10^2_{\text{varying}}$	375.7 ± 30.5	0.024 ± 0.002
$\dot{\varepsilon} \approx 2.5 \times 10^2_{\text{constant}}$	383.9 ± 21.3	0.024 ± 0.003
$\dot{\varepsilon} \approx 1 \times 10^3_{\text{varying}}$	401.9 ± 20.6	0.035 ± 0.003
$\dot{\varepsilon} \approx 1 \times 10^3_{\text{constant}}$	413.9 ± 28.7	0.027 ± 0.001

Table 5.2: Compression test results for dynamic longitudinal bovine bone compression. *Varying* refers to experiments conducted with a uniform area striker. *Constant* refers to experiments where the input bar pulse wash shaped with a tapered striker.

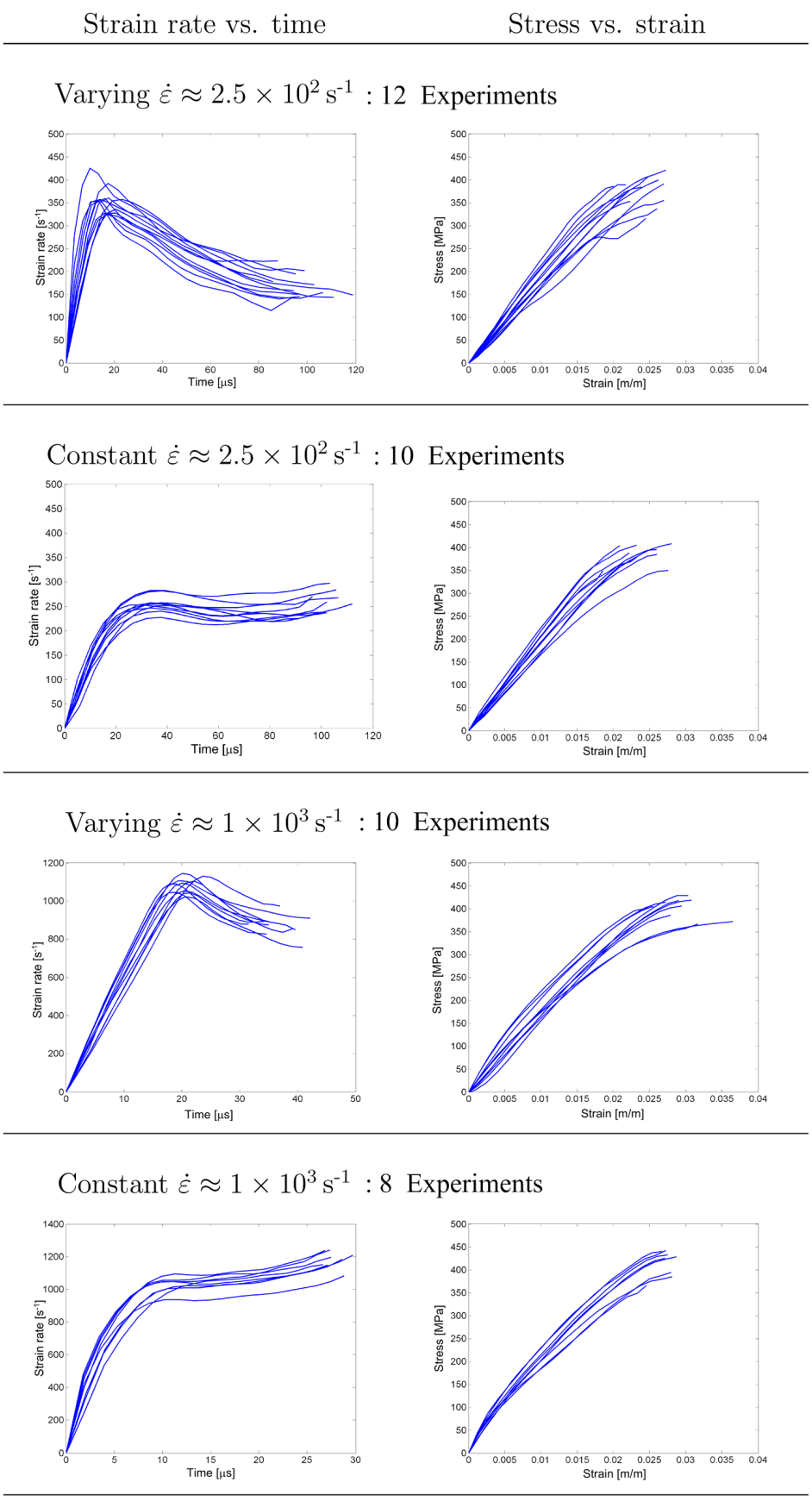

Figure 5.9: Dynamic compression responses of longitudinally orientated specimens on the SHPB. *Varying* refers to experiments conducted with a uniform area striker. *Constant* refers to experiments where the input bar pulse wash shaped with a tapered striker.

Constant vs. varying strain rate dynamic experiments

As discussed in Section 2.2 Adharapurapu et al. [20] argued that a variation in strain rate during a test could result in the measurement of smeared properties if the material is strain rate sensitive. This hypothesis was tested by conducting two series of tests at both the tested dynamic strain rates ($2.5 \times 10^2\,s^{-1}$ and $10^3\,s^{-1}$). One series with a conventional cylindrical striker (which resulted in a varying strain rate) and another series, where the strain rate was controlled constant by pulse shaping with a tapered striker.

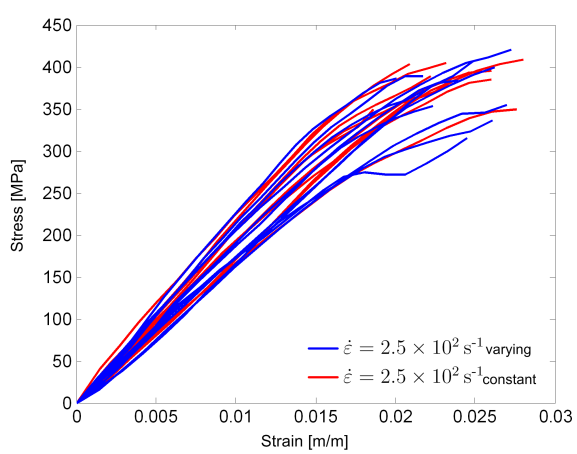

(a) Stress-strain responses at $\dot{\varepsilon} = 2.5 \times 10^2\,s^{-1}$

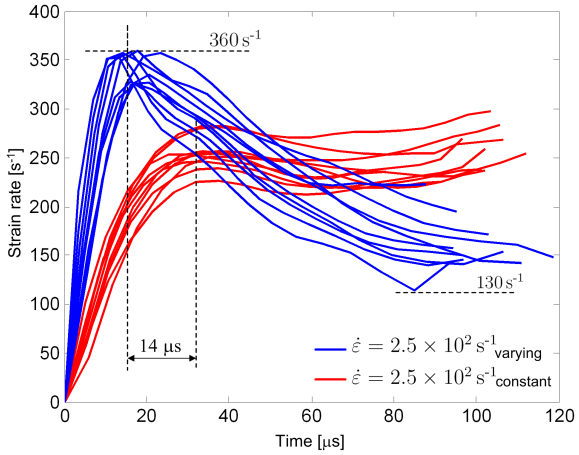

(b) Strain rate vs. time responses at $\dot{\varepsilon} = 2.5 \times 10^2\,s^{-1}$

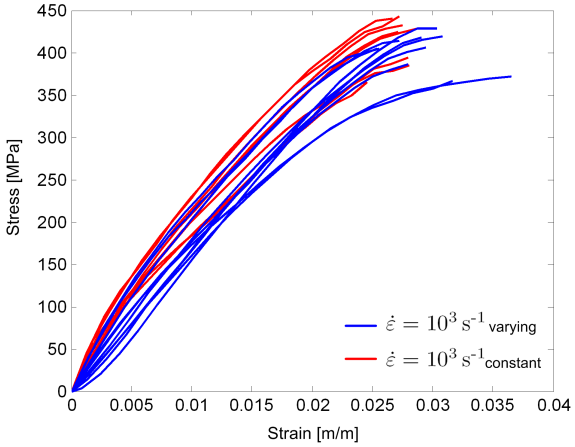

(c) Stress-strain responses at $\dot{\varepsilon} = 10^3\,s^{-1}$

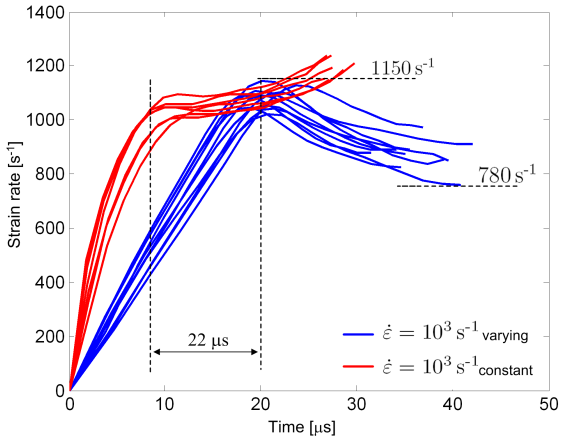

(d) Strain rate vs. time responses at $\dot{\varepsilon} = 10^3\,s^{-1}$

Figure 5.10: Comparison of dynamic response when the strain rate is allowed to vary (conventional SHPB test) and the strain is controlled constant (SHPB test with pulse shaping by a tapered striker)

Fig.5.10 shows the comparison between constant and varying dynamic strain rate responses at $\dot{\varepsilon} = 2.5 \times 10^2\,s^{-1}$ and $\dot{\varepsilon} = 10^3\,s^{-1}$.

The strain rate varied between $360\,s^{-1}$ and $130\,s^{-1}$ for the experiment at a notional strain rate of $\dot{\varepsilon} = 2.5 \times 10^2\,s^{-1}$ test with a uniform striker (Fig.5.10(b)). The results from these experiments are compared to an experiment at a nominally constant strain rate of $\dot{\varepsilon} = 2.5 \times 10^2\,s^{-1}$. For the experiment at a notional strain rate of $\dot{\varepsilon} = 10^3\,s^{-1}$ the rate of deformation varied between $780\,s^{-1}$ and $1150\,s^{-1}$. The results from this experiment are compared with specimen responses at a strain rate of approximately $10^3\,s^{-1}$.

The following observations are made with regards to the effect of strain rate control on the dynamic compressive response of bone:

- **There is virtually no difference between the response corridors for either of the dynamic strain rates** (Figs.5.10(a) and 5.10(c)).
- **At $\dot{\varepsilon} = 2.5 \times 10^2\,s^{-1}$ the strain rate drop towards the end of the test causes irregularity in the curvature of the stress-strain curves** (Fig.5.10(a)).
- **The average ultimate stress results** (Table 5.2) **at both strain rates are slightly lower for tests with a varying strain rate when compared with those where the strain rate was controlled constant.** The stresses are 375.7 MPa vs. 383.9 MPa at $\dot{\varepsilon} = 2.5 \times 10^2\,s^{-1}$ and 401.9 MPa vs. 413.9 MPa at $\dot{\varepsilon} = 10^3\,s^{-1}$. The differences in the ultimate stress at varying vs. constant strain rates is smaller than the standard deviation in the ultimate stress of the respective strain rate regimes. At present it is not possible to conclude if a variation in strain rate in the course of the experiment has a significant influence on specimen ultimate strength.

The variation of strain rate would potentially have the greatest effect for tests in the lower range of dynamic strain rates. The strain rate could vary through the middle strain rate region where reliable data is scarce and the response changes significantly over a small range of strain rates (as was shown by McElhaney [12]. The significant difference between the quasi-static and dynamic response corridors is discussed in Section 5.1.4.

Note that the strain rate rise time is about $14\,\mu s$ longer for the tapered striker test compared to the conventional SHPB test at $\dot{\varepsilon} = 2.5 \times 10^2$. However, the rise time was approximately $22\,\mu s$ shorter for the tapered striker test compared to the uniform striker test at $\dot{\varepsilon} = 10^3\,s^{-1}$. In the case of the $\dot{\varepsilon} = 10^3\,s^{-1}$ there is slight difference in the stiffness of the initial stress-strain response, which is attributed to the difference in the strain rate rise time between the tapered and uniform area striker experiments.

From the results it is recommended that bone compression on the SHPB is conducted with the suitable pulse shaping to achieve a constant strain rate.

- **Even though the corridors of response do not differ, the ultimate properties are slightly affected.**
- **Because of a lack of data where the strain rate history is reported, the possible effects of strain rate variation through the middle strain rate region is unknown (and therefore the effect of such a variation is unknown).** A data set from a single femur by McElhaney [12], predicts a great variation in bone properties within the small range of strain rates in the middle strain rate regime.
- **Strain rate control clarifies the specification of the strain rate at which compression tests were conducted.** This is advantageous, especially when investigating data on a $\log \dot{\varepsilon}$ plot (i.e. for the purposes of determining stress or strain-based fracture criteria as a function of strain rate as shown in Fig. 5.17 of Section 5.1.4).

The tapered striker technique is an advantageous method of pulse shaping because a single tapered striker is effective to control the strain rate of all the specimens tested with this method. Thus, inter-specimen variation does not affect the shape of the striker that is needed to achieve a constant strain rate. The shape of the striker does not have to be conical, therefore the diversity of possible striker shapes offers infinite possibilities with regard to pulse shaping.

High-speed camera images of longitudinal specimen compression of the SHPB

Dynamic compression tests were filmed with a Photron-ultima APX-RS high speed camera at 70000 frames per second and a resolution of 128×128 pixels. Fig.5.11 shows high-speed camera images of the progressive compression and fracture of longitudinal specimens on the 12 mm SHPB. The direction of compression commences horizontally from left to right. The input- and transmitter bars are respectively located towards the left and right of the images, with the specimen in between. The relative time frames of the photographs are specified above each picture in the film strip. The camera was triggered manually just before the SHPB striker was fired. The time frames reported here can therefore not be connected to events on the stress-time curve, but serve merely as an illustration of the relative time of the course of events observed on the photographs. The camera was a new addition to the Blast Impact and Survivability Research Unit (BISRU) at the time of this study and the current filming set-up did not have a synchronised triggering ability. Additionally, we did not possess the lighting or image processing techniques to do any work beyond using the camera to gain a visual understanding to the loading of bone specimens in the SHPB. This tool is invaluable as relatively brittle bone specimens are not

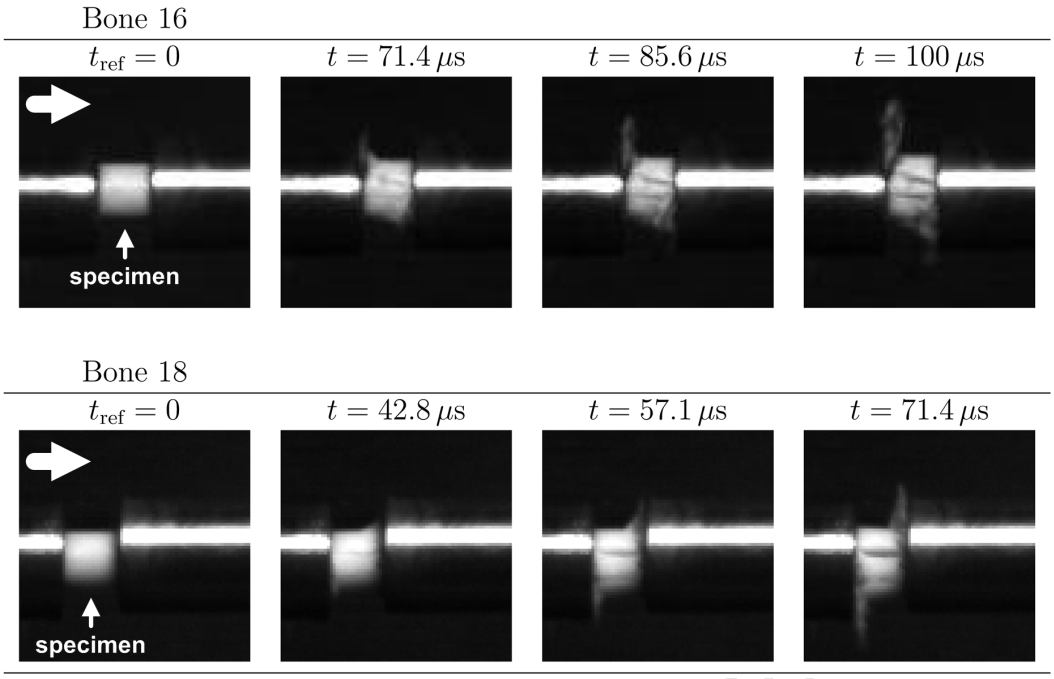

Figure 5.11: High-speed camera pictures of longitudinal specimen compression on the 12 mm diameter SHPB

easily recovered subsequent to SHPB tests. After most tests only a pile of brittle splinters remain of the bone specimens. For this reason the microstructure of dynamically loaded specimens was not investigated. Even if the specimen was still in one piece, the reflections of the stress waves in the input bar of the SHPB cause the specimen to be reloaded. The recovered specimen could therefore be a result of multiple loadings, which complicates the task of isolating the mechanism or pattern of initial fracture.

The progressive compression and fracture of both, the specimen from Bone 16 and Bone 18 (Fig.5.11) shows splitting of the specimen along its length (as opposed to across it). The crack pattern of Bone 16 somewhat resembles a v-shape, which is associated with shear, although the angle appears sharper than the ideal 45°. McElhaney [12] suspected that high strain rate failures in human cortical bone appear to follow the cement lines which mark the extreme boundaries of the secondary osteons. Cement lines are only present at the secondary osteons which were not often found in the bones that are investigated in this study. However, the plexiform and laminar structures encountered in the present bovine cortical bone have osteons, separated by vascular canals, which are predominantly orientated longitudinally along the specimen axis. As is apparent from the progressive fracture of Bone 16 and Bone 18, the direction of the cracks are in the same direction as the orientation of the vascular canals. The combined observations of McElhaney [12] and the present data seem to suggest that the boundaries between osteons (vascular canals) are a weaker part of cortical bone structure which helps cracks to propagate. This could possibly explain why the crack direction deviates from the crack direction for perfect shear.

5.1.4 Summary of longitudinal compression data at all strain rates

Stress vs. strain response

The stress-strain results for all quasi-static and dynamic strain rate compression tests are assembled in Fig.5.12. The goal of this figure is not to show individual responses, but rather to illustrate quasi-static and dynamic responses relative to each other.

It is clear that bone responds to quasi-static and dynamic compression in two very distinct corridors. The dynamic response corridor is significantly more stiff than the quasi-static one. This implies that if a bone specimen is deformed to a certain level, the stress that develops in the material would be much higher if the load was dynamic, than if it were quasi-static. Experiments confirm that bovine bone fractures at a higher stress with increasing strain rate. This trend of increasing failure stress remains consistent throughout the quasi-static and dynamic strain rate regimes.

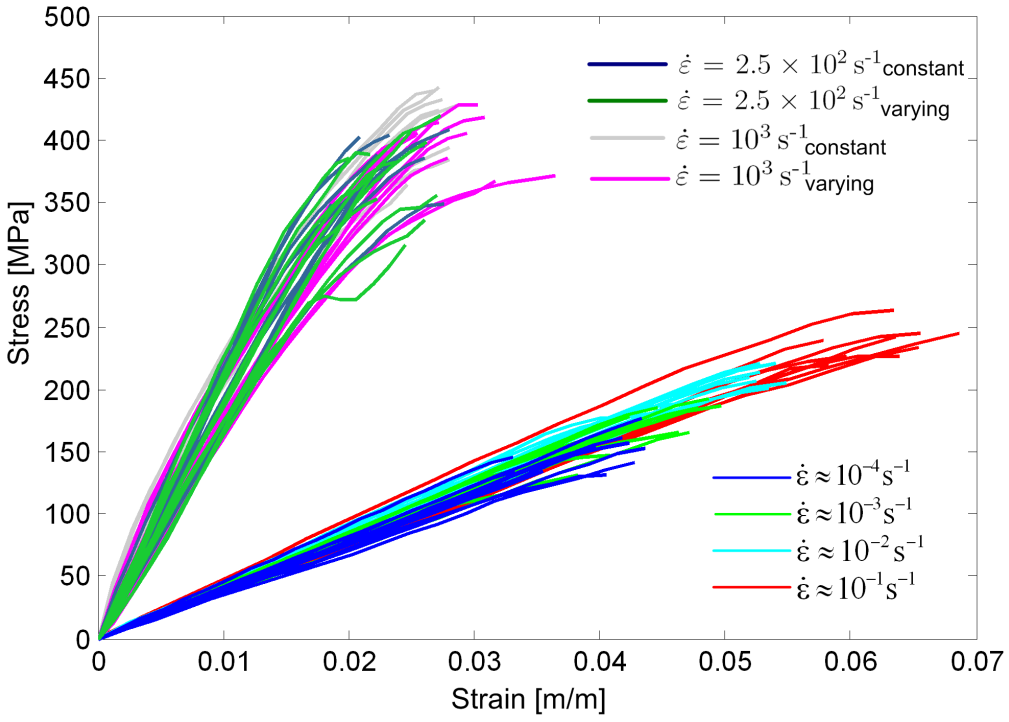

Figure 5.12: Stress strain curves for all longitudinal compression data

As discussed in Section 5.1.1 the ultimate strain at fracture increased consistently from $\dot{\varepsilon} = 10^{-4}\ s^{-1}$ to $\dot{\varepsilon} = 10^{-1}\ s^{-1}$. However, the opposite is true for the transition between quasi-static, where the ultimate strains were about 6.2% as opposed to dynamic strain rates where the ultimate strain is about 2.4%. **The response is more brittle in that specimens fracture at a significantly smaller ultimate strain when they are compressed dynamically.**

There is a significant difference in bone response within the range of strain rates between $\dot{\varepsilon} = 0.1\,\mathrm{s}^{-1}$ and $\dot{\varepsilon} = 2.5 \times 10^2\,\mathrm{s}^{-1}$. Unfortunately these strain rates happen to coincide with the range of strain rates where it is difficult to conduct experiments. The lack of experimental systems and data in the middle strain rate regime is a key factor that prevents the full understanding of the strain rate sensitivity of bone.

Average longitudinal stress-strain response

The stress vs. strain responses shown in Fig.5.12 were averaged at each strain rate to visualise general trends. The stress vs. strain curves were summed at each strain rate and divided by the number of tests. The ultimate stress and strain properties coincide with the average ultimate stress and ultimate strain data reported in Tables 5.1 and 5.2. The result is shown in Fig.5.13.

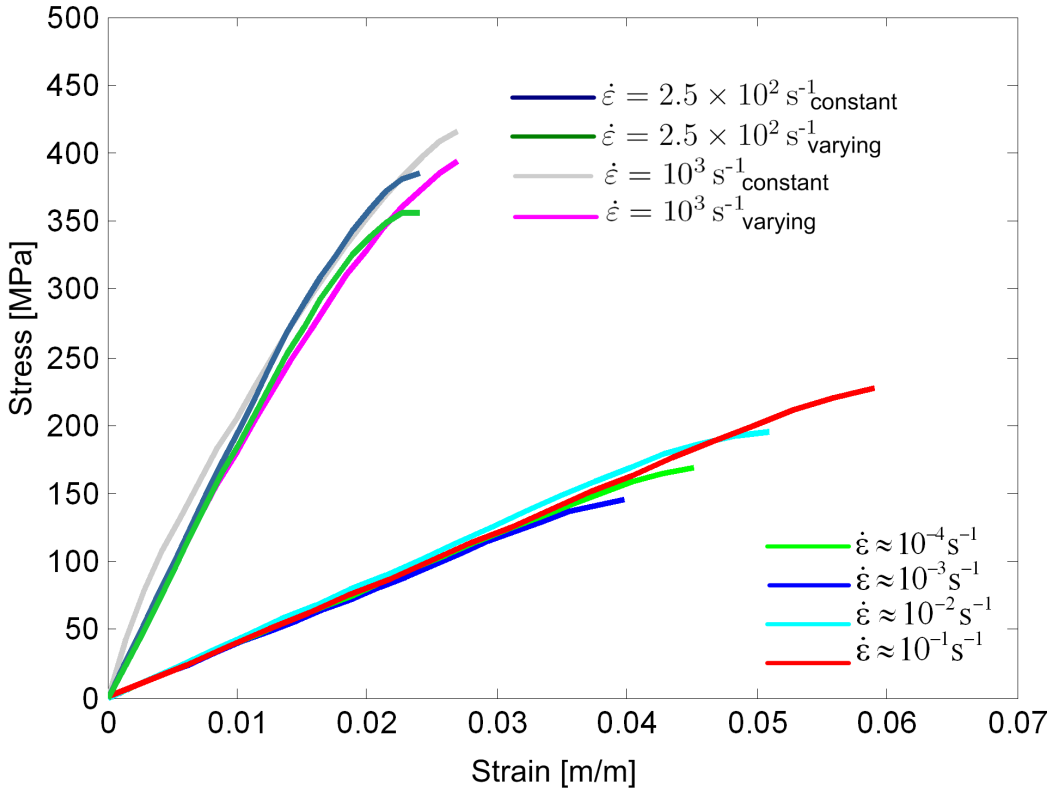

Figure 5.13: Averaged stress vs. strain curves for all longitudinal compression data

Average longitudinal stress-strain response compared to responses in literature

The average stress vs. strain curves (Fig.5.13) were compared with the results of Adharapurapu et al.[20] (discussed in Section 2.4.3), who investigated the strain rate dependent response of bovine cortical bone in longitudinal compression. The current data nominally agrees with the data of Adharapurapu et al.[20] with regards to the ultimate stress and

strain of compressive bone fracture. **The bone specimens tested by Adharapurapu et al.[20] responded with a greater stiffness and ultimate strength across the strain rate regime. The data from the current study presents with much less separation of the stress-strain curves and a significantly smaller stiffness at quasi-static strain rates.** The work of Adharapurapu et al. [20] showed a negative strain rate sensitivity at $\dot{\varepsilon} = 10^{-3}\,\mathrm{s}^{-1}$ which is not apparent from the present work. The dynamic response is in overall good agreement with that found by Adharapurapu et al.[20].

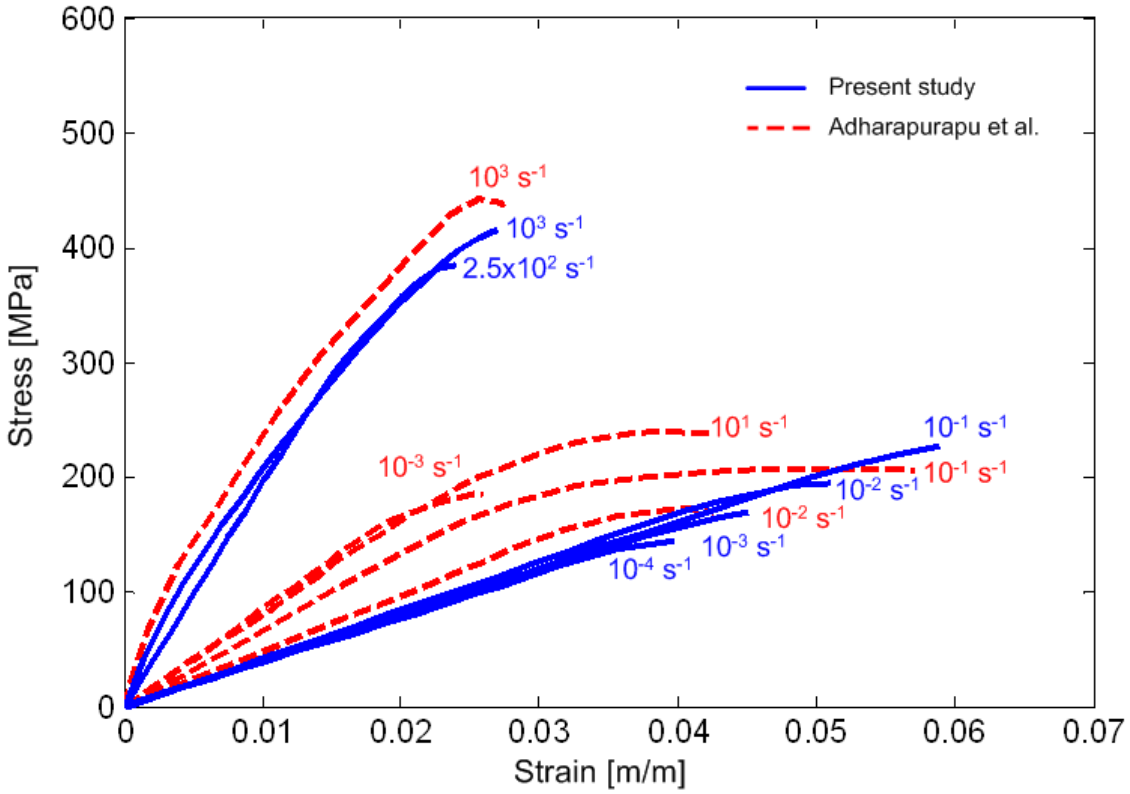

Figure 5.14: Comparison between the data from the present study and that reported by Adharapurapu et al. [20] for the compression of bovine cortical bone

Bone failure and fracture

As discussed in Section 5.1.1 the compressive quasi-static stress vs. strain response of bovine cortical bone can be divided into three parts (as described by Pithiuox et al. [89]):

- The initial response of the material is linear elastic and Youngs modulus can be determined.
- On the second part, the behaviour is weakly non-linear in that the slope of the stress-strain curve softens slightly. According to the works of Pithioux et al. [89] and Shim et al.[21] this weak non-linearity shows that the material is damaged by

micro-cracking. Even though the bone structure has **failed** in micro-cracking, the specimen has not yet lost its load bearing ability.

- In the final stage, **fracture** occurs suddenly. Not much plastic strain is observed before the specimen fractures and loses its ability to sustain a load (indicated by the end of the stress vs. strain curve).

The three stages of the quasi-static stress vs. strain curve are indicated in Fig.5.15 (at $\dot{\varepsilon} = 10^{-2}\,\mathrm{s}^{-1}$).

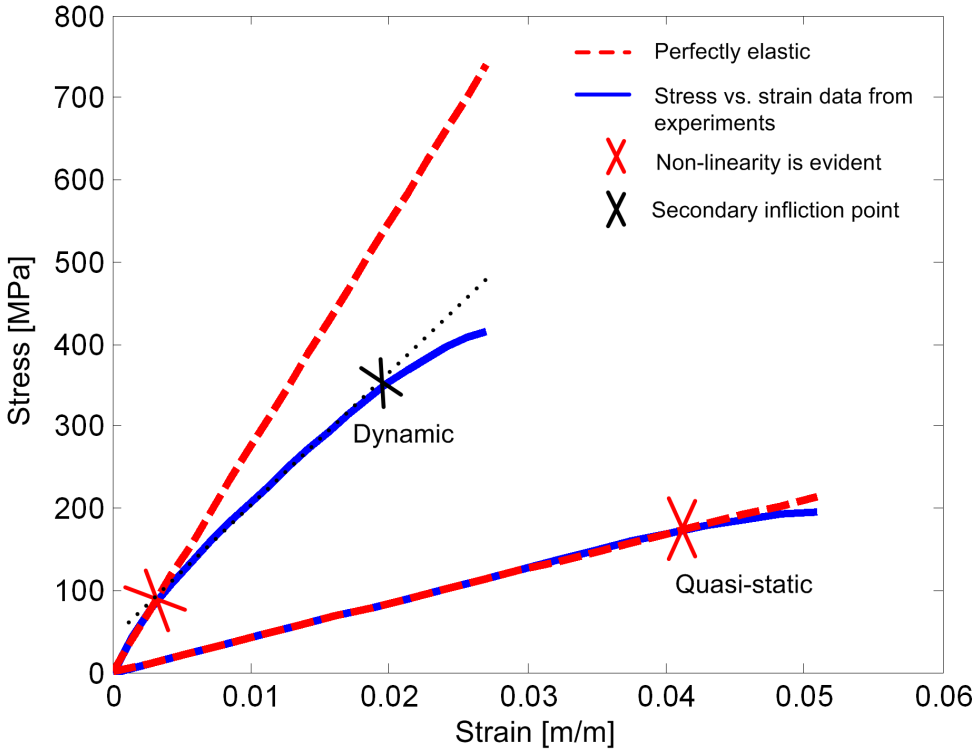

Figure 5.15: The onset of damage in quasi-static and dynamic compression

The dynamic bone response differs from the quasi-static response in that linear elastic portion of this curve is almost non-existent. Thus, the onset of non-linearity is evident very early in the test. Recall that the early stress vs. strain data from SHPB tests are not always reliable (because the input and output faces of the specimen are not in equilibrium as discussed in Section 4.3.4). **At present it is unclear if this early non-linearity can be attributed to micro-damage or viscous effects. The non-linear dynamic stress vs. strain response shows a secondary infliction point** [***Infliction point:*** is defined as a point where the slope of the curve decreases or softens]. **It is assumed here that this point is associated with damage in the material because the average slope of the non-linear curve decreases and fracture follows shortly afterwards.** Ultimate strain and stress varies somewhat from one experiment to another. Over and above variations in bone density and microstructure, this could possibly be attributed

to the distribution of defects in the sample and the dependency of final fracture on how these defects develop. **Therefore the structural integrity of the material beyond the onset of damage is compromised and somewhat unpredictable without the proper knowledge of failure mechanisms and models. Additionally the structure is permanently damaged and its potential to retain its original load bearing ability remains to be investigated.**

In order to quantify the starting point of structural compromise in the material, the yield point of the material is to be determined. Shim et al. [21] defined the yield point as the failure stress for cancellous bone and found that on average this stress was 5% below the ultimate stress. The estimation of the yield point is somewhat subjective because the analyst decides when non-linearity is evident. **In the present work the average yield point was determined as follows:**

- For quasi-static strain rates the stress-strain response was clearly linear for the majority of the test duration. **The yield point at quasi-static strain rates was therefore determined at the point where the stress-strain curve started to deviate from the initial linear response.**
- **The dynamic compressive yield point was chosen at the point where the slope of the strain rate started to increase after reaching an approximately constant level.** The intact specimen structure resists straining by the compressive load. Damage to the bone structure is marked by an increase in strain rate.

The yield stress was associated with the failure of the bone structure. The failure stress magnitude and the failure stress as a percentage of the ultimate stress are listed at different strain rates in Table 5.3. For dynamic tests, the values listed are for the second infliction point because this is assumed to be associated with material damage.

$\dot{\varepsilon}$ [s^{-1}]	σ_f [MPa]	σ_{ut} [MPa]	$\frac{\sigma_f}{\sigma_{ut}} \times 100$ [%]
$\dot{\varepsilon} = 10^{-4}$	130.0	149.6	86.9
$\dot{\varepsilon} = 10^{-3}$	159.6	171.9	92.9
$\dot{\varepsilon} = 10^{-2}$	179.6	202.1	89.0
$\dot{\varepsilon} = 10^{-1}$	197.6	234.8	84.1
$\dot{\varepsilon} = 2.5 \times 10^{2}$	304.3	383.9	80.1
$\dot{\varepsilon} = 10^{3}$	336.0	413.9	81.1

Table 5.3: The strain rate dependent failure stress at which material damage is evident

For the purposes of this study the following distinction is made between *failure stress* and *fracture stress*:

- **Failure stress is defined as the stress at which damage to the bone structure is evident from the stress-strain response.** This assumption is in keeping with the assumption by Shim et al.[21]: the greatest motivation for the present coupling of the onset of damage with failure stress is that damage of the bone structure is likely to be associated with injury in the living structure.

- **Fracture stress: is associated with the ultimate stress where the material loses its load bearing ability.**

One of the motivations for the present research is to supplement the techniques by which the lower extremity injury criterion (IC) for anti-vehicular (AV) landmine resistant vehicles can be extended to include loading rate or *duration*. At present, the injury threshold for the loading of the lower extremity of vehicle occupants in the course of an AV-mine blast is an axial tibial force of 5400 N. **Hight [11] concluded that the strength and other properties of bone are time dependent and therefore expressed the need for a bone fracture criterion which includes a loading-rate dependency.** A criterion was consequently developed (expressed in terms of strain rate or load duration) on the basis of data from McElhaney [12] who conducted strain rate dependent compression tests on bone from human and bovine femurs. In the light of the work of Hight [11], the time durations, which are associated with the failure (t_f) and fracture (t_{ut}) of bovine cortical bone specimens (from the present study) are listed in Table 5.4.

$\dot{\varepsilon}$ [s^{-1}]	t_f [s]	t_{ut} [s]	$\frac{t_f}{t_{ut}} \times 100$ [%]
$\dot{\varepsilon} = 10^{-4}$	3.2×10^{2}	3.8×10^{2}	85.5
$\dot{\varepsilon} = 10^{-3}$	3.9×10^{1}	4.2×10^{1}	89.7
$\dot{\varepsilon} = 10^{-2}$	4.3×10^{0}	4.8×10^{0}	89.7
$\dot{\varepsilon} = 10^{-1}$	5.7×10^{-1}	7.1×10^{2}	80.5
$\dot{\varepsilon} = 2.5 \times 10^{2}$	6.9×10^{-4}	1.0×10^{-4}	68.5
$\dot{\varepsilon} = 10^{3}$	2.0×10^{-4}	2.8×10^{-4}	71.3

Table 5.4: The average failure and fracture times of bovine cortical bone specimens at different strain rates

The failure and fracture stress is correlated to failure and fracture time duration in Fig.5.16. Both the fracture (σ_f) and failure stress (σ_f)are related to time by the following function:

$$\sigma = A \log(t) + B \tag{5.1}$$

Note that σ is expressed in MPa and t is expressed in seconds. The paramaters for Eq.5.1 are listed in Table 5.5.

	A	B
Failure stress vs. time	-27.4	197.8
Fracture stress vs. time	-37.7	235.5

Table 5.5: Parameters for the ultimate and fracture stresses as a function of ultimate and fracture time duration

Both the fracture and failure stresses of bovine cortical bone decreases logarithmically with the time duration of a compressive load. It is concluded that bovine cortical bone can sustain a higher stress for short durations of time. Additionally the time of failure and the time of fracture are more closely related for long load durations than short load durations.

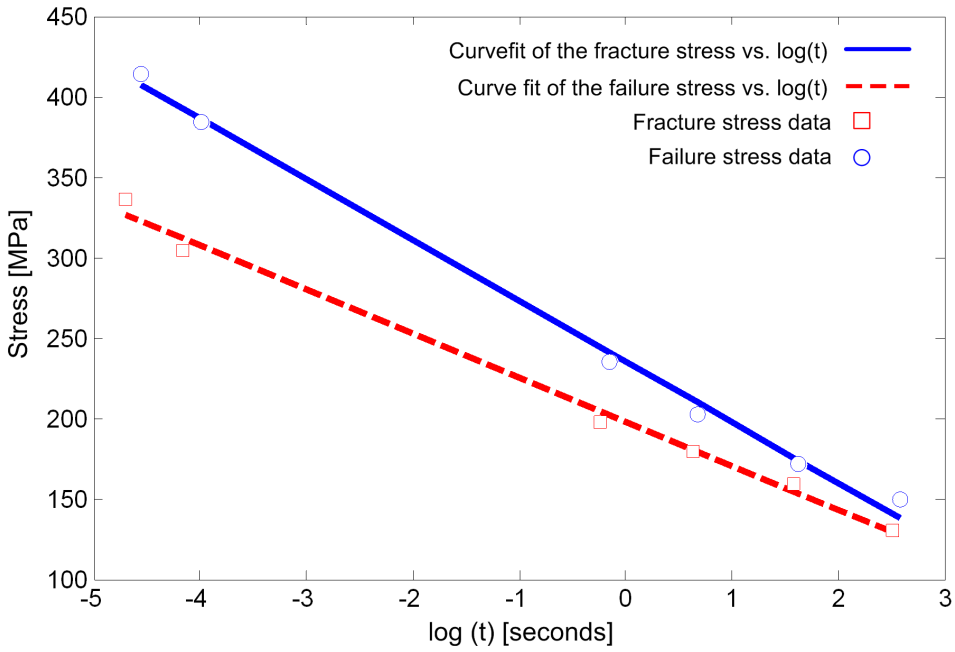

Figure 5.16: Fracture and failure stresses as a function of fracture and failure time duration

True stress history vs. $\log \dot{\varepsilon}$

The compressive stress and strain rate are explicitly related to each other on the $\log \dot{\varepsilon}$ vs. stress plot shown in Fig.5.17. A perfect constant strain rate experiment would be presented by a straight vertical line on this graph. As the specimen is compressed, the stress progressively increases, but the strain rate remains constant. Of course, some strain rate variation is present in actual data. This is especially apparent in the conventional

SHPB dynamic strain rate tests. Notice that the current data ranges over a strain rate regime of seven orders of magnitude, but that the present study lacks information on strain rate dependent compression of bovine bone between $\dot{\varepsilon} = 10^0\,\mathrm{s}^{-1}$ and $\dot{\varepsilon} = 2.5 \times 10^2\,\mathrm{s}^{-1}$. It is

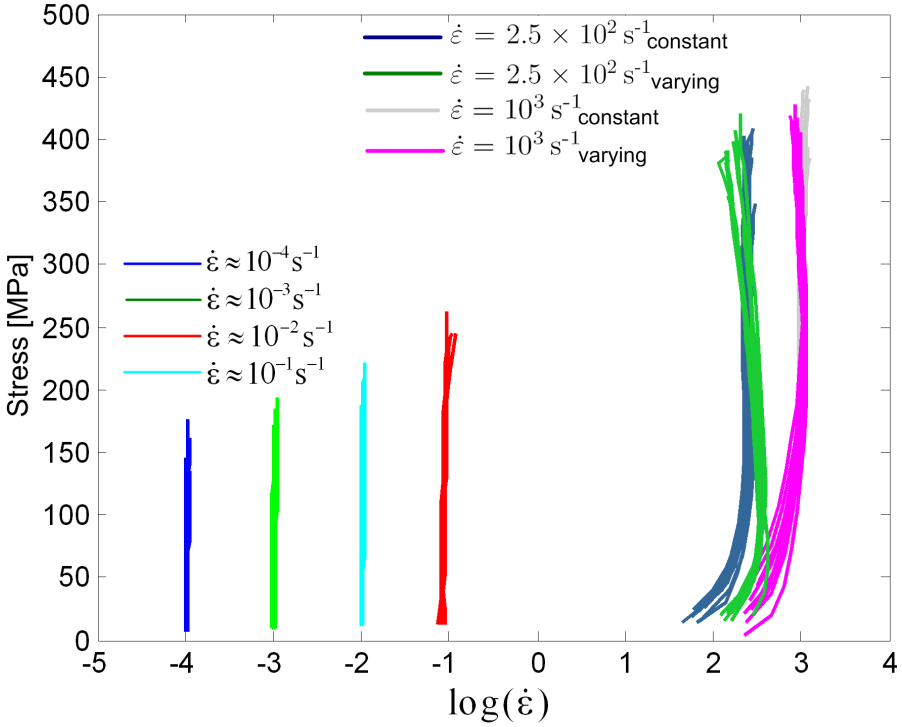

Figure 5.17: Stress vs. $\log \dot{\varepsilon}$ for all longitudinal compression data

useful to visualise the specimen stress in terms of strain rate for the purposes of defining a stress based compressive bone failure criteria. Fig.5.18 shows the average stress of bone samples, interrogated at identical strains for different strain rates of compression. The results of the conventional SHPB tests (with a varying dynamic strain rate) were ignored when making this plot. The stresses were interrogated at four different levels of strain $0,5\%$, 1.0%, 1.5% and 2.0% and at additional strains of 2.5%, 3.0% and 3.5% for quasi-static tests. The connecting lines are thus contours of identical strain on the stress vs. $\log \dot{\varepsilon}$ plot.

It is clear that strain rate has a moderate effect on the material stress at quasi-static strain rates. However the effect is very significant when the strain rate is dynamic (in the order of $\dot{\varepsilon} = 2.5 \times 10^2\,\mathrm{s}^{-1}$ and above). For example, if a bone sample is compressed by 1.5%, the stress in the sample would be roughly $60\,\mathrm{MPa}$ if the rate of compression was quasi-static. However, if the specimen was compressed by the same amount, but at a dynamic rate, the stress in the material would be 4.7 times higher at about $280\,\mathrm{MPa}$.

The ultimate stress that develops in the bone material during compression has a non-linear dependency on the rate of that compression (Fig.5.18). The relationship between the ultimate stress and strain rate could serve as a stress based failure criterion. However, the density of bovine bone is also expected to influence the ultimate failure stress. As discussed in Section 2.6, Carter and Hayes developed such a failure criterion for human bone which depends on both density and strain rate:

$$\sigma_{ut} = 68\ \dot{\varepsilon}^{0.06}\rho^2 \tag{5.2}$$

This criterion parameters were optimised to obtain the best approximation of the ultimate stress and strain rate data in Fig.5.18. The resulting relationship between ultimate, fresh bone density and strain rate is:

$$\sigma_{ut} = 61.2\ \dot{\varepsilon}^{0.06}\rho^2 \tag{5.3}$$

The failure stresses, as listed in Table 5.3, are also plotted as a function of strain rate in Fig.5.18. At a strain rate of $10^{-4}\,s^{-1}$ specimens fail at a stress which is approximately 13%

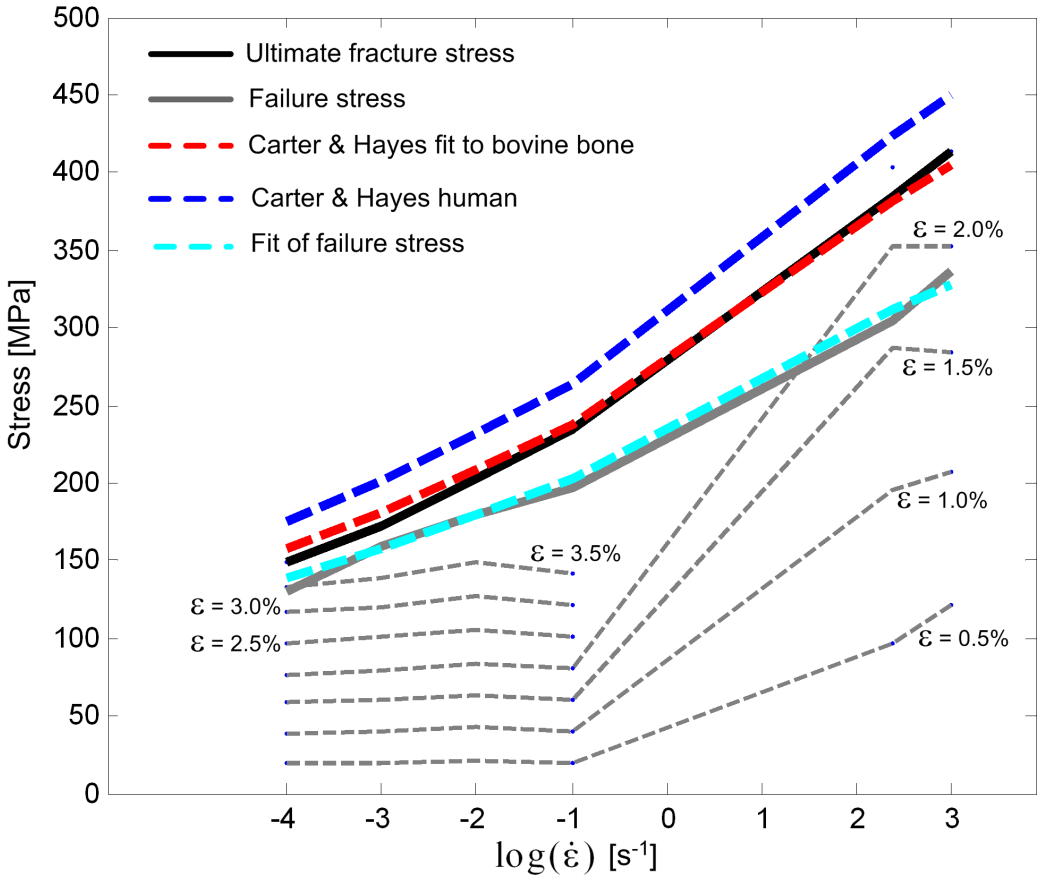

Figure 5.18: Strain contours that show the average sample bone stress over different strain rates

below the ultimate strength. The failure stress is approximately 10% below the ultimate stress for quasi-static compression (at strain rates of $10^{-3}\,s^{-1}$ to $10^{-2}\,s^{-1}$). This fraction increases to about 15% at a quasi-static strain rate of $10^{-1}\,s^{-1}$ and increases further to approximately 20% for specimens loaded dynamically (at strain rates of $2.5 \times 10^{2}\,s^{-1}$ and $10^{3}\,s^{-1}$). A function that gives a good approximation of the failure stress in terms of strain rate and density is:

$$\sigma_f = 51.4\ \dot{\varepsilon}^{0.057}\rho^2 \tag{5.4}$$

Notice that the slope of Eq.5.4 is slightly adjusted from 0.06 to 0.057 to account for the fact that the failure stress is not an equal percentage below the ultimate stress for all strain rates.

Specimen density

As discussed in Section 2.6 the strength relations published by Carter and Hayes [88] and Shim et al. [21] lead to the conclusion that **bone strength increases with both, density and strain rate**. Carter and Hayes explored the hypothesis that cancellous and cortical bone can be mechanically viewed as one material with variable density. The researchers combined the effects of density, strain rate and ultimate stress in one relation (Eq.2.35).

Shim et al.[21] elected to isolate the contribution of strain rate to dynamic strength by assuming that the contribution of density to bone strength would be the same regardless if the strain rate is quasi-static or dynamic. The dynamic strength could therefore be expressed by the summation of two terms, one depending on density and one depending on strain rate (Section 2.6).

The *apparent bone density* or bone mineral density (BMD) is defined [21] as the density of only the bone mineral, without fat or liquids which do not contribute to the load bearing ability of bone (as discussed in Section 2.2.2).
It is most appropriate to correlate apparent bone density with bone strength. Sharp et al.[32] reported that the process of de-fatting specimens can potentially damage the bone structure. For this reason **this study will follow the approach used by Shim et al. [21], who correlated bone strength to *fresh bone density* [fresh bone density:** is defined as the density of the bone which includes fat and fluids].

Adharapurapu et al.[20] measured specimen mass in both, wet (soaked in Hank's balanced salt solution) and dry conditions (after dried in air for 15 days) to determine the possible contribution of moisture to the fresh bone density. Dry specimen density would give a more accurate indication of apparent bone density (which is more correct to correlate with bone strength), but would still contain the effects of fat.

It was also established that density has to be determined for each specimen

to be tested because bone structure is not homogeneous and varies from location to location and within an individual part.

Correlation between ultimate strength and fresh bone density

In the light of the above discussion this study approaches the correlation of density, strength and strain rate as follows:

- Bone strength is correlated to fresh bone density as opposed to apparent bone density in order to avoid damage to the bone structure by de-fatting the specimens.
- The fresh bone density of bone specimens is determined by dimension measurement and weighing on a precision balance Sartorius R200D scale at the Centre for Materials Engineering at the Department of Mechanical Engineering of the University of Cape Town.
- Forty three fresh bone specimens were compressed at $10^{-4}\,s^{-1}$ (the slowest strain rate which is considered in the present work) in order to minimize the effect of strain rate. The specimens, which originated from 28 different bovine femur bones, were compressed after soaking in water for 48 hours. The ultimate strength obtained from these quasi-static tests is correlated with fresh bone density.

The resulting correlation between quasi-static ultimate stress and density is demonstrated in Fig.5.19. Bone specimens with a greater density fracture at a higher ultimate stress. This is expected because a bone with a greater density would have more mineral at its disposal to resist the load deformation compared to a bone with a lesser density. All investigated literature agrees that an increase in density is associated with a better resistance to bone fracture (McElhaney[12], Shim et al. [21], Carter and Hayes [88], Dubbeldam et al. [31]).

The variation in density and quasi-static strength within the 43 specimen sample is summarised in Table 5.6.

	Fresh bone density [kg. m^{-3}]	Ultimate stress [MPa]
Average	2056.2	158.5
Standard deviation	±38.6	±16.0
Minimum	1992.9	131.8
Maximum	2130.1	193.3

Table 5.6: Correlation between density and quasi-static ultimate strength

In the present work the relationship between quasi-static ultimate strength (at $\dot{\varepsilon} = 10^{-4}\,s^{-1}$) and fresh bone density is best approximated by an exponential function:

$$\sigma_{ut} = 158.2e^{0.06\rho} \tag{5.5}$$

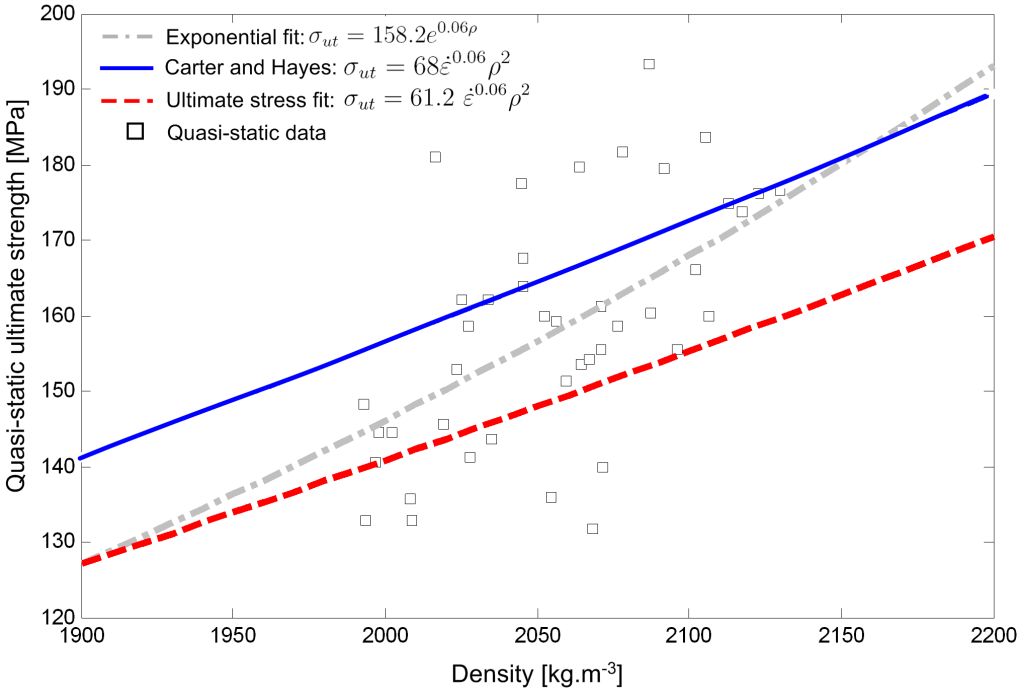

Figure 5.19: Fresh bone density compared to the quasi-static ultimate strength

The correlation coefficient of the exponential function with the ultimate stress and density data is $R^2 = 0.35$. In Fig.5.19 this function is plotted along with the strain rate and density dependent strength relation (Eq.5.2) for human bone by Carter and Hayes [40] and the adapted strain rate and density relation which best describes the ultimate strength of bovine bone (Eq.5.3). Even though the relation of Carter and Hayes [88] was developed for cancellous (or spongy) human and bovine bone specimens with densities between 70 kg. m^{-3} and 970 kg. m^{-3} the relation is surprisingly accurate for the cortical bone densities encountered in the present study which were outside this density range (1992 kg. m^{-3} and 2130 kg. m^{-3}). This correlation is attributed to the fact that Carter and Hayes reported the apparent density of the bone mineral (the branches of the spongy network) to range from 1600 kg. m^{-3} to 2000 kg. m^{-3}, which is comparable to the fresh bone densities of samples from the present study. **The correlation between the relation developed by Carter and Hayes and the present data supports the hypothesis that cancellous and cortical bone can be mechanically viewed as a single material with a variable density.**

Dynamic ultimate strength was determined for 10 specimens (which originated from Bones 1 - 10) at a strain rate of $\dot{\varepsilon} = 6.5 \times 10^2\,\text{s}^{-1}$. The correlation between dynamic ultimate strength and fresh bone density is presented in Fig.5.20. More data is required to establish a relationship between the dynamic strength of bovine bone and fresh bone density. Again, the strain rate and density dependent strength relation (Eq.5.2) for human bone by Carter and Hayes [40], and the adapted strain rate and density relation which

describes the ultimate strength of bovine bone (Eq.5.3) are plotted along with the dynamic compression data. Both these relations over-predict the dynamic ultimate strength of bovine cortical bone. However, the adapted strength relation for bovine cortical bone Eq.5.3 provides the better estimate of dynamic ultimate strength as a function of fresh bone density and strain rate.

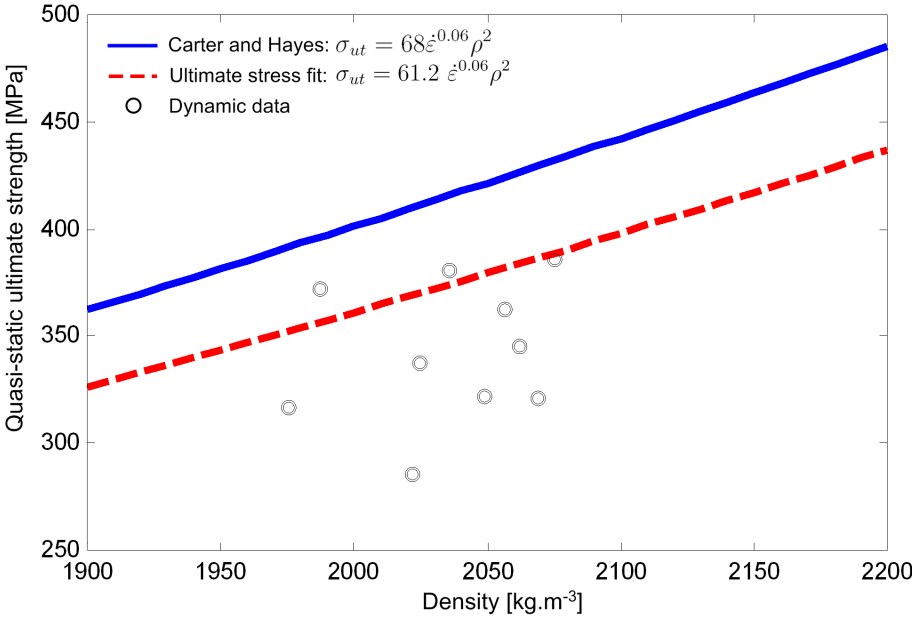

Figure 5.20: The correlation between density and dynamic ultimate strength

The density range of the samples, as well as the dynamic ultimate strength, is reported in Table 5.7.

	Fresh bone density [kg. m^{-3}]	Ultimate stress [MPa]
Average	2035.8	342.8
Standard deviation	±33.8	±32.4
Minimum	1975.4	285.2
Maximum	2075.5	385.6

Table 5.7: Correlation between density and dynamic ultimate strength

Quasi-static and dynamic ultimate strength is compared in Fig.5.21. **In the present investigation of the relationship between density, strain rate and ultimate bone strength the ranges of strain rate and density were** $10^{-4}\,\mathrm{s}^{-1}$ **to** $6.5 \times 10^{2}\,\mathrm{s}^{-1}$ **and** $1975.4\,\mathrm{kg.\,m}^{-3}$ **to** $2056\,\mathrm{kg.\,m}^{-3}$**, respectively. It is clear that the variation in ultimate strength as a result of strain rate is greater than the variation in ultimate strength as a result of density in the present sample.**

The relation developed by Carter and Hayes [88] (Eq.5.2) for human bone, slightly over-estimates ultimate strength, but results in a reasonable overall approximation of the

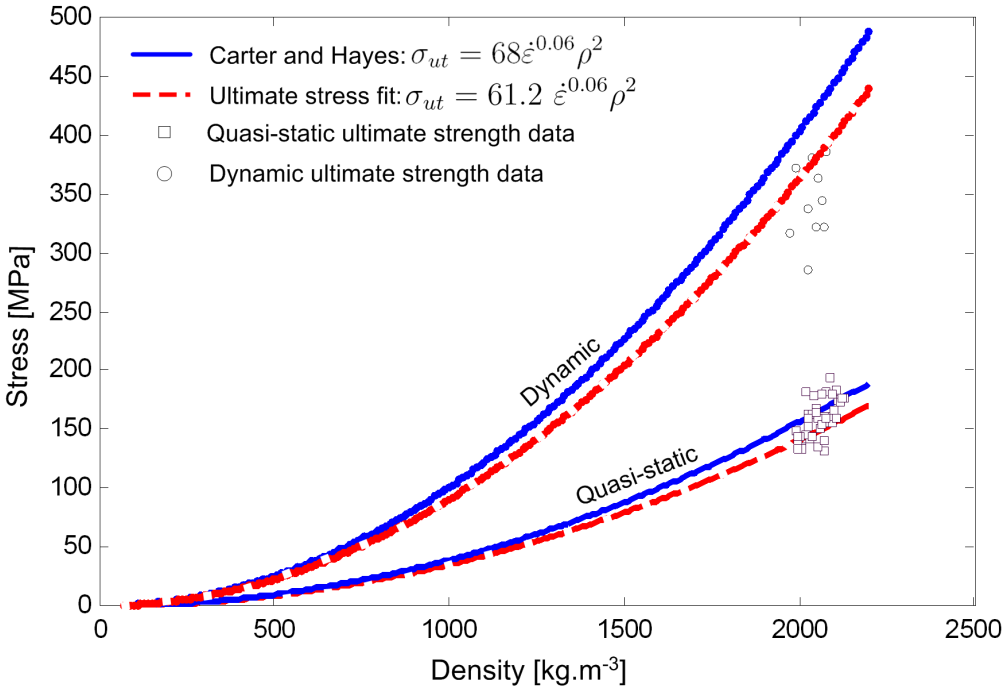

Figure 5.21: Comparison between quasi-static and dynamic ultimate strength as a function of strain rate and density

ultimate strength at both dynamic and quasi-static strain rates. The adapted strength relation for bovine cortical bone ((Eq.5.3) results in the best approximation of ultimate strength as a function of density and strain rate.

Research on the strain rate dependent properties of *cortical bone* does not conventionally include the additional influence of density on bone strength and response (as in the works of McElhaney[12], Crowninshield and Pope[14], Tanabe and Kobayashi [16] and Adharapurapu et al. [20]). **However, the relationship between density, strain rate and the ultimate strength and response of *cancellous bone* is well-addressed** by Shim et al.[21] and Carter and Hayes [88].

A limitation of the present study is that the density variation within an individual bone (and therefore the variation between specimens originating from the same bone) was not initially appreciated. Fresh bone density was therefore not correlated to the strength for each specimen that was exposed to strain rate dependent compression for any test series other than the series at $\dot{\varepsilon} = 10^{-4}\,\mathrm{s}^{-1}$ and $\dot{\varepsilon} = 6.5 \times 10^{2}\,\mathrm{s}^{-1}$. However, the fresh bone density was determined from the remaining specimens from each of the test bones (Bone 1 to 23). The average of the specimen densities was assumed to be the density of all the material originating from the individual test bone. Subsequent investigation has shown that the average density variation within specimens from the same bovine femur diaphysis (determined for 23 bones) is $29.2\,\mathrm{kg.\,m}^3$. The average density of the test sample for each test series was therefore calculated by assuming that there is no variation in the density of the specimens originating from the same femur. The average density of the bones used

for tests at the range of strain rates is summarised in Table 5.8.

Strain rate [s^{-1}]	Test bones	Fresh bone density [$kg.\,m^{-3}$]
$\dot{\varepsilon} = 10^{-4}$	Bones 1-11	2119.6
$\dot{\varepsilon} = 10^{-3}$	Bones 1-11	2119.6
$\dot{\varepsilon} = 10^{-2}$	Bones 1-11	2119.6
$\dot{\varepsilon} = 10^{-1}$	Bones 1-10	2112.2
$\dot{\varepsilon} = 2.5 \times 10^{2}$	Bones 1-9,11	2114.3
$\dot{\varepsilon} = 10^{3}$	Bones 14,16,17,19-23	2089.1

Table 5.8: Average fresh bone density for the bones used in strain rate dependent compression experiments

Fresh bone density vs. dry bone density

In keeping with the approach followed by Adharapurapu et al.[20] the difference between dry and fresh bone densities were determined to achieve a better estimation of the mass of water which is absorbed in the specimen structure. The water in the specimen does not contribute appreciably to its load bearing ability, therefore drying the specimen gives a better indication of the bone mineral density (but does not eliminate the effect of bone fat). The fresh and dry bone densities were determined for 18 specimens originating from 18 different bovine femurs after soaking in water for 48 hours.

The specimens were subsequently dried in air for 90 days. The results are listed in Table 5.9. The dry bone density was found to be 2.5% less than the wet bone density. Individual specimen density data is presented in Section A.4.1 of the Appendix.

	Fresh bone density [$kg.\,m^{-3}$]	Dry bone density [$kg.\,m^{-3}$]
Average density	2114.8	2061.9
Standard deviation	$\pm$48.9	$\pm$53.5
Minimum	2021.0	1957.1
Maximum	2194.6	2145.3

Table 5.9: Comparison between dry and fresh bone densities

The risk of bone fracture

Some injury criteria (IC), such as the lower extremity injury criteria IC for anti-vehicular (AV) landmine resistant vehicles (described in the AEP-55 standard [6] in Section 1.1) is based on an axial force threshold and an acceptable risk of bone fracture. The IC states an axial force threshold of 5400 N measured in the lower tibia load cell of a Hybrid III crash test dummy during an AV mine impact. This force is associated with a 10% incidence of

ankle/foot fracture which was determined from the PMHS tests conducted by Yoganandan et al. [7]. The formulation of such an IC requires bone fracture data to be expressed in terms of fracture risk.

Pithioux et al. [89] investigated the ultimate tensile stress of bovine cortical bone and expressed the probability of failure with a Weibull cumulative distribution (discussed in Section 2.7). This approach is applied to data in the present study. The expression for the Weibull cumulative distribution is given by:

$$P_R(\sigma_{ut}) = 1 - e^{-\frac{\sigma_{ut}}{\sigma_0}^m} \tag{5.6}$$

	σ_0 [MPa]	m
Quasi-static	183.9	6.7
Dynamic	404.0	13.4
Pithioux et al.[89] quasi-static	163.3	5.77

Table 5.10: Parameters for Eq.5.6 at quasi-static and dynamic strain rates

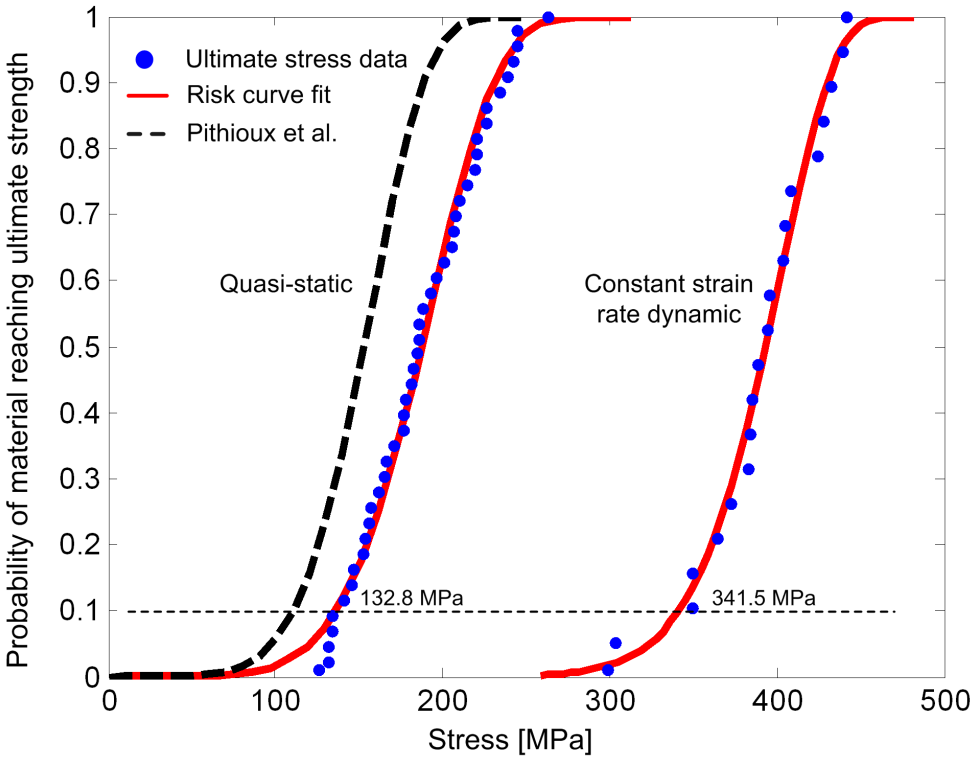

Figure 5.22: Risk curves for dynamic and quasi-static bone fracture

The ultimate stress data and calculated risk curves are plotted in Fig.5.22 along with the quasi-static risk curve by Pithioux et al.[89]. It is concluded that:

- **All bone specimens tested in quasi-static compression failed at a lower stress than any tested occurrence of dynamic failure.**

- There is a 50% chance of sample failure for a stress lower than 173.9 MPa and the risk curve predicts that failure is certain for a stress greater than 254.2 MPa.

- The quasi-static risk of fracture for bovine bone in compression is lower than the risk of fracture determined by Pithioux et al. [89] for bovine bone in tension. The ultimate stress corresponding to a 10% risk of quasi-static bone fracture is 110.6 MPa.

- At dynamic strain rates the stress values corresponding to a 50% and 100% risk of fracture are 393.1 MPa and 479.5 MPa respectively.

Recall that the lower extremity injury criterion (IC) for anti-vehicular (AV) landmine resistant vehicles is based on an axial force threshold (5400 N), measured in the longitudinal direction of the tibia, which represents a 10% risk of simple ankle/foot fracture for dynamic impact to the plantar foot surface. If the above findings from bovine cortical bone can be extended to human cortical bone the significance of these results with regard to the injury criteria for occupants in a landmine protected vehicle is that:

- **The ultimate stress corresponding to a 10% probability of dynamic bone failure ($\sigma = 341.5$ MPa) is approximately 2.6 times larger than the corresponding quasi-static stress ($\sigma = 132.8$ MPa) for a similar risk.**

- The dynamic risk curve is appropriate for estimating the risk of bone fracture for occupants subjected to an AV-mine blast in a conventional vehicle without blast protection. An unprotected structure would offer little resistance to the dynamic blast load, especially if the hull structure tears and allows penetration of the cabin. Under these conditions bone is able to resist a higher level of stress before the incidence of fracture. However, recall that bone is less resistant to deformation under dynamic loading.

- A protected vehicle hull would potentially decrease the velocity of the resulting compressive load on the occupant lower extremity. The appropriate curve for estimating the risk of fracture, could potentially be in the middle strain rate range (for which no risk of fracture data is available at present). A highly effective vehicle structure could even result in quasi-static loading on the lower limb. Under these conditions bone can sustain more deformation, but less stress as is apparent from the quasi-static risk curve.

5.2 Compression results for specimens with a radial orientation

Cylindrical specimens were machined from the mid-diaphyses of five additional bovine femurs. This time, the axis of the specimen was orientated perpendicular to the outer surface of the bone as shown in Figs.5.23(a) and 5.23(b).

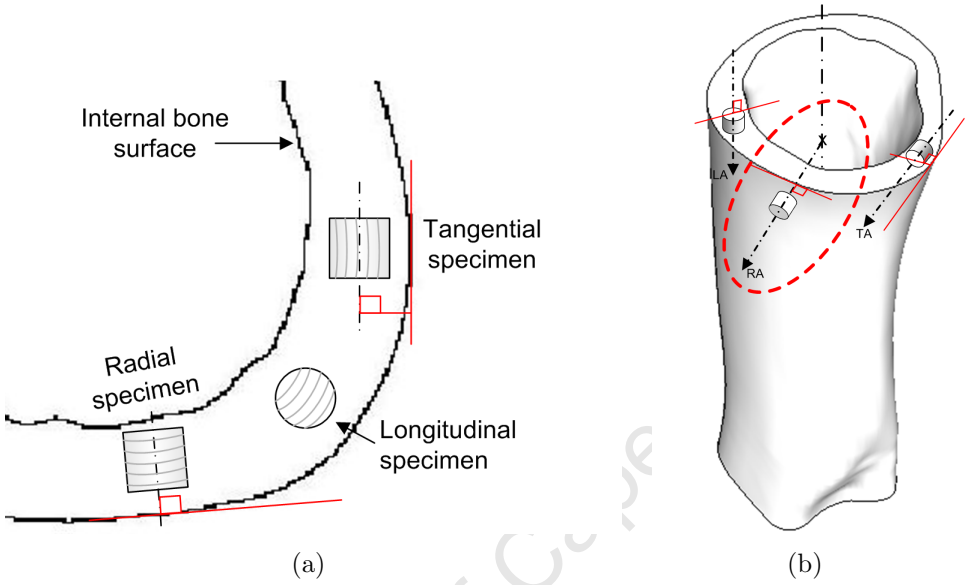

Figure 5.23: Orientation of the radial specimens within the (a) transverse section plane and (b) with respect to the longitudinal axis (LA), radial axis (RA) and tangential axis (TA) in the bone cortex

5.2.1 Quasi-static compression of radially orientated specimens

Quasi-static stress-strain response

The specimens were compressed at quasi-static strain rates between $\dot{\varepsilon} = 10^{-4}\,\mathrm{s}^{-1}$ to $10^{-2}\,\mathrm{s}^{-1}$. The quasi-static stress vs. strain curves are summarised in Fig.5.24 and the ultimate stress and strain are reported in Table 5.11.

$\dot{\varepsilon}$ [s^{-1}]	σ_{ut} [MPa]	ε_{ut} [$\mathrm{m.m}^{-1}$]	E [GPa]
$\dot{\varepsilon} \approx 10^{-4}$	165.64 ± 24.02	0.075 ± 0.02	3.63 ± 0.35
$\dot{\varepsilon} \approx 10^{-3}$	177.80 ± 17.01	0.084 ± 0.01	3.97 ± 0.80
$\dot{\varepsilon} \approx 10^{-2}$	175.17 ± 35.60	0.087 ± 0.03	3.77 ± 0.10

Table 5.11: Quasi-static compression test results for radial compression

The stress-strain curves in Fig.5.24 can be described in four phases:

- An initial linear elastic region where the stress increases proportionaly to the change in strain.
- A region of weak non-linearity beyond the yield point which is associated with damage or micro-cracking of the bone structure.
- **A region of plasticity, where the material deforms in compression without an increase in stress.**
- Fracture at varied amounts of plastic strain.

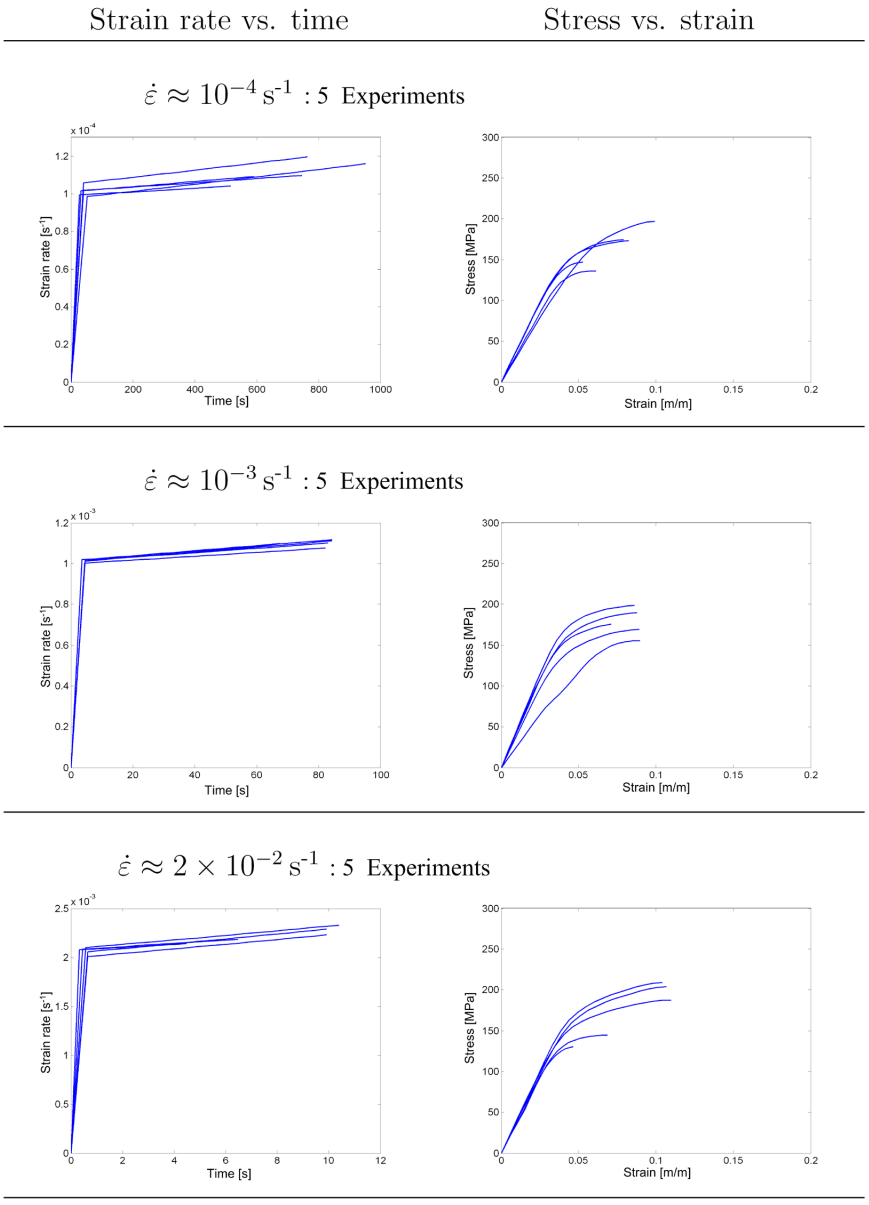

Figure 5.24: Quasi-static responses of radially orientated specimens

Radially orientated specimens displayed the lowest ultimate stress and strain at a strain rate of $10^{-4}\,s^{-1}$. The ultimate stress of fracture at $10^{-3}\,s^{-1}$ is slightly higher than the ultimate stress at $10^{-2}\,s^{-1}$. This is attributed to the fact that a single specimen from the sample at $\dot{\varepsilon} = 10^{-2}\,s^{-1}$ responded with a significantly lower stiffness and compressive strength. The particular stress-strain curve softens at two points before the incidence of fracture, which is indicative of damage to the bone structure. The uniqueness of this response is attributed to the possibility that a vascular canal in the particular specimen could incidentally have been aligned with one of the shear planes which arise in the course of a compression test (as is subsequently discussed as shown in Fig.5.26). This would be detrimental to the excellent ability of the plexiform microstructure to resist cracking across the vascular canals.

The ultimate properties of the individual specimen responses as well as enlarged views of the time vs. strain rate and stress vs. strain rate histories are reported in Appendix B. The stress-strain responses of the radial specimens are presented together in Fig.5.25 for the three rates of quasi-static compression. The responses overlap and do not follow well differentiated corridors. The increase in ultimate deformation with an increase in strain rate is apparent from Table 5.24.

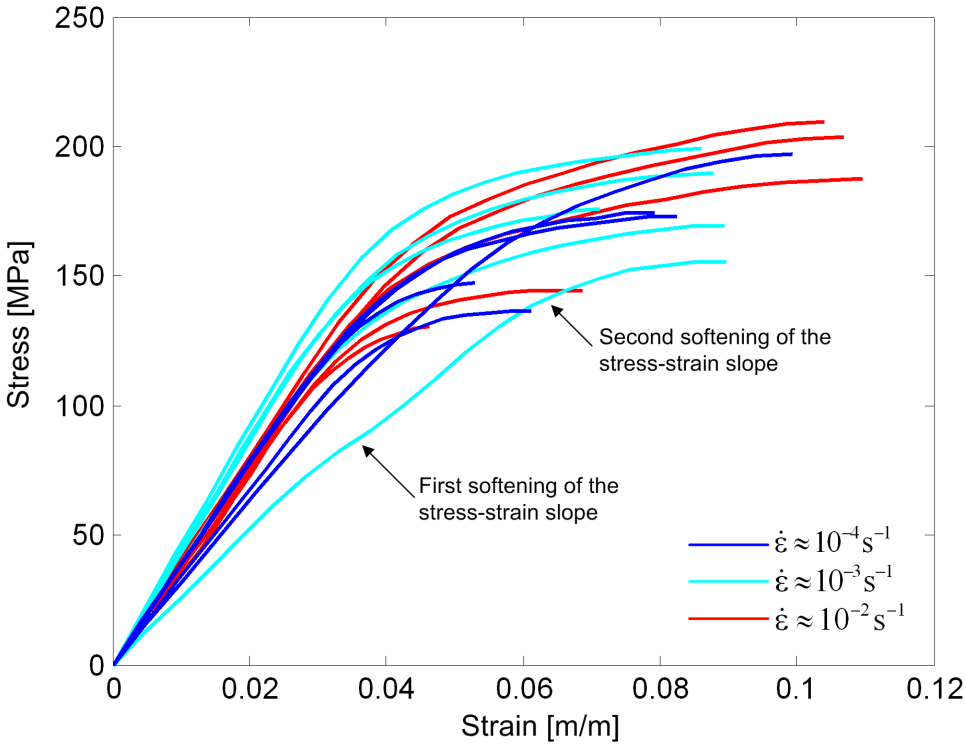

Figure 5.25: Stress-strain responses for radially orientated specimens at three rates of quasi-static compression

Radial specimen microstructure in quasi-static compression

Fig.5.26 shows an example of the microstructure of a radial specimen as a result of quasi-static compression. The specimen microstructure has a plexiform arrangement. The dominant direction of the plexiform porosity is orientated across the specimen axis. The following observations can be made with regards to the radial specimen histology:

- The osteons have a flatter (more squashed) appearance in their damaged state than as per normal.
- An hourglass pattern is visible as two diagonal shear bands have formed.
- The cracking of these specimens is far less apparent than those with longitudinal and tangential orientations. **It is postulated here that the plastic region with variable ultimate strains of fracture incidence can be attributed to the fact that the porosity runs perpendicular to the direction of compression and cracks do not have a weakness along which to propagate.** The incidence of fracture therefore depends on how successful the cell boundaries are at deflecting the cracks before the structure loses its load bearing ability. Fig.5.26(b) shows the region of twisted plexiform histology in the region of the shear zone.

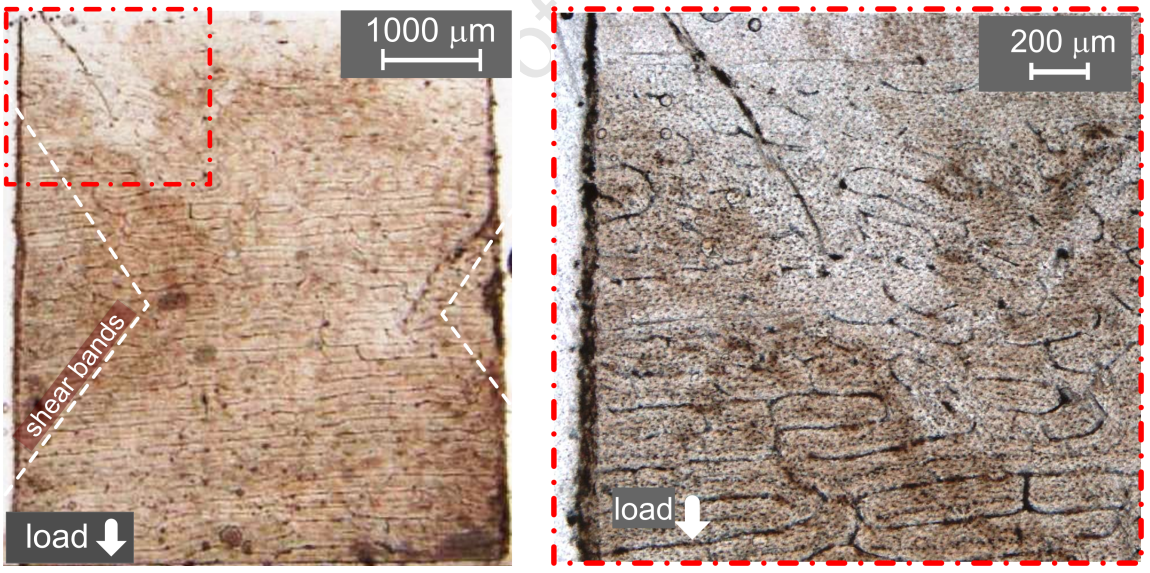

(a) fractured whole radial specimen (b) Magnified view of the crack

Figure 5.26: Radial specimen microstructure as a result of quasi-static compression.

5.2.2 Dynamic compression of radially orientated specimens

Radial compression experiments on the SHPB

The two SHPB experiments, developed for longitudinal specimen compression (in Section 4.3.7) were attempted with radial specimens. The presence of significant plastic deformation response prior to fracture incidence requires a test with a longer duration. In both instances this resulted in overlap of the incident and reflected stress waves in the input bar. These experiments are to be adapted in future to extend the test duration sufficiently to prevent the overlap of stress waves. However, high-speed camera images were obtained in the course of the attempted experiments.

High-speed camera images of radially orientated specimens on the SHPB

When specimens are compressed they generally expand in the lateral directions, which causes an increase in cross sectional area. If the material is isotropic the specimen cross section will remain circular as the specimen is compressed. If the specimen is anisotropic, the resulting cross sectional area will be oval. The stronger material direction will show less deformation and is thus indicated by the direction of the smaller diameter of the squashed oval cross section.

These types of observations are difficult to make in bone because of the small amount of strain needed to fracture the specimens. Additionally, the material is somewhat porous which implies that the constant volume assumption does not hold completely, but neither does the constant area assumption (as is evident from high speed camera pictures). Furthermore, bone is a viscoelastic material, which implies that stresses relax and strains creep after they have been induced by compression tests. The cross-section might therefore not retain its fully deformed shape long enough for post-experimental investigation as a result of short-term relaxation behaviour.

Fig.5.27 shows photographs of the progressive compression of radially orientated bovine cortical bone specimens between the input and transmitter bars of the SHPB system. The input bar is located towards the left of the photographs. The relative time frames of the photographs are specified above each picture in the film strip. Note that the current filming set-up does not have a synchronised triggering ability. The camera was triggered manually just before the SHPB striker was fired. The time frames reported here can therefore not be connected to events on the stress-time curve, but serve merely as an illustration of the relative time of the course of events observed on the photographs.

The test on Bone 26 shows complete fracture of the specimen. Observe that the specimen fractures on two opposing sides (at the top and the bottom of the specimen in each frame). A core of material remains intact in the centre and appears to span the entire width of the specimen. This implies that anisotropy could be present in the specimen and that the weaker material orientation lies in the top-down direction of the photo frame.

Lower magnitude tests were conducted to improve specimen preservation during fracture.

The test on Bone 27 in Fig.5.27 shows the specimen splitting, again on opposing sides, but only partially along the bone length. A possible explanation is that if the circumferential layers (tangentially orientated plexiform structure) of the bone cortex are compressed they will expand laterally. The blood vessels form a weak channel between these consecutive layers and for cracks to propagate. The material will crack first in the weakest material orientation, which is roughly found on opposing sides of a cylindrical specimen. This same phenomenon was observed in two more test cases (out of the total of five) where two sections of bone will fracture out on diametrically opposing sides of the specimen. The crack is arrested and does not continue along the entire specimen length.

Photographs of the initial states of specimens from Bone 26 and Bone 27 were included for an additional reason. The initial photographs certainly correlate to a time before loading because a SHPB test at this strain rate only lasts between 50 to 100 μs and visual evidence of fractures only appear in the photographs after 285 μs and 243 μs respectively. It appears that there is a difference between the initial and loaded area of the specimens. Due to a lack of visual processing techniques and triggering synchronisation the extent of the change in area can regretfully not be assessed and linked to the stress-time history. The change in area is not likely to affect the stress in the specimens severely, because of the small strains at which specimens fracture. These images do seem to indicate that the constant area assumption, although conservative, might not be the appropriate assumption when computing the stress in bone specimens.

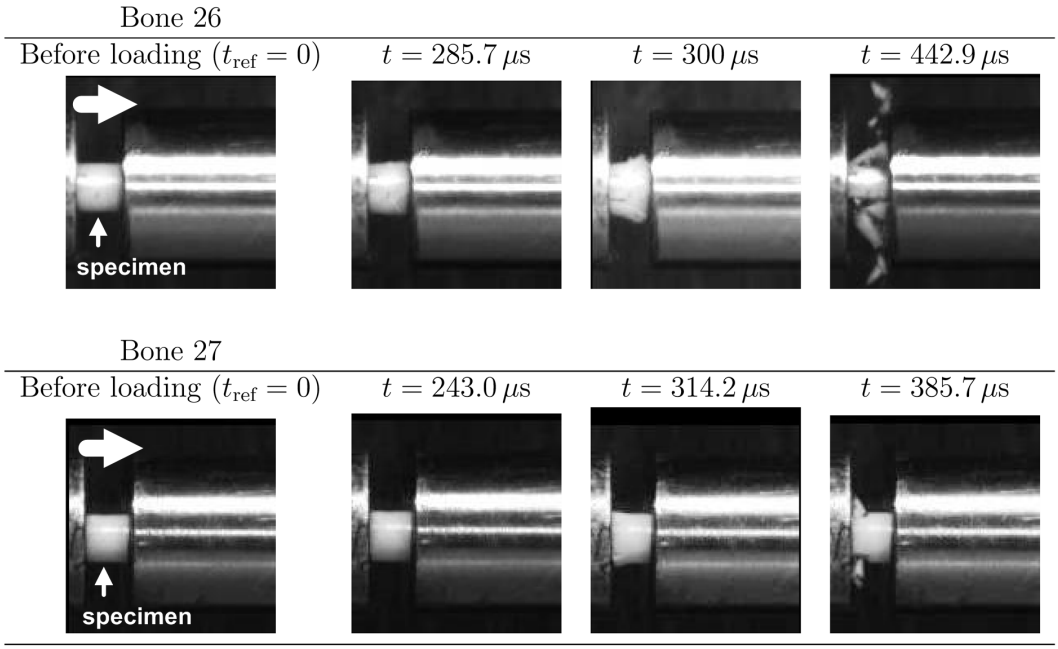

Figure 5.27: High-speed camera pictures of radial specimen compression on the SHPB

5.3 Compression results for tangentially orientated specimens

An investigation of bone response was conducted where the specimen was orientated tangentially to the outer surface of the bone as shown in Figs.5.28(a) and 5.28(b). Cylindrical specimens were machined from the mid-diaphyses of five bovine femurs.

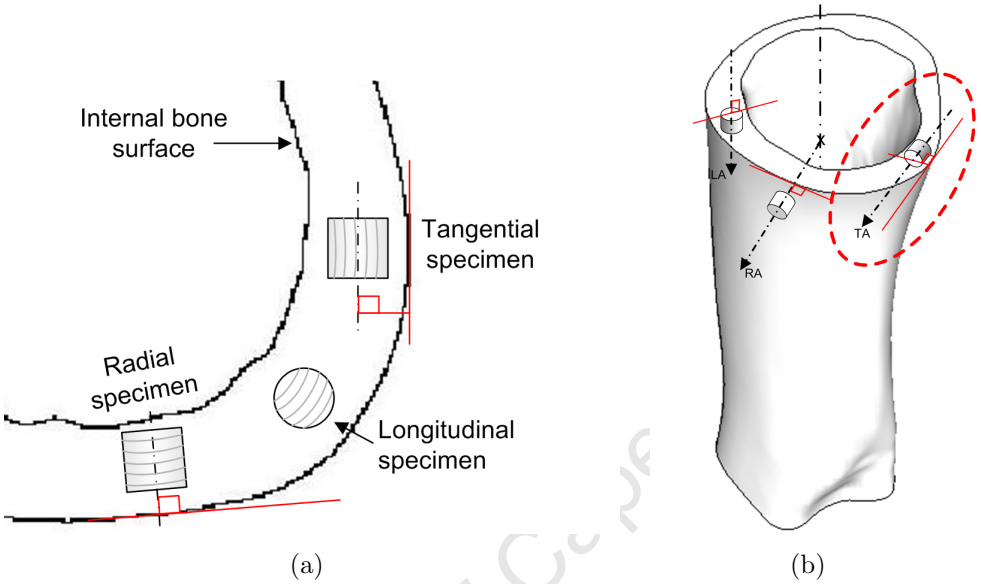

Figure 5.28: Orientation of the tangential specimens within the (a) transverse section plane and (b) with respect to the longitudinal axis (LA), radial axis (RA) and tangential axis (TA) in the bone cortex

5.3.1 Quasi-static response of tangentially orientated specimens

Quasi-static Stress-strain response

Five compression tests were conducted on the Zwick Universal Test Machine at three quasi-static strain rates. The quasi-static specimen responses are reported in Fig.5.29. **Significant strain rate sensitivity is detected in the response of tangentially orientated bovine bone specimens at quasi-static strain rates.** The ultimate properties and Young's moduli for these experiments are reported in Table 5.12. Both the ultimate stress and stiffness of the response increases consistently with strain rate. The ultimate strain of fracture for the faster quasi-static experiments is slightly higher than the ultimate strain for compression ate $\dot{\varepsilon} = 10^{-4}\,\mathrm{s}^{-1}$.

$\dot{\varepsilon}$ [s^{-1}]	σ_{ut} [MPa]	ε_{ut} [$m.m^{-1}$]	E [GPa]
$\dot{\varepsilon} \approx 10^{-4}$	121.4 ± 11.6	0.022 ± 0.00	5.65 ± 0.54
$\dot{\varepsilon} \approx 10^{-3}$	130.2 ± 6.6	0.026 ± 0.01	5.85 ± 0.56
$\dot{\varepsilon} \approx 10^{-2}$	151.4 ± 7.8	0.026 ± 0.00	6.62 ± 0.21

Table 5.12: Quasi-static compression test results for tangential specimens

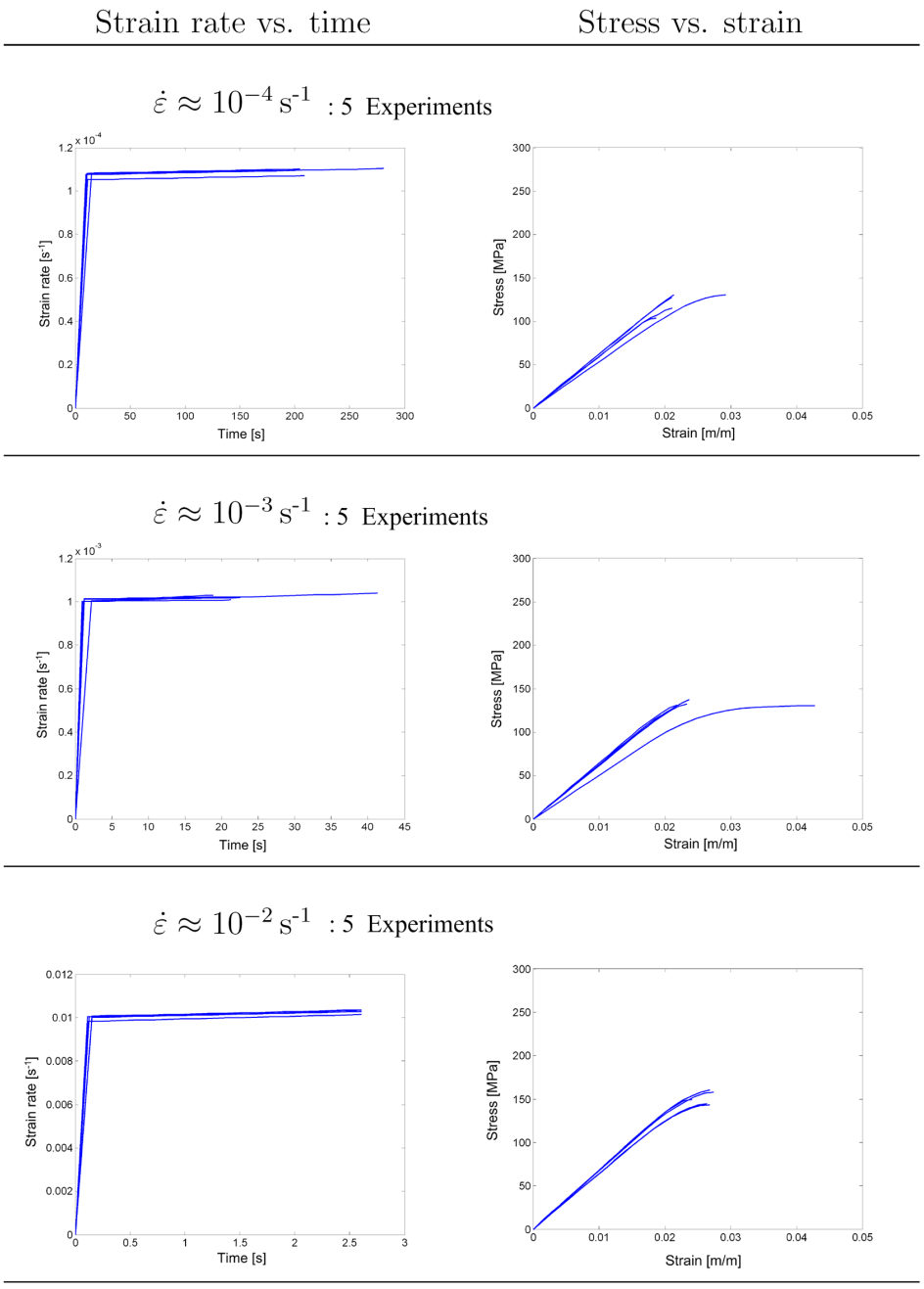

Figure 5.29: Quasi-static responses for tangentially orientated specimens

5.3.2 Dynamic response of tangentially orientated specimens

Tangential compression experiments on the SHPB

An investigation of tangentially orientated specimens was conducted on the 20 mm diameter SHPB. The bars were impacted by the tapered striker that was designed for the constant strain rate compression of longitudinal specimens in Section 4.3.7. The test duration required to fracture tangentially orientated specimens is slightly longer than the duration of longitudinal compression experiments. A slight overlap occurred between the incident and reflected waves in some cases. However, the overlap was short enough to extract preliminary data on the dynamic response of tangentially orientated specimens.

Fig.5.30 presents the incident and reflected pulses as well as the stress vs. strain and strain rate responses of tangentially orientated specimens. **A key observation from Fig.5.30(b) is that the strain rate of the dynamic compression experiment is approximately constant at $\dot{\varepsilon} \approx 3.3 \times 10^2\,\mathrm{s}^{-1}$. Therefore, the same striker that effectively shaped the input pulse for the dynamic compression of longitudinal specimens is also effective for tangentially orientated specimens.** Four successful

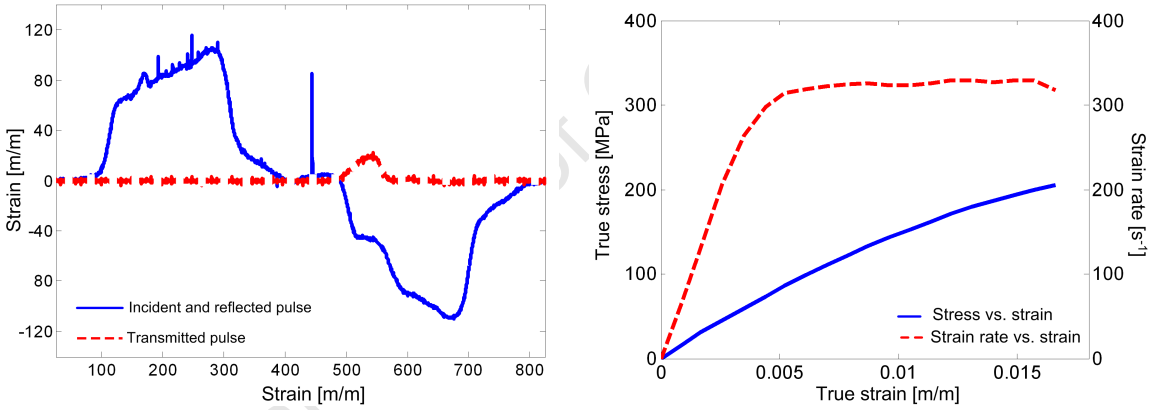

(a) (b)

Figure 5.30: (a) The incident, reflected and transmitted waves and (b) stress vs. strain and strain rate response of tangentially orientated specimens in dynamic compression on the SHPB

compression experiments were conducted on the SHPB at $\dot{\varepsilon} = 3.3 \times 10^{-2}\,\mathrm{s}^{-1}$. The dynamic stress-strain responses and ultimate properties are presented in Fig.5.31 and Table 5.13. There is significant variation between the respective dynamic stress-strain responses. The majority of the specimen response is initially linear elastic. Recall that the initial data is only valid beyond specimen equilibrium. The response is subsequently less stiff than the initial phase and highly non-linear. The slope of the stress-strain curve continues to deteriorate (in some cases almost completely) before ultimate fracture.

One of the dynamic response curves varies significantly from the others in that the response curve softens from the onset of compression. It is possible that the microstructural

orientation of the specimen in question varied from the other specimens in the small sample, such that the circumferentially orientated vascular canals were well-aligned with the shear planes which arise in the course of the compression experiment. This phenomenon is illustrated in Fig.5.40(a) and discussed in Section 5.4.3.

$\dot{\varepsilon}$ [s^{-1}]	σ_{ut} [MPa]	ε_{ut} [$m.m^{-1}$]
$\dot{\varepsilon} \approx 3.3 \times 10^2$	217.67 ± 19.81	0.0147 ± 0.00

Table 5.13: Dynamic test results for tangential specimen compression

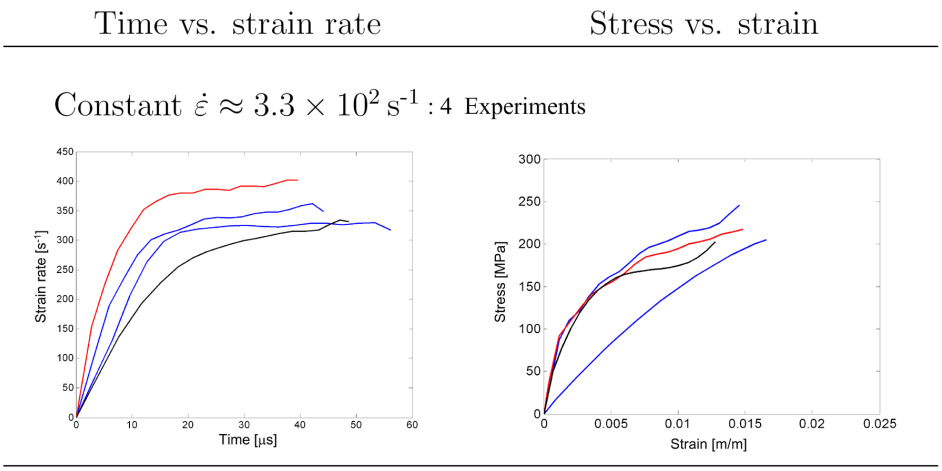

Figure 5.31: The dynamic responses of tangentially orientated specimens

The ultimate properties of the individual tangential specimen responses, as well as the stress-strain curves and strain rate histories are reported in Appendix C.

High-speed camera images of the dynamic compression of tangential specimens on the SHPB

Fig.5.32 shows high-speed camera images that were taken during two SHPB compression tests on tangentially orientated bovine bone specimens. The input bar is located to the left of the images, with the specimen in the middle and the output bar on the right.

Both film strips show the formation of parallel shear- and V-type cracks. It appears that these cracks propagate all the way through the thickness of the specimen and give rise to shear planes that slide over each other as the material is squashed. The slipping planes skew the specimen to one side as the test progresses. None of the films investigated (a total of 4 tests) show evidence of the formation of a shear cone, which is associated with isotropic material behaviour. Results seem to indicate that the bone samples are stronger in one direction along the sample radius than the other or that the bone matrix

is predisposed to slip along a specific plane. Further investigation with a greater number of samples is required to establish if these observations are conclusive.

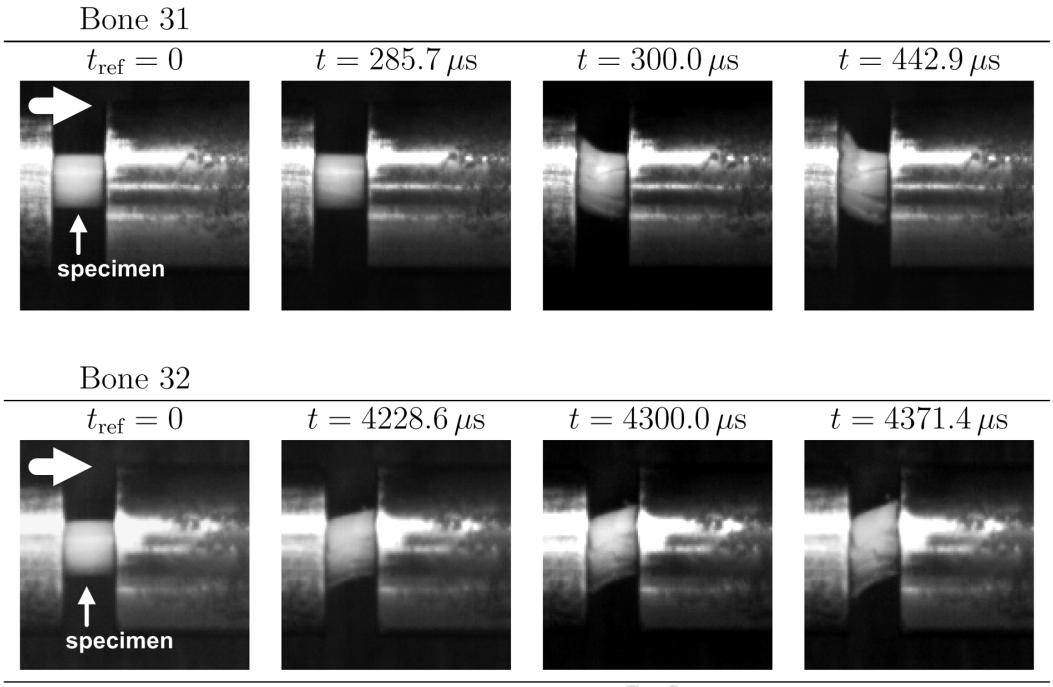

Figure 5.32: High-speed camera pictures of tangential specimen compression on the SHPB

5.3.3 Summary of tangential compression data

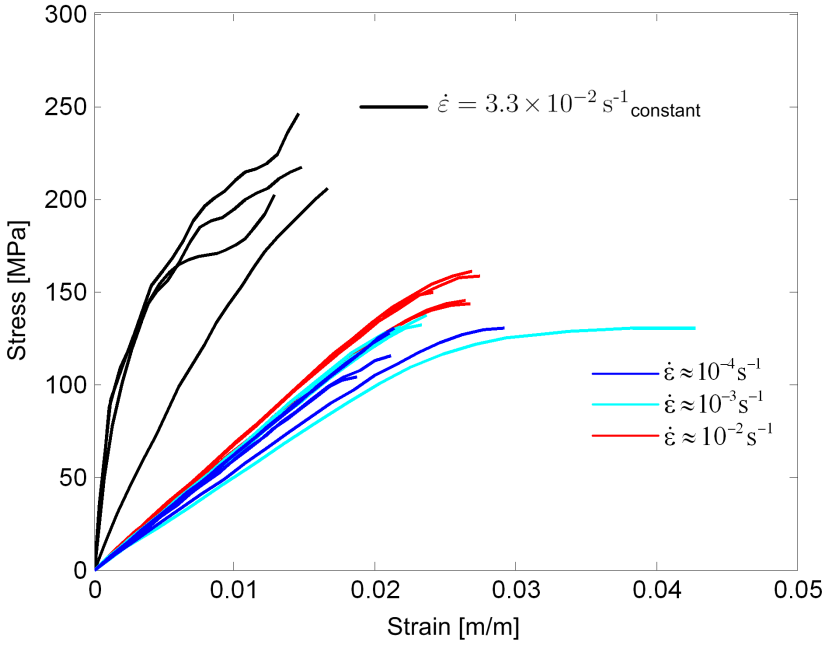

Figure 5.33: Summary of tangentially orientated specimen responses at quasi-static and dynamic strain rates

The stress-strain results for all quasi-static and dynamic strain rate compression tests on tangentially orientated specimens are combined in Fig.5.33. **Tangential specimens respond in two distinct corridors for quasi-static and dynamic compression.** This is similar to the observation for longitudinal specimens. The dynamic response corridor is significantly stiffer than the quasi-static one. The ultimate stress at fracture increases consistently with strain rate. As with the fracture of longitudinal specimens, the fracture of tangential specimens is more brittle at dynamic strain rates. Again, the ultimate strain was found to increase slightly with quasi-static strain rate and decrease significantly at dynamic rates of compression.

At both $\dot{\varepsilon} = 10^{-3}\,s^{-1}$ and $\dot{\varepsilon} = 3.3 \times 10^{2}\,s^{-1}$ responses were measured, which vary significantly from the responses of other specimens tested at the same strain rates. These variations are attributed to a the possibility that the orientation of the vascular canals in the particular specimens differed from the alignment in the majority of the specimens in the small sample. This indicates that care should be taken to ensure that respective tangential specimens have a vascular orientation which is as uniform as possible.

5.4 Summary of data in different orientations

5.4.1 Comparison of the quasi-static stress-strain response

The stress-strain responses of the radial, tangential and longitudinal specimens are presented for three quasi-static strain rates in Fig.5.34. For ease of interpretation the bone axis system is repeated in Fig.5.34(d). The following observations can be made with regards to the compressive responses of specimens from the three tested bone orientations:

- If the stress-strain behaviour in the longitudinal, radial and tangential orientations are unique if the responses are considered up to the point of fracture. Bovine cortical bone is therefore an anisotropic material.
- The response of the tangentially orientated specimens is the stiffest. Additionally, bone is the least resistant to fracture in this direction.
- The radial and longitudinal specimens respond with similar stiffness to quasi-static compression, before the onset of damage in the respective orientations. The yield point of radially orientated specimens is lower than the yield point of longitudinal specimens.
- The greater part of the longitudinal and tangential stress-strain responses is linear elastic. Softening of the stress-strain curves, which is associated with damage to the specimen structure, occurs just before fracture.
- The stress-strain response of radially orientated specimens is initially elastic and displays a region of varied plasticity beyond the point of failure (yield). As a result of this the ultimate stress of the radially orientated specimens is greater than that of the longitudinal and tangential specimens. If the microstructure of radial specimens is considered, this can be explained by the fact that the vascular canals (a weakness in the bone structure) lie across the specimen cracks cannot grow through the specimen so readily. The incidence of fracture therefore depends on how successful the cell boundaries are at deflecting the cracks before the structure loses its load bearing ability. This would explain why there is a variation in the ultimate strain of radial specimens beyond the yield point.
- The above mentioned observations remain consistent for the three quasi-static strain rates that were investigated.

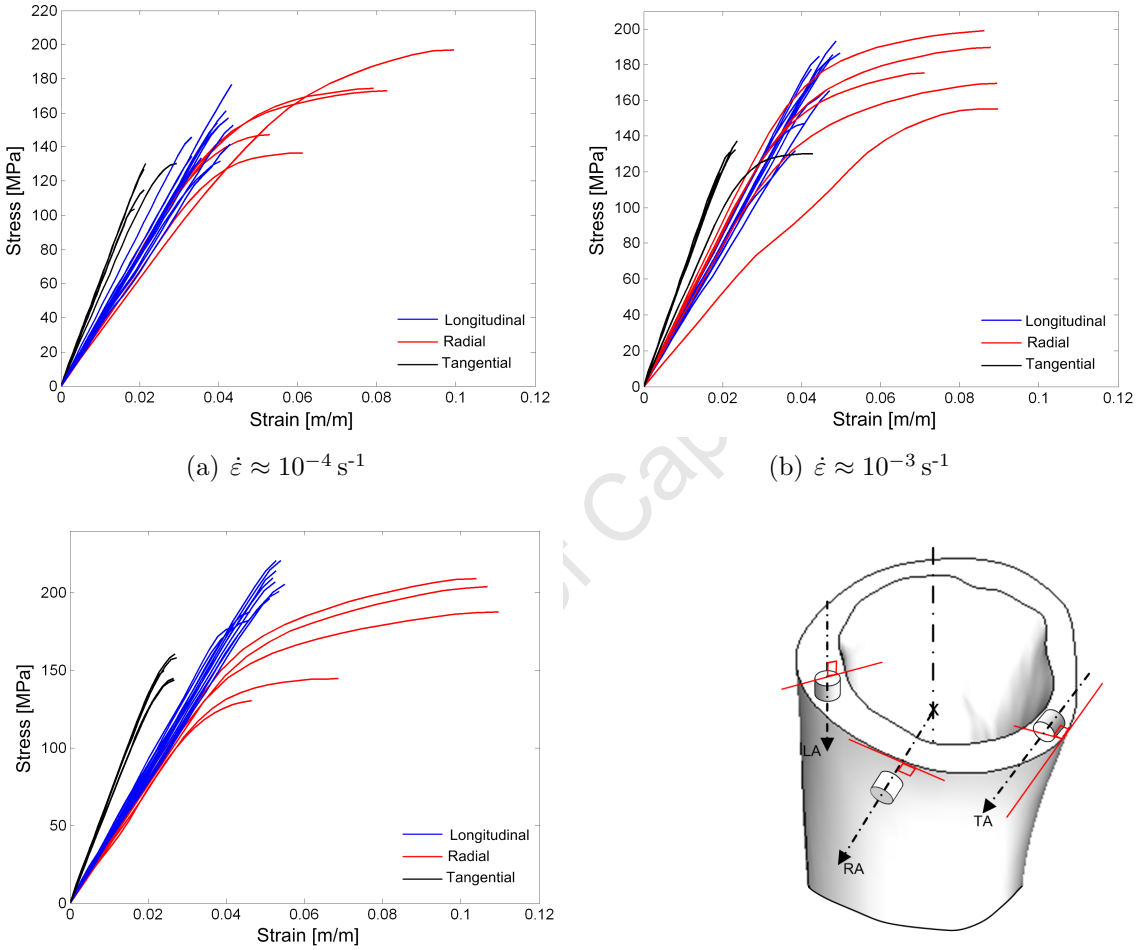

(a) $\dot{\varepsilon} \approx 10^{-4}\,\mathrm{s}^{-1}$

(b) $\dot{\varepsilon} \approx 10^{-3}\,\mathrm{s}^{-1}$

(c) $\dot{\varepsilon} \approx 10^{-2}\,\mathrm{s}^{-1}$

(d) Specimen orientation

Figure 5.34: A comparison of stress-strain responses in different orientations. The bone axis system with the longitudinal axis (LA), radial axis (RA) and tangential axis (TA) is included for the purposes of interpretation.

5.4.2 Comparison of the quasi-static risk of fracture

The quasi-static risk of fracture was determined for the specimens with tangential and radial orientations to supplement the discussion of longitudinal fracture risk in Section 5.1.4. The ultimate stresses determined from the 15 quasi-static experiments at three strain rates, were combined to give a preliminary estimate of the quasi-static risk in the radial and tangential orientations. The cumulative Weibull distribution (repeated in Eq.5.7), used by Pithioux et al. [89] is applied to relate the stress in the specimen to the risk of fracture.

$$P_R(\sigma_{ut}) = 1 - e^{-\frac{\sigma_{ut}}{\sigma_0}^m} \tag{5.7}$$

The parameters for the quasi-static risk curves in the tangential, radial and longitudinal orientations are listed in Table 5.14.

	σ_0 [MPa]	m
Tangential orientation	138.7	10.6
Radial orientation	181.7	6.9
Longitudinal orientation	183.9	6.7

Table 5.14: Parameters for the quasi-static risk of ultimate fracture (Eq.5.7 in the tangential, radial and longitudinal orientations of the cortical bone matrix)

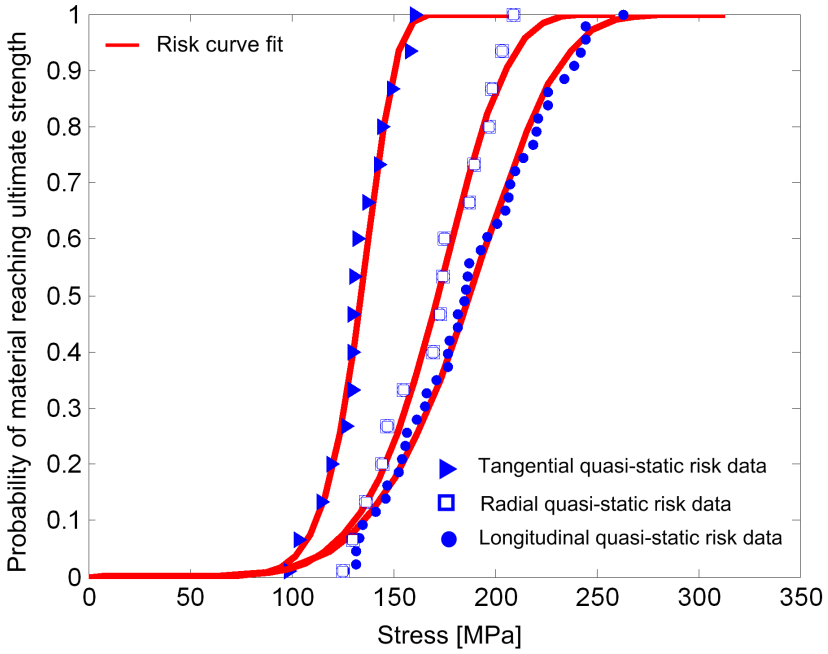

Figure 5.35: Quasi-static fracture risk of tangential, radial and longitudinally orientated specimens

Of the three orientations considered, bovine cortical bone is the weakest in the tangential orientation. This is possibly attributed to the alignment of the porosity in the bone matrix with the shear planes that arise during the compressive loading of tangential specimens (as explained in subsequently in Section 5.4.3). Specimens in the longitudinal orientation were able to resist the most stress before fracturing under quasi-static loads.

5.4.3 Microstructure and macroscopic quasi-static fracture of specimens with longitudinal, radial and tangential orientations

Longitudinal specimen fracture

Fig.5.36 presents a diagram of simplified longitudinal specimen microstructure. The cross-sectional view of the longitudinal specimen is located in the longitudinal section plane, where the blood vessels of the associated laminar microstructure is orientated in the same direction as the longitudinal bone axis. In the case of a reticular structure the orientation of the osteocytes (bone cells) are in the longitudinal direction, but the blood vessels have a random orientation. Shear-type V-fractures were observed in the lengthwise cross-section of quasi-statically loaded specimens. A repetitive angle of the diagonal shear fractures could not be identified from present data. The shear cracks propagate diagonally across the bone porosity, but sometimes deflect lengthwise along the blood vessels if the specimen has a laminar micristructure in the longitudinal plane.

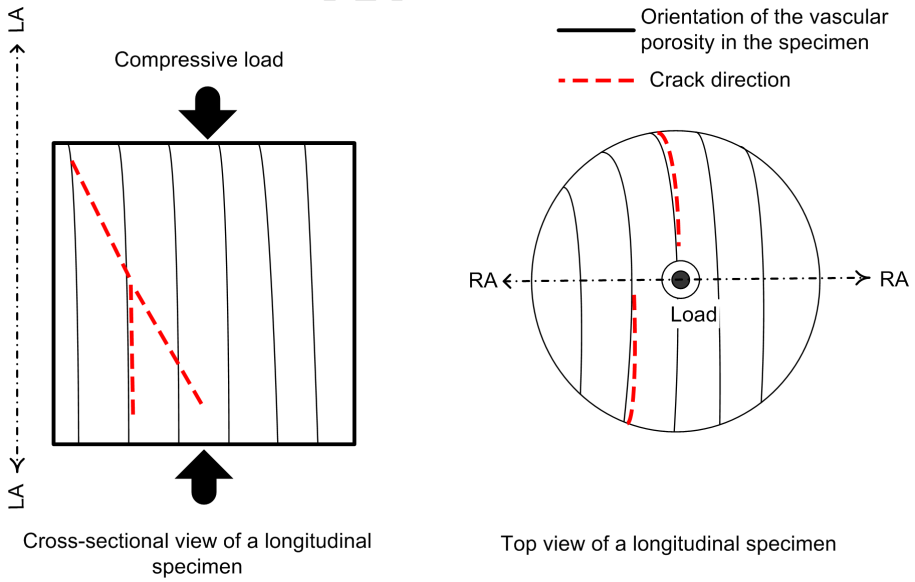

Figure 5.36: Simplified longitudinal specimen microstructure and crack patterns. The longitudinal bone axis (LA) and Radial axis (RA) are indicated to orientate the sections in terms of the whole bone coordinate system.

Additional micrographs of fracture bovine bone histology are presented in Section A.3 of the Appendices. The shear crack of a single specimen with a reticular microstructure runs more or less from corner to corner along the 45° shear plane (Fig.A.10(e)).

The top plane (circular face) of a longitudinal specimen comprises of the same microstructural arrangement as the transverse plane of the femur from which it originates. An investigation of fractured longitudinal specimens as a result of quasi-static compression shows that the cracks in this plane run in the same direction as the dominant direction of the blood vessels of the plexiform arrangement (this observation was discussed in Section 5.1.2). Figs.5.37(a) and 5.37(b) present a lengthwise side view and a top view of the shear fracture of a longitudinal specimen.

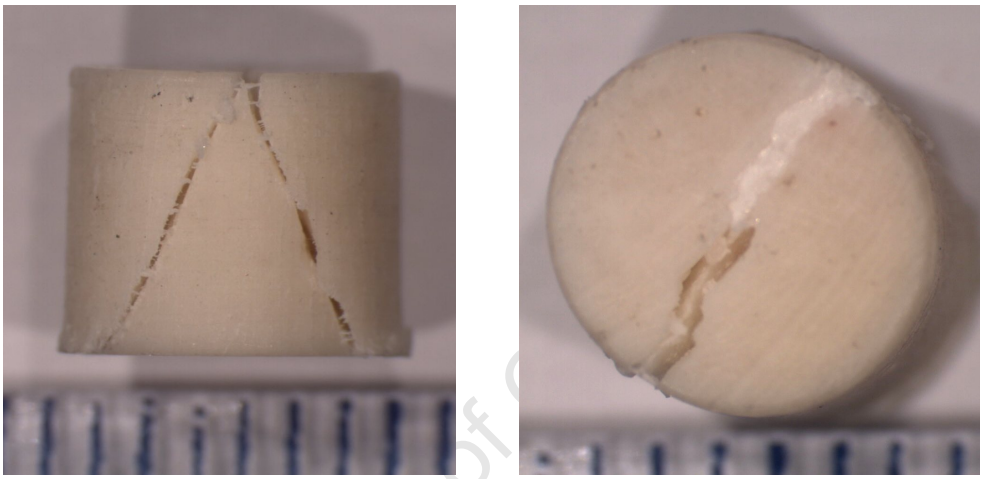

(a) Lengthwise side view (b) Top view

Figure 5.37: Macroscopic bone failure for longitudinal specimens. (a) A V-shaped shear crack across the longitudinal bone porosity. (b) A top view of the shear crack which runs in the direction of the concentric vascular canals in the transverse section of a bovine femur

Radial specimen fracture

Radially orientated specimens showed a resistance to cracking when exposed to quasi-static compression. The direction of the vascular porosity is perpendicular to the direction of the loading. Additionally the porosity of the specimen is poorly aligned with the potential shear planes, which would explain the structure's resistance to cracking. The microstructure of radial specimens exposed to quasi-static compression was discussed in Section 5.2.1, where the hourglass shape, which results from two shear planes, is apparent. The macroscopic investigation of fractured radial specimens (with apparent cracks) show diagonal cracks with steps that sometimes run perpendicular to the specimen length as indicated in Fig.5.38(a). Additionally little ridges are observed that run perpendicular to the specimen length.

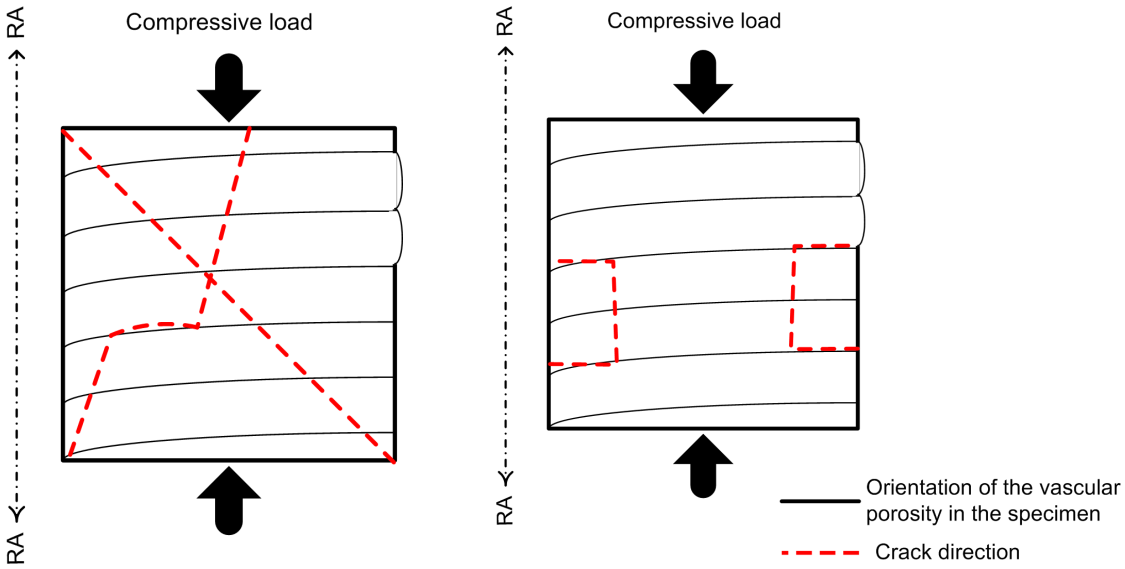

(a) Quasi-static fracture (b) Dynamic fracture

Figure 5.38: Simplified microstructure and crack patterns for radially orientated specimens in quasi-static and dynamic fracture. The radial axis (RA) is indicated to orientate the specimens relative to the whole bovine femur

The resistance of radial specimens to cracking enabled the recovery of some specimens that fractured dynamically in the SHPB. As discussed in Section 5.2.2 a number of cases were observed where two diametrically opposed fragments fracture sideways out of the bone specimen such (as indicated in schematically in Fig.5.38(b)). Photographs of radial specimens that fractured in quasi-static and dynamic compression are respectively presented in Figs.5.39(a) and 5.39(b).

(a) Quasi-static (b) Dynamic

Figure 5.39: Photographs of (a) quasi-static and (b) dynamic fracture patterns in radially orientated specimens

Tangential specimen fracture

A schematic of the simplified microstructure of tangential specimens is shown in Fig.5.40(a). The blood vessels in the transverse section plane of the bovine femur are slightly curved such that their dominant orientation forms concentric rings between the inner- and outer bone surfaces. The combined effect of the inaccuracy of specimen machining and the slight curvature of these blood vessels could mean that the blood vessels are not orientated parallel to the straight specimen edges. More importantly, the blood vessels could be arranged diagonally across the specimen length which would increase their alignment with the shear planes that develop during quasi-static compression. If the vascular porosity in the transverse plane is a weakness in the bone matrix, shear cracks should develop in these planes. Fig.5.40(b) presents an example of a tangential specimen that fractured in quasi-static compression, which shows several slightly curved cracks that run parallel to each other diagonally across the specimen length. **This observation indicates that the alignment of the vascular porosity with the stress concentration in the shear plane results in cracks in the plane of the vascular porosity in the tangential specimen.**

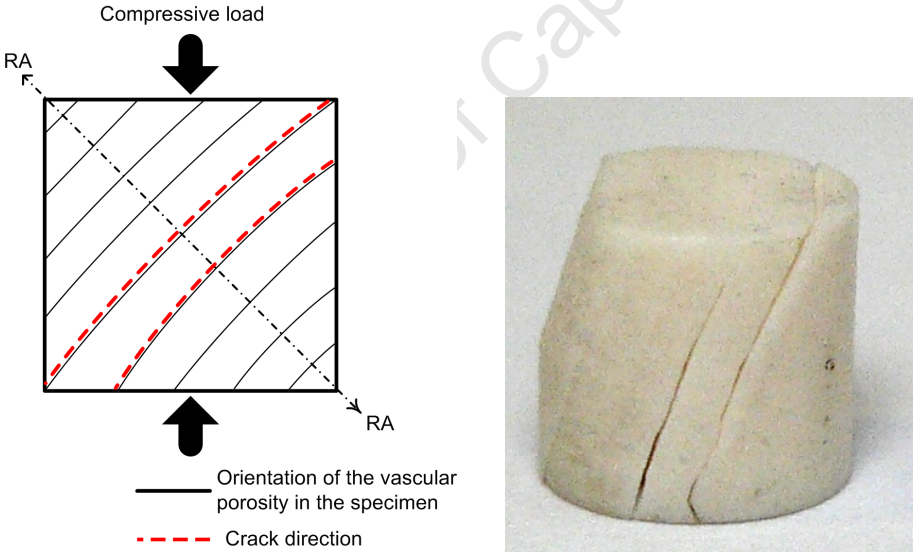

(a) (b)

Figure 5.40: (a) Simplified microstructure and crack patterns for tangentially orientated specimens in quasi-static compression. The radial axis (RA) is indicated to orientate the specimens relative to the whole bovine femur. (b) A photograph of a tangential specimen that fractured as a result of quasi-static compression

Concluding remarks on specimen fracture

The discussion on the fracture and response of longitudinal, radial and tangential specimens has confirmed that bovine femoral cortical bone is anisotropic. The compressive response is strain rate dependent in all the investigated orientations. Furthermore the fracture of bovine cortical bone is influenced by the underlying microstructure. Observations from this study indicate that the tangential porosity in the transverse section plane is associated with a weakness in the bone matrix for the following reasons:

- An investigation of fractured longitudinal specimens as a result of quasi-static compression shows that the cracks in the transverse section plane are orientated in the same direction as the dominant direction of the blood vessels of the plexiform arrangement (Fig.5.7(a)).

- Radially orientated specimens were resistant to cracking when exposed to quasi-static compression. In this case the direction of the vascular porosity is perpendicular to the direction of the loading, therefore the porosity of the specimen is poorly aligned with the potential shear planes (Fig.5.26).

- Quasi-static compression of tangential specimens resulted in several slightly curved cracks that run parallel to each other diagonally across the specimen length. The slight curvature and concentric pattern of the blood vessels in the transverse section plane correspond to the parallel crack pattern observed in fractured specimens. The alignment of the vascular porosity with the shear stress concentration planes results in parallel cracking of the specimen in those planes.

The above observations are preliminary and remain to be confirmed by a thorough microstructural investigation of the quasi-static fracture of bovine cortical bone specimens in different orientations. The preservation of specimens in the course of dynamic compression tests on the SHPB could potentially aid in the understanding of the vast difference between the quasi-static and dynamic response corridors that are measured in strain rate dependent compression.

Chapter 6

Constitutive Model

This chapter discusses the model that was implemented to simulate the response of bovine cortical bone tissue in longitudinal compression. The model developed here is designed to adjust the material response over a wide range of strain rates. It could be argued that it is more optimal to approximate the response of bone material by separate models for quasi-static and dynamic compression. The reasons for developing a model with the capability to simulate all the tested strain rates are as follows:

- The ultimate use of the bone model is to model the response of the human skeleton in armoured vehicles. These vehicles are potentially exposed to both ballistic impacts and crash. The direct application of these loads to the human body would certainly be of a dynamic nature.

- Various structures are instituted in armoured vehicles to protect the vehicle occupants. These devices are designed to absorb impact energy, often by stretching out the load over a longer period of time. This affects the strain rate at which the body is loaded and potentially slows the load down to quasi-static rates.

- It is possible that the bone material can experience different strain rates of deformation in its loading history. For instance, during an AV mine detonation the energy absorbing structure in the vehicle floor could initially absorb the blast energy, reach its full capacity and be penetrated. The resulting rate of deformation of the bones in the occupant limbs could therefore be quasi-static and subsequently dynamic.

- In the light of the present data (presented in Chapter 5) the differentiation of bone response prior to failure at different quasi-static strain rates does not seem essential (Fig.5.13). The Young's modulus does not vary drastically in the quasi-static strain rate regime under consideration (between 3.88 GPa and 4.05 GPa from Table 5.1). The onset of damage and the ultimate properties of bovine bone exhibit significant strain rate dependency at quasi-static strain rates which can be accounted for with the relevant failure or damage models. However, this observation is not in agreement

with the work of Adharapurapu et al.[20] which reports a much more significant variation with quasi-static strain rate (Fig.5.14). In addition a significant variation in bone properties is expected for human bone at quasi-static strain rates such as illustrated by the work of McElhaney [12]. Therefore, it is elected here to include the differentiation of quasi-static response prior to the onset of damage in the constitutive modelling of bovine cortical bone in strain rate dependent compression.

Previous chapters have highlighted that bone is a viscoelastic material which responds in a highly strain rate dependent fashion, becoming stiffer and more brittle as the load speed increases. The experimental programme was designed to illuminate these characteristics. The discussion of this chapter is centred around the selection of a viscoelastic model and identification of model parameters that represent the data from the experimental study accurately. Furthermore to extend the selected viscoelastic model to an isotropic 3-D constitutive relation that can be implemented to model bone material in finite element models (FEM).

The interpretation of viscoelastic models as spring-damper systems was discussed in Section 2.5.2 along with the basic model responses of the Maxwell and Voigt elements. The discussion additionally eluded to the fact that realistic materials can be approximated by a combination of Maxwell and Voigt elements in series and parallel. Bone has mostly been modelled by a single Voigt element such is apparent from the studies of Tennyson et al.[17] and Tanabe and Kobayashi [16]. The models are chosen by curve-fits of the stress-strain curves. The works of Tanabe and Kobayashi [16], Tennyson et al.[17] and Shim et al.[21] use the addition of non-linear strain and strain rate dependency as an alternative means to tailor the model response without adding an extra Voigt or Maxwell element. Shim et al. [21] developed a Voigt and non-linear Maxwell element in parallel to model the response of cancellous bone from the cervical spine at a large range of strain rates in compression. This model was extended from 1-D (Eq.2.30) to 3-D (Eq.2.33) such that it contains the 1-D constitutive relation as a special case (Section 2.5.2). In this chapter it will be shown that Eq.2.33 is not frame invariant in its current form. An alternative isotropic 3-D constitutive relation is developed which allows invariance to be recovered.

The goals of this chapter are therefore:

- To develop the basic responses of linear and non-linear Maxwell and Voigt models and to reproduce the models used by Tanabe and Kobayashi [16], Tennyson et al.[17] and Shim et al.[21].

- Compare the performances of these models and evaluate their ability to represent the experimental response of bovine cortical bone.

- To recommend the most suitable model and model parameters for the constitutive modelling of bovine bone in strain rate dependent compression.

- To extend the selected viscoelastic model to an isotropic 3-D constitutive relation that can be implemented to model bone material in finite element models (FEM).

6.1 Voigt and Maxwell models in parallel

A spring-damper presentation of the combination of the Voigt and Maxwell models in parallel is shown in Fig.6.1. If a finite strain, ε, is applied to the model the stress is found

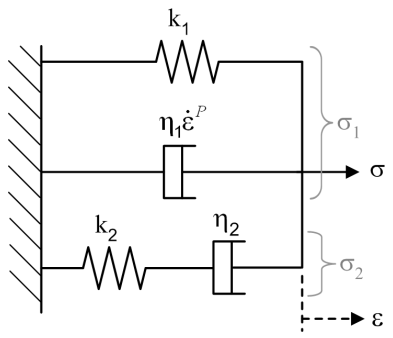

Figure 6.1: A Voigt and Maxwell element in parallel

by superposition of the stress contributions of the Maxwell and Voigt elements. It follows that the stress rate is the cumulative result of the respective Maxwell and Voigt time differentials.

$$\sigma = \sigma_1 + \sigma_2 \tag{6.1}$$

Thus

$$\dot{\sigma} = \dot{\sigma}_1 + \dot{\sigma}_2 \tag{6.2}$$

In order to express the model stress in terms of the total stress, σ, and total strain, ε, the respective stress rate contributions of the Maxwell and Voigt models are substituted into the stress rate relation (Eq.6.2). The Voigt stress rate contribution of the Voigt stress is:

$$\dot{\sigma}_1 = k_1\dot{\varepsilon} + \eta_1\ddot{\varepsilon} \tag{6.3}$$

The Maxwell stress-strain relation is rearranged to make $\dot{\sigma}_2$ the subject.

$$\dot{\sigma}_2 = k_2\dot{\varepsilon} - \frac{k_2}{\eta_2}\sigma_2 \tag{6.4}$$

The Maxwell stress term, σ_2, on the right hand side is eliminated by substitution of the Voigt stress relation into Eq.6.1.

$$\sigma_2 = \sigma - \sigma_1 \qquad \text{where} \qquad \sigma_2 = \sigma - k_1\varepsilon - \eta_1\dot{\varepsilon} \tag{6.5}$$

Thus

$$\dot{\sigma_2} = k_2\dot{\varepsilon} - \frac{k_2}{\eta_2}\left(\sigma - k_1\varepsilon - \eta_1\dot{\varepsilon}\right) \tag{6.6}$$

The substitutions of Eq. 6.3 and Eq.6.4 into Eq.6.2 result in the following inseparable differential equation:

$$\dot{\sigma} + \frac{k_2}{\eta_2}\sigma = \eta_1\ddot{\varepsilon} + \left[k_1 + \left(1 + \frac{\eta_1}{\eta_2}\right)k_2\right]\dot{\varepsilon} + \frac{k_1k_2}{\eta_2}\varepsilon \tag{6.7}$$

Central difference scheme for Voigt and Maxwell models in parallel

Central differences to can be implemented to integrate the differential form of the Maxwell and Voigt elements in parallel. The difference approximations [46] for the time derivatives are:

$$\begin{aligned}
\dot{\sigma} &= \frac{1}{2\Delta t}\left[\sigma_{t+\Delta t} - \sigma_{t-\Delta t}\right] \\
\dot{\varepsilon} &= \frac{1}{2\Delta t}\left[\varepsilon_{t+\Delta t} - \varepsilon_{t-\Delta t}\right] \\
\ddot{\varepsilon} &= \frac{1}{\Delta t^2}\left[\varepsilon_{t+\Delta t} - 2\varepsilon_t + \varepsilon_{t-\Delta t}\right]
\end{aligned} \tag{6.8}$$

The size of the error is of these approximations are $O(\Delta t)$ for the first order and $O(\Delta t^2)$ for second order derivatives. The substitution of the finite difference approximations (Eqs.6.8) into Eq.6.7 gives a finite difference approximation by which the stress can be calculated.

$$\begin{aligned}
\sigma_{t+\Delta t} &= \varepsilon_{t+\Delta t}\left[\frac{2\eta_1}{\Delta t} + k_1 + k_2\left(1 + \frac{\eta_1}{\eta_2}\right)\right] + 2\varepsilon_t\left[\frac{k_1k_2\Delta t}{\eta_2} - \frac{2\eta_1}{\Delta t}\right] \\
&\quad + \varepsilon_{t-\Delta t}\left[\frac{2\eta_1}{\Delta t} - k_1 - k_2\left(1 + \frac{\eta_1}{\eta_2}\right)\right] - 2\sigma_t\left[\Delta t\frac{k_2}{\eta_2}\right] + \sigma_{t-\Delta t}
\end{aligned} \tag{6.9}$$

The creep response of a Voigt and Maxwell element in parallel

An instantaneous step stress is applied to the viscoelastic model in order to derive the creep response. If $\tau \leq t \leq \tau_2$ the initial conditions are: $\sigma = \sigma_0$, $\dot{\sigma} = 0$ and $\varepsilon_0 = 0$. The resulting strain is monitored to find the creep response.

$$\left[\frac{\eta_1\eta_2}{k_2}\right]\ddot{\varepsilon} + \left[\eta_1 + \eta_2\left(1 + \frac{k_1}{k_2}\right)\right]\dot{\varepsilon} + k_1\varepsilon = \sigma_0 \tag{6.10}$$

The equations reduce to a form which resembles that of a damped system. The solution of the second order differential equation is the sum of the homogeneous solution and the

particular solution. The homogeneous equation is shown in Eq. 6.11.

$$m\ddot{\varepsilon} + c\dot{\varepsilon} + k\varepsilon = \sigma \quad \text{where} \quad m = \frac{\eta_1\eta_2}{k_2} \quad c = \eta_1 + \eta_2\left(1 + \frac{k_1}{k_2}\right) \quad \text{and} \quad k = k_1 \tag{6.11}$$

The solution is assumed to have the form, $\sigma = e^{-st}$. The characteristic equation is:

$$s^2 + \frac{c}{m}s + \frac{k}{m} = 0 \tag{6.12}$$

Which has two roots:

$$s_{1,2} = -\frac{c}{2m} \pm \sqrt{\left(\frac{c}{2m}\right)^2 - \frac{k}{m}} \tag{6.13}$$

The discriminant, $c^2 - 4km$ determines if the roots are real (overdamped motion), or complex (underdamped motion) [103]. If $\omega = \sqrt{\frac{k}{m}}$ and $\zeta = \frac{c}{2\sqrt{km}}$, then Eq. 6.13 can be rewritten i.t.o. ζ and ω as:

$$\lambda_{1,2} = -\zeta\omega \pm \omega\sqrt{\zeta^2 - 1} \tag{6.14}$$

The general and particular solution are added:

$$\varepsilon(t) = e^{-\zeta\omega t}\left[Ae^{\sqrt{(\zeta^2-1)}\omega t} + Be^{-\sqrt{(\zeta^2-1)}\omega_n t}\right] - \frac{\sigma_0}{k} \tag{6.15}$$

The solution of the creep response is expected to be over-damped for all cases in this study. For the over-damped case:

$$A = \frac{-\dot{\varepsilon}(0) + \left(-\zeta + \sqrt{\zeta^2 - 1}\right)\omega\varepsilon(0)}{2\omega\sqrt{\zeta^2 - 1}} \tag{6.16}$$

$$B = \frac{\dot{\varepsilon}(0) + \left(\zeta + \sqrt{\zeta^2 - 1}\right)\omega\varepsilon(0)}{2\omega\sqrt{\zeta^2 - 1}} \tag{6.17}$$

Fig.6.2 shows the creep and release response for a model which comprises of Maxwell and Voigt elements in parallel. The solution is assumed to be overdamped.

The relaxation response for a Voigt and Maxwell element in parallel

The relaxation response reflects the stress history as a result of an instantaneously applied constant strain. The relaxation response of the Voigt and Maxwell models in parallel are determined by superposition.

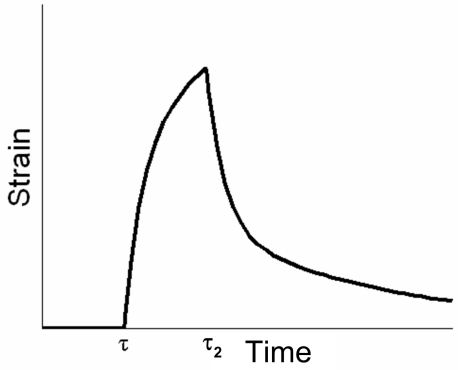

Figure 6.2: Creep and release response of a model that consists of Voigt and Maxwell models in parallel

The respective relaxation responses of these models were discussed in Section 2.5.2. The total relaxation response is given by Eq.6.18 and shown in Fig.6.3.

$$\sigma(\tau) = \delta(\tau) + \varepsilon(\tau)\left[k_1 + k_2 e^{-\left(\frac{t-\tau}{\theta_2}\right)}\right] \tag{6.18}$$

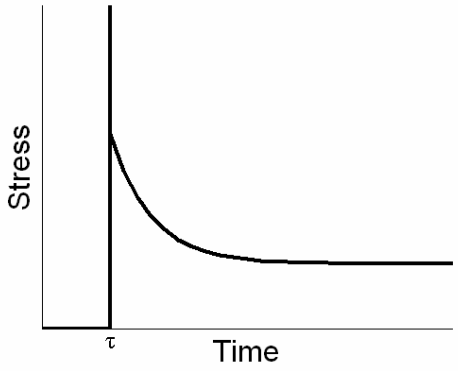

Figure 6.3: Relaxation response of a model which consists of Voigt and Maxwell models in parallel

As expected the step response curves resemble a combination of the Kelvin and Voigt models (Fig.6.3).

The system response due to a unit step input with zero initial conditions is known as the *indicial response* [104]. Now that the indicial response of the system is known, the approach can be extended to find the model response for an arbitrary strain history. If the indicial response of a system is $\sigma_u(t)$, then the system response is the superposition of the response due to each of the individual steps. The superposition integral (also known

as Duhamel's integral) due to each of the individual steps is:

$$\sigma(t) = \varepsilon(0)\sigma_u(t) + \int_0^t \dot{\varepsilon}(\tau)\sigma_u(t-\tau)d\tau \tag{6.19}$$

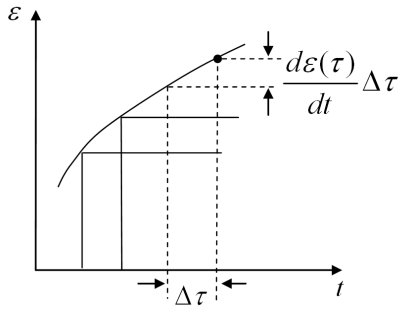

Figure 6.4: A schematic of Duhamel's integral, representing an arbitrary strain history as the superposition of individual steps in time

The time derivative of $\varepsilon(\tau)$ at $t = \tau$ is $\dot{\varepsilon}(\tau)$. The equation accounts for the force function value at $t = 0$, $\varepsilon(0)\sigma_u(t)$, but does not take the initial slope into account. Duhamel's integral may be applied to the model, for an arbitrary strain history, $\varepsilon(t)$. The relaxation function is the appropriate indicial response. For initial conditions of $\varepsilon(0) = 0$:

$$\sigma(t) = k_1\varepsilon(t) + \eta_1\dot{\varepsilon}(t) + \int_0^t k_2\dot{\varepsilon}(\tau)e^{-\frac{t-\tau}{\theta_2}}d\tau \tag{6.20}$$

This reduces to the exact relation formulated by Shim et al. [21] shown in Eq.2.28 in Section 2.5.2, with the single difference that the viscous stress contribution in the present derivation is linear.

6.1.1 Non-linear strain rate dependency in the Voigt and Maxwell models

Both, the study by Tennyson et al.[16] and Shim et al.[21] implemented viscoelastic models where the stress depends non-linearly on strain rate. The theory of the Voigt (Fig.6.5(a)) and Maxwell (Fig.6.5(b)) models is developed here for general non-linear dependencies on strain rate to the power, P and Q respectively.

The stress in a Voigt material with non-linear strain rate dependency (Fig.6.5(a)) is described by:

$$\sigma_1 = k_1\varepsilon + \eta_1\dot{\varepsilon}^P \tag{6.21}$$

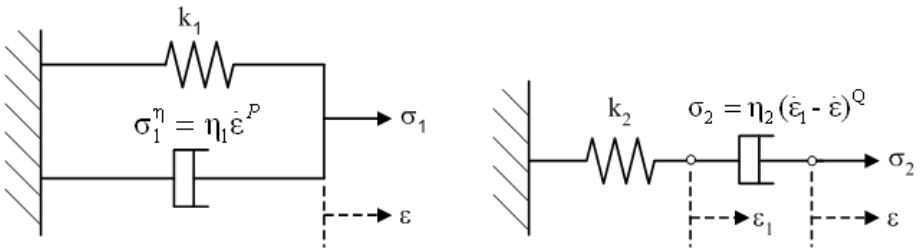

Figure 6.5: (a) Voigt and (b) Maxwell models with non-linear strain rate dependency

The stress balance in the Maxwell system is:

$$\sigma_2 = k_2\varepsilon_1 = \eta_2\left(\dot{\varepsilon}_1 - \dot{\varepsilon}\right)^Q$$

Eliminating ε_1:

$$\dot{\sigma_2} = k_2\left[\dot{\varepsilon} - \left(\frac{\sigma_2}{\eta_2}\right)^{\frac{1}{Q}}\right] \tag{6.22}$$

Note that the differential form of the non-linear Maxwell equation (Eq. 6.22) does not allow Q to be zero. The non-linear differential equation is discretized as follows:

$$\sigma_{2_{t+\Delta t}} = \sigma_{2_t} + \frac{\Delta t}{2}\left[\dot{\sigma}_{2_t} + \dot{\sigma}_{2_{t+\Delta t}}\right]$$

$$\sigma_{2_{t+\Delta t}} + \frac{k_2\Delta t}{2}\left(\frac{\sigma_{2_{t+\Delta t}}}{\eta_2}\right)^{\frac{1}{Q}} = \sigma_{2_t} - \frac{k_2\Delta t}{2}\left(\frac{\sigma_{2_t}}{\eta_2}\right)^{\frac{1}{Q}} + \frac{k_2\Delta t}{2}\left[\dot{\varepsilon}_t + \dot{\varepsilon}_{t+\Delta t}\right] \tag{6.23}$$

Eq. 6.23 is a non-linear inseparable differential equation. The stress at each time step can be found by iteration in a numerical scheme such as Newton-Rahpson strain and strain rate history. Here:

$$f\left(\sigma_{2_{t+\Delta t}}\right) = \sigma_{2_{t+\Delta t}} + \frac{k_2\Delta t}{2}\left(\frac{\sigma_{2_{t+\Delta t}}}{\eta_2}\right)^{\frac{1}{Q}} - \sigma_{2_t} + \frac{k_2\Delta t}{2}\left(\frac{\sigma_{2_t}}{\eta_2}\right)^{\frac{1}{Q}} - \frac{k_2\Delta t}{2}\left[\dot{\varepsilon}_t + \dot{\varepsilon}_{t+\Delta t}\right] \tag{6.24}$$

$$f'\left(\sigma_{2_{t+\Delta t}}\right) = 1 + \frac{\eta_2^Q k\Delta t}{2Q}\left[\sigma_{2_{t+\Delta t}}\right]^{\frac{1-Q}{Q}} \tag{6.25}$$

The stress value for the next iteration, $i+1$ is:

$$\sigma^{i+1}_{2_{t+\Delta t}} = \sigma^{i}_{2_{t+\Delta t}} - \frac{f\left(\sigma^i_{2_{t+\Delta t}}\right)}{f'\left(\sigma^i_{2_{t+\Delta t}}\right)} \tag{6.26}$$

The iterations are continued until the value of

$$\frac{f\left(\sigma^{i}_{2_{t+\Delta t}}\right)}{f'\left(\sigma^{i}_{2_{t+\Delta t}}\right)} < \mathrm{e} \tag{6.27}$$

where e is the maximum error tolerance allowed.

Note that successful numerical implementation requires that negative signs are applied separately to the strain rate for negative strain rates and values where $Q = 2, 4, 6, ...$

If the response of non-linear Maxwell and Voigt models in parallel is required the stress can be calculated by superposition of Eq.'s 6.26 and 6.21.

6.2 The constitutive modelling of experimental results

This section discusses how constitutive relations were used to simulate the stresses that arise in bone during compression experiments at different strain rates. The constitutive modelling of bone comprises of two steps: Firstly, a viscoelastic model must be chosen, i.e. the number and arrangement of elastic and viscous elements. Secondly, the model parameters must be identified through an optimisation process which minimises the discrepancy between the experimental data and model prediction. The process of parameter and model identification is discussed under the following topics:

- The conditioning of experimental data for use in the optimisation algorithm
- The cost function and method of parameter identification
- Comparison of the ability of different viscoelastic models to represent bone response
- Selection of the constitutive viscoelastic model and parameters

6.2.1 The conditioning of experimental data for use in the optimisation algorithm

The responses for each tested strain rate were not averaged and then optimised. Rather, the time, strain and strain-rate history of each experiment was extracted and used as an input to the optimisation scheme. The scheme therefore identified the best fit by accounting for all the data. Additionally the optimisation scheme automatically converges to the average best fit response.

To avoid excessive computational expense **twenty data points were extracted from the time, strain and strain rate history of the experimental measurements. The points were spaced at equal increments of strain ranging from zero to the ultimate stress at fracture.** The inclusion of the instantaneous strain rate allows the optimisation scheme to include strain rate variation during the test. This is particularly useful if bone response is to be considered as a result of varying strain rate.

The twenty points, from each of the time, strain and strain rate histories of the experiments were used as input arguments to the constitutive relation in question. The stress history was calculated from the constitutive model and compared with the experimental result. **The aim of the parameter identification process was to change the parameter values of the constitutive relation such that the discrepancy between the experimental and model stress is minimised.**

Fig.6.6 shows a comparison between raw time-strain history and the data points extracted at equal intervals of strain for use in the optimisation scheme. The initial slack in

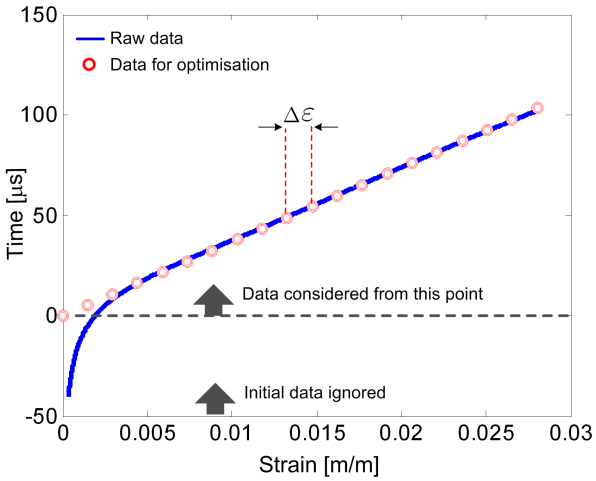

Figure 6.6: The test time data extracted at equal increments of strain from the bone compression experiment

the strain response is ignored.

Examples of raw stress-strain and strain rate-strain histories with extracted data are shown in Figs.6.7(a) and 6.7(b). The stress and strain rate histories are very well approximated by the data fits. Note that the extraction process has a smoothing effect on the data. All local peaks are eliminated, which implies that no instantaneous effects are included in the optimisation process. The more data is chosen throughout the experimental history, the more representative the curves are of the experimental data.

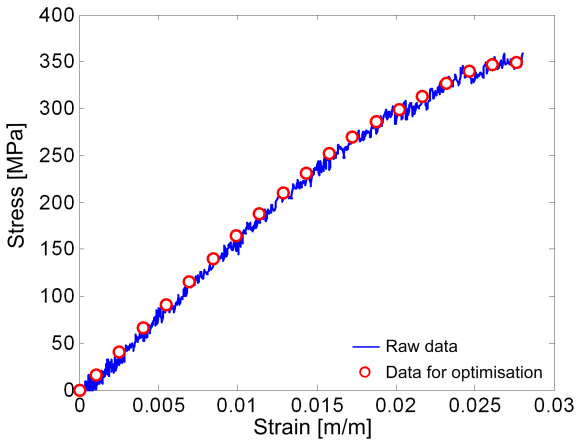

(a) Stress data at equal intervals of strain

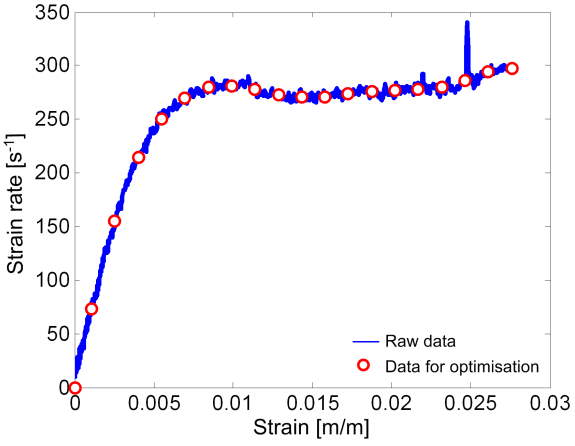

(b) Strain rate data at equal intervals of strain

Figure 6.7: Comparison between raw data and extracted points used for parameter identification

6.2.2 Parameter identification methodology

The method of parameter identification involves the minimisation of the error between the experimental stress response and the stress predicted by the constitutive relation in the material as a result of a given strain history. Fig.6.8 shows an example of two stress-strain curves. The first curve is a stress-strain result which was obtained from a dynamic compression experiment. The second curve comprises of the stress which is predicted by a viscoelastic model at equal strain increments along the experimental response history.

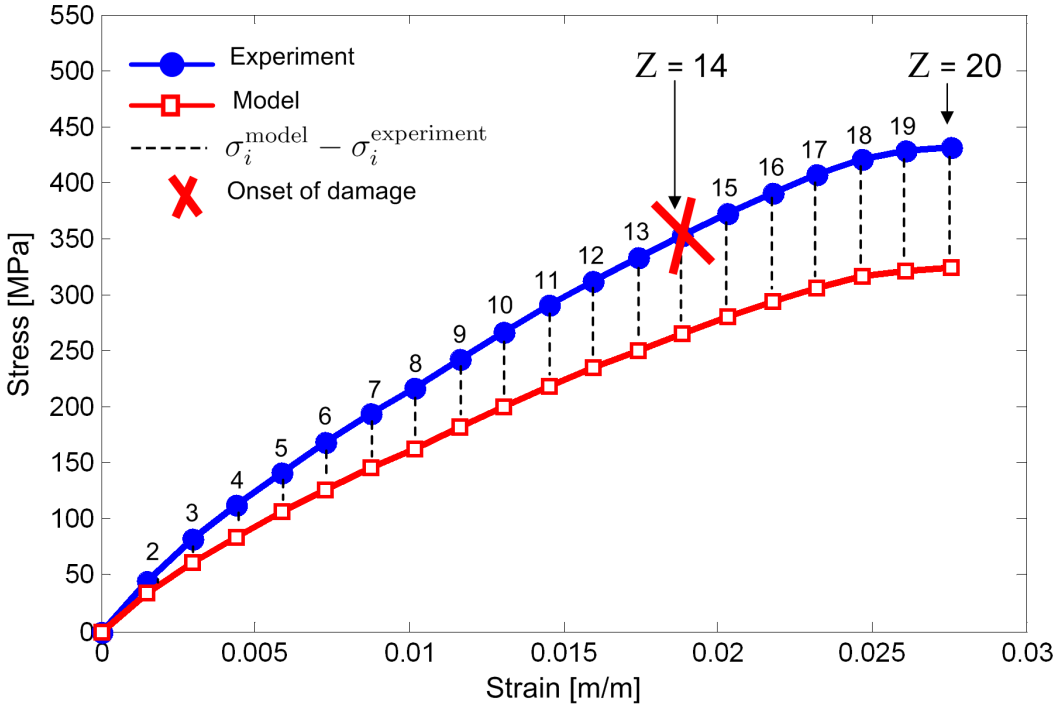

Figure 6.8: A diagram which explains the calculation of the discrepancy between the experimental and model responses

The error for each data set is calculated by using the Euclidean norm which is defined as the square root of the sum of the discrepancy between the experimental and model stress over the strain history, which is described by Z data points. If the error was to be calculated for the whole stress-strain curve, then $Z = 20$. If damage is excluded, Z varies according to where in the data the onset of damage is evident.

$$\|\text{Error}\|_e = \left(\sum_{i=1}^{Z} (\sigma_i^{\text{model}} - \sigma_i^{\text{experiment}})^2 \right)^{\frac{1}{2}} \tag{6.28}$$

Here $\sigma_i^{\text{experiment}}$ is the stress calculated from experiments and σ_i^{model} is the stress predicted by the constitutive model. Recall that compression experiments were conducted at six different strain rates. A good material representation would therefore result in a small

discrepancy between experimental stress and model predictions at all the strain rates in question. In order to minimise the error over the entire strain rate regime the error at each strain rate is accumulated to reflect the total model error as follows:

$$\text{Total error} = \sum_{k=1}^{6} \|\text{Error}\|_e = \sum_{k=1}^{6} \left(\sum_{i=1}^{Z} (\sigma_i^{\text{model}} - \sigma_i^{\text{experiment}})^2 \right)^{\frac{1}{2}} \tag{6.29}$$

Eq.6.29 reflects the sum of the errors in the model stress response for one test at each of the six strain rate regimes in question (where k is the number of the strain rate regime test series). If a number of data sets are taken into account at each strain rate, the root-mean square value of the Euclidean norm of those sets is calculated and added to the root-mean-square of the Euclidean norms at the other strain rates. This ensures that data at the different strain rates is weighted equally if the number of experiments considered in each strain rate regime is not identical. Eq.6.30 presents the relation by which the model error is calculated for data originating from N_k compression tests at each of k different strain rates.

$$\text{Error}_A = \sum_{k=1}^{6} \sum_{j=1}^{N_k} \left(\frac{1}{N_k} \sum_{i=1}^{Z} (\sigma_i^{\text{model}} - \sigma_i^{\text{experiment}})^2 \right)^{\frac{1}{2}} \tag{6.30}$$

In order to find the most suitable parameter values to present experimental results, Eq.6.30 is minimised. Eq.6.30 represents the sum of the root-mean-square values of the total errors that result from the approximation of all the experiments at each of 6 strain rates. This error is chosen because it is well-behaved in an optimisation context: the quadratic function ensures that positive and negative errors are equally penalised. Furthermore the derivative of Eq.6.30 is well defined. Notice that the error in question is an absolute error. This means that the magnitude of the discrepancy between experimental and model results is accosted to the error value, regardless of the percentage it comprises of the desired result. The algorithm will, for instance, work harder to eliminate a 30 MPa error if the desired value is 300 MPa than it will to eliminate a 10 MPa error on a desired value of 100 MPa. Even though both these errors equal a 10% of the desired value.

The `fmincon` function from the MATLAB optimisation toolbox was used to find the constrained minimum of several variables. The function inputs are:

- The cost function which is to be minimised, i.e. Eq.6.30
- Initial estimates of the parameter values, X_0. The initial parameter values were randomised. The resulting optimum parameter values, X_{opt} were the result of fifty optimisation loops with new random starting values at the beginning of each run.
- Linear parameter constraints. None were used in the present parameter identification process.

- Lower and upper bounds for parameter values. All parameter values were constrained such that $X_{opt} \geq 0$.

6.2.3 Evaluation of various viscoelastic models to approximate the strain rate dependent response of bone

In this section a variety of viscoelastic models are evaluated for their ability to model a sample of well-behaved stress strain curves determined from bone compression experiments over seven orders of strain rate. The comparison is undertaken here to facilitate and motivate the choice of a constitutive relation to approximate the strain rate dependent response of bovine cortical bone in compression. The ideal constitutive relation is required to:

- Simulate an increase in stress with an increase in strain (i.e. an elastic component) and incorporate rate dependent effects (i.e. a viscous component).
- Approximate the strain rate dependent response with the smallest margin of error and as few as possible parameters.
- A single model is required to simulate bone response at all the strain rates in question.

The Voigt or Maxwell models are the most basic models that comply with these requirements because they contain elements of elasticity and rate sensitivity. The dashpot in the Voigt model includes the effect of the instantaneous strain rate, whereas the Maxwell model takes strain rate history into account. The ability of Maxwell and Voigt models to simulate bone response is evaluated here. The relations suggested by other authors such as Tennyson et al. [17], Tanabe and Kobayashi [16] and Shim et al. [21] are also evaluated to assess if they offer significant advantages over the basic models. The evaluation considers three groups of viscoealstic models. A diagram of each model, along with its stress-strain relationship and identified parameter values are summarised in the figures listed below:

- The basic Voigt and Maxwell models (Fig.6.10)
- A Maxwell model in parallel with an elastic model (Fig.6.11)
- A Maxwell model in parallel with a Voigt model (Fig.6.12)

Magnified graphs of the model approximations and parameters (in Figs.6.10, 6.11 and 6.12) are presented in Appendix D.

The well behaved data sample is a set of stress vs. strain curves for which the stiffness of the material response increases monotonically with strain rate (Fig.6.9). The failure stresses as discussed in Section 5.1.4 are indicated on the stress-strain curves. Recall that beyond the failure stress the bone structure is considered to have sustained damage and

have a compromised structural integrity. Even though the ultimate fracture stress is about 10% and 20% higher for quasi-static and dynamic response curves respectively, damage and therefore injury is expected to occur beyond the failure stress. Shim et al. [21] only considered the material response up to yield (i.e. failure) when modelling cancellous bone from the human cervical spine. If bone response is to be modelled beyond yield it must be realised that the model includes aspects of damage.

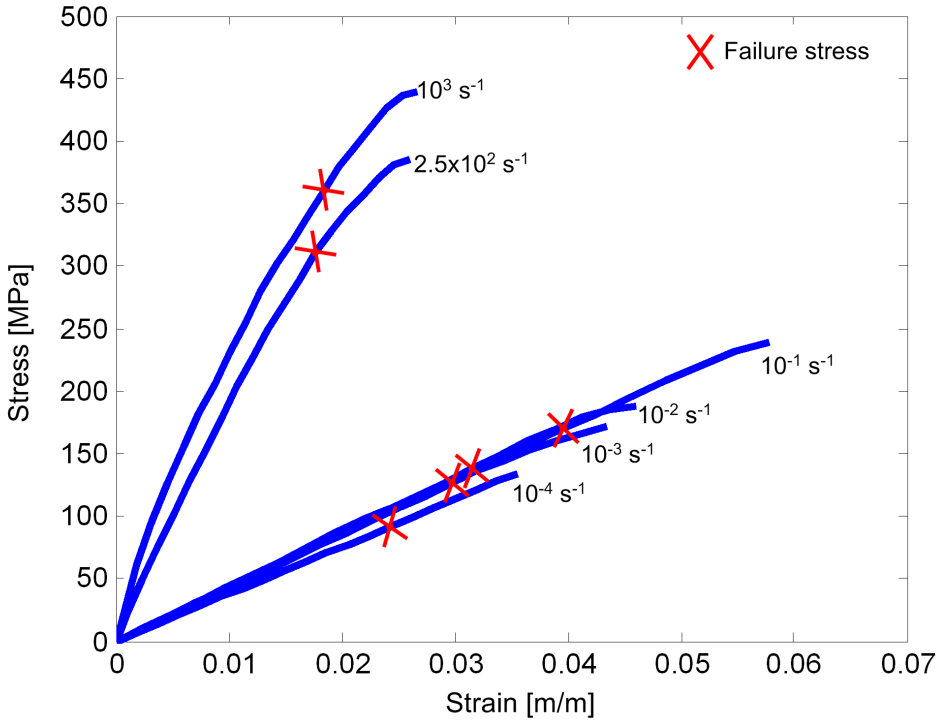

Figure 6.9: A sample of well behaved data which is used to evaluate different viscoelastic models

The development of a simulation model for bone response requires knowledge of the ultimate use of the model. **If the model was required to evaluate injury, the constitutive relation would include only the material response up to yield or failure (where the structure incurs damage). The number of points considered (Z in Eq.6.30) for the well behaved data set are listed in Table 6.1. However, if the model was to establish if a bone fractured or not, the bone response, including the damage in the material should be modelled up to the point of fracture. This study is predominantly aimed at predicting the risk of injury and will therefore focus on modelling the response up to the point of damage.** However, models that include damage will be briefly considered for one model in each of the three groups of viscoelastic models under investigation.

Strain rate [s^{-1}]	10^{-4}	10^{-3}	10^{-2}	10^{-1}	2.5×10^{2}	10^{3}
Z	17	18	17	16	14	14

Table 6.1: The number of data points to be considered if the model response was considered up to the onset of damage for the well behaved data set

Single Voigt and Maxwell models (Fig.6.10)

A. Maxwell model

Recall that the basic Maxwell model comprises of a dashpot and spring in series. If a finite strain is applied to the model, the stress in the dashpot of the Maxwell element must equal the stress in the spring to satisfy stress equilibrium. However, if the strain rate is not significant the stress in the dashpot will tend to zero, which forces the stress in the whole link to follow. For this reason the Maxwell model alone is not able to simulate the desired increase in stress with an increase in strain at quasi-static strain rates.

B. Voigt model

A sole elastic element would give a single stress response for all loading rates. An elastic element is required in parallel with a dashpot to prevent the result of an insignificant model stress if the strain rate is very small. A dashpot in parallel could additionally differentiate between the responses at different strain rates. The resulting model is a Voigt element, such as the model used by Tennyson et al. [17]. The Voigt dashpot contributes a constant stress at a constant strain rate whereas the elastic element results in a constant slope or stress increase with an increase in strain. Because the quasi-static strain rate is insignificant (in comparison with the dynamic rates) the stress contribution of the dashpot tends to zero at quasi-static strain rates. The slope parameter value of the elastic element in the Voigt model is consequently dictated by the slope of the quasi-static stress-strain curves. The slopes of the dynamic stress-strain data curves are significantly steeper than those at quasi-static strain rates. As the elastic parameter is dictated by the quasi-static slope, it is up to the viscous damping parameter to approximate the dynamic response. The viscous stress is directly proportional to the dynamic strain rate, which was more or less constant for the data under consideration. Therefore the dynamic stress from the Voigt model results in stress-strain curves with a single slope (which is dictated by the value of k_1) at constant in increments of stress which are proportional to the strain rate. This explains why a single spring Voigt model does not approximate the data effectively.

C. Tanabe and Kobayashi [16] model (DAMAGE INCLUDED)

The above problem persists even if both elastic and viscous components are assumed to have non-linear contributions as proposed by Tanabe and Kobayashi [16]. The non-linear spring limits the contribution of the elastic component as the strain increases and resembles aspects of damage. For this reason all the data up to fracture was considered in the parameter identification of this model. The inclusion of data up to fracture places much greater demands on the constitutive relation as the model is required not only to represent strain rate dependency, but also the change in the slope of the material response which is attributed to damage. The original model used by Tanabe and Kobayashi [16] was described by:

$$\sigma(t) = k_1(\varepsilon(t) - \alpha\varepsilon(t)^D) + \eta_1 \left(\frac{\dot{\varepsilon}(t)}{\dot{\varepsilon}_0}\right)^P \tag{6.31}$$

For the present data it was found that the model response did not display appreciable sensitivity to the parameter, α. This parameter is therefore excluded from the parameter identification process, such that:

$$\sigma(t) = k_1(\varepsilon(t) - \varepsilon(t)^D) + \eta_1 \left(\frac{\dot{\varepsilon}(t)}{\dot{\varepsilon}_0}\right)^P \tag{6.32}$$

Tanabe and Kobayashi [16] as well as Tennyson et al.[17] required a constitutive relation that would serve to model bone responses over two to four magnitudes of strain rate variation. However the implementation of these viscoelastic models here require the constitutive relation to approximate bone response over a strain rate range of seven orders of magnitude. For this reason the models used by these authors do not serve as effectively when applied to a range that include dynamic strain rates. The rate sensitivity of the Voigt element is not able to capture the dynamic response of bovine bone in longitudinal compression accurately.

A Maxwell model in parallel with an elastic model (Fig.6.11)

The previous discussion highlights the need for a second elastic slope to simulate the difference between the quasi-static and dynamic stress-strain curves. It is desirable that this slope is only activated when the material is experiencing a significant strain rate. Additionally, the stress in the model should increase with an increase in strain at quasi-static strain rates. An elastic model is therefore added in parallel with a Maxwell element. As mentioned before the spring and dashpot in the Maxwell element are required to have the same stress in order to maintain stress equilibrium. The dashpot in the Maxwell element almost acts as a switch, which activates the stress contribution as soon as the material experiences a significant strain rate.

Fig.6.11 shows a group of models with an elastic element in parallel with a Maxwell element. There is a significant reduction in the modelling error from previous group of models in Fig.6.10 because these models are able to differentiate between quasi-static and dynamic response.

D. Elastic and Maxwell model

The linear combination of Maxwell and elastic elements result in two distinct linear stress-strain curves which do not differentiate between individual quasi-static or dynamic responses. The model underestimates the dynamic response and overestimates quasi-static response prior to damage. The value of the dashpot constant, η_2, is dictated by the stress jump between the quasi-static and dynamic responses.

E. Elastic and non-linear Maxwell model

The differentiation between quasi-static strain rates is slightly improved by the addition of non-linear strain rate dependency to the Maxwell dashpot. The non-linear power Q is smaller than 1, which implies that a small increment of Maxwell stress contribution is possible for a large increment in strain rate. This is desirable to achieve distinct response curves in the quasi-static strain rate regime. However the difference between the dynamic strain rates is too small to realise a differentiated response. The dynamic approximation of the $2.5 \times 10^2\,\mathrm{s}^{-1}$ response is almost exact over the entire strain rate regime even though the parameter identification only took the response prior to damage into account.

F. Both non-linear elastic and Maxwell model (DAMAGE INCLUDED)

All the data up to fracture was included in the parameter identification for this model, which places additional demands on the model performance. The quasi-static responses are well differentiated with a slight over-prediction in the initial responses. The dynamic response remains initially under-predicted, with an overall poor approximation of the $10^3\,\mathrm{s}^{-1}$ response.

Maxwell and Voigt models in parallel (Fig.6.12)

A final group of viscoelastic models are shown in Fig.6.12. This group is investigated in the light of the study of Shim et al. [21], who combined Voigt and Maxwell elements in parallel to model the strain rate dependent mechanical properties of cancellous bone from the human cervical spine. **An attractive characteristic of this group of models is that they include both the effect of instantaneous strain rate (Voigt dashpot) and strain rate history (Maxwell model).**

G. Maxwell and Voigt model

The linear form of this model requires four parameters. The model displays only a slight variation in the responses at quasi-static strain rates but differentiates well between the two dynamic responses. The quasi-static responses are well approximated, except for

the response at $10^{-4}\,s^{-1}$ which lies below the model prediction. The dynamic response curves are virtually linear which result in a good approximation of the initial and failure stresses (where damage occurs), but the under-estimation of the stress in between.

H. Shim et al. [21] model

The addition of non-linear viscosity to the Voigt dashpot results in an excellent approximation of both the non-linear dynamic response curves. Again, the quasi-static responses are well represented, except for the response at $10^{-4}\,s^{-1}$. This model gives a good overall approximation of bovine cortical bone response.

I. Both non-linear Voigt and Maxwell model (DAMAGE INCLUDED)

The addition of non-linearity to the Maxwell dashpot shows great promise in the modelling of the bovine cortical bone up to fracture. The differentiation of quasi-static response is further improved but is slightly overestimated initially. The entire response at $2.5\times10^{2}\,s^{-1}$ is represented very accurately, whereas the ultimate dynamic response at $10^{3}\,s^{-1}$ is over-estimated slightly. This model is the most effective of all the assessed models for the modelling of bovine cortical bone response with damage. *This model was also considered without damage in which case the value of Q tended to 1 and the model parameters reduced to those listed for the model by Shim et al. [21] (model H).*

Model	Best fit	Parameters
A. Maxwell	$\sigma(t) = \int_0^t k_2 \dot{\varepsilon}(\tau) e^{-\frac{k_2}{\eta_2}(t-\tau)} d\tau$ 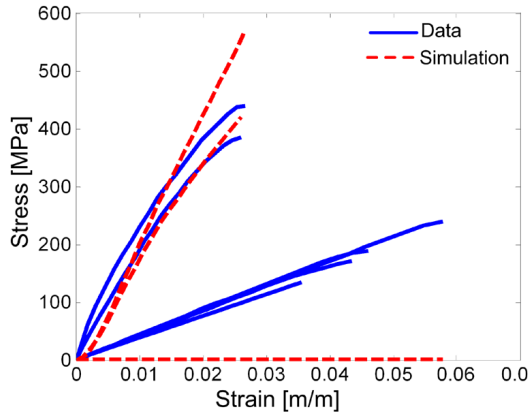 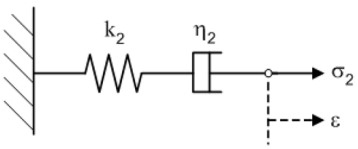	$k_2 = 25.52\,\text{GPa}$ $\eta_2 = 2.91\,\text{MPa.s}^{-1}$
B. Voigt Tennyson et al. [3]	$\sigma(t) = k_1 \varepsilon(t) + \eta_1 \dot{\varepsilon}(t)$ 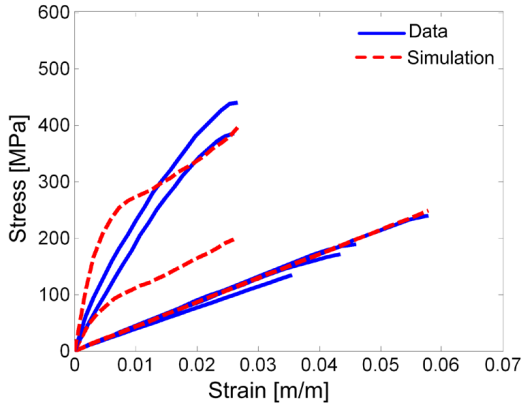 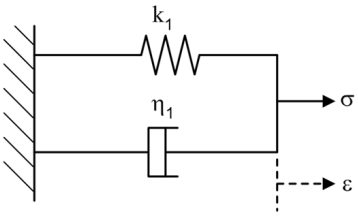	$k_1 = 4.28\,\text{GPa}$ $\eta_1 = 2.28\,\text{MPa.s}^{-1}$
C. With damage: Tanabe and Kobayashi [4]	$\sigma(t) = k_1(\varepsilon(t) - \varepsilon(t)^D) + \eta_1 \left(\frac{\dot{\varepsilon}(t)}{\dot{\varepsilon}_0}\right)^P$ 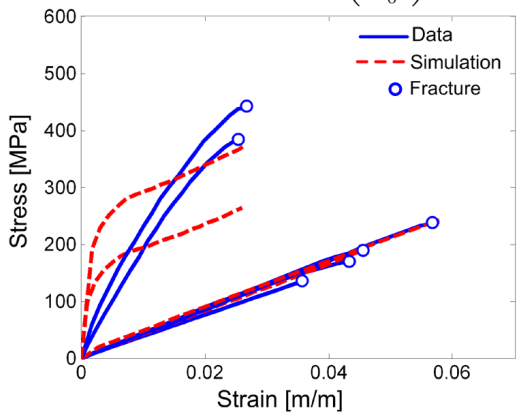 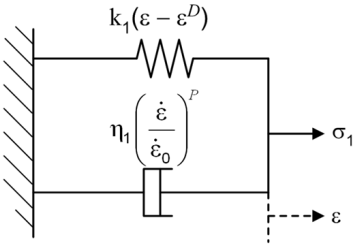	$k_1 = 4.15\,\text{GPa}$ $\eta_1 = 185.38\,\text{MPa.s}^{-1}$ $D = 2.43$ $P = 0.38$

Figure 6.10: Comparison of the ability of basic Maxwell and Voigt models to simulate the behaviour of bovine bone in longitudinal compression at different strain rates

Model	Best fit	Parameters
D. Elastic and Maxwell	$\sigma(t) = k_1\varepsilon(t) + \int_0^t k_2\dot{\varepsilon}(\tau)e^{-\frac{\eta_2}{k_2}(t-\tau)}d\tau$	$k_1 = 4.27\,\text{GPa}$ $k_2 = 20.62\,\text{GPa}$ $\eta_2 = 1.83\,\text{MPa.s}^{-1}$
E. Elastic and non-linear Maxwell	$\sigma(t) = k_1\varepsilon(t) + \text{result Eq.6.26}$	$k_1 = 4.20\,\text{GPa}$ $k_2 = 21.17\,\text{GPa}$ $\eta_2 = 15.12\,\text{MPa.s}^{-1}$ $Q = 0.53$
F. With damage: Both non-linear elastic and Maxwell	$\sigma(t) = k_1(\varepsilon(t) - \varepsilon(t)^D) + \text{result Eq.6.26}$	$k_1 = 4.06\,\text{GPa}$ $k_2 = 20.32\,\text{GPa}$ $\eta_2 = 28.91\,\text{MPa.s}^{-1}$ $D = 2.68$ $Q = 0.409$

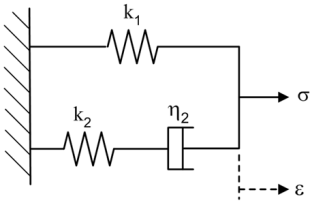

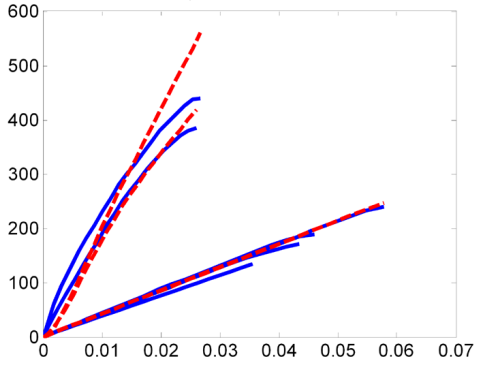

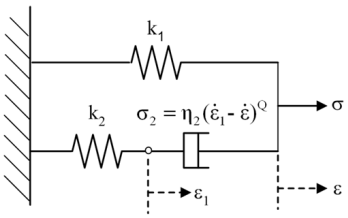

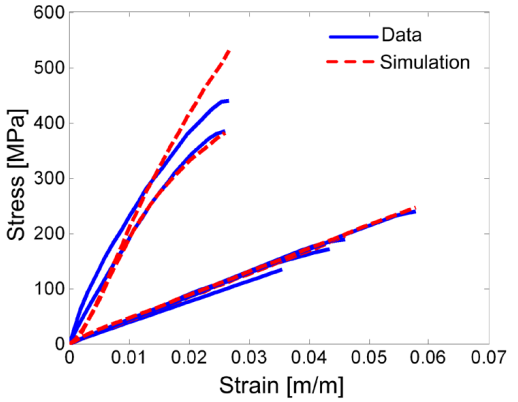

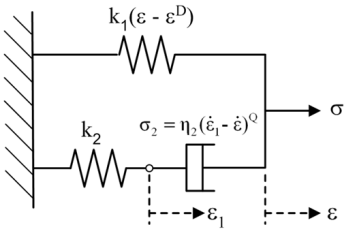

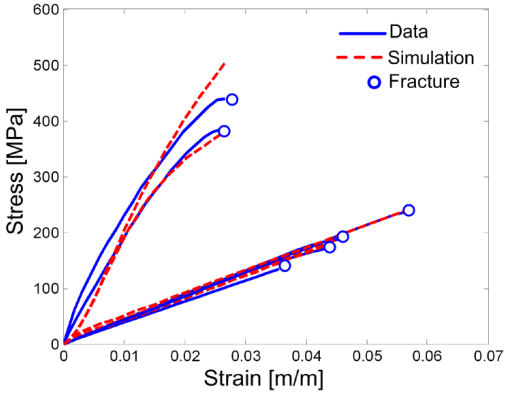

Figure 6.11: Comparison of the ability of models with elastic and Maxwell elements in parallel to simulate the behaviour of bovine bone under different strain rates of longitudinal compression

Model	Best fit	Parameters
G. Maxwell and Voigt parallel	$\sigma(t) = k_1\varepsilon(t) + \eta_1\dot{\varepsilon}(t) + \int_0^t k_2\dot{\varepsilon}(\tau)e^{-\frac{\eta_2}{k_2}(t-\tau)}d\tau$	$k_1 = 4.25$ GPa $\eta_2 = 0.78$ MPa. s^{-1} $k_2 = 14.04$ GPa $\eta_2 = 14.90$ MPa. s^{-1}
H. Shim et al.[5]	$\sigma(t) = k_1\varepsilon(t) + \eta_1\dot{\varepsilon}(t)^P + \int_0^t k_2\dot{\varepsilon}(\tau)e^{-\frac{\eta_2}{k_2}(t-\tau)}d\tau$	$k_1 = 4.21$ GPa $\eta_2 = 34.7$ MPa. s^{-1} $k_2 = 13.11$ GPa $\eta_2 = 10.09$ MPa. s^{-1} $P = 0.46$
I. With damage: Both non-linear Voigt and Maxwell	$\sigma(t) = k_1\varepsilon(t) + \eta_1\dot{\varepsilon}(t)^P +$ result Eq.6.26	$k_1 = 4.04$ GPa $\eta_2 = 77.815$ MPa. s^{-1} $k_2 = 13.06$ GPa $\eta_2 = 21.19$ MPa. s^{-1} $P = 0.33$ $Q = 0.48$

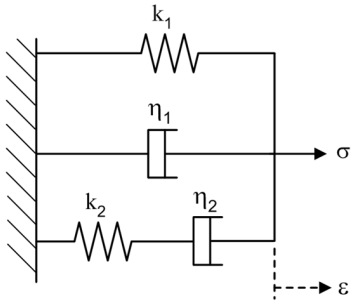

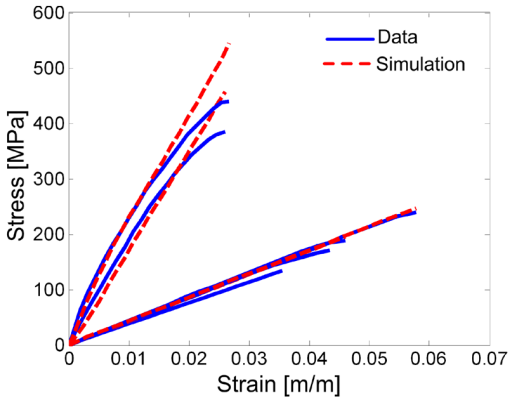

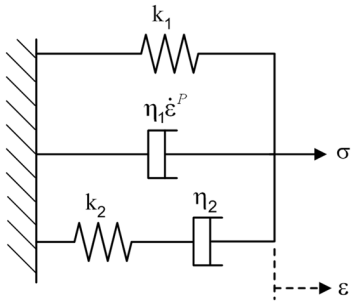

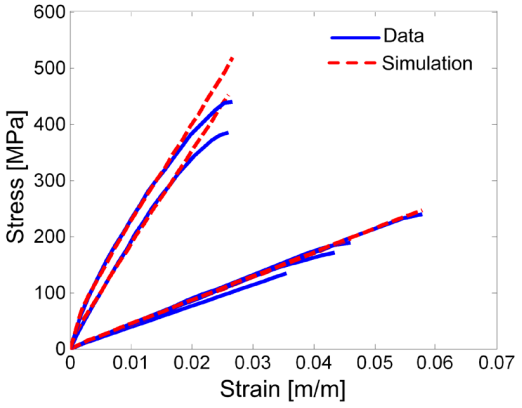

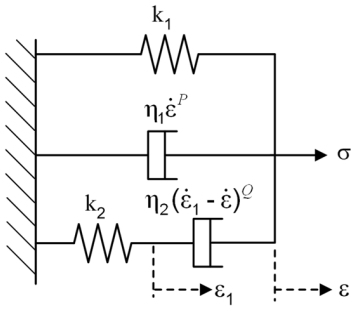

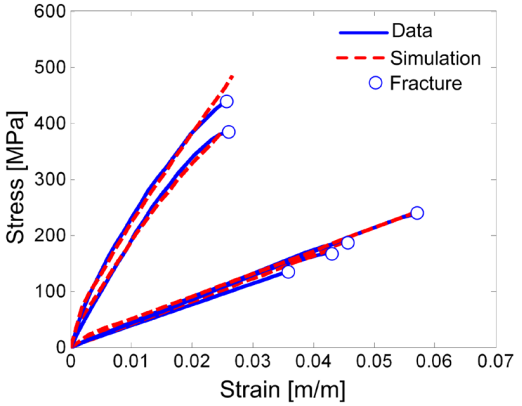

Figure 6.12: Comparison of the ability of models with Voigt and Maxwell elements in parallel to simulate the behaviour of bovine bone under different strain rates of longitudinal compression

The relative root-mean-square error percentage

The optimal parameter values for the nine viscoelastic models, which were discussed in Figs.6.10, 6.11 and 6.12 were identified by minimisation of the absolute error over six strain rate regimes (Eq.6.30). The absolute model error at each strain rate is presented in Table 6.2 to summarise the performance of the models relative to each other.

The models were further interrogated in terms of the relative root-mean-square error percentage. **The reason for this interrogation is not to change the optimisation objective function, but rather to express the absolute errors, which were reported in Table 6.2 in a context which can be easily interpreted. The relative root-mean-square errors of the nine viscoelastic models (for which the parameter values were determined by Eq.6.30) were therefore expressed as a percentage of the desired value.**

The relative root-mean-square error:

- Differs from the absolute error in that it is expressed as a fraction of the desired value. As an example, an error of 100 MPa is 1000% if the desired value is 10 MPa, but only 10% if the desired value is 1000 MPa.
- Is very large when desired values ($\sigma^{experiment}$) with a small magnitude are not well approximated. For instance, if the desired stress value is 1 MPa and the model predicts a stress of 2.5 MPa the relative error percentage at that point is 150%. Therefore, discrepancies in the model approximation in the early stages of the stress-strain curves contribute significantly to the relative error percentage.

The relative root-mean-square error of the model representation over Z data points for a single stress-strain curve at a single strain rate is:

$$\text{Error}_{\text{RMS}} = \left[\frac{1}{Z} \sum_{i=1}^{Z} \left(\frac{\sigma_i^{\text{model}} - \sigma_i^{\text{experiment}}}{\sigma_i^{\text{experiment}}} \right)^2 \right]^{\frac{1}{2}} \tag{6.33}$$

If damage was not considered the relative error was only calculated up to the yield point. All the data points were of course included in the error estimate for the three models that approximate damage in which case $Z = 20$. The relative root-mean-square error can be expressed as a percentage of the desired value by:

$$\text{Error}_{\text{RMS\%}} = 100 \left[\frac{1}{Z} \sum_{i=1}^{Z} \left(\frac{\sigma_i^{\text{model}} - \sigma_i^{\text{experiment}}}{\sigma_i^{\text{experiment}}} \right)^2 \right]^{\frac{1}{2}} \tag{6.34}$$

The relative root-mean-square percentage errors of the nine viscoelastic models were evaluated at each strain rate and reported in Table 6.3. The standard deviation of the relative

error was expressed as a percentage and is also stated in Table 6.3. If the standard deviation is small this implies that model accuracy does not fluctuate much about the relative error. To summarise the overall performance of the models the root-mean-square error percentage for a single stress-strain curve at each of the six strain rates was calculated. This value results from the calculation of the root-mean-square error percentage of the root-mean-square errors (which follow from Eq.6.33) for each the six strain rates.

$$\text{Total}_{\text{RMS\%}} = 100 \left[\frac{1}{6} \sum_{k=1}^{6} (\text{Error}_{\text{RMS}})^2 \right]^{\frac{1}{2}} \tag{6.35}$$

The total relative error percentages are presented in Table 6.3 and Fig.6.13. These error percentages offer an immediate interpretation of model accuracy as their magnitudes are independent of the scale of the absolute error value.

Model	$10^{-4}\,s^{-1}$	$10^{-3}\,s^{-1}$	$10^{-2}\,s^{-1}$	$10^{-1}\,s^{-1}$	$2.5\times10^{2}\,s^{-1}$	$10^{3}\,s^{-1}$	Damage	Error_A [MPa]
A. Maxwell								
Total error [MPa]	272.1	407.1	410.9	458.0	73.6	142.5	No	**1764.1**
Stdev [MPa]	33.5	48.1	50.4	58.5	9.8	31.5		
B. Voigt (Tennyson et al.[17])								
Total error [MPa]	37.5	8.8	[1]9.0	[1]1.4	369.3	171.4	No	**597.5**
Stdev [MPa]	4.6	1.8	1.2	0.4	62.5	46.8		
C. Tanabe and Kobayashi [16]								
Total error [MPa]	35.2	11.0	16.4	17.2	351.0	330.0	Yes	**760.7**
Stdev [MPa]	3.5	2.6	3.3	3.0	76.8	74.5		
D. Maxwell and elastic								
Total error [MPa]	36.7	[3]8.1	[2]9.9	[2]1.8	56.8	127.1	No	**240.4**
Stdev [MPa]	4.5	1.7	1.3	0.5	7.2	28.0		
E. Non-linear Maxwell and elastic								
Total error [MPa]	[3]32.1	[1]5.3	[3]12.1	9.8	[3]43.3	[3]119.3	No	[3]**221.9**
Stdev [MPa]	3.9	1.3	2.0	1.4	8.9	27.8		
F. Both non-linear Maxwell and elastic								
Total error [MPa]	[2]28.9	12.3	19.5	23.4	52.8	161.2	Yes	**298.0**
Stdev [MPa]	2.8	2.6	3.9	3.7	8.6	37.7		
G. Maxwell and Voigt								
Total error [MPa]	42.6	15.6	15.8	7.6	115.1	163.7	No	**360.4**
Stdev [MPa]	4.7	3.5	2.9	1.8	27.1	33.1		
H. Shim et al.[21]								
Total error [MPa]	33.2	[2]5.6	13.0	[3]4.6	[1]14.9	[1]16.7	No	[1]**88.0**
Stdev [MPa]	4.0	1.4	1.8	1.1	4.3	4.8		
I. Both non-linear Voigt and Maxwell								
Total error [MPa]	[1]28.4	12.9	20.3	21.6	[2]36.7	[2]61.8	Yes	[2]**181.7**
Stdev [MPa]	2.9	2.7	3.9	3.5	8.5	14.4		

Table 6.2: The absolute errors errors and standard deviations of the errors of the viscoelastic model fits with experimental stress-strain curves at each tested strain rate. [1,2,3] Allocated to the model with the first, second and third smallest average error at each strain rate

Model	$10^{-4}\,s^{-1}$	$10^{-3}\,s^{-1}$	$10^{-2}\,s^{-1}$	$10^{-1}\,s^{-1}$	$2.5 \times 10^{2}\,s^{-1}$	$10^{3}\,s^{-1}$	Damage	$\text{Total}_{\text{RMS\%}}$ (%)
A. Maxwell								
Total error (%)	100.0	100.0	100.0	100.0	26.8	31.6	No	**83.3**
Stdev (%)	0.0	0.0	0.1	0.5	22.1	22.2		
B. Voigt (Tennyson et al.[17])								
Total error (%)	13.8	2.8	[1]2.5	[1]1.2	47.5	31.6	No	**24.0**
Stdev (%)	0.2	1.0	1.0	0.8	17.6	23.8		
C. Tanabe and Kobayashi [16]								
Total error (%)	[3]11.8	3.2	6.3	15.6	94.8	68.6	Yes	**48.5**
Stdev (%)	1.9	2.5	5.0	13.8	79.4	56.5		
D. Maxwell and elastic								
Total error (%)	13.6	[2]1.3	[2]2.6	[2]1.2	25.4	31.7	No	**17.5**
Stdev (%)	0.2	1.0	1.0	1.0	19.6	23.5		
E. Non-linear Maxwell and elastic								
Total error (%)	12.0	[1]1.1	3.1	9.9	23.8	30.8	No	**17.2**
Stdev (%)	0.4	0.7	1.2	8.5	20.3	23.5		
F. Both non-linear Maxwell and elastic								
Total error (%)	[2]9.9	3.6	8.1	20.1	20.5	26.9	Yes	**17.0**
Stdev (%)	2.2	2.4	6.4	17.7	18.0	20.7		
G. Maxwell and Voigt								
Total error (%)	13.0	2.4	[3]2.8	[3]3.3	[2]17.1	[3]11.2	No	[2]**10.1**
Stdev (%)	0.3	2.1	1.1	2.8	11.3	7.6		
H. Shim et al.[21]								
Total error (%)	12.2	[3]2.1	2.9	4.6	[1]11.1	[2]6.6	No	[1]**7.6**
Stdev (%)	0.4	1.8	1.1	4.1	9.4	4.9		
I. Both non-linear Voigt and Maxwell								
Total error (%)	[1]9.5	3.4	7.6	19.3	[3]18.2	[1]5.3	Yes	[3]**12.2**
Stdev (%)	2.1	2.1	5.6	17.3	16.9	3.6		

Table 6.3: Relative root-mean-square error percentages and standard deviation of the viscoelastic model fits with experimental stress-strain curves at each tested strain rate. [1,2,3] Allocated to the model with the first, second and third smallest average error at each strain rate

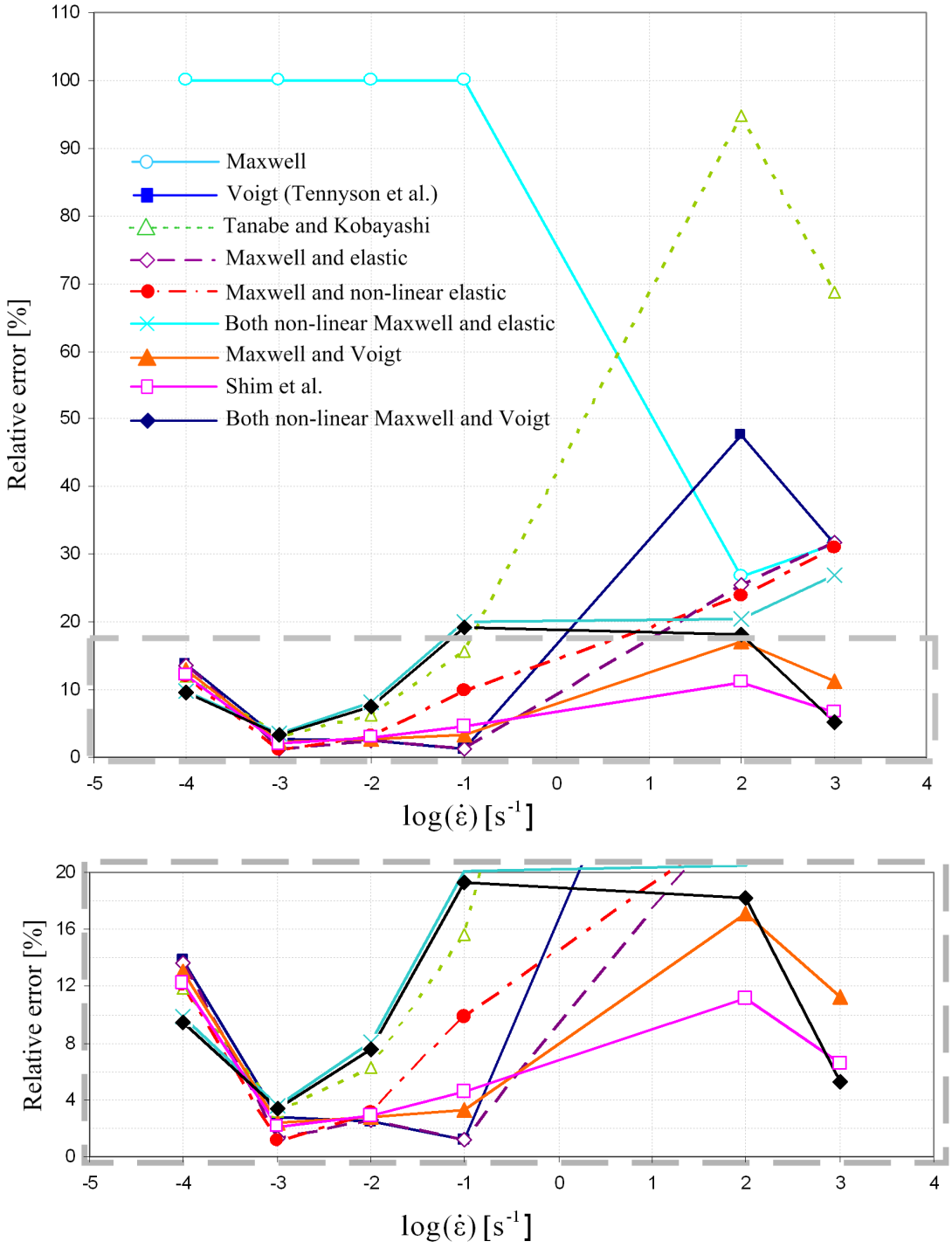

Figure 6.13: Relative root-mean-square error percentages of the nine investigated viscoelastic models over the experimental strain rate regime. NOTE: The errors for $\dot{\varepsilon} = 2.5 \times 10^2\ \mathrm{s}^{-1}$ were plotted at 2 instead of 2.5 on the x-axis for the sake of clarity

6.2.4 Viscoelastic model and parameter selection

The combined consideration of the absolute model errors (Table 6.2) and relative model errors (Table 6.3) lead to the following conclusions:

- It is clear that the Maxwell model greatly misrepresents compressive cortical bone response at quasi-static strain rates. The absolute errors at these strain rates contribute to the majority of the absolute error of 1764.1 MPa. Interrogation of this model in terms of the relative error percentage results in a relative error of 83.3%.

- The stress approximation of the viscoelastic model by Shim et al.[21] resulted in the smallest absolute error (88 MPa) and relative root-mean-square percentage error (7.6%) of all the models considered. The model response displays the greatest inaccuracy at a strain rate of $\dot{\varepsilon} = 10^{-4}\,\mathrm{s}^{-1}$ where the absolute response error is 33.2 MPa (which corresponds to a relative root-mean-square error percentage of 12.2%).

- An additional benefit of choosing the model developed by Shim et al. [21] is that it has been proven effective for the modelling of cancellous bone from the human cervical spine. A single model can therefore be implemented for both bone types, with only a change in parameters required to switch between cortical and cancellous bone.

- *Model I* shows great promise if the modelling of bone response is required to the point of ultimate fracture. The absolute error and relative root-mean-square error percentage is 181.7 MPa and 12.2% respectively. It is important to note that the modelling of damage imposes greater demands on a constitutive relation, which is reflected in both of the currently implemented error measures. This model was also considered without damage in which case the value of Q tended to 1 and the model parameters reduced to those listed for the model by Shim et al. [21] (model H).

***Model H* (based on the model by Shim et al. [21]) was selected to model the strain rate dependent response of bovine cortical bone in longitudinal compression.**

The selected constitutive model for the strain rate dependent response of bovine cortical bone comprises of a Maxwell model and a Voigt model (with non-linear strain rate dependency) in parallel. This model is identical to the model implemented by Shim et al.[21] (for cancellous bone from the human cervical spine) in al respects except that the non-linearity of the viscous stress was not fixed at $P = 0.5$, but was instead included as a model parameter.

The parameters were identified by the minimisation of Eq.6.30 over the complete set of compression data (Table 6.4). The data set included compression data from 43 quasi-static

experiments (Fig.5.1) and 18 dynamic experiments at constant strain rates (Fig.5.9). The resulting fit of the experimental data is shown in Fig.6.14.

The model parameters are listed in Table 6.4. The purely elastic parameter value, $k_1 = 3.98\,\text{GPa}$ is approximately equal to the quasi-static Young's modulus (Table 5.1). Notice that the non-linearity of the Voigt dashpot, P for all the data is no longer close the value found for the well behaved data set, $P = 0.47$ or the value identified by Shim et al.[21], $P = 0.5$.

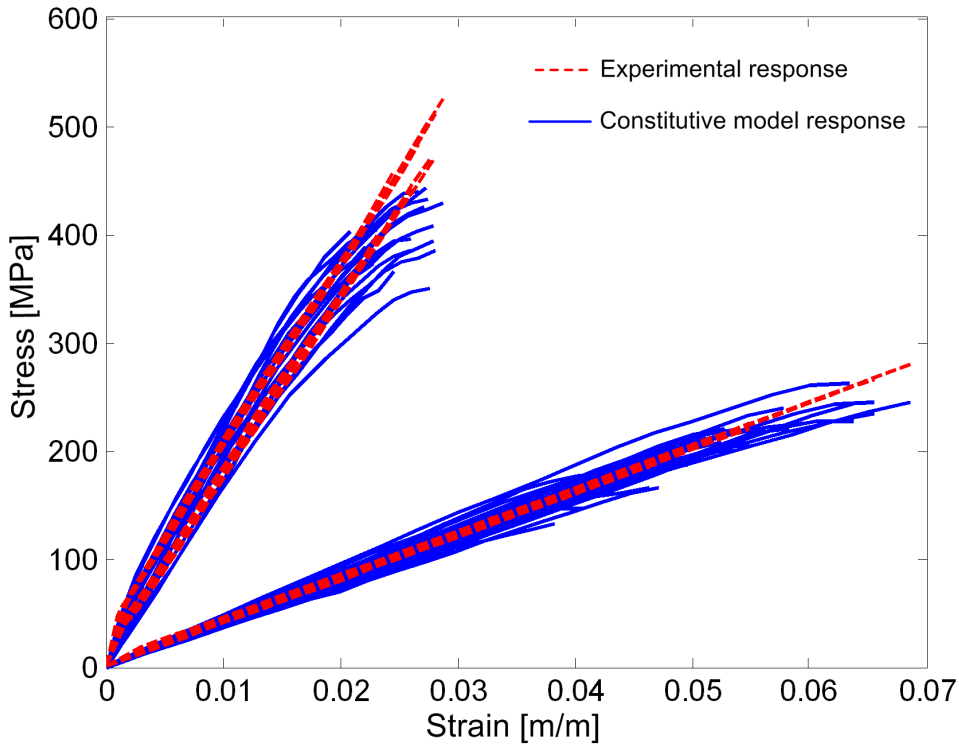

Figure 6.14: The experimental and constitutive response curves subsequent to parameter identification

k_1 [GPa]	η_1 [MPa. s^{-1}]	k_2 [GPa]	η_2 [MPa. s^{-1}]	P
3.98	8.58	12.84	14.37	0.28

Table 6.4: The five parameters for *Model H* that were identified for the constitutive modelling of the strain rate dependent response of bovine cortical bone in longitudinal compression.

6.3 Current approach to the 3-D expansion of the viscous term as reported by Shim et al.[21]

Shim et al. [21] extended their viscoelastic relation into 3-D such that it contains the 1-D model as a special case.

$$\begin{aligned}\boldsymbol{\sigma}(t) &= \frac{k_1}{1+\nu}\left(\frac{\nu}{1-2\nu}\mathrm{tr}(\boldsymbol{\varepsilon})(t)\mathbb{I}+\boldsymbol{\varepsilon}(t)\right)+\frac{\eta_1}{(1+\nu)^{\frac{1}{2}}}\left(\frac{\nu}{1-2\nu}\mathrm{tr}(\dot{\boldsymbol{\varepsilon}}(t))\mathbb{I}+\dot{\boldsymbol{\varepsilon}}(t)\right)^{\frac{1}{2}} \\ &+\int_0^t \frac{k_2}{1+\nu}\left(\frac{\nu}{1-2\nu}\mathrm{tr}(\dot{\boldsymbol{\varepsilon}}(\tau))\mathbb{I}+\dot{\boldsymbol{\varepsilon}}(\tau)\right)e^{-\frac{t-\tau}{\theta_2}}d\tau \end{aligned} \tag{6.36}$$

Observe that the non-linear rate dependence of the Voigt damping term, $\eta_1\dot{\varepsilon}^{\frac{1}{2}}$, is now extended to the second term in Eq.6.36 in 3-D. As written the viscous term could imply: Either, the square root of a tensor, which requires the tensor, $\left(\frac{\nu}{1-2\nu}\mathrm{tr}(\dot{\boldsymbol{\varepsilon}})\mathbf{I}+\dot{\boldsymbol{\varepsilon}}\right)$ to be positive definite. For the general case it could be required that the Voigt term for 1-D experiments is proportional to, $\dot{\varepsilon}^P$, where P is an arbitrary number (as in Table 6.4). Therefore this formulation limits the possible values of P as it implies the computation of $\frac{\eta_1}{(1+\nu)^P}\left(\frac{\nu}{1-2\nu}\mathrm{tr}(\dot{\boldsymbol{\varepsilon}})\mathbf{I}+\dot{\boldsymbol{\varepsilon}}\right)^P$ in the 3-D expansion.

Alternatively, $\frac{\eta_1}{(1+\nu)^{\frac{1}{2}}}\left(\frac{\nu}{1-2\nu}\mathrm{tr}(\dot{\boldsymbol{\varepsilon}})\mathbf{I}+\dot{\boldsymbol{\varepsilon}}\right)^{\frac{1}{2}}$ implies the sign of the strain elements, multiplied by the square root of the absolute values of the elements of the tensor [105], in brackets: If $\boldsymbol{T}=\left(\frac{\nu}{1-2\nu}\mathrm{tr}(\dot{\boldsymbol{\varepsilon}})\mathbf{I}+\dot{\boldsymbol{\varepsilon}}\right)$ this implies:

$$\boldsymbol{T}^{\frac{1}{2}}=\begin{bmatrix}\mathrm{sgn}(T_{11})\,|T_{11}|^{\frac{1}{2}} & \mathrm{sgn}(T_{12})\,|T_{12}|^{\frac{1}{2}} & \mathrm{sgn}(T_{13})\,|T_{13}|^{\frac{1}{2}}\\ \mathrm{sgn}(T_{21})\,|T_{21}|^{\frac{1}{2}} & \mathrm{sgn}(T_{22})\,|T_{22}|^{\frac{1}{2}} & \mathrm{sgn}(T_{23})\,|T_{23}|^{\frac{1}{2}}\\ \mathrm{sgn}(T_{31})\,|T_{31}|^{\frac{1}{2}} & \mathrm{sgn}(T_{32})\,|T_{32}|^{\frac{1}{2}} & \mathrm{sgn}(T_{33})\,|T_{33}|^{\frac{1}{2}}\end{bmatrix} \tag{6.37}$$

This interpretation allows for any value of P but is not invariant as will be shown in subsequent paragraphs. The principle of material frame invariance requires that a constitutive equation must be invariant under change of frame [106]. This means that a material subjected to a specific load should experience the same stress regardless of the frame of reference in which the stress is calculated.

The invariance of the constitutive equation is tested in subsequent paragraphs by applying a strain, $\boldsymbol{\varepsilon}$ to the model and calculating the stress that arises in the viscous term, $\boldsymbol{\sigma}_{\eta_1}$. The same strain is transformed to a new frame, which lies at an angle ϕ to the reference frame. The stress, $\boldsymbol{\sigma}^{*}_{\eta_1}$ is calculated due to the strain, $\boldsymbol{\varepsilon}^{*}$. The stress in the transformed frame is rotated back to the original frame, $\boldsymbol{\sigma}^{test}_{\eta_1}$. For the model to be invariant, $\boldsymbol{\sigma}^{test}_{\eta_1}$ must equal $\boldsymbol{\sigma}_{\eta_1}$.

Thus, if $\boldsymbol{Q}$ is the proper orthogonal operator that transforms a second order tensor from a frame, $(x; y)$ to a new frame, $(x^*; y^*)$ (Fig.6.15) then:

$$\boldsymbol{\sigma^*} = \boldsymbol{Q\sigma Q}^T$$

If a simple longitudinal strain, ε, is applied to an isotropic material in the x-direction of

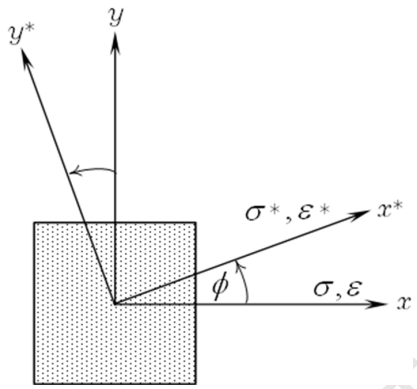

Figure 6.15: Rotation of the reference frame $(x; y)$ by an angle, ϕ, to the transformed frame, $(x^*; y^*)$

the $(x; y)$ frame, the relevant isotropic strain rate tensor is:

$$\dot{\boldsymbol{\varepsilon}} = \begin{bmatrix} \dot{\varepsilon} & 0 & 0 \\ 0 & -\nu\dot{\varepsilon} & 0 \\ 0 & 0 & -\nu\dot{\varepsilon} \end{bmatrix} \tag{6.38}$$

Then, the stress contribution of the Voigt dashpot reduces to:

$$\boldsymbol{\sigma}_{\eta_1} = \frac{\eta_1}{(1+\nu)^{\frac{1}{2}}} \left(\frac{\nu}{1-2\nu} \mathrm{tr}(\dot{\boldsymbol{\varepsilon}})\mathbf{I} + \dot{\boldsymbol{\varepsilon}} \right)^{\frac{1}{2}} = \begin{bmatrix} \eta_1 \dot{\varepsilon}^{\frac{1}{2}} & 0 & 0 \\ 0 & 0 & 0 \\ 0 & 0 & 0 \end{bmatrix} \tag{6.39}$$

If this frame is rotated anti-clockwise by an angle, ϕ, the transformed equivalent strain rate tensor in the $(x^*; y^*)$ frame is:

$$\dot{\boldsymbol{\varepsilon}}^* = \boldsymbol{Q}\dot{\boldsymbol{\varepsilon}}\boldsymbol{Q}^T = \dot{\varepsilon} \begin{bmatrix} \cos^2\phi - \nu\sin^2\phi & -(1+\nu)\cos\phi\sin\phi & 0 \\ -(1+\nu)\cos\phi\sin\phi & \sin^2\phi - \nu\cos^2\phi & 0 \\ 0 & 0 & -\nu \end{bmatrix} \tag{6.40}$$

Note that $\dot{\varepsilon}$ refers to the 1-D strain rate scalar and $\dot{\boldsymbol{\varepsilon}}$ refers to the strain rate tensor.

According to the model by Shim et al. [21] the viscous stress contribution in the rotated $(x^*; y^*)$ frame is given by:

$$\begin{aligned}\boldsymbol{\sigma^*}_{\eta_1} &= \frac{\eta_1}{(1+\nu)^{\frac{1}{2}}}\left(\frac{\nu}{1-2\nu}\mathrm{tr}(\dot{\boldsymbol{\varepsilon}^*})\mathbf{I}+\dot{\boldsymbol{\varepsilon}^*}\right)^{\frac{1}{2}} \\ &= \frac{\eta_1\dot{\varepsilon}^{\frac{1}{2}}}{(1+\nu)^{\frac{1}{2}}}\begin{bmatrix}(1+\nu)\cos^2\phi & -(1+\nu)\cos\phi\sin\phi & 0\\ -(1+\nu)\cos\phi\sin\phi & (1+\nu)\sin^2\phi & 0\\ 0 & 0 & 0\end{bmatrix}^{\frac{1}{2}}\end{aligned} \tag{6.41}$$

Taking the square roots of the absolute values of the individual elements as shown in Eq.6.37:

$$\boldsymbol{\sigma^*}_{\eta_1} = \eta_1\dot{\varepsilon}^{\frac{1}{2}}\begin{bmatrix}|\cos\phi| & -\sqrt{|\cos\phi\sin\phi|} & 0\\ -\sqrt{|\cos\phi\sin\phi|} & |\sin\phi| & 0\\ 0 & 0 & 0\end{bmatrix} \tag{6.42}$$

The equivalent stress tensor in the original frame is found by rotating $\boldsymbol{\sigma^*}_{\eta_1}$ clockwise from the $(x^*; y^*)$ frame back to the $(x; y)$ frame. The equivalent stress tensor, $\boldsymbol{\sigma}^{test}_{\eta_1}$, is compared with the original frame stress tensor, $\boldsymbol{\sigma}_{\eta_1}$, to test model invariance.

$$\boldsymbol{\sigma}^{test}_{\eta_1} = \boldsymbol{Q}^T\boldsymbol{\sigma^*}_{\eta_1}\boldsymbol{Q} \tag{6.43}$$

$$\begin{aligned}\sigma^{11_{test}}_{\eta_1} &= \eta_1\dot{\varepsilon}^{\frac{1}{2}}(\cos^2\phi\,|\cos\phi| + \sin^2\phi\,|\sin\phi| + 2\cos\phi\sin\phi\sqrt{|\cos\phi\sin\phi|}) \\ \sigma^{12_{test}}_{\eta_1} &= \sigma^{21_{test}}_{\eta_1} = \eta_1\dot{\varepsilon}^{\frac{1}{2}}((|\cos\phi| - |\sin\phi|)\cos\phi\sin\phi + (\sin^2\phi - \cos^2\phi)\sqrt{|\cos\phi\sin\phi|}) \\ \sigma^{22_{test}}_{\eta_1} &= \eta_1\dot{\varepsilon}^{\frac{1}{2}}(\cos^2\phi\,|\sin\phi| + \sin^2\phi\,|\cos\phi| - 2\cos\phi\sin\phi\sqrt{|\cos\phi\sin\phi|}) \\ \sigma^{13_{test}}_{\eta_1} &= \sigma^{31_{test}}_{\eta_1} = \sigma^{23_{test}}_{\eta_1} = \sigma^{32_{test}}_{\eta_1} = \sigma^{33_{test}}_{\eta_1} = 0\end{aligned}$$

The correct value for $\sigma^{11}_{\eta_1}$ is $\eta_1\dot{\varepsilon}^{\frac{1}{2}}$ and zero for all other elements in order to satisfy the principle of frame invariance. $\boldsymbol{\sigma}^{test}_{\eta_1}$ does not equal $\boldsymbol{\sigma}_{\eta_1}$ and shows that the formulation is not invariant. The values of the elements of the stress tensor (that result from frame transformation of the applied strain rate, calculated with the Shim constitutive equation and transformation back to the original frame) are shown in Fig.6.16 for all angles, ϕ. A maximum error of 41.4% occurs for $\sigma^{11_{test}}_{\eta_1}$ and $\sigma^{22_{test}}_{\eta_1}$ when the frame is rotated by $\phi = \frac{\pi}{4}$ and $\phi = \frac{5\pi}{4}$, respectively. The errors of the other stress elements are zero at these angles. The plotted values are normalised by dividing through with $\eta_1\dot{\varepsilon}^{\frac{1}{2}}$. The correct value for σ_{11} is thus 1 and zero for all other elements on the plot.

The magnitude of the total error is periodic and is calculated by:

$$\text{error} = \sqrt{(\sigma_{\eta_1}^{11_{test}})^2 + 2(\sigma_{\eta_1}^{12_{test}})^2 + (\sigma_{\eta_1}^{22_{test}})^2} \tag{6.44}$$

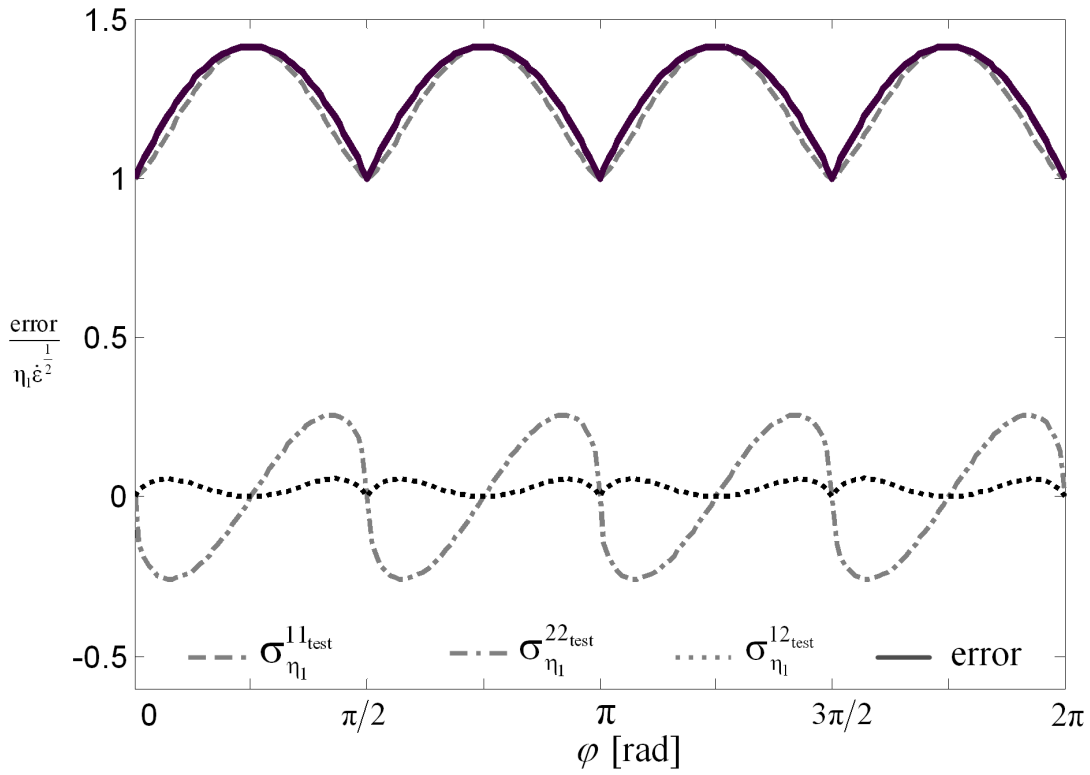

Figure 6.16: Errors in the elements of the stress tensor due to model violation of invariance for rotation of the reference frame through all angles, ϕ.

The following section proposes a slight modification which recovers invariance and is applicable to any viscoelastic model with a non-linear dependence on strain rate (such as the model of Tanabe and Kobayashi [16].

6.4 Proposed 3-D expansion of the viscous term and recovery of frame invariance

Constitutive equations describe the relationship between the measured stress, strain and strain rate. The 1-D curve-fit of stress vs. strain rate provides guidance as to what the form of the 3-D form of the viscous term should be. If the best fit of experimental data results in a relationship where the viscous stress is proportional to $\dot{\varepsilon}^P$, the 1-D formulation can be regrouped as:

$$\sigma_{\eta_1} = \eta_1 \dot{\varepsilon}^P = \eta_1 \dot{\varepsilon}^{(P-1)} \dot{\varepsilon} \tag{6.45}$$

It could be interpreted that η_1 is a non-linear function of $\dot{\varepsilon}^{(P-1)}$ and that their product is the parameter that relates the measured strain and stress. The strain rate, ε, is expanded to the strain rate tensor, $\boldsymbol{\varepsilon}$, when the formulation is expanded to 3-D. It is proposed that the parameter, η_1, is adjusted to be a function of the scalar quantity $\dot{\varepsilon}_{eq} = \sqrt{\frac{\dot{\boldsymbol{\varepsilon}}:\dot{\boldsymbol{\varepsilon}}}{1+2\nu^2}}$, (a contraction of the strain rate tensor with itself), when the constitutive relation is expanded from 1-D to 3-D. The parameter that relates the stress and strain tensors is thus expanded to the product, $\eta_1 \dot{\varepsilon_{eq}}^{(P-1)}$. The power operates on the scalar quantity ε_{eq} and allows the computation of any proportionality of the stress and strain rate:

$$\boldsymbol{\sigma}_{\eta_1} = f(\eta_1, \dot{\varepsilon}_{eq}, P)\dot{\boldsymbol{\varepsilon}} = \eta_1 \dot{\varepsilon}_{eq}^{P-1} \dot{\boldsymbol{\varepsilon}} \tag{6.46}$$

This formulation allows invariance to be recovered as will be shown in subsequent paragraphs. If the tensor relation, $\boldsymbol{\sigma}_{\eta_1}$ is replaced with: $\frac{\eta_1 \dot{\varepsilon}_{eq}^{P-1}}{(1+\nu)} \left(\frac{\nu}{1-2\nu} \mathrm{tr}(\dot{\boldsymbol{\varepsilon}})\mathbf{I} + \dot{\boldsymbol{\varepsilon}} \right)$ then:

$$\boldsymbol{\sigma^*}_{\eta_1} = \frac{\eta_1 \dot{\varepsilon}_{eq}^{P-1}}{(1+\nu)} \left(\frac{\nu}{1-2\nu} \mathrm{tr}(\dot{\boldsymbol{\varepsilon}}^*)\mathbf{I} + \dot{\boldsymbol{\varepsilon}}^* \right) = \eta_1 \dot{\varepsilon}^P \begin{bmatrix} \cos^2\phi & -\cos\phi\sin\phi & 0 \\ -\cos\phi\sin\phi & \sin^2\phi & 0 \\ 0 & 0 & 0 \end{bmatrix} \tag{6.47}$$

Here $\dot{\varepsilon}_{eq} = \sqrt{\frac{\dot{\boldsymbol{\varepsilon}}:\dot{\boldsymbol{\varepsilon}}}{1+2\nu^2}} = \dot{\varepsilon}$ and therefore $P = \frac{1}{2}$ if a proportionality of $\sigma \propto \dot{\varepsilon}^{\frac{1}{2}}$ is desired. The rotation $\boldsymbol{\sigma}_{\eta_1}^{test} = \boldsymbol{Q}^T \boldsymbol{\sigma}_{\eta_1}^* \boldsymbol{Q}$ gives:

$$\sigma_{\eta_1}^{11_{test}} = \eta_1 \dot{\varepsilon}^{\frac{1}{2}} \left(\cos^2\phi(\cos^2\phi + \sin^2\phi) + \sin^2\phi(\cos^2\phi + \sin^2\phi) \right) = \eta_1 \dot{\varepsilon}^{\frac{1}{2}}$$

$$\sigma_{\eta_1}^{12_{test}} = \eta_1 \dot{\varepsilon}^{\frac{1}{2}} \left(\sin\phi\cos\phi(\cos^2\phi + \sin^2\phi) - \cos\phi\sin\phi(\cos^2\phi + \sin^2\phi) \right) = 0$$

with all other entries easily reducing to zero. Simplifying,

$$\boldsymbol{\sigma}_{\eta_1} = \eta_1 \dot{\varepsilon}^{\frac{1}{2}} \begin{bmatrix} 1 & 0 & 0 \\ 0 & 0 & 0 \\ 0 & 0 & 0 \end{bmatrix} \tag{6.48}$$

Thus, $\boldsymbol{\sigma}_{\eta_1}^{test}$ equals the original untransformed stress tensor, $\boldsymbol{\sigma}_{\eta_1}$ for any angle of frame rotation, showing that the proposed model is invariant. Additional advantages of this formulation are that 3-D stress calculations are possible for any desired proportionality of stress and strain rate as all values of P operate on $\dot{\varepsilon}_{eq}$, which is a scalar quantity. The proposed 3-D expansion of the Shim et al. [21] viscoelastic model is thus proposed as:

$$\begin{aligned}\boldsymbol{\sigma}(t) &= \frac{k_1}{1+\nu}\left(\frac{\nu}{1-2\nu}\mathrm{tr}(\boldsymbol{\varepsilon}(t))\mathbb{I}+\boldsymbol{\varepsilon}(t)\right)+\frac{\eta_1\dot{\varepsilon}_{eq}^{P}}{(1+\nu)}\left(\frac{\nu}{1-2\nu}\mathrm{tr}(\dot{\boldsymbol{\varepsilon}}(t))\mathbb{I}+\dot{\boldsymbol{\varepsilon}}(t)\right)\\ &\quad+\int_0^t\frac{c_1}{1+\nu}\left(\frac{\nu}{1-2\nu}\mathrm{tr}(\dot{\boldsymbol{\varepsilon}}(\tau))\mathbb{I}+\dot{\boldsymbol{\varepsilon}}(\tau)\right)e^{-\frac{t-\tau}{\theta}}d\tau \qquad (6.49)\end{aligned}$$

It is concluded that:

- **It is possible to improve the modelling of the strain rate dependent material response of viscoelastic materials by adding viscous effects that depend non-linearly on strain rate** (i.e. $\sigma_\eta = \eta\dot{\varepsilon}^P$).
- When this formulation is expanded to 3-D the strain rate is replaced with the strain rate tensor, which implies that the equivalent 3-D form of $\dot{\varepsilon}^P$ must be found. **The limitation of possible values of P and invariance problems are overcome if the viscous damping parameter is modelled as a function of the equivalent strain rate $\dot{\varepsilon}_{eq}$ instead of the strain rate tensor, $\dot{\boldsymbol{\varepsilon}}$. This formulation allows invariance to be recovered and does not present computational difficulty for any value of P.**

Chapter 7

Model verification and validation

The strain rate dependent mechanical properties of bovine cortical bone in compression was determined through experimentation and modelled with a viscoelastic constitutive relation in 1-D. The relation was extended to an isotropic 3-D model in the previous chapter. The subsequent discussion will present the implementation of this model in finite elements, where the isotropic 3-D model was implemented in the finite element (FE) package, ABAQUS. ABAQUS allows users to implement a user-defined material model as a VUMAT. The existing viscoelastic models in ABAQUS require the determination of material parameters through creep or relaxation testing. As discussed earlier in Section 2.3.2, no existing methods were found in literature for testing the relaxation behaviour of materials at dynamic strain rates in the order of $\dot{\varepsilon} = 10^2\,\mathrm{s}^{-1}$. For this reason a constitutive relation was developed from strain rate dependent compression test responses. In the present chapter this isotropic 3-D constitutive model will be implemented in a user defined material subroutine, which is discussed under the topics of *verification* and *validation.*The concepts of verification and validation are defined based on a description of these concepts by Krauthammer [107]:

- *Verification:* Determining if the simulation tool can correctly produce results consistent with the models on which it is based.
- *Validation* against quasi-static and dynamic experiments to determine the appropriateness of the principles and mathematical methods used to develop a simulation tool.

7.1 User defined material models in ABAQUS

The implementation of a material model in ABAQUS involve the integration of the state of the material at integration points over the time increment in the course of a non-linear analysis. Each material integration point is treated separately and therefore material

behaviour can be assumed to be defined locally. Element behaviour in ABAQUS is formulated in terms of the updated Lagrangian or material description. In this formulation the element deforms with the material. The state of the element at the beginning of each time step is treated as the reference state and hence small strain assumptions are valid throughout the analysis.

A VUMAT is a user defined subroutine that is used to define the constitutive mechanical behaviour of a material in ABAQUS [108]. This subroutine is suitable for implementation with the ABAQUS/Explicit solver. The computation of the material state with a VUMAT subroutine is described in the following steps:

- Strain measures are calculated with respect to the mid-increment configuration. At each time step the total strain increment components for each integration point are passed to the user subroutine.

- Field variables (such as the material density) are passed into the subroutine by ABAQUS.

- The strain increments are subsequently used to calculate the stresses with user-defined constitutive relations. All tensor quantities are defined in a corotational coordinate system which means that the coordinate system rotates with the material as it deforms. The stress tensor and state variables are therefore directly computed in the user subroutine VUMAT. The tensors do not have to be rotated by the user.

- Any user defined material constants that are needed in the user subroutine must be specified as part of the user defined material definition. All mechanical material calculations are to be programmed into the subroutine. The user can use and update solution-dependent-state variables which can be defined according to the needs of the constitutive algorithm (such as the stress or strain in the previous time step).

- Element deletion in a mesh can be controlled in the course of an ABAQUS/Explicit analysis through the VUMAT user subroutine. A state variable is created for this purpose. The value of this variable must be set to either one or zero in the VUMAT. A value of one indicates that the material point is active. A value of zero indicates that ABAQUS/Explicit should delete the material point by setting the stresses to zero. Deleted elements have no ability to carry stress and therefore have no contribution to the stiffness of the model. Once a material point has been deleted it can not be reactivated.

7.1.1 A VUMAT for bovine cortical bone

The VUMAT user subroutine is based on the 3-D isotropic extension of the five parameter viscoelastic constitutive relation which was developed in Section 6.4:

$$\begin{aligned}\boldsymbol{\sigma}(t) &= \frac{k_1}{1+\nu}\left(\frac{\nu}{1-2\nu}\mathrm{tr}(\boldsymbol{\varepsilon}(t))\mathbf{I}+\boldsymbol{\varepsilon}(t)\right)+\frac{\eta_1\dot{\varepsilon}^P_{eq}}{(1+\nu)}\left(\frac{\nu}{1-2\nu}\mathrm{tr}(\dot{\boldsymbol{\varepsilon}}(t))\mathbf{I}+\dot{\boldsymbol{\varepsilon}}(t)\right)\\ &\quad+\int_0^t\frac{c_1}{1+\nu}\left(\frac{\nu}{1-2\nu}\mathrm{tr}(\dot{\boldsymbol{\varepsilon}}(\tau))\mathbf{I}+\dot{\boldsymbol{\varepsilon}}(\tau)\right)e^{-\frac{t-\tau}{\theta}}d\tau \qquad (7.1)\end{aligned}$$

Five of the parameter values that are required for the implementation of this model were determined for the 1-D case in Section 6.2.3 as a result of a parameter identification process. The Poisson's ratio was not determined experimentally, but taken directly from literature (by Ashman et al.[61], Katsamanis and Raftopoulos [15] and Ebacher et al.[38] (see Table 2.4 in Section 2.4.1)) to be $\nu = 0.36$. The eight parameters which are required for the implementation of the 3-D viscoelastic constitutive model are listed in Table 7.1. The final two parameters α and β describe material failure and are discussed in Section 7.1.2.

k_1 [GPa]	η_1 [MPa. s^{-1}]	k_2 [GPa]	η_2 [MPa. s^{-1}]	P	ν	α	β
3.98	8.58	12.84	14.37	0.28	0.36	51.4	0.057

Table 7.1: The parameters and parameter values which were used in the viscoelastic VUMAT subroutine to approximate the mechanical behaviour of the strain rate dependent compression of bovine cortical bone

The calculation of the material state through Eq.6.49 with the VUMAT subroutine is presented in Appendix D. Since the model is isotropic the stress and strain tensors are symmetric. The component order is given by the natural permutation of the indices of the tensor in Table 7.2.

Component	1	2	3	4	5	6
3-D stress tensor	σ_{11}	σ_{22}	σ_{33}	σ_{12}	σ_{23}	σ_{31}

Table 7.2: Tensor component order for the user subroutine

The subroutine utilizes 34 state variables which are listed in Table 7.3. Only variables 1 - 12 and 32 are essential for the operation of the subroutine. The other variables were supplied to facilitate the verification process.

State variable number	Property
1 - 6	The total strain components
7 - 12	$\frac{\nu}{1-2\nu}\left(\mathrm{tr}(\dot{\boldsymbol{\varepsilon}}(t))\mathbf{I} + \dot{\boldsymbol{\varepsilon}}(t)\right)$
13 - 18	Maxwell stress contributions
19 - 24	Elastic stress contributions
25 - 30	Viscous stress contributions
31	$\dot{\varepsilon}^P_{eq}$
32	Parameter that controls element deletion
33	Failure stress
34	Von Mises stress

Table 7.3: Solution-dependent-state variables which were stored in the course of the VUMAT user subroutine

7.1.2 Criteria for element deletion

Element deletion in a mesh can be controlled in the course of an ABAQUS/Explicit analysis through the VUMAT user subroutine. Deleted elements have no ability to carry stress and therefore have no contribution to the stiffness of the model. Three different failure criteria are applied in the course of this chapter. The criteria arise form the discussion in Section 5.1.4 where curve-fit approximations were developed that describe the failure and fracture stresses in terms of specimen density and strain rate.

Material failure criterion

The first is associated with material failure, which is described in Section 5.1.4. The relation that describes the strain rate dependent failure of bone is repeated here for convenience:

$$\sigma_f = 51.4\ \dot{\varepsilon}^{0.057}\rho^2 \tag{7.2}$$

An argument which motivates the implementation of this criterion is that the onset of failure in bone is associated with the formation of damage and the incidence of injury. If an element is deleted when its stress has reached a level which is associated with failure, this could serve as method to induce damage in the structure. Another positive argument for the use of the failure criterion to dictate element deletion is that the compressive yield point is more representative of the ultimate tensile and yield stresses for bone. As discussed in Section 2.2.5, Ebacher et al. [38] reported that the tensile and compressive response of bone is similar up to tensile yield. Beyond this point tensile bone response displays significant plastic deformation before fracture. The use of the material failure criterion (which corresponds to material yield) would therefore be the most appropriate available criterion if the current model (which was developed for compression) were to be

implemented to model bending or tensile response.

Material fracture criterion

The second criterion is that which describes the material ultimate stress. In this case the constitutive relation is required to describe material response up to the point of fracture. Recall from Section 6.2.3 that Eq.7.1 was developed on a premise which excludes damage. The model response does not represent the significant softening in the stress-strain curves which is associated with the onset of material failure. The implementation of the material fracture criterion is acceptable at quasi-static strain rates because the stress-strain curves soften very close to the point of ultimate fracture. **However, it is not recommended that this criterion is implemented in cases which consider higher strain rate loads (above $\dot{\varepsilon} = 10^{-1}\,\mathrm{s}^{-1}$): the deviation from response in the middle strain rate region is not known; and at strain rates of $\dot{\varepsilon} = 10^{2}\,\mathrm{s}^{-1}$ and above it is known that the constitutive stress-strain relationship over-estimates the response beyond failure (Section 6.2.3)** .

Recall from Section 5.1.4 that this criterion is described by:

$$\sigma_f = 61.2\ \dot{\varepsilon}^{0.06}\rho^2 \tag{7.3}$$

Carter and Hayes [88] criterion

The density and strain rate dependent criterion developed by Carter and Hayes [88] (Eq.7.4) is widely used to predict the incidence of bone fracture. This criterion is implemented in the present analysis to further inform the hypothesis that all bone can be viewed as a single material with a varying density.

$$\sigma_f = 68\ \dot{\varepsilon}^{0.06}\rho^2 \tag{7.4}$$

Furthermore the implementation of the Carter an Hayes criterion enables the assessment of its applicability to the current data. As discussed in Section 5.1.4 this criterion over-predicts the ultimate stress for bovine cortical bone in quasi-static and dynamic experiments as presented in this study.

The extension of failure criteria for implementation in 3-D

The three stress based failure criteria can be presented by a relation of the form:

$$\sigma_f = \alpha\rho^2\dot{\varepsilon}^{\beta} \tag{7.5}$$

This relation can be extended to present the compressive strength in multi-axial loading in 3-D by replacing the 1-D failure stress with an appropriate measure of the multi-axial stress

state in 3-D. It was decided that **elements are to be deleted when the Von Mises stress reaches a critical value. The Von Mises stress describes the element distortion which is associated with shear stress. It was deemed to be the appropriate stress measure for failure because cortical bone is perceived to fail in shear during compression.** Furthermore the equivalent strain rate replaces the 1-D strain rate when the multi-axial deformation rate of the material is to be described.

$$\sigma_{VM} = \alpha \rho^2 \dot{\varepsilon}_{eq}^{\beta} \tag{7.6}$$

where

$$\dot{\varepsilon}_{eq} = \sqrt{\frac{\dot{\boldsymbol{\varepsilon}} : \dot{\boldsymbol{\varepsilon}}}{1 + 2\nu^2}}$$

and

$$\sigma_{VM} = \sqrt{\frac{(\sigma_1 - \sigma_2)^2 + (\sigma_2 - \sigma_3)^2 + (\sigma_1 - \sigma_3)^2}{2}}$$

The implementation of the VUMAT for bovine cortical bone thus requires two parameters α and β to describe the stress based failure response of this material.

7.2 The stable time increment

Due to their inherent lack of convergence problems explicit finite element techniques are widely used for analysing non-linear mechanical processes [109]. With an explicit method the state of the model is advanced through an increment of time, Δt, based on the state of the models at the start of the increment at time t. **The stability limit dictates the maximum time increment of the ABAQUS/Explicit solver and has a great effect on reliability and accuracy. The stability limit must therefore be determined consistently and conservatively.** For computational efficiency ABAQUS/Explicit chooses the stable time increment to be as close as possible to the stability limit without exceeding it. If the time increment is larger than the stability limit this could lead to numerical instability, which may result in an unbounded solution.

The stable time increment is effected by the:

- **Mesh size**
- **The stiffness and damping characteristics of the elements which influence the highest frequency of the system.**

On an element to element basis, the stability limit can be defined using the element

length, L^e and the wave speed of the material, c.

$$\Delta t_{stable} = \frac{L^e}{c} \tag{7.7}$$

Eq.7.7 indicates that the maximum time increment of the explicit analysis should not exceed the time in which a stress wave can travel the length of an element. Consider the example where an elastic stress wave is propagating through a material towards element E_N (Fig.7.1(a)). At a $t = t_1$ the wave front is located in element E_{N-1}. The distance that the wave travels is equal to $c\Delta t$. If the time increment is too large, the elastic wave front could be located at element E_{N+1} at $t = t_1 + \Delta t$ (Fig.7.1(b)). Thus, the elastic wave front has passed through element E_N, without the algorithm detecting the presence of the elastic wave. To prevent this the maximum time increment is bounded by Eq.7.7. This implies that the explicit analysis is forced to choose smaller stable time increments for finer meshes.

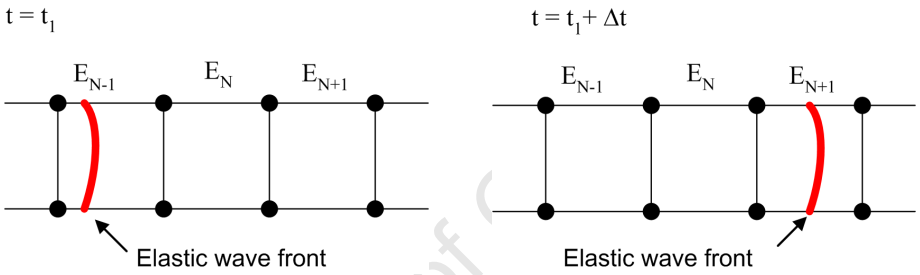

Figure 7.1: An elastic wave passes through element E_N undetected because the time increment, Δt is too large

The stability limit is also defined in terms of the highest frequency in the system (ω_{max}). **ABAQUS cautions users that care should be taken when introducing dashpots into the finite element mesh as the explicit solver does not take them into account when determining the stable time increment [108].** The stable time increment is determined at $t = 0.0$ when ABAQUS sends a set of fictitious strains to the VUMAT. The initial elastic wave speeds are calculated from this step in which the strain rate is zero. A dashpot introduces a damping force between two degrees of freedom, without introducing a mass at the nodes or a stiffness between them. For a material element described by the Shim viscoelastic model, the Voigt dashpot introduces such a damping force. The dynamic equation of the system is described by Eq.6.11 which was discussed in Section 6.1. The stable time increment is computed by ABAQUS with:

$$\Delta t_{stable} = \frac{2}{\omega}\left(\sqrt{1+\zeta^2} - \zeta\right) \quad \text{where} \quad \omega = \sqrt{\frac{k}{m}} \quad \text{and} \quad \zeta = \frac{\eta}{2\sqrt{km}} \tag{7.8}$$

In Eq.7.8, ζ (which defines the limit between oscillatory and non-oscillatory motion) is the fraction of critical damping in the mode with the highest frequency. **Contrary to**

engineering intuition, damping always reduces the stability limit. For this reason the stable time increment is in fact smaller than the time increment which is estimated by the explicit solver. If the stiffness of the spring elements of the chosen material model is such that the stable time increment of the dashpot and spring is smaller than that calculated by ABAQUS the user has to set the time increment.

Because of the stiffness and damping properties of the material model, **ABAQUS calculated the stable time increment for a** 1 mm **cubed element to be** 1.398×10^{-7} seconds **which is reduced to** 2.162×10^{-8} seconds **for a mesh size of** 0.5 mm**. However it was found that the model solutions were only reliable when the maximum time increments were dictated to be** 1×10^{-9} seconds **and** 1×10^{-10} seconds **respectively.** This is further discussed in Section 7.4.

The present model therefore requires significant simulation time when considering the strain rate dependent response of bone in quasi-static experiments. As an example, the compression to fracture of a specimen at $\dot{\varepsilon} \approx 10^{-3}\,\text{s}^{-1}$ could last up to 36 seconds. This would require billions of time steps to complete if the stable time increment is of the order of 1×10^{-10} seconds. This problem is rectified by using a technique called mass scaling.

7.3 Mass scaling

The modelling of strain rate dependent quasi-static compression requires that the FEM analysis be conducted in ABAQUS/Explicit (as opposed to ABAQUS standard).

If a model has a very small stable time step, Δt_{stable} this slows the analysis down a great deal. If, for example, the stable time step is $1 \times 10^{-10}\,\text{s}^{-1}$ and the quasi-static compression event lasts for 40 seconds, the processor is required to compute the material state at each increment, that is $n = 4 \times 10^{11}$ increments.

It is therefore desirable to decrease the ratio of the event time to the time of wave propagation across the element. A further requirement is that the event time should remain fixed, so that the strain rate dependency of the material remains unaffected. The computational cost for a quasi-static analysis can be decreased by using mass scaling.

With the approach of mass scaling, the material density is artificially increased by a factor f^2, which reduces the number of increments, n, to $\frac{n}{f}$. It is possible to include rate dependent behaviour in the analysis because mass scaling reduces the ratio of the event time to the time for wave propagation across an element, while leaving the event time fixed. Mass scaling has exactly the same effect on inertia forces as speeding up the time of the simulation. **It is an attractive technique because it can be used in rate-dependent problems. Care must be taken to ensure that inertia forces do not change and dominate the solution. Either fixed or variable mass scaling can be invoked.**

7.4 A single element bone model

7.4.1 Verification of isotropic model response and mathematical integrity

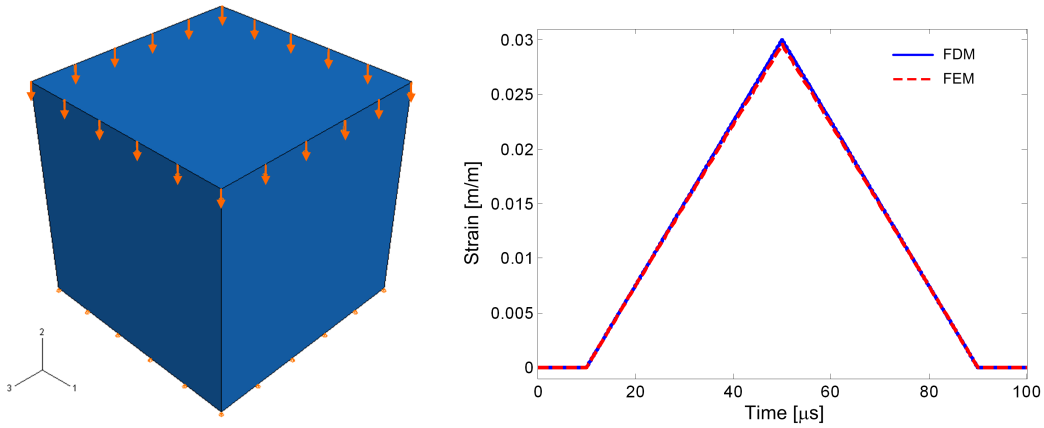

(a) (b)

Figure 7.2: (a) The single element FEM (b) Comparison of the applied strain history

A single bone element (1 mm ×1 mm ×1 mm) was compressed in ABAQUS to test if the finite element model (FEM) stress predictions agree with the element stress from the finite difference model (FDM) which was constructed in MATLAB. The element was tested by applying a triangular strain pulse of 0.03 m/m at a strain rate of 800 s^{-1} (Fig.7.2(b)). No element deletion was implemented at present. The single element model was deformed in all three principle directions to test if the supposedly isotropic material provided the same response regardless of the direction of loading. The time histories of the elastic (Fig.7.3(a)), Maxwell (Fig.7.3(b)) and viscous (Fig.7.3(c)) terms as calculated by the FDM model in MATLAB and the FEM in ABAQUS are compared in Table 7.4.

		FDM [MPa]		FEM [MPa]
Elastic stress component		+119.4		+117.7
Viscous stress component	Max	+54.5	Max	+54.4
	Min	-54.5	Min	-54.5
Maxwell stress component		+377.8		+372.8
Total stress	Max	+551.7	Max	+542.2
	Min	-67.3	Min	-67.6

Table 7.4: Comparison between FEM and FDM stress predictions

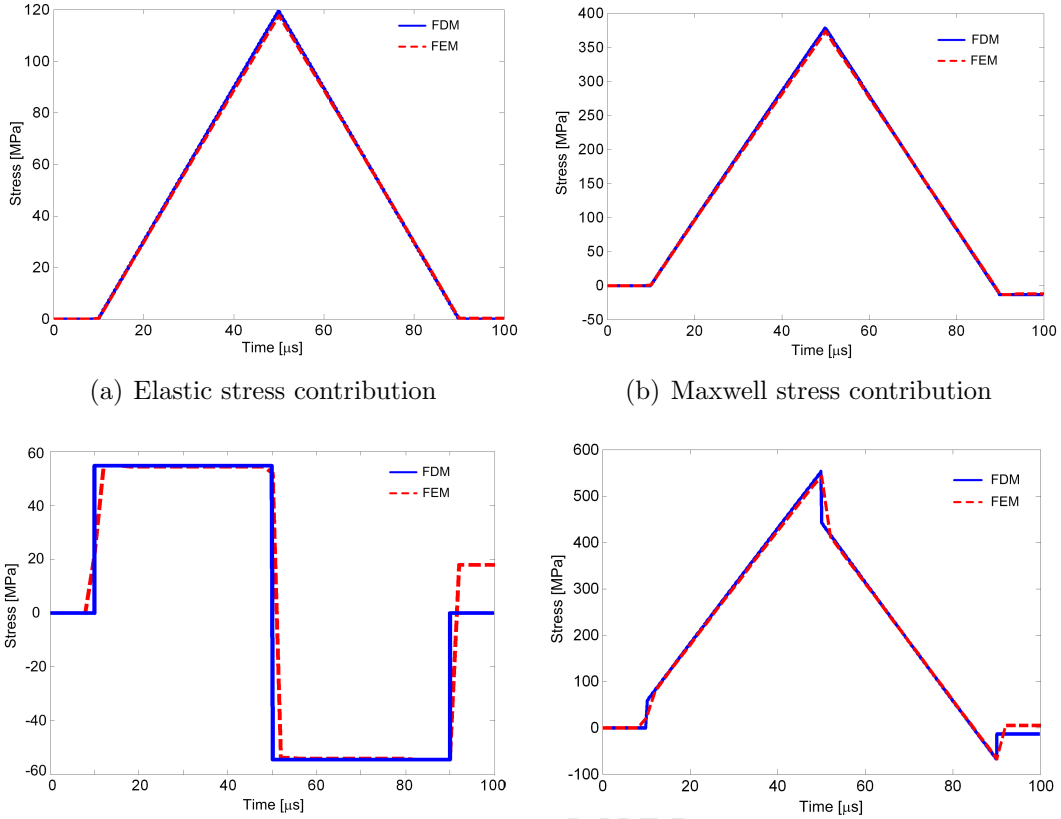

(a) Elastic stress contribution

(b) Maxwell stress contribution

(c) Viscous stress contribution

(d) Total element stress

Figure 7.3: Comparison of the elastic, viscous and Maxwell stress components which are predicted by the FEM and FDM

The stress histories of the elastic and Maxwell terms in the FE simulation are a perfect match for their analytical counterparts. The Voigt stress fails to return to the desired value of zero (between $90 - 100\,\mu s$) in the final stage of the verification test. This inaccuracy is attributed to the fact that the time increment, which is calculated by the explicit solver, is too large. The algorithm which determines the stable time step ignores the effect of damping which always reduces the stability limit. The Voigt damping term therefore dictates the magnitude of the stable time increment.

The stress contribution of the Voigt dashpot is further investigated to determine the effect of time incrementation on model response. Fig.7.4 presents the resulting viscous stress history if a user defined time increment is supplied to the ABAQUS/Explicit solver. Automatic calculation of the stable time step by ABAQUS/Explicit results in a stable time step, $\Delta t_{stable} \approx 1.398 \times 10^{-7}$ seconds. The accuracy of the viscous response improves if the time step is decreased. The solution is most accurate when the viscous material state is advanced by $\Delta t \approx 10^{-9}$ to 10^{-10} seconds. A further decrease in the time increment results in a suboptimal solution which is attributed to numerical noise. The time increment is so small that a slight increase in strain results in an uncharacteristically high strain rate. Recall that the response of the Voigt model to an instantaneous strain rate is a contant

stress and the *dirac-delta* impulse function. **It is therefore concluded that the optimal time increment for the numerical stability of the viscoelastic bone VUMAT model is between $\Delta t \approx 10^{-9}$ to 10^{-10} seconds if the viscous stress contribution is expected to be significant. This significantly increases the computational cost of the present VUMAT model. Additionally, caution is advised if the model response is to be considered in cases where the loading is expected to have sharp, rapid changes in strain rate.**

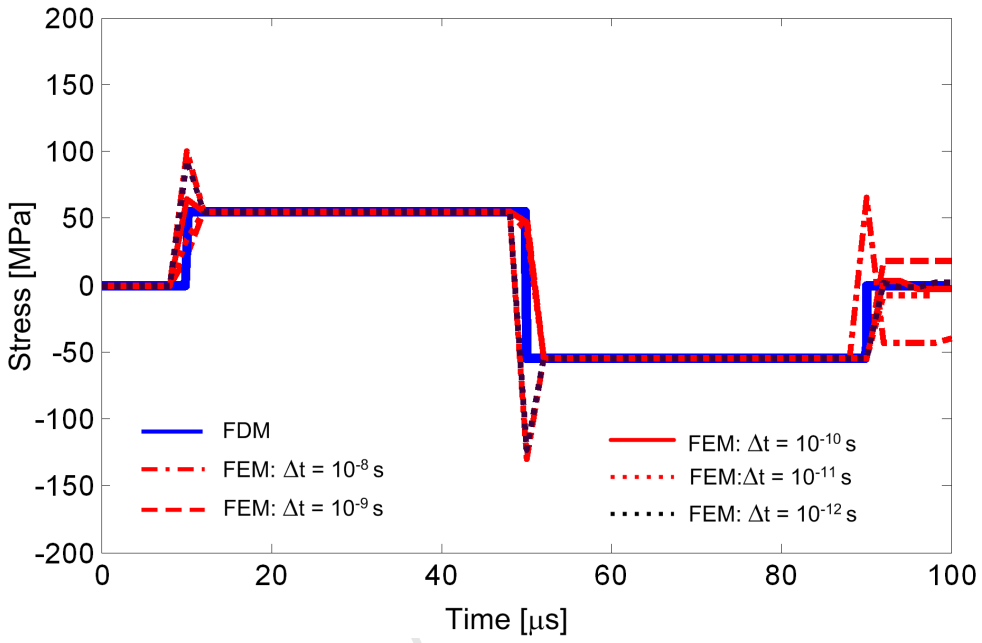

Figure 7.4: The effect of the time increment on the Voigt stress response

Notice that the effect of the inaccuracy (at a stable time increment of $t_{stable} = 10^{-10}\,\text{s}^{-1}$ in the Voigt stress response contributes very little to the error in the total element stress (Fig.7.3(d)). The capabilities of the VUMAT model were purposely demonstrated at a high strain rate to illustrate the potential magnitude of an excessively large stable time increment. This effect is increasingly smaller at lower strain rates.

7.4.2 Verification of responses and failure in tension and compression

Fig.7.5 shows the tensile and compressive responses (and failure) of a single element FEM model (Fig.7.2(a)) as a result of displacements at different strain rates. The bottom surface of the element was constrained from movement in the direction of the load. A ramp displacement was applied to the top surface of the element. This resulted in an immediate and constant strain rate in the element which is proportional to the slope of the ramp displacement. Notice that the immediate presence of a finite strain rate causes instantaneous stress in the material which is attributed to the stress contribution of the

Voigt dashpot. The element stress increases with increasing strain.

Elements were deleted when the Von Mises stress reached a critical value as determined by the material failure criterion ($\alpha = 54.2$ and $\beta = 0.057$). A material test density of $\rho = 2000\,\text{kg.m}^{-3}$ was used. It was verified that bone elements fail at identical stresses in tension and compression. Table 7.5 presents a comparison of the analytical and FEM failure stresses. The FEM model elements fail at stresses which are within 4% of the analytical result.

$\dot{\varepsilon}[\text{s}^{-1}]$	Analytical σ_{f_A}[MPa]	FEM $\sigma_{f_{FEM}}$[MPa]	Error [%]
$\dot{\varepsilon} = 10^{-3}$	138.7	143.5	3.5
$\dot{\varepsilon} = 10^{-2}$	158.1	162.0	2.5
$\dot{\varepsilon} = 10^{-1}$	180.3	184.8	2.5
$\dot{\varepsilon} = 2.5 \times 10^{2}$	281.6	278.0	1.2
$\dot{\varepsilon} = 10^{3}$	304.8	307.0	1.0

Table 7.5: Verification of the strain rate dependent failure stress

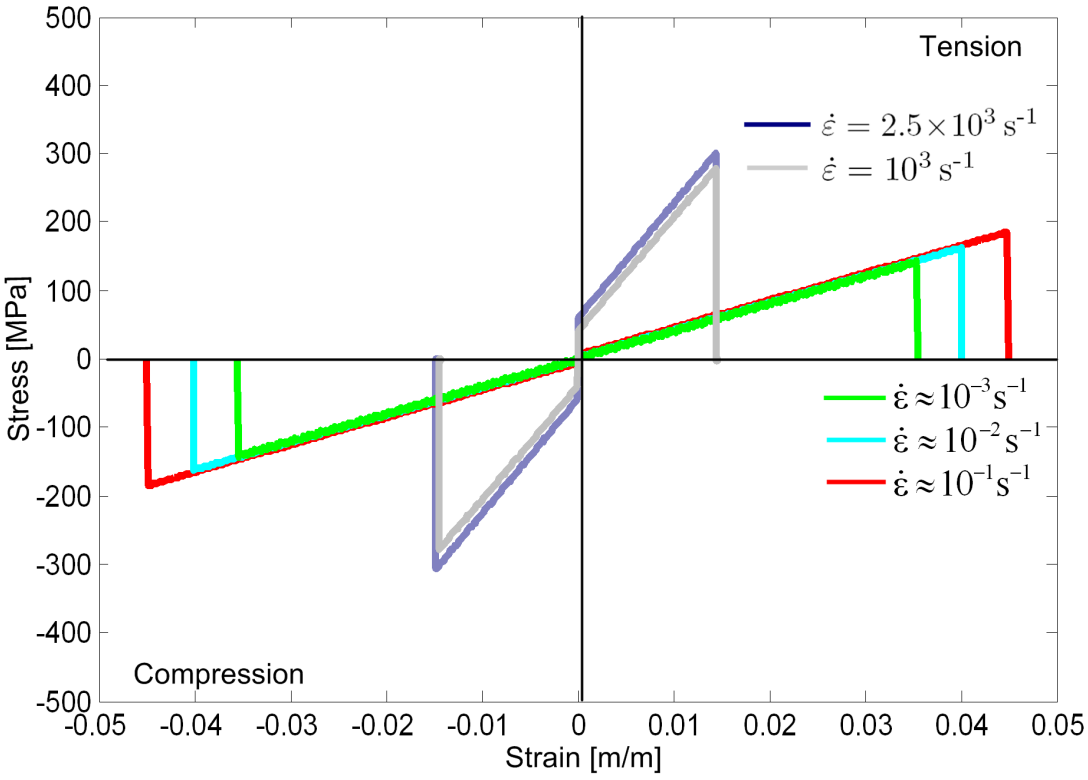

Figure 7.5: Tensile and compressive response of a single 1 mm bone element with failure at different strain rates

The VUMAT user subroutine is therefore verified in that it responds consistently with the models which govern its stress-strain responses and failure. It has been confirmed that the subroutine results are indeed isotropic and that it is capable of simulating bone response in both tension and compression.

7.5 Quasi-static model validation experiment

This section presents a quasi-static compression experiment on a bovine mid-diaphysis section. A 50 mm section of the mid-diaphysis of a bovine femur was compressed in the Zwick Universal Test Machine at the Centre for Materials Engineering at the Department of Mechanical Engineering of the University of Cape Town. The head displacement of the screw driven test machine was set to $0.5\,\mathrm{mm.\,s^{-1}}$. The time, force and displacement of the machine head were recorded.

A finite element model of the experiment was created in ABAQUS. The geometry of the bone diaphysis was accurately recreated from CT-scan images. The VUMAT user subroutine was implemented without any further material tests on the actual femur diaphysis material. Only the material density was determined. In the FEM analysis the diaphysis was compressed by applying the displacement measured from the Zwick Universal test machine to the top face of the specimen. The FEM model reaction force was recorded at the base of the bone by a reference point on an analytical rigid surface. This reaction force was compared to the force measurement of the Zwick test machine during the diaphysis compression experiment.

The successful correlation of the simulation and experimental force-time histories would serve:

- Verify that the VUMAT material model represents the quasi-static strain rate sensitivity of bone in compression.
- Test the performance of the material model when implemented in multiple element, quasi-static, whole bone problems.
- Assess the ability of a FEM model with a well characterised material and accurate geometry to identify the regions in the bone which are predisposed to injury. The regions of stress concentration and bone damage will be compared with the fractures encountered in the test specimen.

7.5.1 The quasi-static finite element model

Bone geometry and meshing

The modelling of the diaphysis compression experiment requires the acquisition of bone geometry. Computer Tomography (CT) scan data sets are frequently used as a reference for the creation of biomechanical models of the skeleton [110, 30]. Bone solid geometry is conventionally created by the extraction of edge contours from CT images with segmentation or in-house software [110]. No segmentation software was available to the author at the time of this study. In the absence of a standard bovine femur bone finite element

geometry a basic tool was developed in MATLAB to extract the surface geometry from CT-scan images. This tool would also facilitate bone modelling in future work.

A CT-scan was conducted on the bovine diaphysis specimen at the University of Cape Town Medical Centre. An example of a CT imaqe is shown in Fig.7.6(a). The image format is `.JPEG` with a resolution is a 512×512 and covers an area of $10.6\,\text{cm} \times 10.6\,\text{cm}$. This provides a means of scaling the image to its real life size. A total of 56 images were taken at 3 mm increments (of which 16 contain bone geometry data). The MATLAB Image Processing Toolbox was used to read the `.JPEG` CT-scan images with the command `imread`. MATLAB interprets an image as a 512×512 matrix, where the pixel position is related to the row-column index and the colour is equal to the entry value (Fig.7.6(b)). The CT image annotations were removed by selecting a smaller window of points within the image data. The colourmap of the data was converted to grayscale, in which the value of each matrix entry (i.e. the colour of each pixel) is scaled to a value between 0 and 1. Because the CT-scan consisted only of bone and air, a simplified approach was applied to easily identify the bone edges. The grayscale image was used to create a purely black or white image by using a thresholding technique. In thresholding all the colours that are darker than a certain value were changed to black. The remaining pixels are set to be white (Fig.7.6(c)). The bone edges lie where the pixel colour changes from black to white. The inside and outside edges of the bone geometry were extracted by using edge-detection techniques available in the Image Processing Toolbox (Fig.7.6(d)). The algorithm detects edges by taking the derivative of the matrix values in the matrix space, therefore detecting the change in colour. The uniform geometry of the bone diaphysis enables the anticipation of the approximate diameters of the edge curves. The algorithm is instructed to count the amount of edge curves and calculate their diameters. If more than two curves are found it indicates that an imperfection such as an artery canal is present in the bone cortex. This curve is eliminated on the basis of its diameter. At this stage imperfections were not included in the diaphysis model. It is computationally expensive to extract the many edge points for every slice. Again, a simplified approach was implemented in which 31 of the edge points were extracted. An approximate central axis was calculated by finding the mid-point of the endo-osteal space for each slice and averaging over all the slices. The cartesian coordinates of the edge curves were converted to polar coordinates (using the `cart2pol` functions). A stencil of lines was created at 31 angle increments with the central axis as the origin (Fig.7.7(a)). The intersection of the bone edge-curves and the stencil lines were calculated for the inside and outside edges of every CT-slice as shown in Fig.7.7(b). The `x-y` edge data are assigned a `z` -value on the basis of the slice number. This results in a grid of points that map the bone surface geometry (Fig.7.7(c)). In Fig.7.7(d) the inner- and outer bone faces can be visualised by creating surfaces between the grid points with the `patch` command. This step is included to check the smoothness of the face geometry and the spacing of the grid point data. The

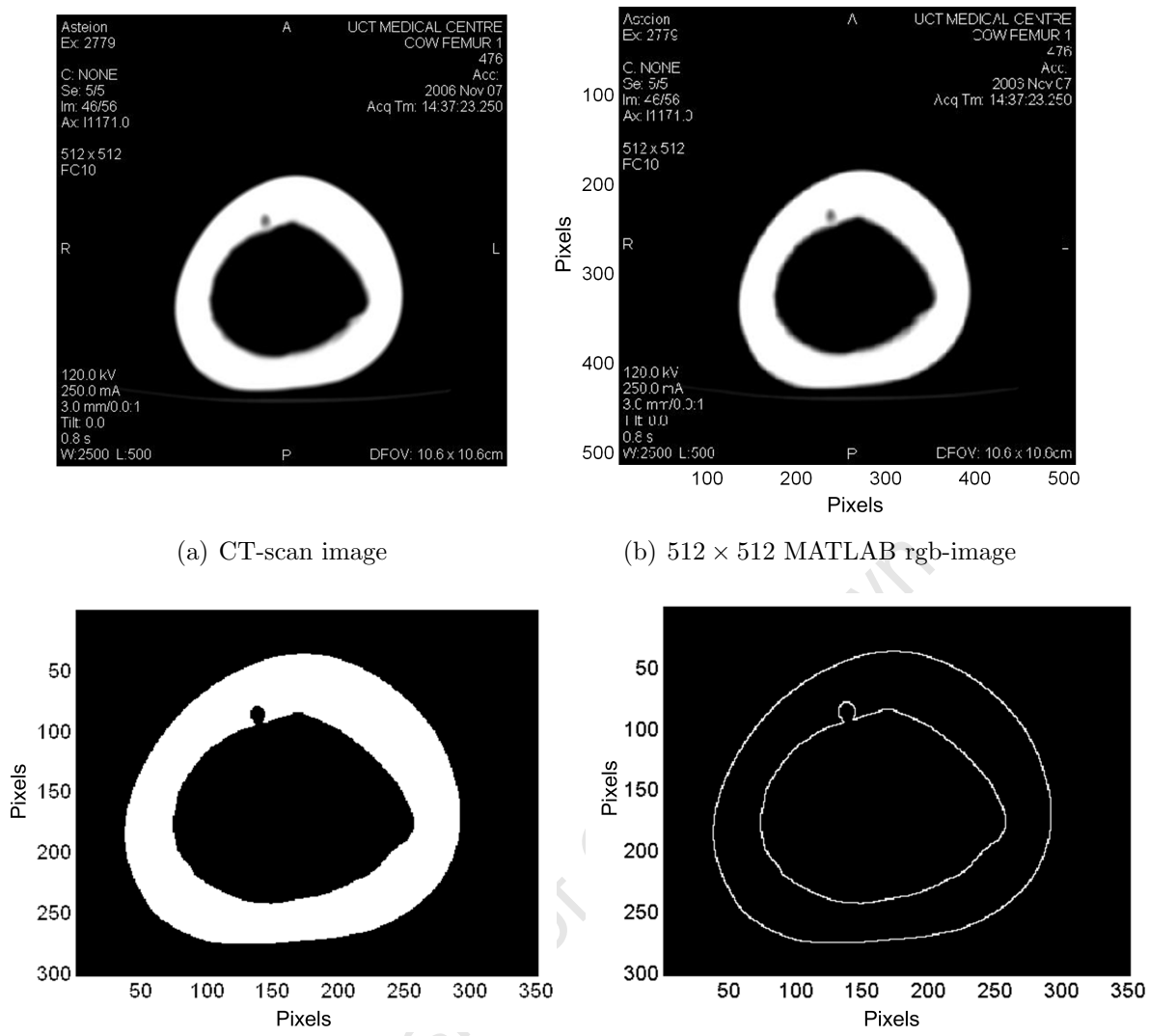

(a) CT-scan image

(b) 512 × 512 MATLAB rgb-image

(c) Black and white bone image

(d) Bone edge curves

Figure 7.6: Extracting the bone edges from CT-images

edge points are written into a python script file such that they are automatically included in a command that instructs ABAQUS to make a wire spline through all the data points on each of the inside and outside edges of every slice. The result is a collection of splines on the inside and outside surfaces of the bone (Fig.7.8(a)). A solid bone geometry is generated by creating a solid loft between the splines that define the outer edge of the bone. The hollow endo-osteal space is created in a similarly, but this time by using a loft cut (Fig.7.8(b)). Notice the black seam line on the outer surface of the solid shape. This indicates the loft path and is located at the start and finish points of the splines.

It is possible to achieve a structured hex mesh (as opposed to a free or sweep mesh) for the solid bone shape by creating multiple partitions. Fig.7.8(c) shows the bone shape, which has been partitioned into ten cells. The colours represent the mesh structure that has been assigned by ABAQUS. The green cells indicate that the software is able to map

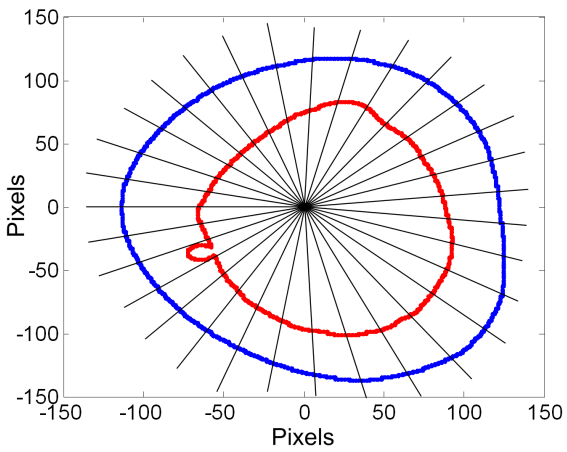

(a) Stencil at 31 angle increments

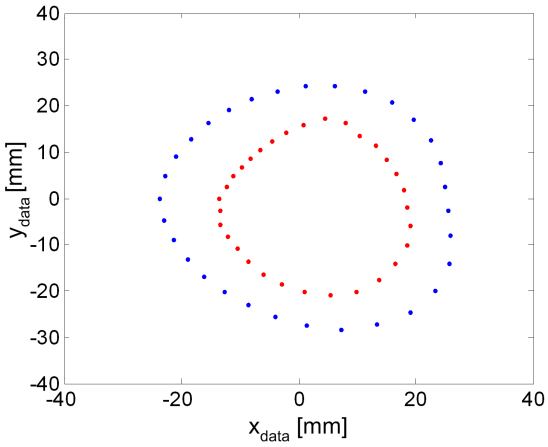

(b) 31 data points on the inner and outer bone edges

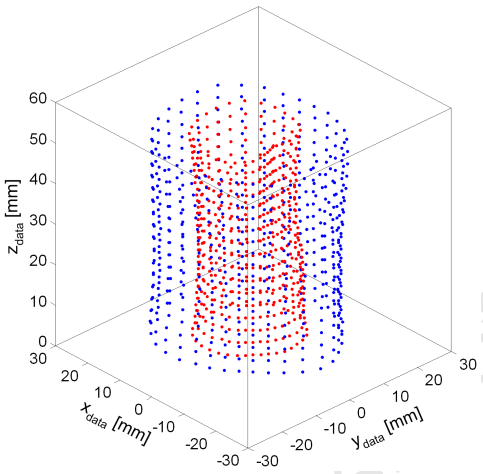

(c) Whole bone surface points

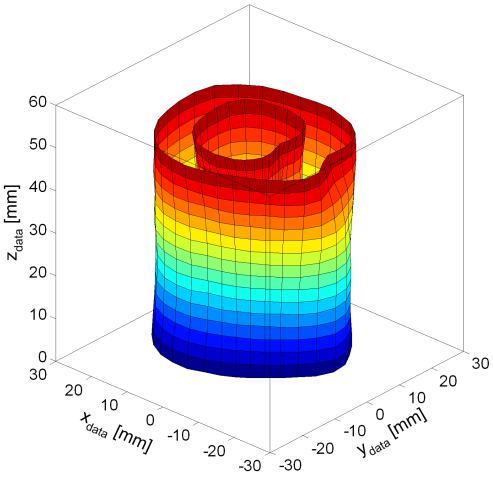

(d) Patch surfaces of the bone faces

Figure 7.7: Creating a grid of edge points which define the inner and outer bone surfaces

a structured mesh. The yellow indicates the assignment of a swept mesh. Upon closer inspection it is observed that there is a small discrepancy between the partition boundary and the seam line (from Fig.7.8(b)). This discrepancy causes ABAQUS to interpret the surface as two separate faces, with adverse effects on the mesh structure. This problem is corrected by using the `Virtual Topology Tool`, which merges the two faces and enables the use of a structured mesh (Figs.7.8(d) and 7.8(e)).

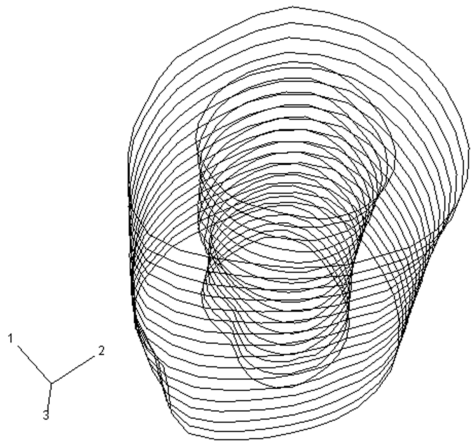

(a) Splines

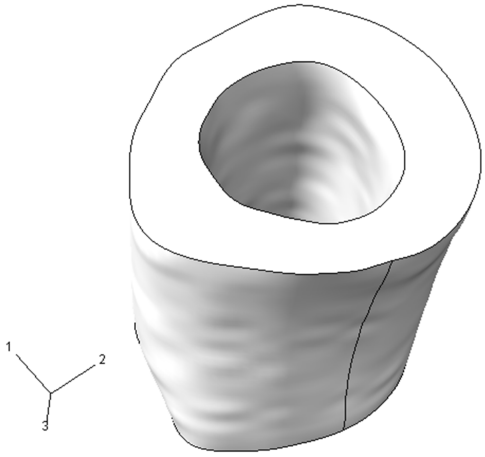

(b) Solid shape

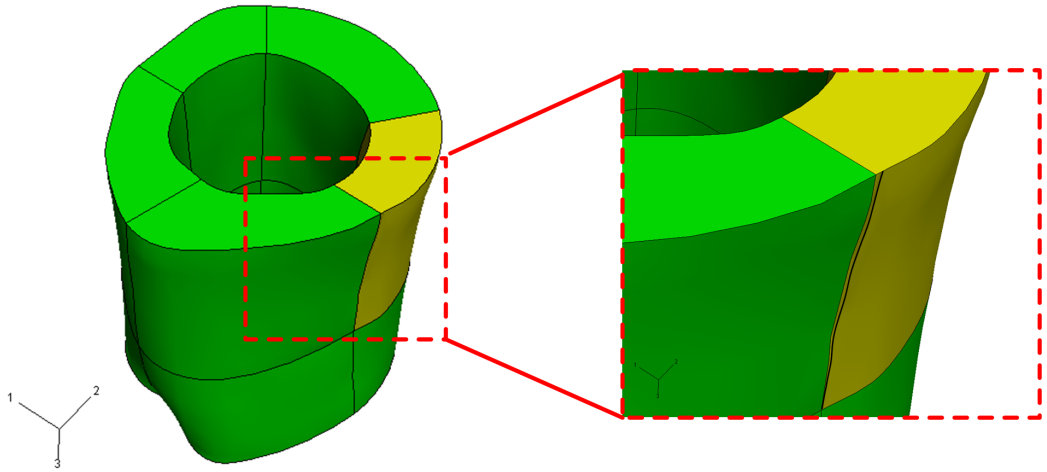

(c) Partitioning and the use of the `Virtual Topology Tool`

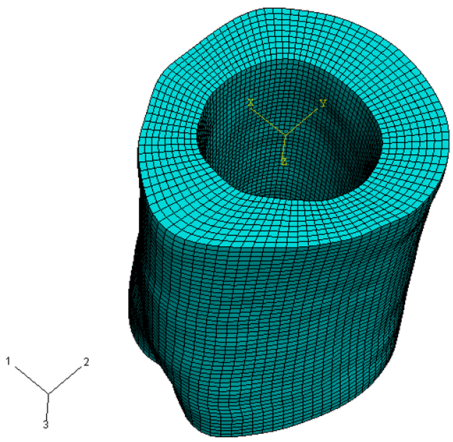

(d) 1 mm element mesh

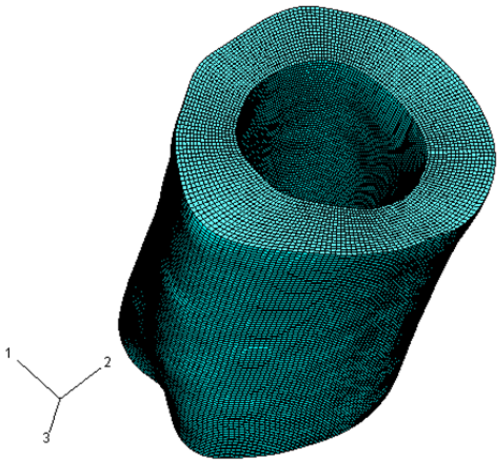

(e) 0.5 mm element mesh

Figure 7.8: Creating the solid bone part and FE mesh

Assembly and boundary conditions

To simulate the quasi-static diaphysis compression test, the solid bone geometry was assembled with an analytical rigid surface, which represents the machine bed. The analytical rigid was placed flush with the bottom bone surface and tied to it. A reference point was created on the analytical rigid. This point was constrained in all six degrees of freedom.

The displacement measured form the Zwick machine head during the experiment was directly applied to the top bone surface. The displacement of the machine head reached an ultimate value of 1.82 mm in 37.26 seconds after which it remained constant (Fig.7.9). The test recording ceased after 42 seconds, but was continued for simulation purposes to the required time.

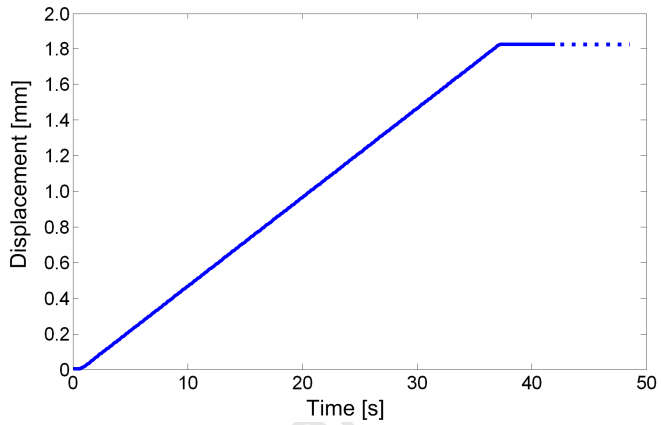

Figure 7.9: Zwick head displacement during the diaphysis compression test

The resulting reaction force on the analytical rigid was recorded at the reference point which is associated with the part. Two views of the model assembly are provided in Fig.7.10.

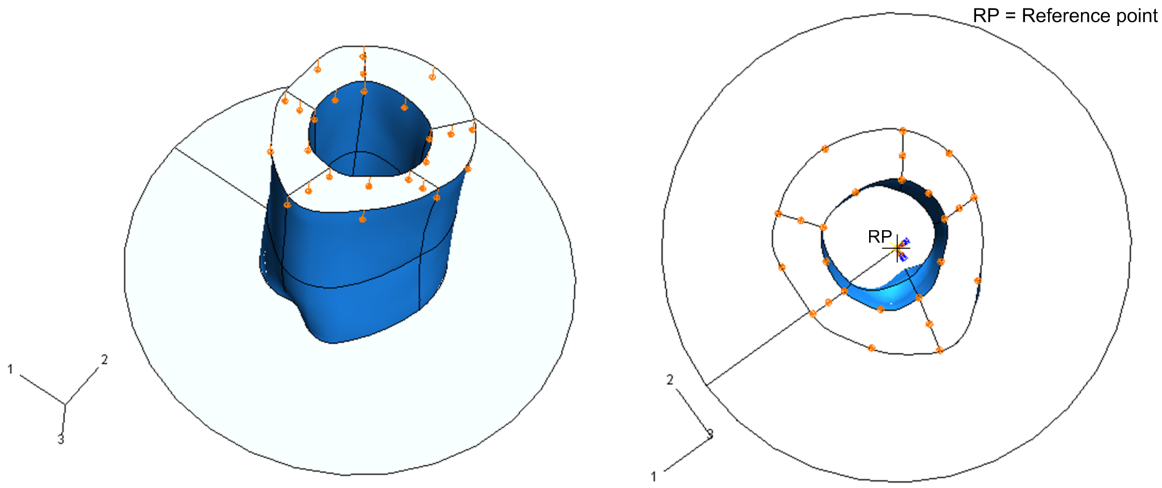

(a) Isometric view (b) Top view

Figure 7.10: The FEM model of the quasi-static diaphysis experiment.

Mass scaling

The ABAQUS/Explicit solver determined that the stable time increments for the diaphysis model as reported in Table 7.6. The mass was scaled significantly in the course of the quasi-static analysis to achieve a target time step of $\Delta t_{stable} = 1 \times 10^{-3}$ seconds. Earlier analysis on single elements has shown that a better (yet conservative) estimate of the stable increment is 1.5×10^{-1} seconds smaller than that calculated by ABAQUS. For this reason a user defined maximum time increment was additionally implemented at $t_{stable} = 5 \times 10^{-4}$ seconds. The mass scaling factors, f^2 for the 0.5 mm and 1 mm meshes are listed in Table 7.6. Scaling the mass by these factors reduced the original number of time increments to conduct a 42 seconds simulation, n to $\frac{n}{f}$.

Element size	Δt_{stable}	f^2	n	$\frac{n}{f}$
0.5 mm mesh	1.75×10^{-8}	4.317×10^{11}	2.4×10^{9}	3.6×10^{3}
1.0 mm mesh	8.75×10^{-9}	1.134×10^{11}	4.8×10^{9}	1.4×10^{4}

Table 7.6: The average mass scaling factors that were required to accomplish quasi-static explicit analysis with the strain rate dependent bone VUMAT model

Notably, the mass scaling factors are very large. An adverse effect of excessive mass scaling is that the increased mass could introduce unwanted, non-physical, inertia effects in the structure under consideration [109]. To ensure that the analysis results are reliable, it must be shown that the calculated kinetic energy is insignificant when compared to the strain energy absorbed by the specimen [111].

Fig.7.11 presents the kinetic energy and external work done during the course of the FEM diaphysis compression analysis. The diaphysis failed at $t = 31.2$ seconds in the present analysis as elements were deleted according to the material fracture criterion (as shown in Fig.7.12. The external work increases as the specimen is compressed and remains constant beyond failure. Before failure the kinetic energy is insignificant in comparison with the external work done. For this reason mass scaling as used here results in a valid response prior to failure. Beyond failure the kinetic energy is significant and the response can no longer be trusted.

It is advised that future use of the VUMAT bone model in quasi-static explicit analyses be conducted with great care in the following respects:

- **Sudden changes in the velocity of the loading or deformation of the bone material should be applied as smoothly as possible to limit material acceleration and therefore the inertia forces.**
- **The calculated kinetic energy should always be compared to the strain energy absorbed by the specimen to ensure that the quasi-static explicit analysis is valid.**

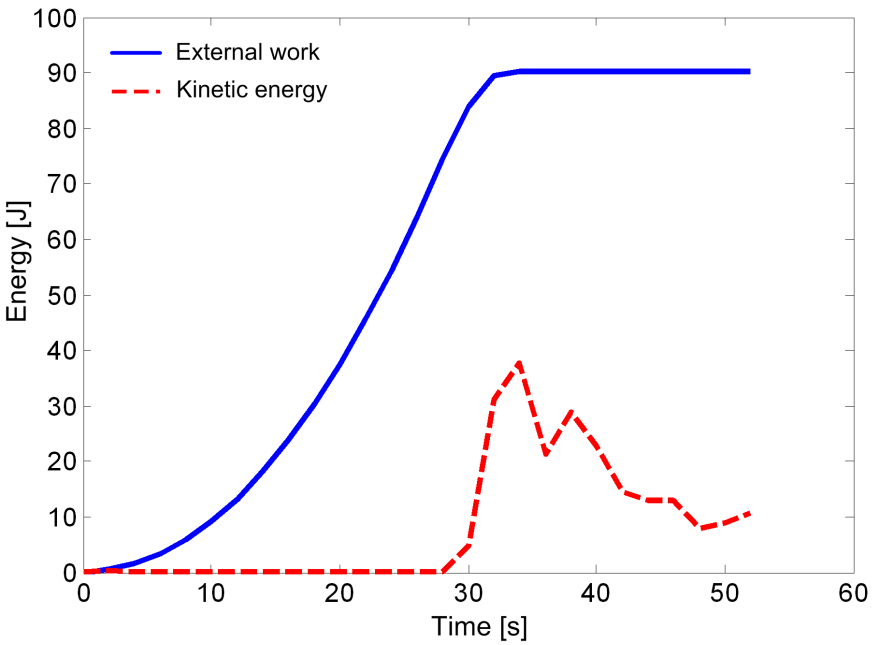

Figure 7.11: The total external work and the kinetic energy as a result of mass scaling

7.5.2 Comparison of experimental and FEM results

Comparison of the reaction force-time history

The force-time history of the specimen compression is shown in Fig.7.12. The bovine mid-diaphysis was able to sustain a constant velocity displacement of its upper surface at 0.5 mm. s^{-1} for 33.5 seconds before fracturing. At the time the machine head was pushing of the diaphysis with a force of 136 kN.

There is an excellent correlation between the experimental and FE pre-fracture responses. The model slightly underestimates the slope of the force-time history and therefore the actual stiffness of the material. This could be explained by the relatively high density of the diaphysis ($\rho = 2193\,\text{kg.m}^{-3}$) compared to the average density of specimens tested. Shim et al.[21] developed a relationship between specimen density and Young's modulus for cancellous bone from the human cervical spine. This enables the model to produce a stiffer response for specimens with a higher density. Such a course of action is advised in the future improvement of the current VUMAT. The effect of the viscous term (Voigt dashpot) is visible in the early transient force response. The viscous term causes a stress to arise in the material as soon as the strain rate is significant.

Failure was included in the FE simulations by using the three criteria for element deletion discussed in Section 7.1.2. Table 7.7 reports the reaction force and time of bone failure according to FE simulations. Both the material failure criterion and material fracture criterion underestimate the strength of the diaphysis specimen. The criterion of Carter and Hayes [88] provides the most accurate estimation of specimen fracture even though it has been shown to overestimate of the compressive strength of specimens in the present data

from which VUMAT subroutine was developed (Section 5.1.4). **Observe that the material response does not present with significant softening before the incidence of fracture. For this reason the constitutive relation is well suited to model specimen response up to the point of ultimate fracture. It is therefore recommended that the material fracture criterion is the most appropriate criterion for element deletion if bone response is to be approximated at quasi-static strain rates.**

	α	β	$t_{fracture}$ [seconds]	$F_{fracture}$ [kN]
Diaphysis compression experiment			33.5	136.2
Element deletion: material failure	51.4	0.057	26.4	104.7
Element deletion: material fracture	61.2	0.06	31.2	121.9
Element deletion: Carter and Hayes [88]	68.0	0.06	34.8	137.0

Table 7.7: The force and time of bone failure according to FE simulations with different criteria for element deletion

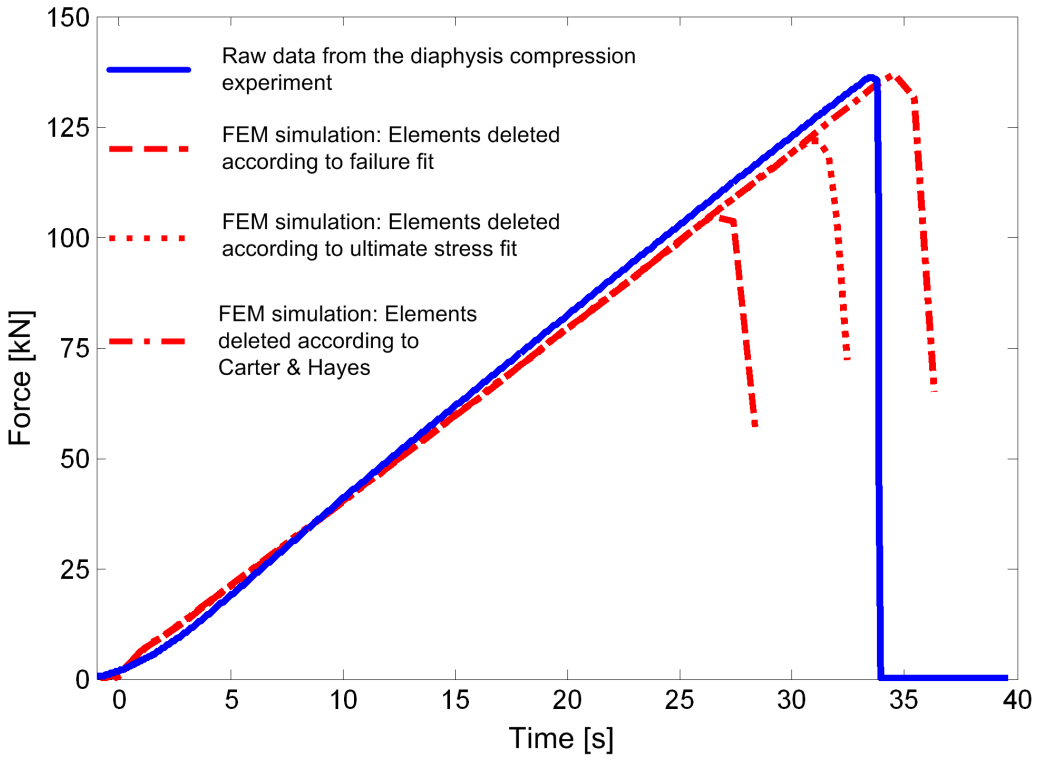

Figure 7.12: Force-time histories recorded during the diaphysis compression experiment and FE simulations

Visual comparison of bone fracture and simulation model

The state of the fractured diaphysis

Figs.7.13 and 7.14 show the state of the bone diaphysis subsequent to quasi-static compression on the Zwick Universal test machine. The bone fractured suddenly in multiple locations. A section of the diaphysis wall has shattered completely and is no longer intact. High speed photography of the event was attempted, but was not successful. Earlier discussions on macroscopic and microscopic observations of bone fracture have eluded to the observation that cracks in the transverse section of the bone shaft grow in the direction of the concentrically arranged vascular canals. This observation is again apparent on the diaphysis bottom surface (Fig.7.13(b)) where several cracks have formed concentrically in the bone wall. The outer laminae of the cortical wall seem to be peeled apart from the inner cortex which remains intact.

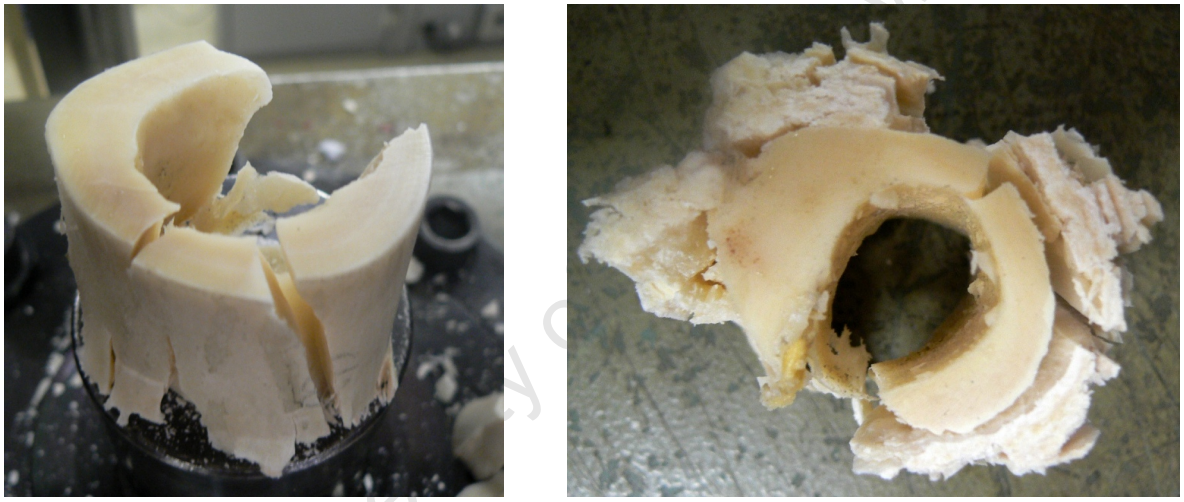

(a) (b)

Figure 7.13: Visual inspection of the (a) top surface and (b) bottom surface of the bovine femur diaphysis after fracture

Inspection of the bone wall fractures show at least four longitudinal cracks which run at a slight diagonal along the diahysis length (Figs.7.14(a) and 7.14(b)). These cracks seem to have propagated through the entire thickness of the bone cortex. From the cross-sectional views in Figs.7.13(a) and 7.13(b) it is observed that these cracks propagated perpendicularly across the concentrically arranged vascular canals.

Bone fractures compared to FEM model element status

The post-experiment state of the bone diaphysis is compared with the status (stress bearing or deleted) of the FEM model elements to assess the ability of a FEM model with a well characterised material and accurate geometry to predict which regions of the bone are viable to fracture or injury. Inspection of the top surface shows that the stress concentrates

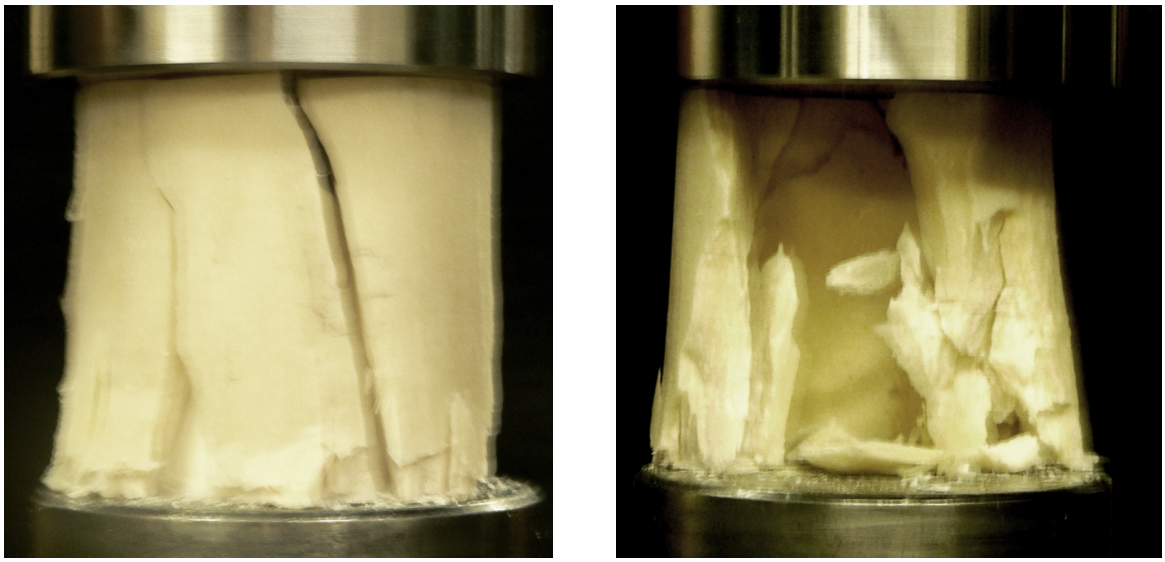

(a) (b)

Figure 7.14: Visual inspection of the diaphysis wall fractures after quasi-static compression

on the inner cortical rim of the bone top surface around marker **1** (Fig.7.15(b)). According to the simulation, the first incidence of material failure anywhere in the diaphysis is also in this region (Fig.7.15(c)). The top surface subsequently fails in region **2**. From here, failure progressively spreads around the top surface. The material in area **4** fails before the systematic propagation of top surface element failures can reach the region, which leaves only the surface between area **3** and **4** intact.

Fig.7.16 shows the progressive status of the finite elements on the bottom surface of the bone diaphysis. The propagation of deleted elements in the simulation is compared with a photograph of the diaphysis bottom surface after the experiment. According to the simulation the first incidence of fracture on the bottom surface of the bone is after fracture of the elements on the top surface. Fracture initiates in region **1** which is indicated in Figs.7.16(a) and 7.16(d). The bone subsequently fails in region **2** on the opposing side of the cortical circumference (Figs.7.16(a) and 7.16(e)). The model predicts that the bone diaphysis will fail through the entire thickness of the cortex, whereas a group of concentric cracks are visible on the post-test photograph (Fig.7.16(a)). The future addition of anisotropy to the bone material response is anticipated to improve the model capabilities in this respect. From quasi-static compression tests on bone specimens it appears that bone is weaker in tangential compression than longitudinal compression (Section 5.4.2). This would increase the inclination of the material to fail in the tangential direction. The simulation is able to predict that region **3** is the final segment of the bottom surface which does not fail.

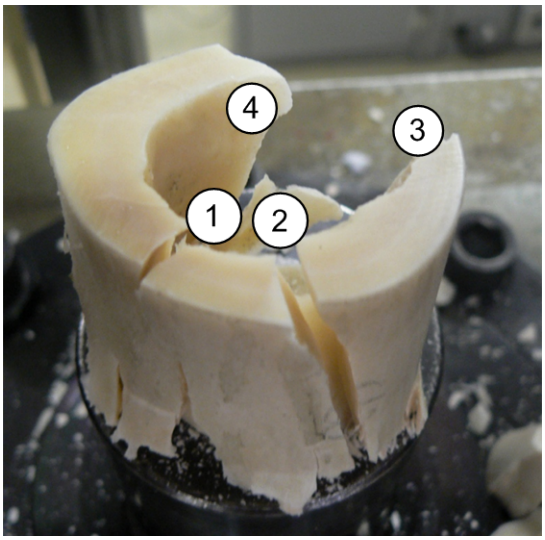

(a) Fractured diaphysis top surface

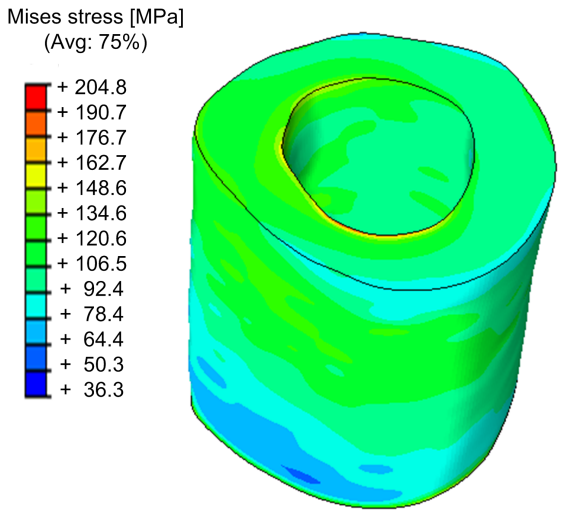

(b) Von Mises stress just before failure on the inner cortical rim. Step time = 24.00 s

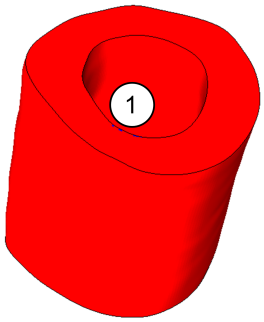

(c) Step time = 26.25 s

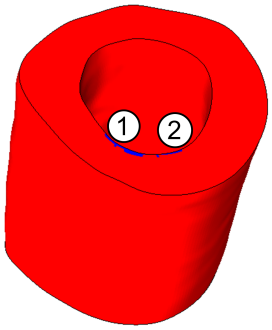

(d) Step time = 27.25 s

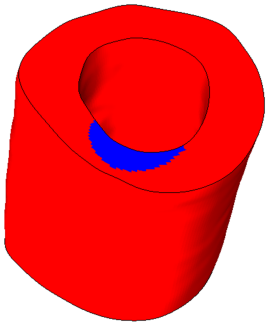

(e) Step time = 28.50 s

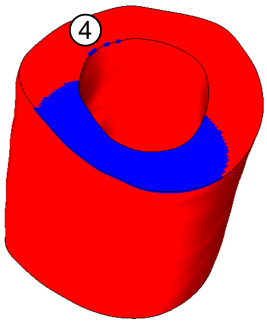

(f) Step time = 30.00 s

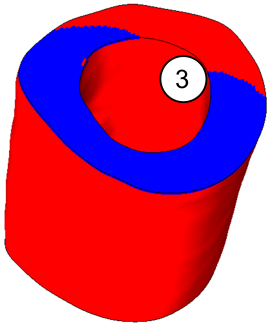

(g) Step time = 31.50 s

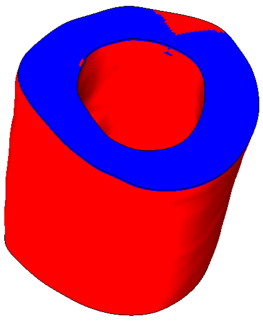

(h) Step time = 32.75 s

Stress bearing elements Deleted elements

Figure 7.15: The fractures on the top surface compared to the stress concentrations and element status of the FEM model in the course of quasi-static diaphysis compression

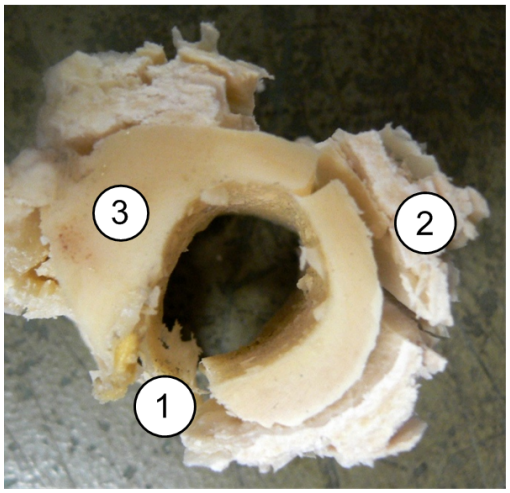

(a) Bone bottom surface

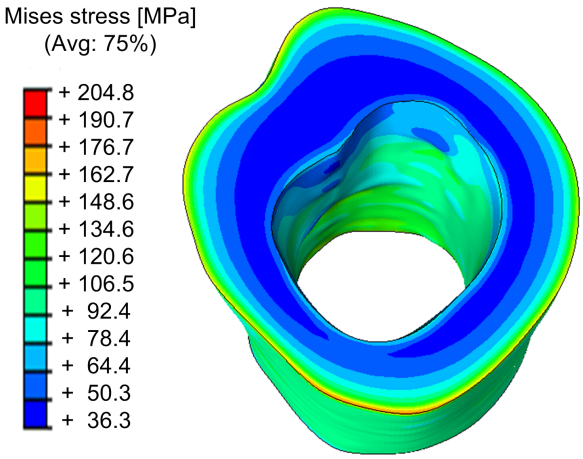

(b) Von Mises stress concentration on the outer cortical rim of the bottom surface. Step time = 24.00 s

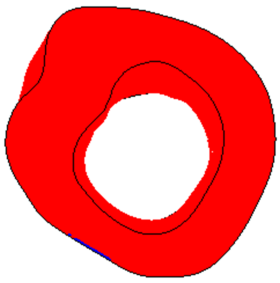

(c) Step time = 34.75 s

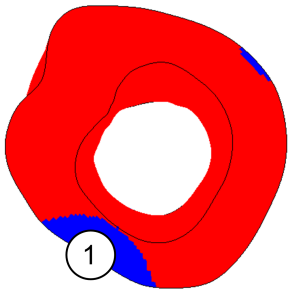

(d) Step time = 35.75 s

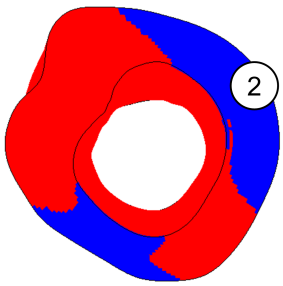

(e) Step time = 37.75 s

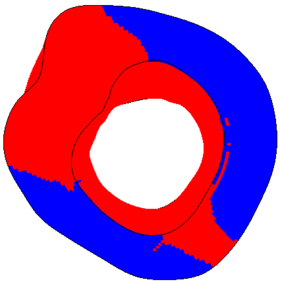

(f) Step time = 38.50 s

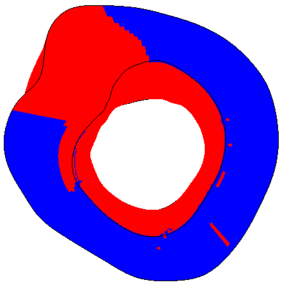

(g) Step time = 40.00 s

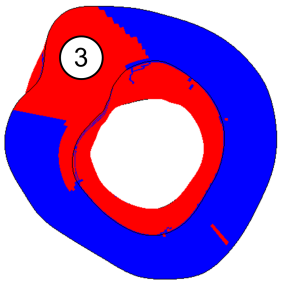

(h) Step time = 50.00 s

Stress bearing elements Deleted elements

Figure 7.16: The fractures on the bottom surface compared to the stress concentrations and element status of the FEM model in the course of quasi-static diaphysis compression

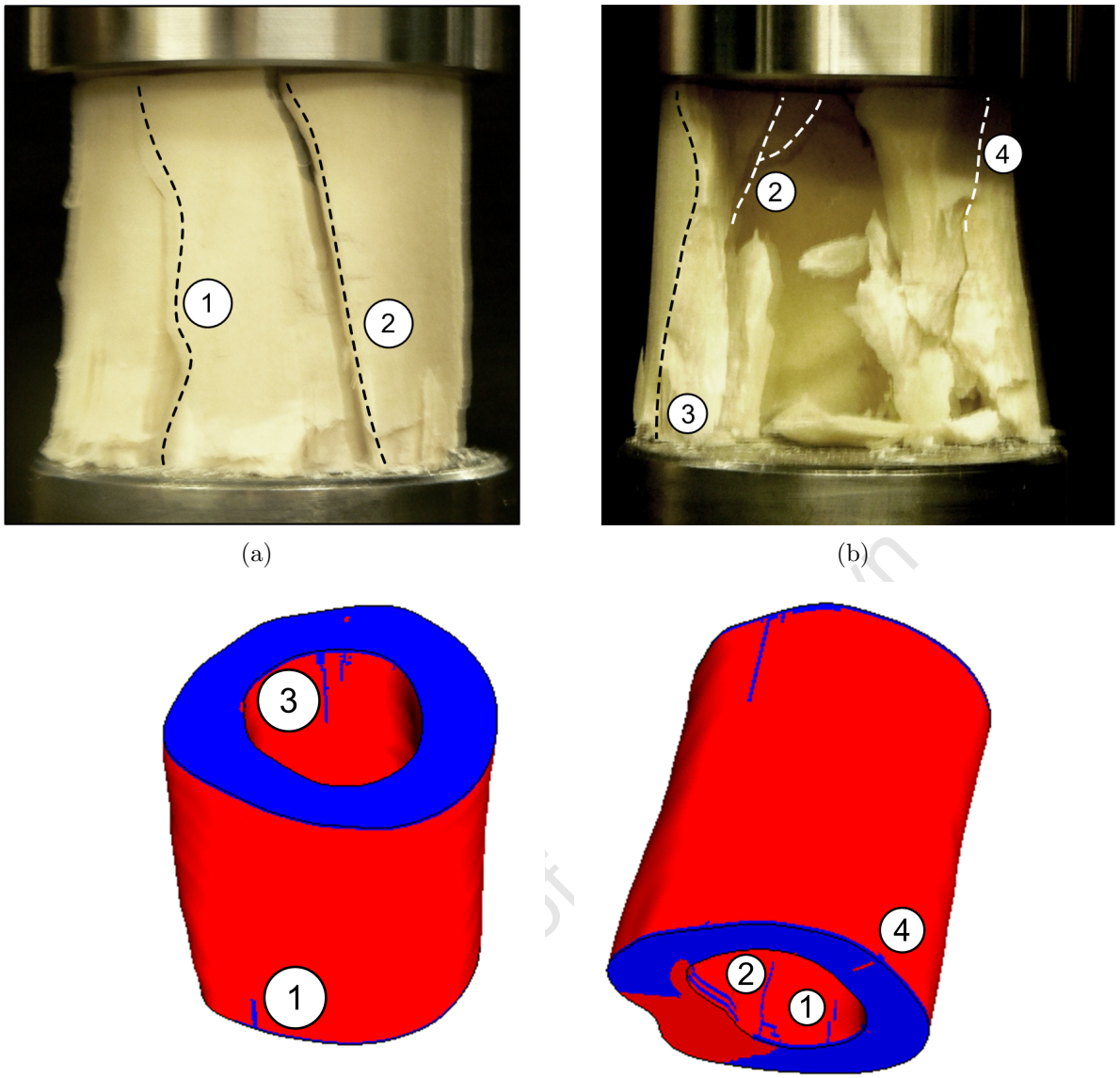

(a) (b)

(c) Step time = 50.00 s (d) Step time = 50.00 s

Figure 7.17: The fractures of the diaphysis wall compared to the stress concentrations and element status of the FEM model in the course of quasi-static diaphysis compression

The FEM diaphysis only cracks along its longitudinal axis after the elements on the top and bottom surfaces have failed (Fig.7.17). The model is able to predict the approximate positions of the four longitudinal through-thickness cracks. **The present model shows promise in the indication of potential regions of bone damage and fracture in compression.**

7.6 Dynamic validation experiment on the SHPB

Dynamic validation of the cortical bone VUMAT requires an experiment in which the specimen deformation is known and the time history is measured. The dynamic compression of a whole femur shaft could possibly be conducted on a high drop tester where the impactor reaches a sufficient speed to result in the required strain rate. At present the Blast Impact and Survivability Research Unit does not have such a large capacity load cell at its disposal to facilitate the measurement of the dynamic femur response history. For this reason a 6 mm cylindrical specimen was fractured in dynamic compression on the 12 mm SHPB system. The experiment was conducted with the tapered striker developed in Section 4.3.7. Impact of the striker ($l_s = 152.74$ mm, $d_0 = 11.88$ mm and $d_1 = 6.52$ mm) at 13.1 ms^{-1} resulted in a strain rate of approximately 6.5×10^2 s^{-1} in the specimen. The stress waves in the SHPB and the specimen responses are indicated in Fig.7.18.

7.6.1 Finite element model of the SHPB experiment

A quarter symmetry model was constructed of the 12 mm SHPB system and analysed with the ABAQUS/Explicit solver. The two SHPB bars and the specimen were included in the model. The steel Hopkinson bars were modelled with linear elastic material properties as SHPB tests are conducted on the premise that the bars are not loaded beyond yield. The dimensions and material constants are supplied in Table 7.8. The bone specimen density was measured to be 2071.5 kg. m^{-3}. The constants for the viscoelastic VUMAT user-material were defined as reported in (Section 6.2.3, Table 6.4).

A hard normal contact interaction was defined between the appropriate specimen and bar surfaces. Symmetry boundary conditions were enforced on the specimen and bar

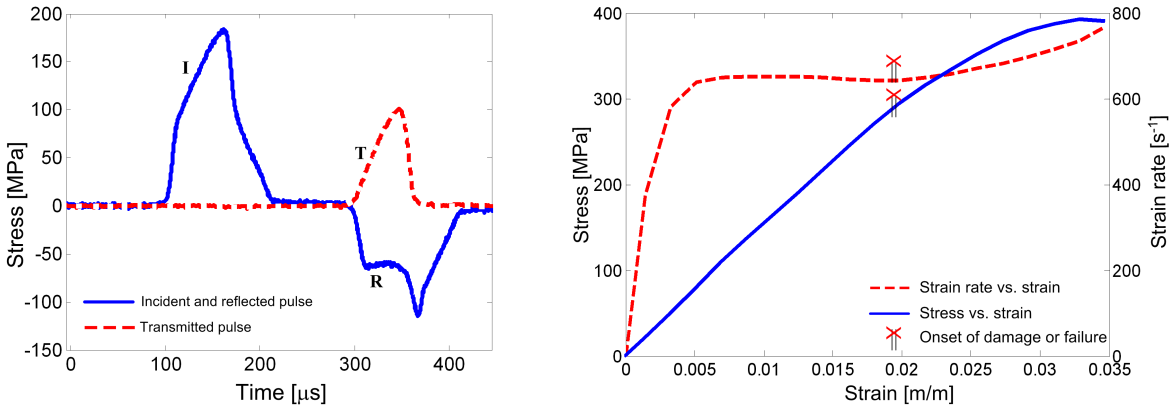

(a) (b)

Figure 7.18: The (a) incident (**I**), transmitted (**T**) and reflected (**R**) bar stress waves and (b) the specimen stress-strain and strain rate-strain responses during the dynamic validation experiment on the SHPB

	l [mm]	d [mm]	ρ [kg. m^{-3}]	ν	E [GPa]
Hopkinson bars	1000.0	12.0	7948.9	0.30	209.0
Bone specimen	6.0	6.0	2071.5	0.36	–

Table 7.8: Specimen and bar parameters for the dynamic validation test

surfaces that were located in the symmetry planes (Fig.7.19(a)). The loading of the striker was introduced by applying a pressure to the face on the striker end of the input bar. The pressure amplitude was extracted from the mid-bar stress-time history measured during the SHPB experiment. The modelling of the conical striker and the stress pulse that results from this impact is omitted because the response of the cortical bone VUMAT is to be assessed. For this reason it is required that the specimen in the experiment and the specimen in the model are exposed to an identical load. The duration of the pressure pulse was approximately 120 μs. The model was analysed for 500 μs to capture the transmitted and reflected stress waves. The respective mesh sizes of the Hopkinson bars and bone specimen were 1.0 mm and 0.5 mm as indicated in Fig.7.19(b). The time increment was scaled by a factor of 0.1 to ensure a conservative estimate the stable time step and an accurate analysis of the viscoelastic material stress. To limit the size of the output files, partitions and element sets were created in the middle and at both ends of the Hopkinson bars. Detailed output histories were recorded for only the elements in the element sets. The transmitted and reflected stress waves in the bars were subsequently compared to evaluate the FEM prediction and experimental measurements.

7.6.2 Correlation between experimental and FEM results

The modelling focus of this study was directed toward modelling bone response up to the onset of damage as this is associated with injury. For this reason the onset of damage is considered as the failure of the material. The judgement of the onset of damage is somewhat subjective as mentioned in Section 5.1.4. As previously mentioned a secondary infliction point was observed in the non-linear responses of dynamically compressed specimens. This infliction point is identified by monitoring the slope of the specimen strain rate history. In the present experiment structural damage was associated with an increase in the slope of the strain rate, which was found to occur after approximately 29.0 μs after the onset of loading. The associated point is indicated on the transmitter bar stress history curve. The method for determining the onset of damage is consistent with the method used for determining the criterion for material failure from experimental data ($\sigma_{VM} = 51.4\ \rho^2 \dot{\varepsilon}_{eq}^{0.057}$).

A comparison of the experimental and FEM model responses is presented in Fig.7.20. Element deletion in the FE analysis was conducted on the premise of material failure.

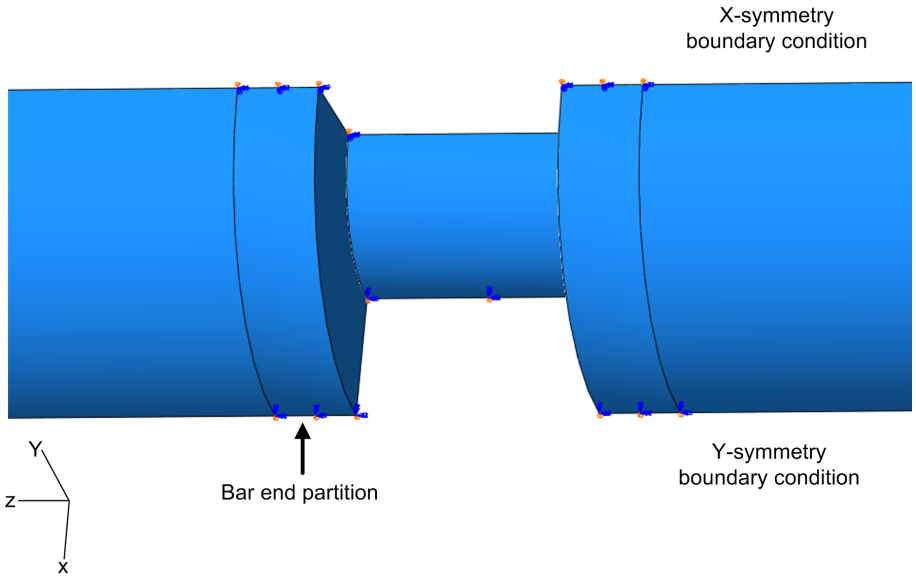

(a) Boundary conditions

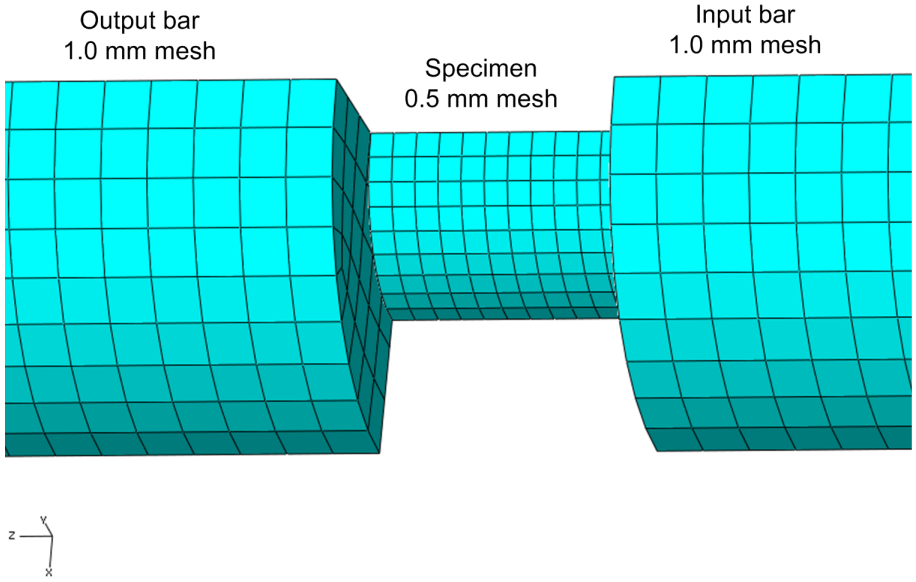

(b) Specimen and bar meshes

Figure 7.19: FEM model of a dynamic SHPB experiment

The incident (**I**) and transmitted (**T**) stress waves are indicated as well as the point which is associated with the onset of damage. The incident stress wave (denoted by **I**) of the FE input bar is identical to the stress recorded during the SHPB experiment. The loading pulse of the model is therefore representative of the loading recorded during the experiment. The stiffness of the FEM response is slightly lower than that encountered in the SHPB test, but gives a good approximation of the dynamic behaviour of bovine cortical bone prior to failure. The VUMAT bone response predicts that the specimen will fail at 328.6 μs whereas the specimen in the experiment failed at 328.3 μs. The estimate of the time of fracture is therefore very accurate. The bar stress at the onset of specimen failure was measured to be 77.0 MPa, whereas the FE model predicted 61.2 MPa. The stress at failure is therefore under-predicted by approximately 20%.

A further correlation between the experimental measurements and predicted transmitted and reflected stress waves in the Hopkinson bars are presented in Fig.7.21. Elements were deleted according to the three criteria that were discussed in Section 7.1.2. All three of the criteria used for the deletion of elements resulted in the under-estimation of ultimate dynamic bone strength. The associated transmitter bar stress and time for the incidence of specimen failure are listed in Table 7.9. The estimate of the failure stress can be improved if elements are deleted according to the premise of material fracture ($\sigma_{VM} = 61.2\ \rho^2 \dot{\varepsilon}_{eq}^{0.06}$) which predicts that the specimen will fail at 77.3 MPa.

	α	β	$t_{fracture}$ [μs]	σ_b [MPa]
Bar stress at ultimate specimen failure			352.1	106.6
Bar stress at onset of specimen damage			328.3	77.0
Element deletion: material failure	51.4	0.057	328.6	61.7
Element deletion: material fracture	61.2	0.06	335.6	77.3
Element deletion: Carter and Hayes [88]	68.0	0.06	339.8	87.3

Table 7.9: Transmitter bar stress magnitude and time of bone fracture as predicted FE simulations with different criteria for element deletion

Earlier discussions demonstrated that the implementation of the current viscoelastic model results in the over-estimation of dynamic compressive response beyond the point of damage. It was therefore recommended (in Section 6.2.3) that this viscoelastic model should not be implemented to model dynamic specimen response beyond the onset of damage. Furthermore the investigation of model response as a result of element deletion according to material fracture and Carter and Hayes is only included for informative purposes. Element deletion according to the fit of material failure is the only criterion that is substantiated by data from strain rate dependent compres-

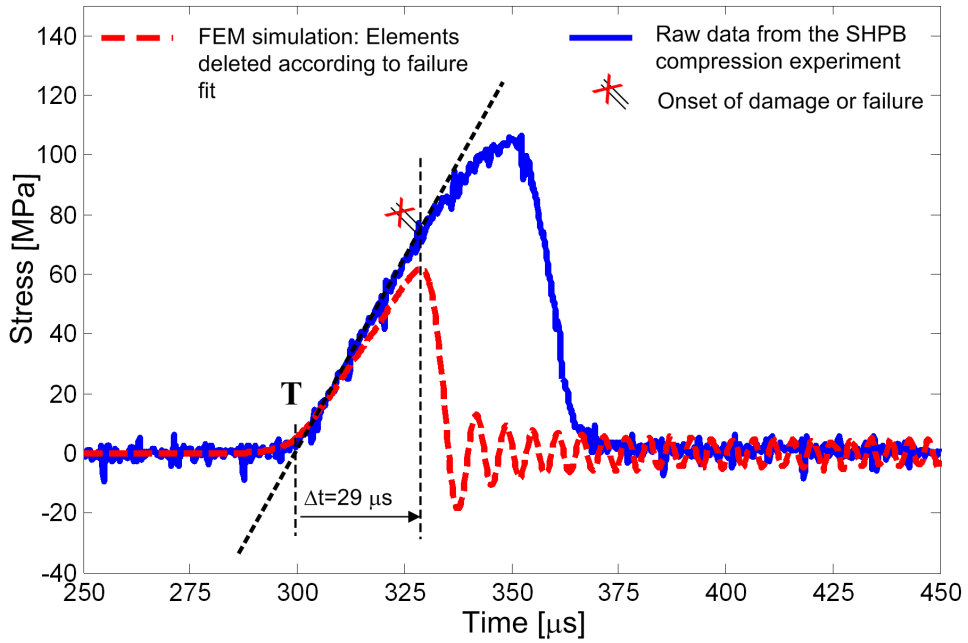

Figure 7.20: A comparison of the experimental and FEM responses up to the point of damage

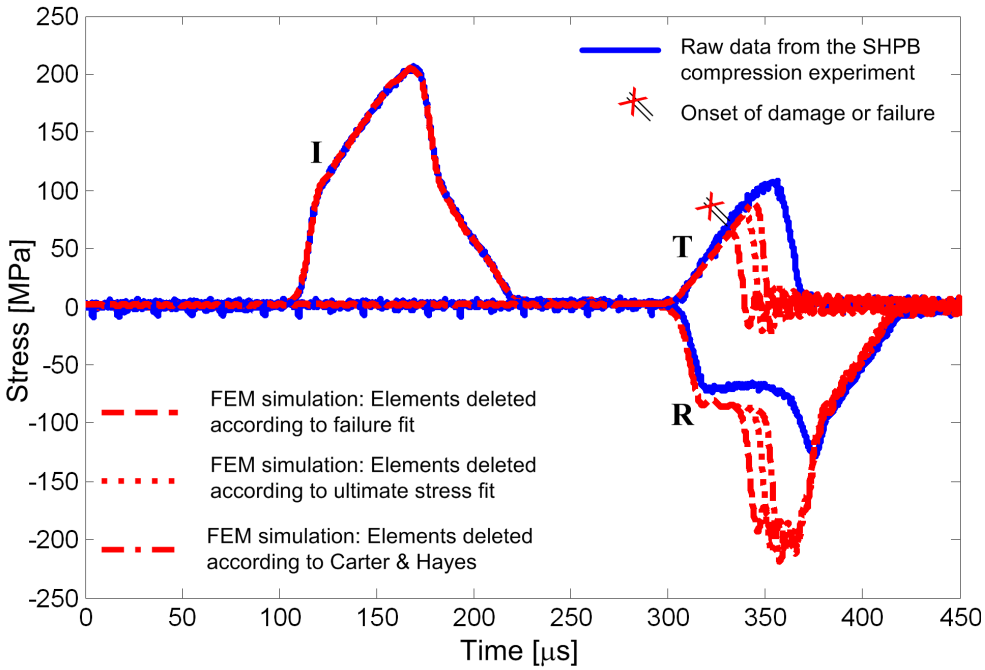

Figure 7.21: The correlation between the transmitted (**T**) and reflected stress waves (**R**) measured in the SHPB and predicted by FEM. The response of the specimen is measured as result of the incident wave (**I**) in the SHPB.

sion. The conclusion of this discussion is therefore that the present VUMAT material model underestimates the stiffness and failure stress of bovine bone in dynamic compression, but provides an excellent estimate of the time of failure.

7.7 Concluding remarks on the VUMAT subroutine for bovine cortical bone

The discussion in this chapter has verified that the VUMAT subroutine is isotropic and responds according to the models that govern its stress-strain history and failure. Additionally the model provided a successful representation of bovine cortical bone response to a quasi-static and a dynamic experiment. The model slightly underestimates the stiffness of the response in both the quasi-static and dynamic cases. The use of the *material fracture criterion* is recommended for the modelling of quasi-static bone response, whereas the *material failure criterion* is deemed appropriate for dynamic cases. The current failure criteria under-estimate the experimental stresses at the onset of damage in the bone structure.

Chapter 8

Conclusions and recommendations

1. **The longitudinal compressive strength and response of bovine cortical bone is strain rate dependent.** Longitudinally orientated specimens were compressed at quasi-static strain rates ($\dot{\varepsilon} \approx 10^{-4}\,\text{s}^{-1}$, $\dot{\varepsilon} \approx 10^{-3}\,\text{s}^{-1}$, $\dot{\varepsilon} \approx 10^{-2}\,\text{s}^{-1}$ and $\dot{\varepsilon} \approx 10^{-1}\,\text{s}^{-1}$) and dynamic strain rates ($\dot{\varepsilon} \approx 2.7 \times 10^{2}\,\text{s}^{-1}$ and $\dot{\varepsilon} \approx 10^{3}\,\text{s}^{-1}$). It is clear that bone responds to quasi-static and dynamic compression in two very distinct corridors. The dynamic response corridor is distinctly more stiff than the quasi-static one. Experiments confirm that bovine bone fractures at a higher stress with increasing strain rate. This trend of increasing failure stress remains consistent throughout the quasi-static and dynamic strain rate regimes. The lack of experimental techniques and data in the middle strain rate regime is a key factor that prevents the full understanding of the strain rate sensitivity of bone.

2. **Tapered strikers were found to be highly effective in shaping the stress wave in SHPB experiments in order to achieve constant strain rate compression.** It was found that if a conical striker impacts a SHPB with its small end first, this will result in an accelerator pulse in the bar that increases in steepness as a function of the cone angle. Advantages of conical strikers over sacrificial pulse shapers include:

   - Test repeatability because the same striker is effective to control the strain rate of all the tested specimens. Thus, inter-specimen variation does not affect the shape of the striker that is needed to achieve a constant strain rate.
   - Improved control of the pulse shape [73] because of the possible variations in striker geometry.
   - Tapered strikers are reusable, therefore a single striker is used to conduct an entire series of tests if inter-specimen variation is not significant (as was the case for the cortical bone investigated in the present study).

   The challenges of the use of tapered strikers are:

- Buckling of the striker tip as a result of excessive stress or bad alignment with the input bar.
- Shortening of the possible test duration in a given length of bar, because of the 'tail' that occurs in the signal. This phenomena can be explained as follows: When the striker impacts the input bar, stress waves originate at the impact surfaces. The stress wave in a uniform area striker would run to the end of the striker and back to the interface. At this point the striker will lose contact with the bar if it has a smaller diameter than the bar. This is not the case with a non-uniform striker, impacting with the small end first. The diameter increase across length implies that there is a residual mass that must be decelerated and this accounts for the 'tail'.

An investigation into an innovative technique to remove the 'tail' from tapered striker stress waves could increase the possible test duration in a Hopkinson bar with a given length.

3. **There is virtually no difference between the response corridors that result from conventional dynamic compression with a varying strain rate and dynamic compression with pulse shaping.** The effect of varying strain rate histories is only apparent in that the drop in strain rate towards the end of of a conventional SHPB test causes irregularity in the curvature of the stress-strain response curves. The results reported in existing literature are not likely to be effected by the variation in strain rate history. From the results it is recommended that bone compression on the SHPB is conducted with the suitable pulse shaping to achieve a constant strain rate for the following reasons:
   - Even though the corridors of response do not differ, the ultimate properties are slightly affected.
   - Because of the lack of reliable data, the possible effects of strain rate variation through the middle strain rate region is unknown (and therefore the effect of such a variation is unknown).
   - Strain rate control clarifies the specification of the strain rate at which compression tests were conducted. This is advantageous, especially when investigating data on a $\log \dot{\varepsilon}$ plot (i.e. for the purposes of determining stress or strain-based fracture criteria as a function of strain rate).
4. **The approximation of the experimental stress-strain responses with the viscoelastic model by Shim et al.[21] resulted in the smallest average relative error percentage (2.5%) over the entire strain rate regime.** An attractive characteristic of this model is that both the effect of instantaneous strain

rate (Voigt daspot) and strain rate history (Maxwell model) are included. The additional benefit of choosing the model developed by Shim et al. [21] is that it has been proven effective for the modelling of cancellous bone from the human cervical spine. A single model can therefore be developed with only a change in parameters required to switch between cortical and cancellous bone.

5. **It is possible to improve the modelling of the strain rate dependent material response of viscoelastic materials by adding viscous effects that depend non-linearly on strain rate** (i.e. $\sigma_\eta = \eta\dot{\varepsilon}^P$). When this formulation is expanded to 3-D the strain rate is replaced with the strain rate tensor, which implies that the equivalent 3-D form of $\dot{\varepsilon}^P$ must be found. **The limitation of possible values of P and invariance problems are overcome if the viscous damping parameter is modelled as a function of the equivalent strain rate $\dot{\varepsilon}_{eq}$ instead of the strain rate tensor, $\dot{\boldsymbol{\varepsilon}}$. This formulation allows invariance to be recovered and does not present computational difficulty for any value of P.**

6. **The current 3-D expansion reported by Shim et al. [21] was found to violate the principle of frame invariance. An alternative approach is recommended which recovers invariance and is applicable to any viscoelastic model with a non-linear dependency on strain rate. The isotropic 3-D constitutive relation was implemented in a VUMAT user subroutine. It was verified that the VUMAT subroutine response is isotropic and behaves according to the models that govern its stress-strain history and failure. Additionally the model provided a successful representation of bovine cortical bone response to a quasi-static and a dynamic experiment.**

7. **Bone structure is anisotropic and can be approximated by three orthogonal material orientations (longitudinal, radial and tangential) with unique mechanical properties.** A thorough investigation of the strain rate dependent radial and tangential properties is recommended to facilitate the extension of the current isotropic model to incorporate anisotropic strain rate dependent response.

8. **The fracture and response of bovine cortical bone is influenced by the underlying microstructure.** Observations from this study indicate that the tangential porosity in the transverse section plane is associated with a weakness in the bone matrix for the following reasons:

    - An investigation of fractured longitudinal specimens as a result of quasi-static compression shows that the cracks in the transverse section plane are orientated

in the same direction as the dominant direction of the blood vessels of the plexiform arrangement (Fig.5.37(b)).

- Radially orientated specimens were resistant to cracking when exposed to quasi-static compression. In this case direction of the vascular porosity is perpendicular to the direction of the loading, therefore the porosity of the specimen is poorly aligned with the potential shear planes (Fig.5.38(a)).
- Quasi-static compression of tangential specimens resulted in several slightly curved cracks that run parallel to each other diagonally across the specimen length. The slight curvature and concentric pattern of the blood vessels in the transverse section plane correspond to the parallel crack pattern observed in fractured specimens. The alignment of the vascular porosity with the shear stress concentration planes results in parallel cracking of the specimen in those planes.

The above observations are preliminary and remain to be confirmed by a thorough microstructural investigation of the quasi-static fracture of bovine cortical bone specimens in different orientations. The preservation of specimens in the course of dynamic compression tests on the SHPB could potentially aid in the understanding of the vast difference between the quasi-static and dynamic response corridors that are measured in strain rate dependent compression.

References

[1] V. Radonic, L. Gionio, M. Biocic, B. Tripcovic, A. Luksic, and D. Primorac. Injuries from antitank mine in South Croatia. *Military Medicine*, 169(4):320–324, 2004.

[2] J. Manseau and M. Keown. Evaluation of the complex lower leg (CLL) for its use in anti-vehicular mine testing applications. In *IRCOBI Conference, Prague (Czech Republic)*, pages 299–310, 2005.

[3] C. Bir, A. Barbir, M. Wilhelm, M. Van der Horst, F. Dosquet, and G. Wolfe. Validation of lower limb surrogates as injury assessment tools in floor impacts due to antivehicular land mines. In *IRCOBI conference, Madrid (Spain)*, 2006.

[4] E.A. Nechaev, A.I. Gritsanov, N.F. Fomin, and I.P. Minnullin. Experience from the war in Afghanistan. Translator: Khlunovskaya, G.P. Stockholm: Falths Tryckeri; 1995.

[5] C.L. Giliomee and B. Van der Walt. ABOMA: Scaling of blast hulls. Technical Report R1/000346/1 Issue 1, Land Mobility Technologies, June 2004.

[6] *AEP-55. Procedures for evaluating the protection level of logistic and light armored vehicles, Edition 1(2), 2006.*

[7] N. Yoganandan, F.A. Pintar, M. Boynton, P. Begeman, P. Prasad, S.M. Kuppa, R.M. Morgan, and R.H. Eppinger. Dynamic axial tolerance of the human foot-ankle complex. In *Society of Automotive Engineers, Warrendale, PA, USA*, number 962426, 1996.

[8] S. Nell. *Landmine protected wheeled vehicles: design, development and evaluation of.* RMSS, October 2000. RSA-MIL-STD-37.

[9] J.R. Funk, J.R. Crandall, L.J. Tourret, C.B. MacMahon, C.R. Bass, J.T. Patrie, N. Khaewpong, and R.H. Eppinger. The axial tolerance of the human foot-ankle complex and the effect of Achilles tension. *Journal of Biomechanical Engineering*, 124:750–757, 2002.

[10] J. Wang, B. Bird, B. Swinton, and A Krstic. Protection of lower limbs against floor impact in army vehicles experiencing landmine explosion. *Journal of Battlefield Technology*, 4:8–12, 2001.

[11] T. Hight. Long-bone criteria for use with the articluated total body model. Technical report, Air Force Medical Research Laboratory, Wright-Patterson, 1981.

[12] J.L. McElhaney. Dynamic response of bone and muscle tissue. *Journal of Applied Physiology*, 21(4):1231–1236, 1966.

[13] J. Vigue and E. Martin. *Atlas of the human body.* Chartwell books Incorporated, 2008.

[14] R.D. Crowninshield and M.H. Pope. The response of compact bone in tesion ate various strain rates. *Annals of Biomedical Engineering*, 2:217–225, 1974.

[15] F. Katsamanis and D.D. Raftopoulos. Determination of mechanical properties of human femoral cortical bone by Hopkinson bar stress technique. *Journal of Biomechanics*, 23(11):1173–1184, 1990.

[16] Y. Tanabe and K. Kobayashi. Anisotropy in the dynamic non-linear viscoealstic properties of bovine compact bone. *Journal of Materials Science: Materials in Medicine*, 5:397–401, 1994.

[17] R.C. Tennyson, R. Ewert, and V. Niranjan. Dynamic viscoelastic response of bone. *Experimental Mechanics*, 12(1):502–507, 1972.

[18] J.L. Lewis and W. Goldsmith. The dynamic fracture and prefracture response of compact bone by split Hopkinson bar methods. *Journal of Biomechanics*, 8(1):27–40, 1974.

[19] F. Ferreira, M.A. Vaz, and J.A. Simoes. Mechanical properties of bovine cortical bone at high strain rate. *Materials Characterization*, 57:71–79, 2006.

[20] R.R. Adharapurapu, F. Jiang, and K.S. Vecchio. Dynamic fracture of bovine bone. *Materials Science Engineering C*, 26(8):1325–1332, 2006.

[21] V.P.W. Shim, L.M. Yang, J.F. Liu, and V.S. Lee. Characterisation of the dynamic compressive mechanical properties of cancellous bone from the human cervical spine. *International Journal of Impact Engineering*, 32(1):525–540, 2005.

[22] K.L. Moore and A.F. Dalley. *Clinically Oriented Anatomy,Fourth Edition.* Lippicott Williams and Wilkins, 1999.

[23] J.R. Funk, L.J. Tourret, and J.R. Crandall. Estimation of fibula load-sharing during dynamic axial loading of the lower extremity. Automobile Safety Laboratory, University of Virginia, Charlottesville, Virginia.

[24] R.B. Martin and D.B. Burr. *Skeletal Tissue Mechanics*. Springer-Verlag, New York, 1998.

[25] D.B. Schaffler, M.B.and Burr and R.G. Fredrickson. Morphology of the cement line in human bone. *The Anatomical Record*, 217(1):223–228, 1987.

[26] A. Ascenzi and E. Bonucci. *E.A. Balazs (ed.) Chemistry and molecular biology of the intercellular matrix: The mechanical properties of the osteon in relation to its structural organisation*. Academic Press, New York., 1970.

[27] Y.C. Fung. *A first course in continuum mechanics: for physical and biological scientists and engineers*. Prentice-Hall International (UK) Limited, London, 3rd edition, 1994.

[28] R. Krone and P. Schuster. An investigation on the importance of material anisotropy in finite-element modelling of the human femur. In *SAE Internaional 2006-01-0064*, volume No. 2006-01-0064, 2006.

[29] P. Lasaygues and M. Pithioux. Ultrasonic characterization of orthotropic elastic bovine bones. *Ultrasonics*, 39:567573, 2002.

[30] I. Ionescu, T. Conway, A. Schonning, M. Almutairi, and D.W. Nicholson. Solid modelling and static finite element analysis of the human tibia. In *Summer Bioengineering Conference,Sonesta Beach Resort in Key Biscayne, Florida*, pages 889–890, 2003.

[31] R. Dubbeldam, G. Nilson, B. Pal, N. Eriksson, C. Owen, A. Roberts, J. Crandall, l G. Hal, P. Manning, and A. Wallace. A MADYMO of the foot and leg for frontal impacts. In *43rd Stapp Car Crash Conference*, number 99SC12, 1999.

[32] D.J. Sharp, K.E. Tanner, and W. Bonfield. Measurement of the density of trabecular bone. *Journal of Biomechanics*, 23(8):853–857, 1990.

[33] J. Rittweger, G. Beller, J. Ehrig, C. Jung, U. Koch, J. Ramolla, F. Schmidt, D. Newitt, S. Majumar, H. Schiessl, and D. Felsenberg. Bone-muscle strength indices for the human lower leg. *Bone*, 27(2):319–326, 2000.

[34] P. Zioupos and J.D. Currey. Changes in the stiffness, strength and toughness of human cortical bone with age. *Bone*, 22:57–66, 1998.

[35] I. Saeed, C.F. Njeh, M. Grigorian, J. Szechinski, D. Hans, and H.K. Genant. Comparison of speed of sound measurements in multiple bone sites and ages using the omnisense device. Osteoporosis & Arthritis Research Group, Department of Radiology, University of California San Francisco, St. Louis 1999.

[36] E.F. Morgan and T.M. Keaveby. Dependence of yield strain of human trabecular bone on anatomic site. *Journal of Biomechanics*, 34(1):569–577, 2001.

[37] C. Mercer, M.Y. He, R. Wang, and A.G. Evans. Mechanisms governing the inelastic deformation of cortical bone and application to trabecular bone. *Acta Biomaterialia*, 2(1):5968, 2006.

[38] V. Ebacher, C. Tang, H. McKay, T.R. Oxland, P. Guy, and R. Wang. Strain redistribution and cracking behavior of human bone during bending. *Bone*, 40(1):1265–1275, 2007.

[39] D.T. Reilly and A.H. Burnstein. The elastic and ultimate properties of compact bone tissue. *Journal of Biomechanics*, 8:393–405, 1975.

[40] D.R. Carter and W.C. Hayes. The compressive behaviour of bone as a two-phase porous structure. *The Journal of Bone and Joint Surgery*, 59(1):954–962, 1977.

[41] D.T. Reilly and A.H. Burnstein. The elastic modulus for bone. *Journal of Biomechanics*, 7:271–275, 1974.

[42] J.H. Bargren, C. Andrew, L. Basset, and A. Gjelsvik. Mechanical properties of hydrated cortical bone. *Journal of Biomechanics*, 7:239–245, 1974.

[43] E.P. Popov and A.B. Toader. *Engineering Mechanics of Solids*. Prentice Hall International, Inc., 1999.

[44] E. Haug, H. Choi, S. Robin, and M. Beaugonin. Human models for crash and impact simulation. page 375, 2004.

[45] J.D. Currey. *Bones: Structure and Mechanics*. Princeton University Press, 2002.

[46] F.G. Evans and M. Lebow. The strength of human compact bone revealed by engineering technics. *American Journal of Surgery*, 83:326, 1952.

[47] A. Ascenzi and E. Bonucci. The ultimate tensile strength of single osteons. *Acta Anatomica*, 58:160–183, 1964.

[48] E.D. Sedlin. A rheological model for cortical bone. *Acta Orthopaedia Scandanavica*, 83:3–77, 1965.

[49] J.D. Currey. How well are bones designed to resist fracture? *Journal of Bone and Mineral Research*, 18(4):591–598, 2003.

[50] American Society for Metals. *Metals Handbook Ninth Edition, Vol.8: Mechanical testing*. 1985.

[51] N. Sasaki, Y. Nakayama, M. Yoshikawa, and A. Enyo. Stress relaxation of bone and bone collagen. *Journal of Biomechanics*, 26(1):1369–1376, 1993.

[52] A.A. Lugassy and E. Korostof. *Viscoelastic behaviour of bovine femoral cortical bone and sperm whale dentin. In: Korostof K.(ed.) Research in Dental and Medical Materials*. Plenum Press, New York, 1969.

[53] T. Goto, N. Sasaki, and K. Hikichi. Early stage-stress relaxation in compact bone. *Journal of Biomechanics*, 32(1):93–97, 1999.

[54] T. Iyo, Y. Maki, N. Sasaki, and M. Nakata. Anisotropic viscoelastic properties of cortical bone. *Journal of Biomechanics*, 37(1):1433–1437, 2004.

[55] T. Iyo, N. Sasaki, Y. Maki, and M. Nakata. Mathemetical description of bovine femoral cortical bone. *Biorheology*, 43(2):117 – 132, 2006.

[56] M.M. Panjabi, A.A. White, and W.O. Southwick. Mechanical properties of bone as a function of rate of deformation. *Journal of Bone and Joint Surgery*, 55A(2):322–330, 1973.

[57] B. Bernstein, A. Kearsley, and L.J. Zapas. A study of stress relaxation with finite strain. *Transactions of the Society of Rheology*, 7(1):391–410, 1963.

[58] R. Ko. The tension test upon the compact substance of the long bones of human extremities. *Journal of Kyoto Prefectural University of Medicine*, 53:503–525, 1953.

[59] M.S. Lappi, V.G. King and I.L. May. Determination of elasticconstants for human femurs. *Journal of Biomechanical Engineering*, 101:193–197, 1979.

[60] W. Abendschein and G.W. Hyatt. Ultrasonics selected physical properties of bone. *Clinical Orthopaedics*, 69:294–301, 1970.

[61] R.B. Ashman, S.C. Cowin, W.C. Van Buskirk, and J.C. Rice. A continuous wave technique for the measurement of the elastic properties of cortical bone. *Journal of Biomechanics*, 17(5):349–361, 1984.

[62] B. Hopkinson. A method of measuring the pressure produced in the detonation of high explosives or by the impact of bullets. *Philosophical Transactions of the Royal Society of London*, Series A(213):437–456, 1914.

[63] R.M. Davies. A critical study of the Hopkinson pressure bar. *Philosophical Transactions of the Royal Society*, A240(1):375–457, 1948.

[64] H. Kolsky. An investigation of the mechanical properties of materials at very high rates of strain. *Proceedings of the Royal Physical Society*, Section B(62):676–700, 1949.

[65] F.E. Hauser. Techniques for measuring stress-strain relations at high strain rates. *Experimental Mechanics*, 6:395–402, 1966.

[66] H. Zhao and G. Gary. On the use of SHPB techniques to determine the dynamic behaviour of materials in the range of small strains. *International Journal of Solids and Structures*, 33(23):3363–3375, 1996.

[67] S.T. Marais. Development and proving of a Split Hopkinson Pressure Bar used for high strain rate materials testing. Master's thesis, Deprtment of Mechanical Engineering, University of Cape Town, 2001.

[68] S. Ellwood, L.J. Griffiths, and D.J. Parry. Materials testing at high constant strain rates. *Journal of Physics E: Scientific Instruments*, 15:280–282, 1981.

[69] B. Songa, W. Chen, Y. Ge, and T. Weerasooriya. Dynamic and quasi-static compressive response of porcine muscle. *Journal of Biomechanics*, 40:2999–3005, 2007.

[70] D.J. Frew, M.J. Forrestal, and W. Chen. Pulse shaping techniques for testing brittle materials with a split Hopkinson pressure bar. *Experimental Mechanics*, 42:93–106, 2002.

[71] H. Kobayashi, M. Daimaruya, T. Nojima, and T. Kajino. Effect of strain rate change during uniaxial dynamic tensile tests on instability strain. *Journal of Physics IV France*, 10:433–438, 2000.

[72] T.S. Lok, M. ASCE, and P.J. Zhao. Impact response of steel fiber-reinforced concrete using a split Hopkinson pressure bar. *Journal of Materials in Civil Engineering*, 16:54–59, 2004.

[73] A. Kumar, T.S. Lok, and Z. Pengjun. Design of an impact striker for a split Hopkinson pressure bar. *Journal of the Institution of Engineers, Singapore*, 4(1):119–130, 2004.

[74] C. Salisbury. Spectral analysis of wave propogation through a polymeric Hopkinson bar. Master's thesis, University of Waterloo, 2001.

[75] B. Chen, W. Zhang and M.J. Forrestal. A split Hopkinson bar technique for low-impedance materials. *Experimental Mechanics*, 39(2):81–85, 1999.

[76] A. Hosokawa and T. Otani. Ultrasonic wave propagation in bovine cancellous bone. *Acoustical Society of America*, 101(1):558–562, 1997.

[77] K.I. Lee and S.W. Yoon. Comparison of acoustic characteristics predicted by Biot's theory and the modified Biot Attenborough model in cancellous bone. *Journal of Biomechanics*, 39:364–368, 2006.

[78] J.L. Williams. Ultrasonic wave propogation in cancellous and cortical bone. prediction of some experimental results by Biot's theory. *Journal of the Acoustical Society of America*, 91(2):1106 – 1112, 1992.

[79] M.A. Biot. Generalized theory of acoustic propagation in porous dissipative media. *Journal of the Acoustical Society of America*, 34:12541264., 1962.

[80] E. Garner, R. Lakes, T. Lee, C. Swan, and R. Brand. Viscoelastic dissipation in compact bone: implications for stress-induced fluid flow in bone. *Transactions of the ASME*, 122:166–172, 2000.

[81] N. Sasaki and A. Enyo. Viscoelastic properties of bone as a function of water content. *Journal of Biomechanics*, 28(7):809–815, 1995.

[82] G. E. Mase. *Schaum's outline of theory and problems of continuum mechanics.* McGraw-Hill, 1970.

[83] J.R. Funk, G.W. Hall, Crandall J.R., and W.D. Pilkey. Linear and quasi-linear viscoelastic characterization of ankle ligaments. *Journal of Biomechanical Engineering*, 122(1):15–22, 2000.

[84] L.M. Yang, V.P.W. Shim, and C.T. Lim. A visco-hyperelastic approach to modelling the constitutive behaviour of rubber. *International Journal of Impact Engineering*, 24(1):545–560, 1999.

[85] F.J. Lockett. *Non-linear viscoelastic solids.* New York: Academic Press Inc. Ltd., 1972.

[86] P.J. Carreau, D.C.R. De Kee, and R.P. Chabra. *Rheology of polymeric systems: principles and applications.* Hanser Publishers, 1997.

[87] W.F. Findley, S.L James, and K. Onaran. *Creep and relaxation of nonlinear viscoelastic materials witha an introduction to linear viscoelasticity.* Dover Publications Inc., New York, 1989.

[88] D.R. Carter and W.C. Hayes. Bone compressive strength: The influence of density and strain rate. *Science, New Series*, 194(4270):1174–1176, 1976.

[89] M. Pithioux, D. Subit, and P. Chabrand. Comparison of compact bone failure under two different loading rates: experimental and modelling approaches. *Medical Engineering and Physics*, 26(1):647–653, 2004.

[90] J.D. Currey. Tensile yield in compact bone is determined by strain, post-yield behaviour by mineral content. *Journal of Biomechanics*, 37(1):549556, 2004.

[91] Magnussa. www.magnussa.com/cowscele.jpg.

[92] A. Chinsamy and M.A. Raath. Preparation of fossil bone for histological examination. *Paideontology Africa*, 29:39 – 44, 1992.

[93] A. Chinsamy-Turan. *The microstructure of dinosaur bone: deciphering biology with fine scale techniques*. Baltimore: Johns Hopkins University Press, 2005.

[94] J.H. Kim, M. Niinomi, J. Akahori, T.and Takeda, and Hiroyuki Toda. Effect of microstructure on fatigue strength of bovine compact bones. *JSME International Journal, Series A*, 48(4):472–480, 2005.

[95] Y. Quirion and A. S. Lesaffre. Hydraulic machine tests for compression of a quasi-brittle material at medium strain rate. *Journal de Physique IV*, 134:553–558, 2006.

[96] M.F. Spotts. *Mechanical Design Analysis*. Prentice-Hall, Inc., Englewood Cliffs, New Yersey, 1964.

[97] S.R. Reid, M.M. Al-Mousawi, and W.F. Deans. The use of split Hopkinson pressure bar techniques in high strain rate materials testing. *Journal of Mechanical Engineering Science*, 221(C):273–292, 1997.

[98] P. Follansbee. The Hopkinson Bar. *Metals Handbook, American Society for Metals*, 8:198–203, 1985.

[99] R. Merle and H. Zhao. On the errors associated with the use of large diameter shpb, correction for radially non-uniform distribution of stress and particle velocity in shpb testing. *International Journal of Impact Engineering*, 32:1964–1980, 2006.

[100] D. Hull. *An Introduction to Composite Materials*. Press syndicate of the University of Cambridge, 1981.

[101] J.D. Currey and K. Brear. Tensile yield in bone. *Calcified Tissue Research*, 15(1):173–179, 1974.

[102] M. Watanabe, C. Mercer, C.G. Levi, and A.G. Evans. A probe for the high temperature deformation of thermal barrier oxides. *Acta Materialia*, 52:1479–1487, 2004.

[103] D.J. Inman. *Engineering Vibration*. Prentice Hall Inc., 1996.

[104] F.S. Tse, E.M. Morse, and R.T. Hinkle. *Mechanical Vibrations Theory and Applications*. Allyn and Bacon Inc., 2nd edition, 1983.

[105] The definition of the square-root-of the strain rate tensor. Personal communication with Dr. Shim. Impact Mechanics Laboratory, Department of Mechanical Engineering, National University of Singapore. October to November 2007.

[106] M.W. Lai, D. Rubin, and E. Krempl. *Introduction to Continuum Mechanics*. Butterworth-Heinemann Ltd, 1999.

[107] T. Krauthammer, A. Jenssen, and M. Langseth. Precision testing in support of computer code validation and verification. Technical Report 234/96, Norwegian defence construction service, May 1996.

[108] *ABAQUS Analysis User's Manual*. Version 6.5, volume IV, section 18.2.1.

[109] L. Olovsson, K. Simonsson, and M. Unosson. Selective mass scaling for explicit finite element analyses. *International Journal for Numerical Methods in Engineering*, 63:1436–1445, 2005.

[110] M. Vicenoti, C. Zannoni, L. Pierotti, and C. Massimiliano. Spatial positioning of a hip stem solid model within the CT data set of the host bone. *Computer Methods and Programs in Biomedicine*, 58:219–226, 1999.

[111] V. Tarigopula, M. Langseth, O.S. Hopperstad, and A.H. Clausen. Axial crushing of thin-walled high-strength steel sections. *International Journal of Impact Engineering*, 32:847–882, 2006.

Appendices

Appendix A

Longitudinal bone compression results

A.1 Ultimate properties of longitudinal specimens

$\dot{\varepsilon} \approx 10^{-4}\,\mathrm{s}^{-1}$	σ_{ut} [MPa]	ε_{ut} [m/m]
Bone 1	133.8626	0.0355
Bone 2	134.7213	0.0332
Bone 3	145.9889	0.0331
Bone 4	141.4726	0.0428
Bone 5	152.8431	0.0437
Bone 6	176.6218	0.0433
Bone 7	131.6101	0.0405
Bone 8	161.3936	0.0418
Bone 9	156.9545	0.0424
Bone 10	154.1624	0.0397
Bone 11	156.3654	0.0422
Average	149.64	0.0398

Table A.1: Quasi-static compression test results for longitudinal specimens at $\dot{\varepsilon} = 10^{-4}\,\mathrm{s}^{-1}$. The stress vs. strain and strain rate vs. time histories are presented in Fig.A.1.

$\dot{\varepsilon} \approx 10^{-3}\,\mathrm{s}^{-1}$	σ_{ut} [MPa]	ε_{ut} [m/m]
Bone 1	147.2126	0.0408
Bone 2	171.3539	0.0435
Bone 3	131.8966	0.0383
Bone 4	186.4322	0.0497
Bone 5	165.3455	0.0472
Bone 6	184.8297	0.0446
Bone 7	185.5062	0.0479
Bone 8	181.8037	0.0463
Bone 9	193.0807	0.0487
Bone 10	177.7898	0.0424
Bone 11	166.1415	0.0463
Average	171.94	0.0451

Table A.2: Quasi-static compression test results for longitudinal specimens at $\dot{\varepsilon} = 10^{-3}\,\mathrm{s}^{-1}$. The stress vs. strain and strain rate vs. time histories are presented in Fig.A.2.

Varying $\dot{\varepsilon} \approx 10^{-2}\,\mathrm{s}^{-1}$	σ_{ut} [MPa]	ε_{ut} [m/m]
Bone 1	177.2460	0.0422
Bone 2	187.8324	0.0461
Bone 3	182.1799	0.0458
Bone 4	220.8648	0.0540
Bone 5	207.2376	0.0525
Bone 6	214.4554	0.0528
Bone 7	205.5885	0.0549
Bone 8	196.5060	0.0511
Bone 9	209.7209	0.0519
Bone 10	220.9733	0.0528
Bone 11	200.8992	0.0535
Average	202.137	0.051

Table A.3: Quasi-static compression test results for longitudinal specimens at $\dot{\varepsilon} = 10^{-2}\,\mathrm{s}^{-1}$. The stress vs. strain and strain rate vs. time histories are presented in Fig.A.3.

Varying $\dot{\varepsilon} \approx 10^{-1}\,\mathrm{s}^{-1}$	σ_{ut} [MPa]	ε_{ut} [m/m]
Bone 1	207.9554	0.0550
Bone 2	239.4020	0.0578
Bone 3	242.5349	0.0636
Bone 4	262.9244	0.0635
Bone 5	226.4986	0.0639
Bone 6	244.5141	0.0656
Bone 7	234.2693	0.0655
Bone 8	244.6745	0.0687
Bone 9	219.3200	0.0583
Bone 10	225.9761	0.0597
Average	234.8069	0.0622

Table A.4: Quasi-static compression test results for longitudinal specimens at $\dot{\varepsilon} = 10^{-1}\,\mathrm{s}^{-1}$. The stress vs. strain and strain rate vs. time histories are presented in Fig.A.4.

Varying $\dot{\varepsilon} \approx 2.5 \times 10^{2}\,\mathrm{s}^{-1}$	σ_{ut} [MPa]	ε_{ut} [m/m]
Bone 1	336.6426	0.0261
Bone 2	407.5329	0.0249
Bone 3	398.9782	0.0262
Bone 4	420.4433	0.0273
Bone 5	352.9231	0.0223
Bone 6	386.1600	0.0201
Bone 7	372.2995	0.0218
Bone 8	388.6286	0.0217
Bone 9	315.5213	0.0245
Bone 10	390.9993	0.0270
Bone 11	383.2603	0.0240
Bone 12	355.1840	0.0270
Average	375.71	0.024

Table A.5: Conventional SHPB compression test results for longitudinal specimens at strain rates of $\dot{\varepsilon} = 2.5 \times 10^{2}\,\mathrm{s}^{-1}$. The stress vs. strain and strain rate vs. time histories are presented in Fig.A.5.

Constant $\dot{\varepsilon} \approx 2.5 \times 10^2\,\mathrm{s}^{-1}$	σ_{ut} [MPa]	ε_{ut} [m/m]
Bone 1	388.2830	0.0222
Bone 2	395.3021	0.0260
Bone 3	408.1475	0.0281
Bone 4	349.3101	0.0276
Bone 5	383.1540	0.0237
Bone 6	385.0092	0.0260
Bone 7	372.9212	0.0228
Bone 8	404.7216	0.0232
Bone 9	349.2162	0.0186
Bone 10	403.3491	0.0209
Average	383.94	0.024

Table A.6: SHPB compression test results for longitudinal specimens at strain rates of $\dot{\varepsilon} = 2.5 \times 10^2\,\mathrm{s}^{-1}$ with a tapered striker. The stress vs. strain and strain rate vs. time histories are presented in Fig.A.6.

Varying $\dot{\varepsilon} \approx 10^3\,\mathrm{s}^{-1}$	σ_{ut} [MPa]	ε_{ut} [m/m]
Bone 14	428.1808	0.0303
Bone 15	366.6279	0.0317
Bone 16	404.8840	0.0256
Bone 17	405.6773	0.0294
Bone 18	419.0164	0.0308
Bone 19	386.1604	0.0279
Bone 20	371.9117	0.0365
Bone 21	417.9084	0.0291
Bone 22	404.6240	0.0254
Bone 23	413.8760	0.0273
Average	401.89	0.0294

Table A.7: Conventional SHPB compression test results for longitudinal specimens at strain rates of $\dot{\varepsilon} = 10^3\,\mathrm{s}^{-1}$. The stress vs. strain and strain rate vs. time histories are presented in Fig.A.7.

Constant $\dot{\varepsilon} \approx 10^3\,\mathrm{s}^{-1}$	σ_{ut} [MPa]	ε_{ut} [m/m]
Bone 14	439.8628	0.0267
Bone 16	442.1849	0.0273
Bone 17	432.1125	0.0275
Bone 19	420.4433	0.0273
Bone 20	424.6453	0.0272
Bone 21	394.3608	0.0280
Bone 22	428.4652	0.0287
Bone 23	384.6428	0.0281
Average	413.90	0.027

Table A.8: SHPB compression test results for longitudinal specimens at strain rates of $\dot{\varepsilon} = 10^3\,\mathrm{s}^{-1}$ with a tapered striker. The stress vs. strain and strain rate vs. time histories are presented in Fig.A.8.

A.2 Longitudinal specimen response histories

A.2.1 Quasi-static compression at $\dot{\varepsilon} = 10^{-4}\,\mathrm{s}^{-1}$

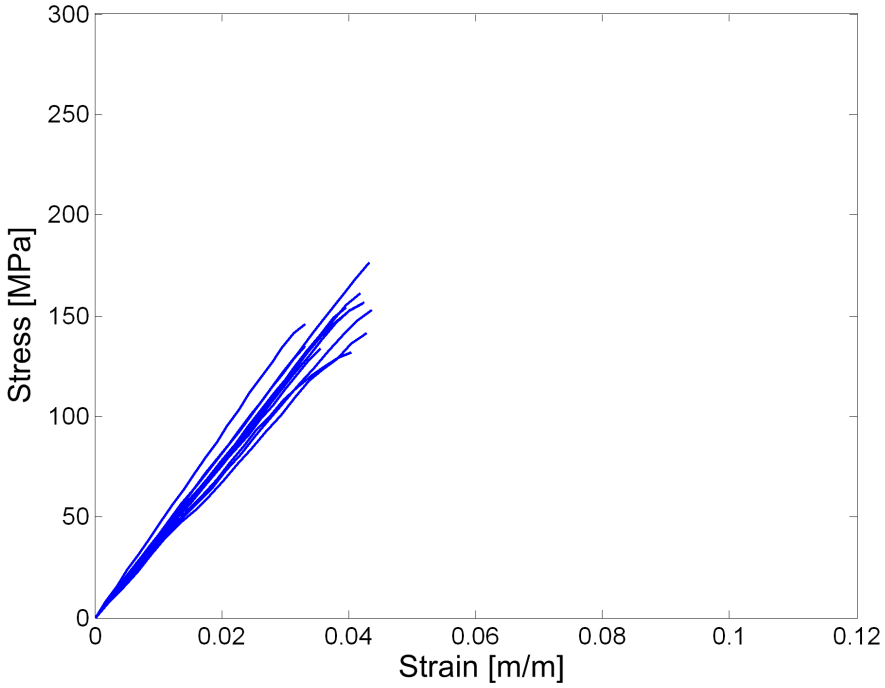

(a) Stress vs. strain

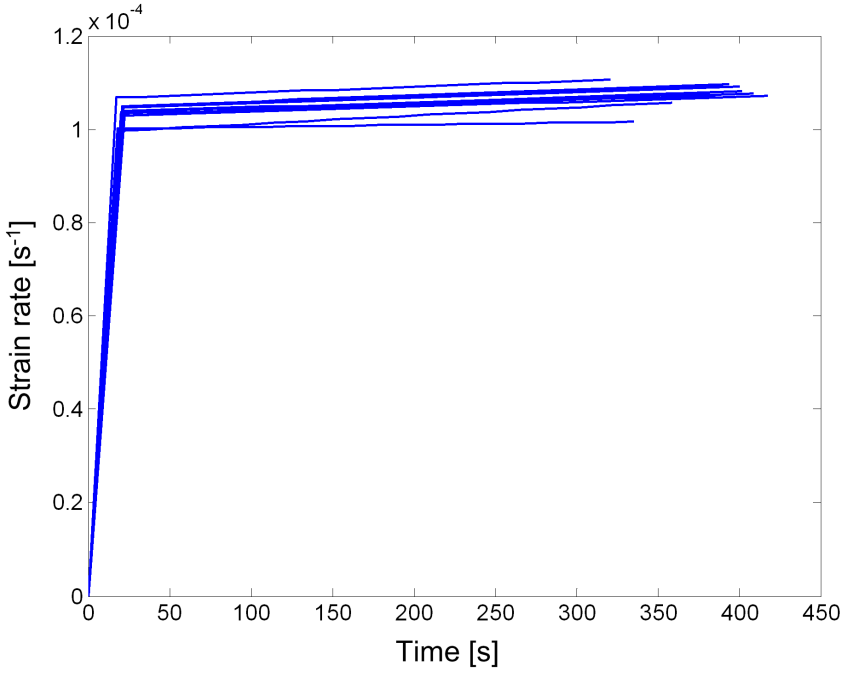

(b) Strain rate vs. time

Figure A.1: Longitudinal bovine cortical bone compression at $\dot{\varepsilon} = 10^{-4}\,\mathrm{s}^{-1}$. Ultimate properties for these responses are reported in Table A.1.

A.2.2 Quasi-static compression at $\dot{\varepsilon} = 10^{-3}\,\mathrm{s}^{-1}$

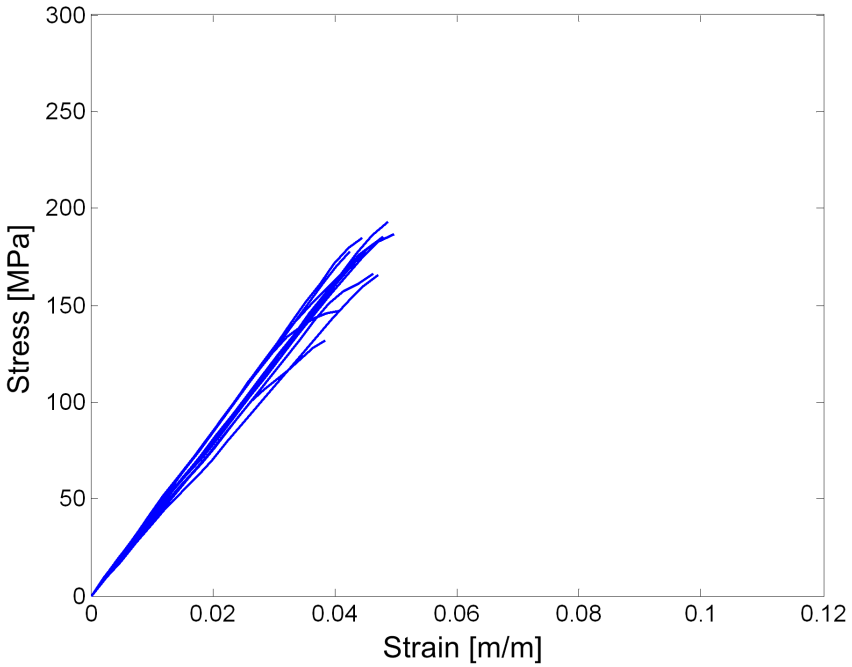

(a) Stress vs. strain

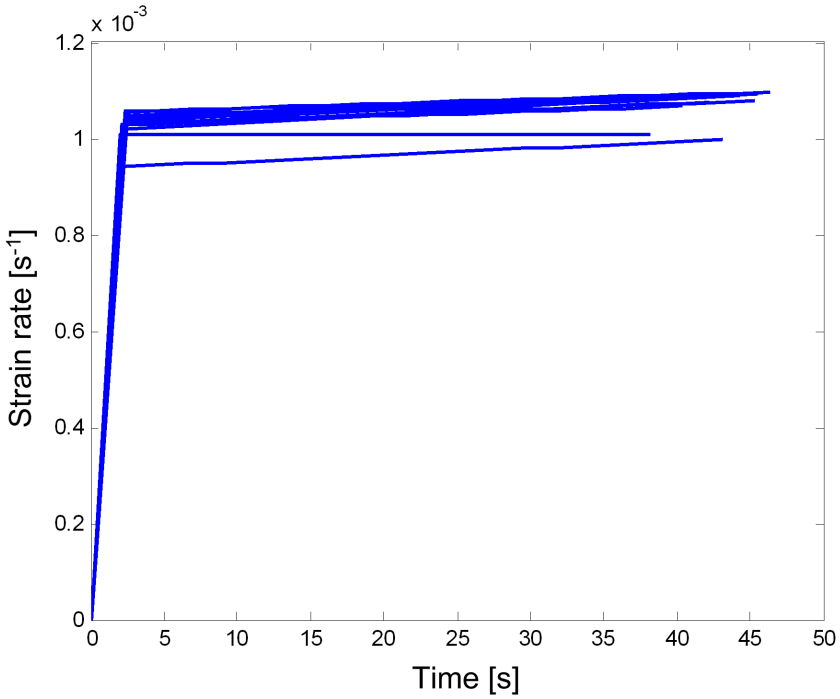

(b) Strain rate vs. time

Figure A.2: Longitudinal bovine cortical bone compression at $\dot{\varepsilon} = 10^{-3}\,\mathrm{s}^{-1}$. Ultimate properties for these responses are reported in Table A.2.

A.2.3 Quasi-static compression at $\dot{\varepsilon} = 10^{-2}\,\mathrm{s}^{-1}$

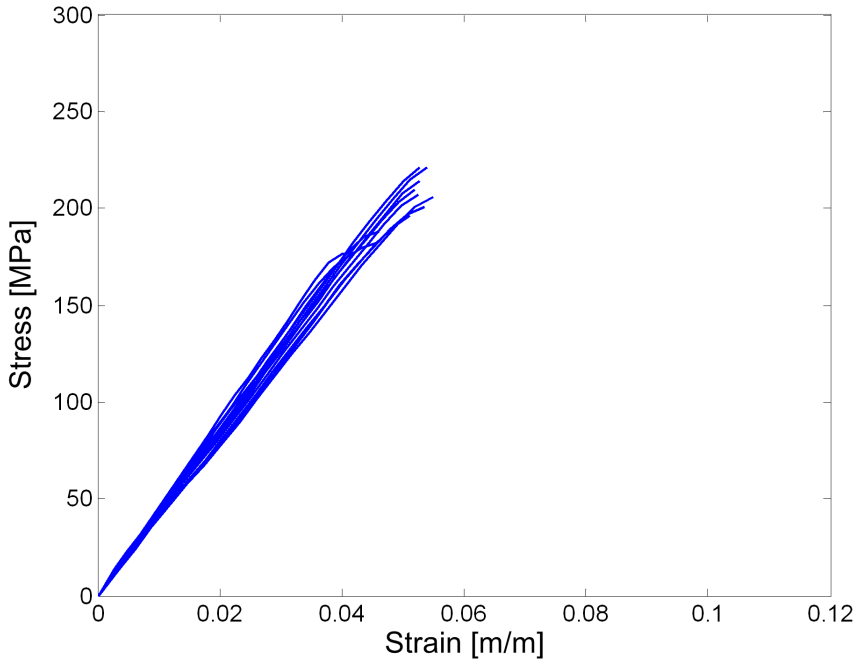

(a) Stress vs. strain

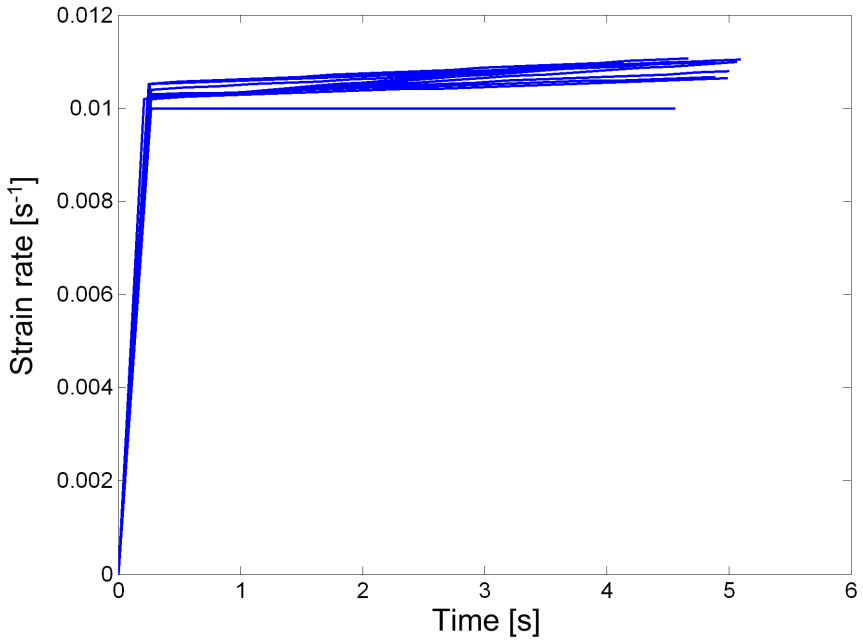

(b) Strain rate vs. time

Figure A.3: Longitudinal bovine cortical bone compression at $\dot{\varepsilon} = 10^{-2}\,\mathrm{s}^{-1}$. Ultimate properties for these responses are reported in Table A.3.

A.2.4 Quasi-static compression at $\dot{\varepsilon} = 10^{-1}\,\mathrm{s}^{-1}$

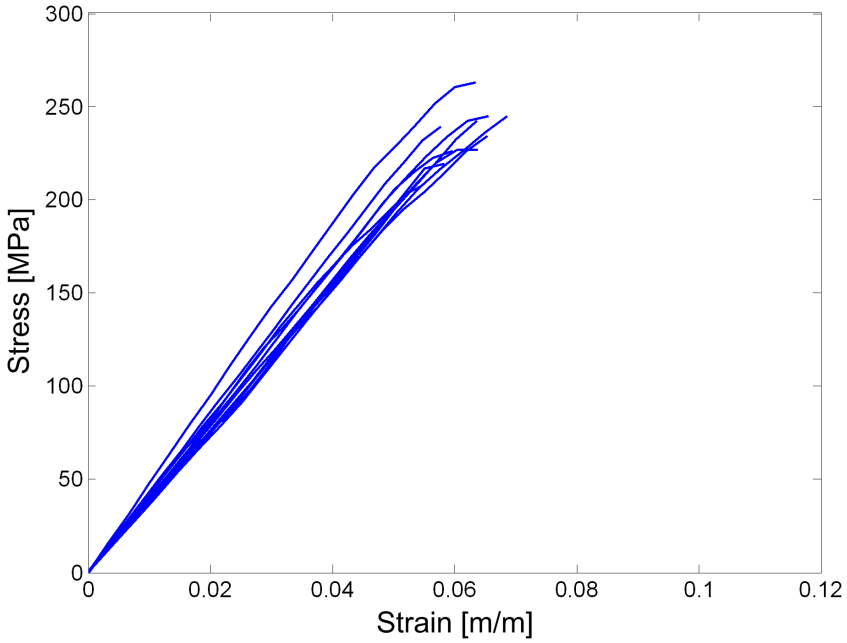

(a) Stress vs. strain

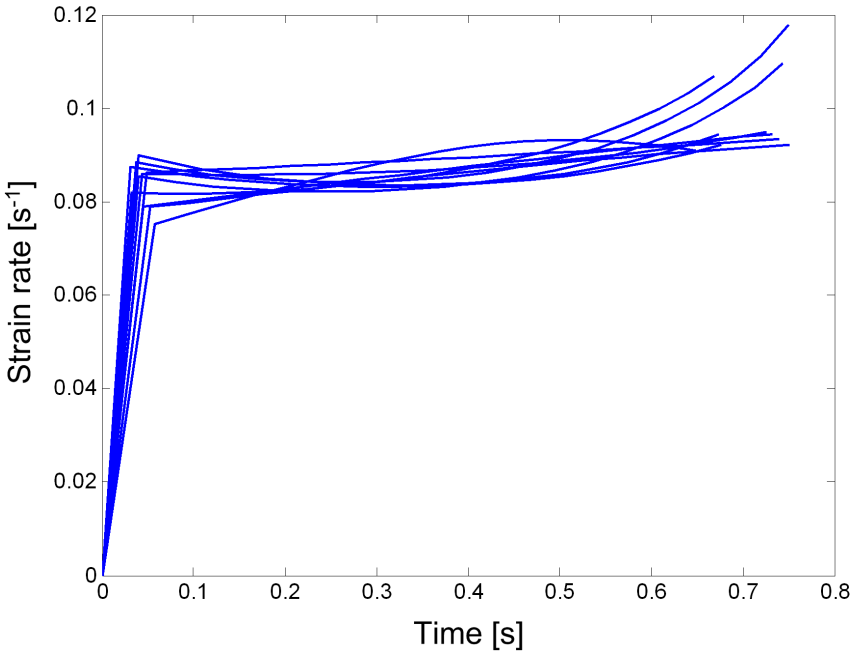

(b) Strain rate vs. time

Figure A.4: Longitudinal bovine cortical bone compression at $\dot{\varepsilon} = 10^{-1}\,\mathrm{s}^{-1}$. Ultimate properties for these responses are reported in Table A.4.

A.2.5 Dynamic compression with a cylindrical striker on the SHPB at $\dot{\varepsilon} \approx 2.5 \times 10^2\,\mathrm{s}^{-1}$

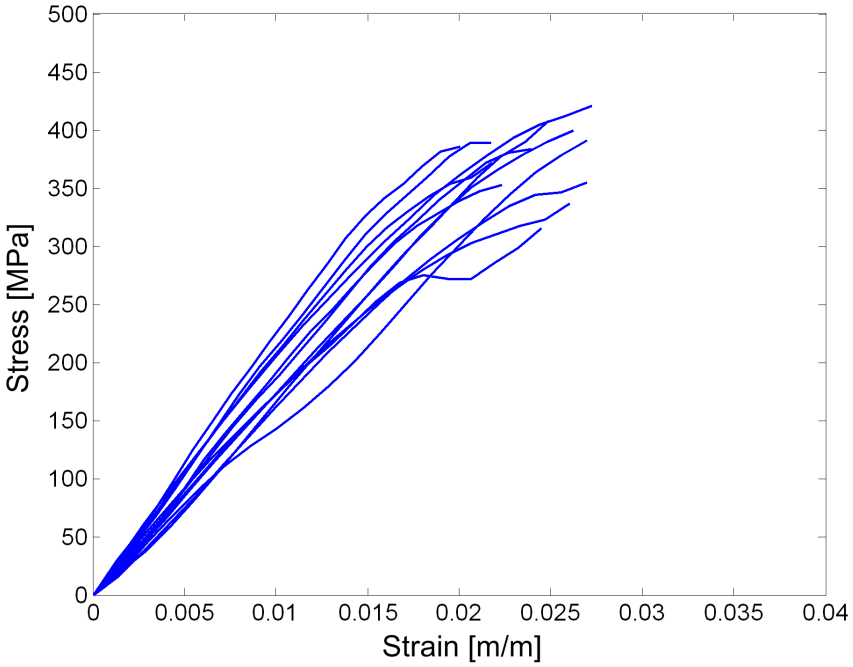

(a) Stress vs. strain

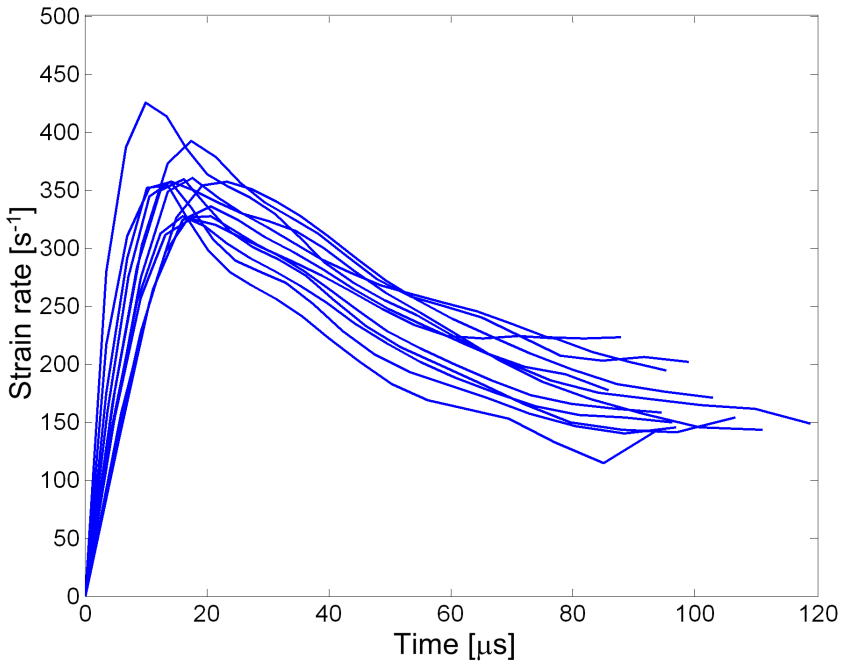

(b) Strain rate vs. time

Figure A.5: Longitudinal bovine cortical bone compression with a conventional striker (on the SHPB) at a strain rate that varies around $\dot{\varepsilon} \approx 2.5 \times 10^2\,\mathrm{s}^{-1}$. Ultimate properties for these responses are reported in Table A.5.

A.2.6 Dynamic compression with a tapered striker on the SHPB at $\dot{\varepsilon} \approx 2.5 \times 10^2\,\mathrm{s}^{-1}$

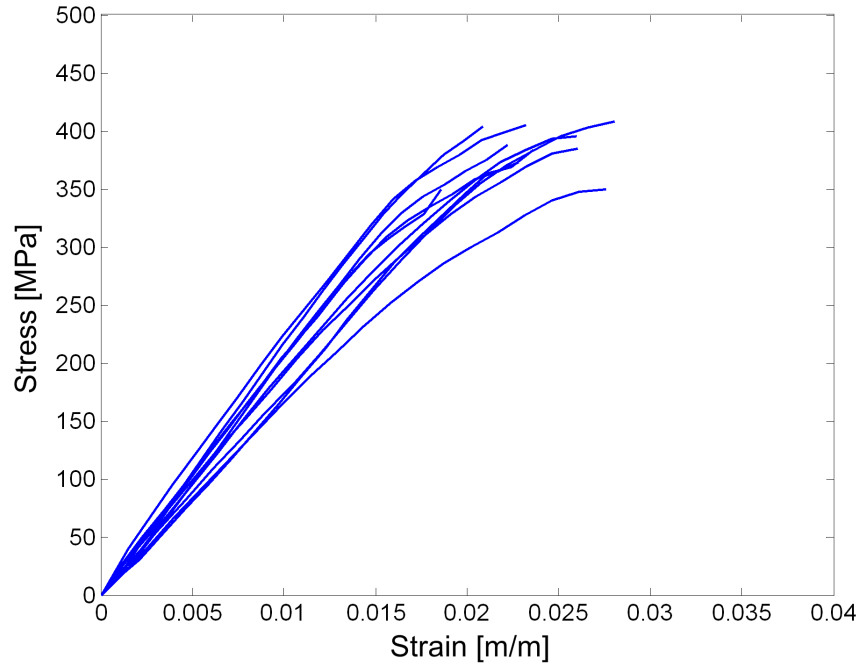

(a) Stress vs. strain

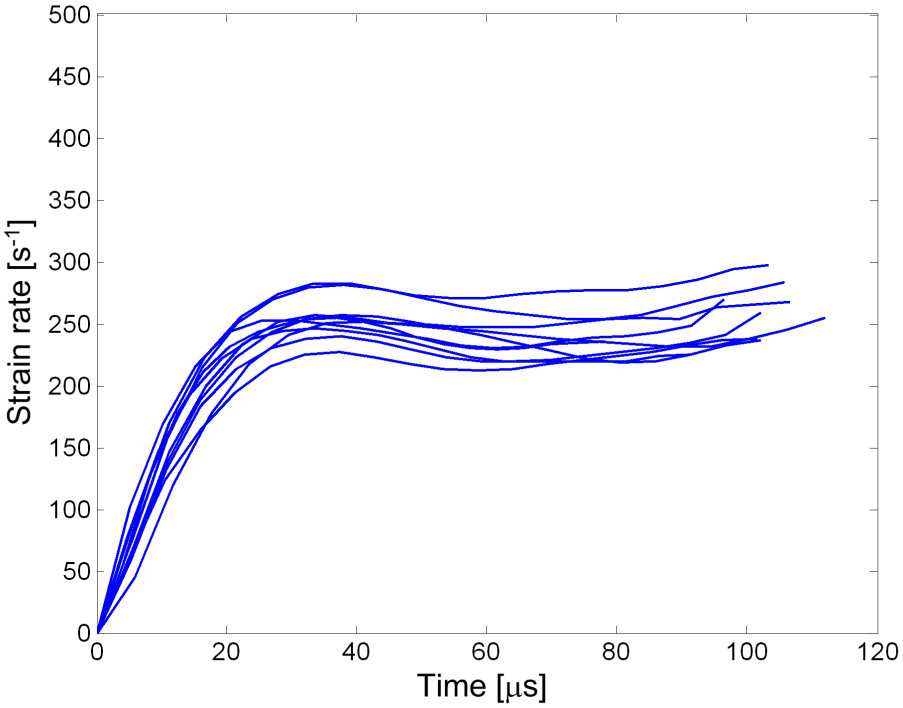

(b) Strain rate vs. time

Figure A.6: Longitudinal bovine cortical bone compression with a tapered striker at a strain rate that is constant around $\dot{\varepsilon} \approx 2.5 \times 10^2\,\mathrm{s}^{-1}$. Ultimate properties for these responses are reported in Table A.6.

A.2.7 Dynamic compression with a cylindrical striker on the SHPB at $\dot{\varepsilon} = 10^3\,\mathrm{s}^{-1}$

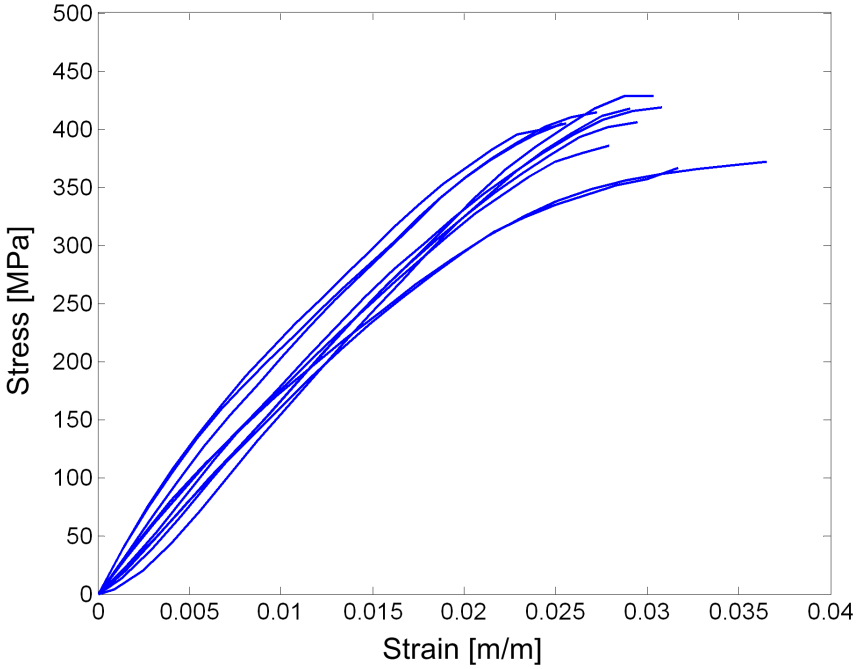

(a) Stress vs. strain

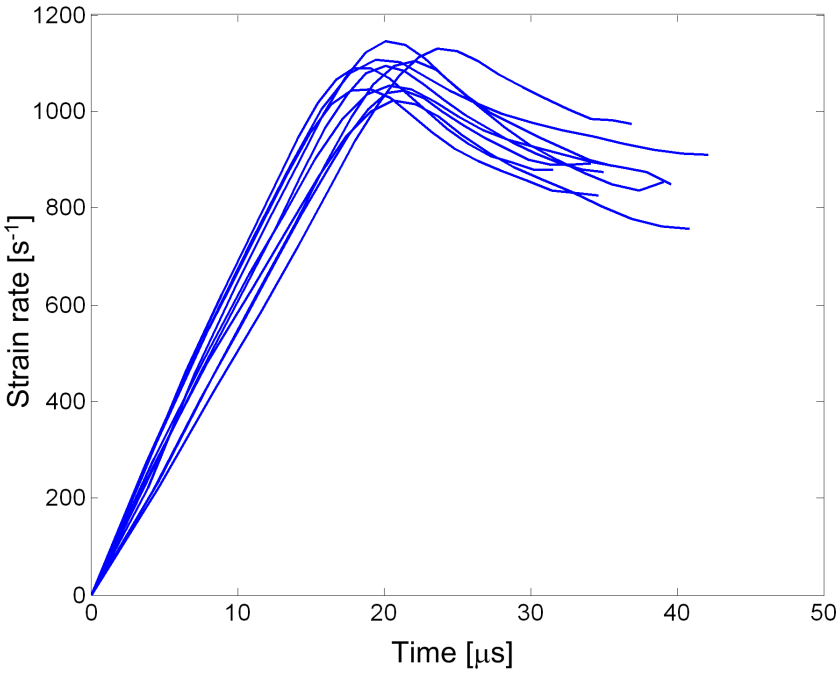

(b) Strain rate vs. time

Figure A.7: Longitudinal bovine cortical bone compression with a conventional striker (on the SHPB) at a strain rate that varies around $\dot{\varepsilon} \approx 10^3\,\mathrm{s}^{-1}$. Ultimate properties for these responses are reported in Table A.7.

A.2.8 Dynamic compression with a tapered striker on the SHPB at $\dot{\varepsilon} = 10^3\,\mathrm{s}^{-1}$

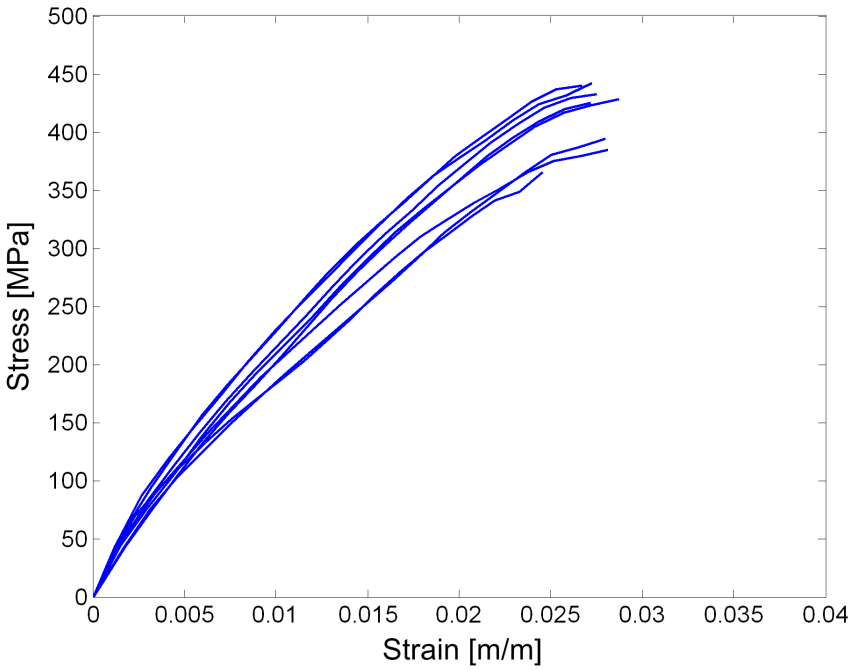

(a) Stress vs. strain

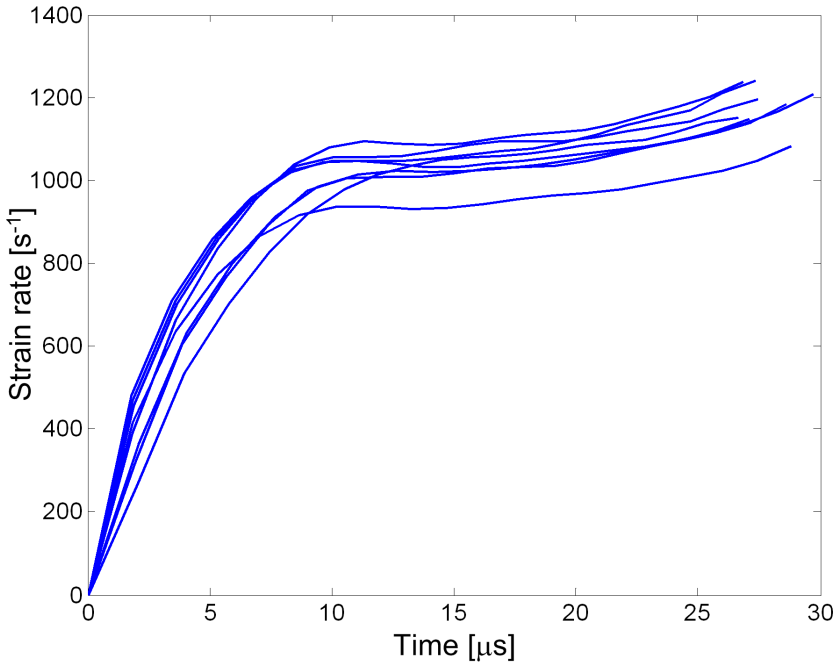

(b) Strain rate vs. time

Figure A.8: Longitudinal bovine cortical bone compression with a tapered striker at a strain rate that is constant around $\dot{\varepsilon} \approx 10^3\,\mathrm{s}^{-1}$. Ultimate properties for these responses are reported in Table A.8.

A.3 Microstructure of bone specimens that failed in quasi-static compression

This section presents additional slides of the microstructure of longitudinal cortical bone specimens that fractured in quasi-static compression.

All fractures were shear type fractures where the crack moved across the bone porosity. Quasi-static bone compression of Bone 1 at $\dot{\varepsilon} = 10^{-4}\,\mathrm{s}^{-1}$ (Figs.A.9(c) and A.9(d)) shows alignment of the vascular canals along the crack direction. There is a transition between laminar and reticular microstructural arrangements in the particular specimen. It seems that the crack originates at a blood vessel on the specimen surface.

These slides are included for informative purposes as no conclusive observations are possible at present.

(a) Bone 6: $\dot{\varepsilon} = 10^{-2}\,\mathrm{s}^{-1}$

(b) Bone 8: $\dot{\varepsilon} = 10^{-2}\,\mathrm{s}^{-1}$

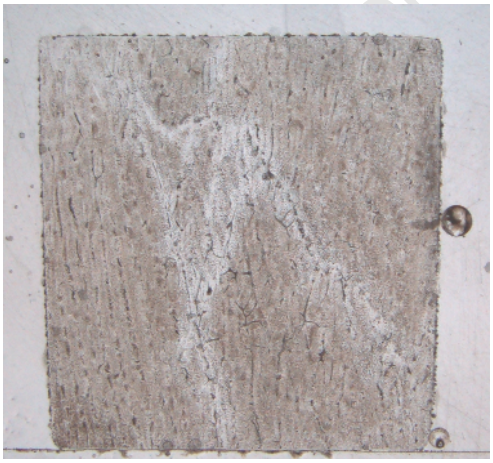

(c) Bone 1: $\dot{\varepsilon} = 10^{-4}\,\mathrm{s}^{-4}$

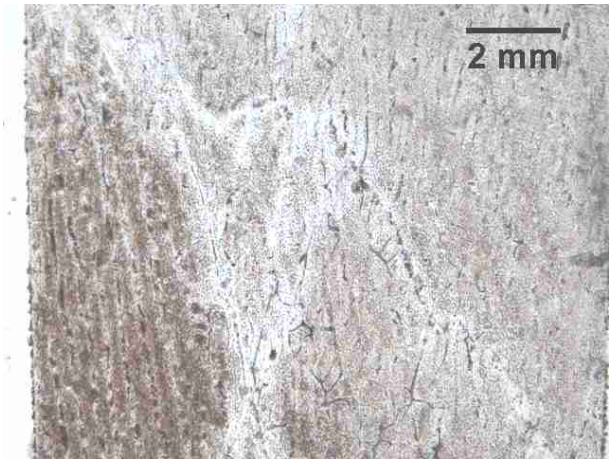

(d) Bone 1: $\dot{\varepsilon} = 10^{-4}\,\mathrm{s}^{-1}$ enlarged view

Figure A.9: Longitudinal sections of specimens that failed in quasi-static compression

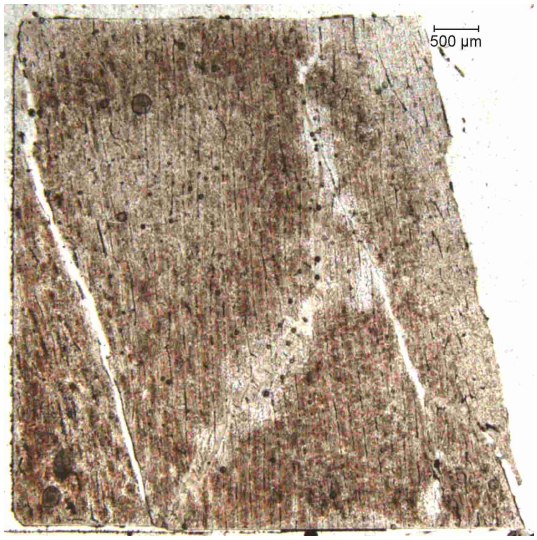

(a) Bone 10: $\dot{\varepsilon} = 10^{-2}\,\mathrm{s}^{-1}$

(b) Bone 11: $\dot{\varepsilon} = 10^{-3}\,\mathrm{s}^{-1}$

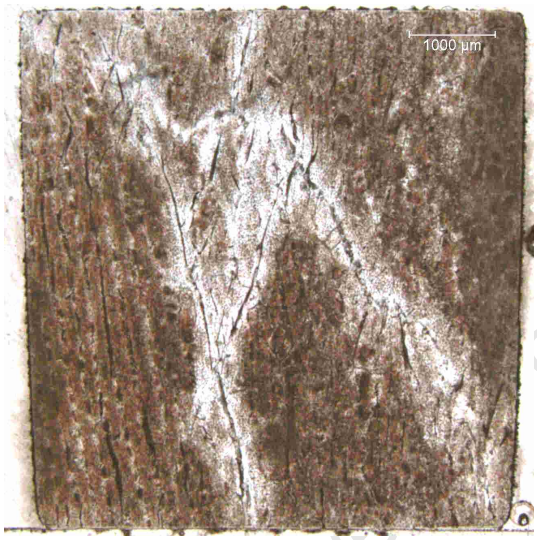

(c) Bone 1: $\dot{\varepsilon} = 10^{-4}\,\mathrm{s}^{-1}$

(d) Bone 3 $\dot{\varepsilon} = 10^{-3}\,\mathrm{s}^{-1}$

(e) Bone 4: $\dot{\varepsilon} = 10^{-3}\,\mathrm{s}^{-1}$

(f) Bone 6: $\dot{\varepsilon} = 10^{-3}\,\mathrm{s}^{-1}$

Figure A.10: Longitudinal sections of specimens that failed in quasi-static compression

A.4 Specimen density data

A.4.1 Apparent bone density

	Length [mm]	Diameter [mm]	Mass [mg]	Volume [mm^3]	Density [$kg.\,m^{-3}$]
Bone 1	6.10	6.04	351	174.8	2008.2
Bone 2	6.00	6.08	362	174.2	2078.1
Bone 3	6.08	6.08	356	176.5	2016.7
Bone 4	5.94	5.96	342	165.7	2063.8
Bone 5	5.94	6.10	352	173.6	2027.7
Bone 6	5.98	6.02	352	170.2	2068.0
Bone 7	5.98	6.08	346	173.6	1992.9
Bone 8	5.98	6.04	347	171.0	2025.2
Bone 9	5.90	6.04	352	169.0	2082.2
Bone 10	5.90	6.02	345	167.9	2054.4
Bone 11	5.90	6.02	352	167.9	2096.1
Bone 12	5.86	6.12	355	172.3	2059.4
Bone 13	5.90	6.10	356	172.4	2064.7
Bone 14	6.04	6.10	373	176.5	2113.1
Bone 15	6.02	5.98	356	169.0	2105.5
Bone 16	6.08	6.00	364	171.9	2117.4
Bone 17	5.88	6.06	354	169.6	2087.3
Bone 18	6.04	6.10	376	176.5	2130.1
Bone 19	5.92	6.08	356	171.8	2071.2
Bone 20	5.88	6.06	360	169.6	2122.7
Bone 21	6.08	6.04	367	174.2	2106.7
Bone 22	5.98	6.08	365	173.6	2102.3
Bone 23	5.92	6.10	361	173.0	2086.6

Table A.9: The fresh bone density of test specimens from Bones 1 - 23

	Length [mm]	Diameter [mm]	Mass [mg]	Volume [mm^3]	Density [$kg.\,m^{-3}$]
Bone 34	5.96	6.04	343	170.8	2008.6
Bone 34	6.08	6.02	345	173.0	1993.6
Bone 34	5.96	6.02	345	170.0	2033.7
Bone 34	5.98	6.04	346	171.3	2019.3
Bone 35	5.92	6.02	349	168.5	2071.2
Bone 35	5.98	6.08	352	173.6	2027.4
Bone 35	6.10	6.02	357	173.6	2056.2
Bone 35	5.94	6.08	354	172.4	2052.7
Bone 36	6.08	6.02	362	173.0	2091.8
Bone 36	6.00	6.02	353	170.8	2067.0
Bone 36	6.02	6.02	355	171.3	2071.8
Bone 36	6.00	6.04	357	171.9	2076.6
Bone 37	6.02	6.04	349	172.5	2023.3
Bone 37	6.10	6.04	350	174.8	2002.5
Bone 37	6.04	6.00	341	170.8	1996.8
Bone 37	5.94	6.04	340	170.2	1997.7
Bone 38	5.98	6.08	355	173.6	2044.7
Bone 38	6.00	6.06	354	173.0	2045.6
Bone 38	5.90	6.04	344	169.0	2034.9
Bone 38	5.96	6.02	347	169.6	2045.5

Table A.10: The fresh bone density of test specimens from Bones 34 - 38

A.4.2 Dry vs. wet bone density

	Length [mm]	Diameter [mm]	Wet mass [mg]	Volume [mm^3]	Wet density [$kg.\,m^{-3}$]	Dry mass [mm^3]	Dry density [$kg.\,m^{-3}$]
Bone 4	5.95	5.88	346	161.6	2141.5	339	2098.2
Bone 5	5.97	6.04	356	171.1	2081.2	347	2028.6
Bone 6	5.80	5.90	348	158.6	2194.6	340	2144.2
Bone 7	5.84	6.02	355	166.2	2135.7	348	2093.6
Bone 8	5.84	5.94	344	161.8	2125.6	335	2070.0
Bone 9	5.88	5.92	355	161.8	2193.4	347	2143.9
Bone 10	5.76	5.94	346	159.6	2167.7	338	2117.5
Bone 11	5.82	5.94	353	161.3	2188.7	346	2145.3
Bone 14	5.97	6.07	364	172.8	2109.3	355	2054.9
Bone 15	6.01	5.84	339	161.0	2104.5	330	2049.9
Bone 16	6.08	6.04	366	174.2	2102.7	357	2049.3
Bone 17	5.95	5.90	341	162.7	2096.3	332	2040.9
Bone 18	6.09	6 00	348	172.2	2021.0	337	1957.1
Bone 19	5.97	6 00	345	168.8	2042.1	334	1978.7
Bone 20	5.97	6.05	359	171.6	2090.6	349	2033.5
Bone 21	6.05	5.75	327	157.1	2084.0	319	2030.5
Bone 22	6.10	6.06	370	175.9	2105.3	360	2046.2
Bone 23	5.92	6.20	372	178.7	2082.5	363	2031.0

Table A.11: Dry vs. wet bone density

Appendix B

Radial bone compression results

B.1 Ultimate properties of radial specimens

$\dot{\varepsilon} \approx 10^{-4}\,\mathrm{s}^{-1}$	σ_{ut} [MPa]	ε_{ut} [m/m]
Bone 24	147.2303	0.0529
Bone 25	174.3706	0.0791
Bone 26	136.4766	0.0612
Bone 27	197.0358	0.0995
Bone 28	173.1010	0.0827
Average	165.64	0.075

Table B.1: Quasi-static compression test results on radial specimens at $\dot{\varepsilon} \approx 10^{-4}\,\mathrm{s}^{-1}$. The stress vs. strain and strain rate vs. time histories are presented in Fig.B.1.

$\dot{\varepsilon} \approx 10^{-3}\,\mathrm{s}^{-1}$	σ_{ut} [MPa]	ε_{ut} [m/m]
Bone 24	155.4812	0.0850
Bone 25	175.5621	0.0712
Bone 26	169.4414	0.0894
Bone 27	189.6915	0.0879
Bone 28	198.8430	0.0862
Average	177.80	0.084

Table B.2: Quasi-static compression test results on radial specimens at $\dot{\varepsilon} \approx 10^{-3}\,\mathrm{s}^{-1}$. The stress vs. strain and strain rate vs. time histories are presented in Fig.B.2.

$\dot{\varepsilon} \approx 10^{-2}\,\mathrm{s}^{-1}$	σ_{ut} [MPa]	ε_{ut} [m/m]
Bone 24	130.5489	0.0464
Bone 25	203.8834	0.1068
Bone 26	209.3145	0.1040
Bone 27	144.5768	0.0688
Bone 28	187.5047	0.1096
Average	175.17	0.087

Table B.3: Quasi-static compression test results on radial specimens at $\dot{\varepsilon} \approx 10^{-2}\,\mathrm{s}^{-1}$. The stress vs. strain and strain rate vs. time histories are presented in Fig.B.3.

B.2 Radial specimen response histories

B.2.1 Quasi-static compression at $\dot{\varepsilon} = 10^{-4}\,\mathrm{s}^{-1}$

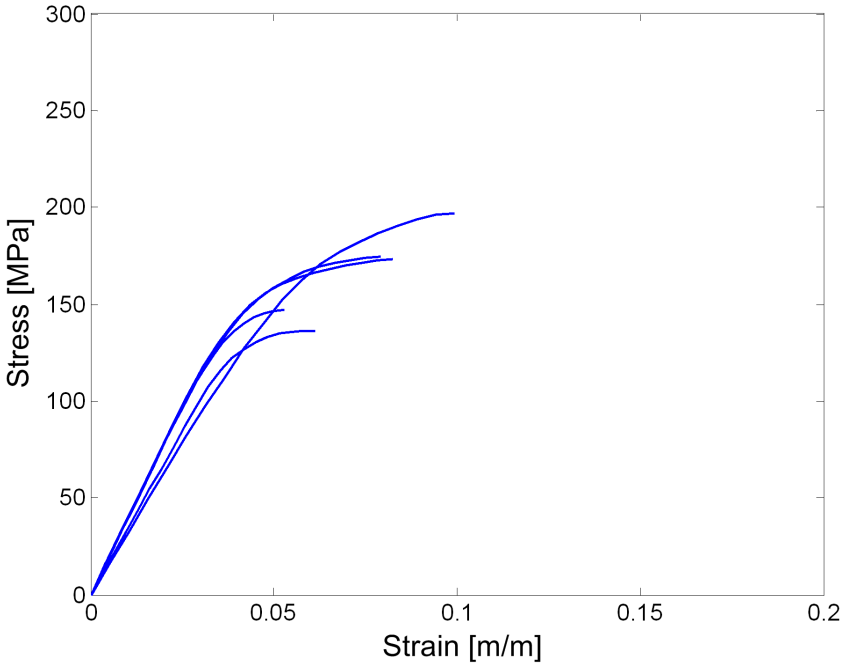

(a) Stress vs. strain

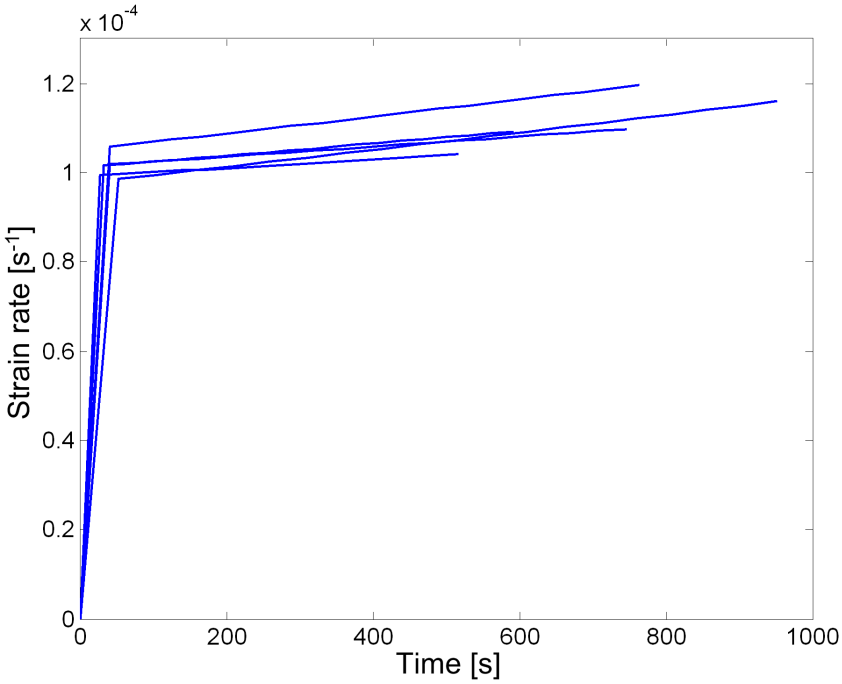

(b) Strain rate vs. time

Figure B.1: Radial bovine cortical bone compression at $\dot{\varepsilon} = 10^{-4}\,\mathrm{s}^{-1}$. Ultimate properties for these responses are reported in Table B.1.

B.2.2 Quasi-static compression at $\dot{\varepsilon} = 10^{-3}\,\mathrm{s}^{-1}$

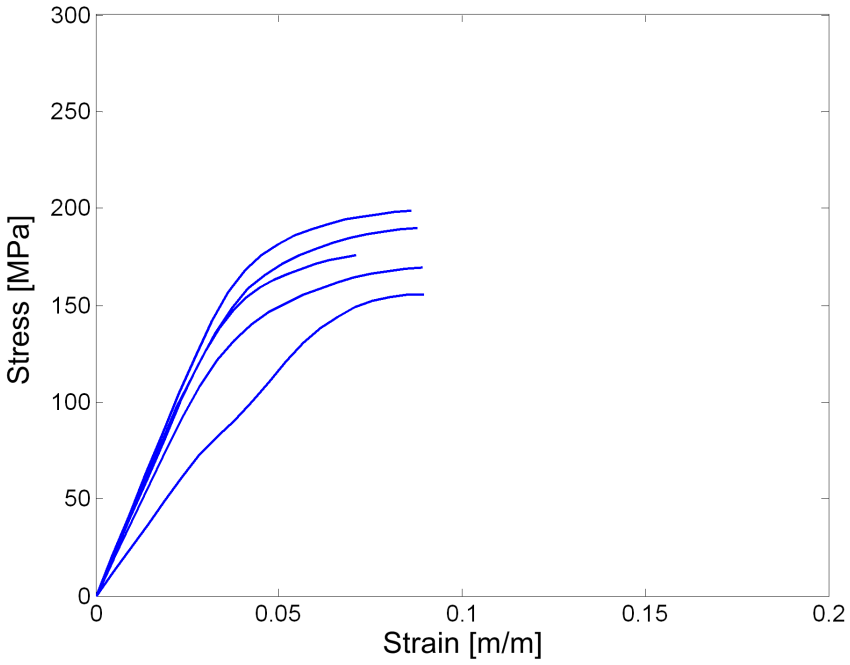

(a) Stress vs. strain

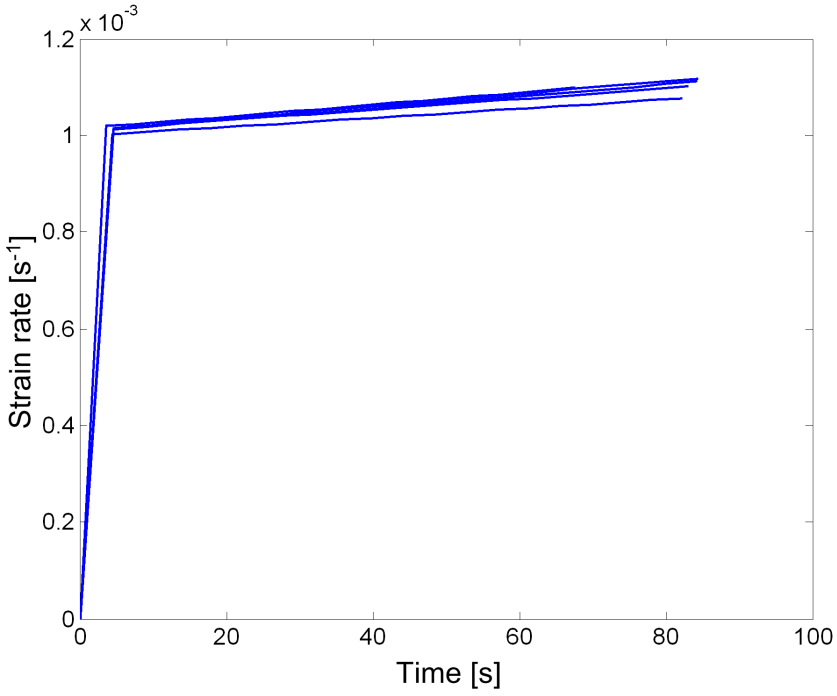

(b) Strain rate vs. time

Figure B.2: Radial bovine cortical bone compression at $\dot{\varepsilon} = 10^{-3}\,\mathrm{s}^{-1}$. Ultimate properties for these responses are reported in Table B.2.

B.2.3 Quasi-static compression at $\dot{\varepsilon} = 2 \times 10^{-2}\,\mathrm{s}^{-1}$

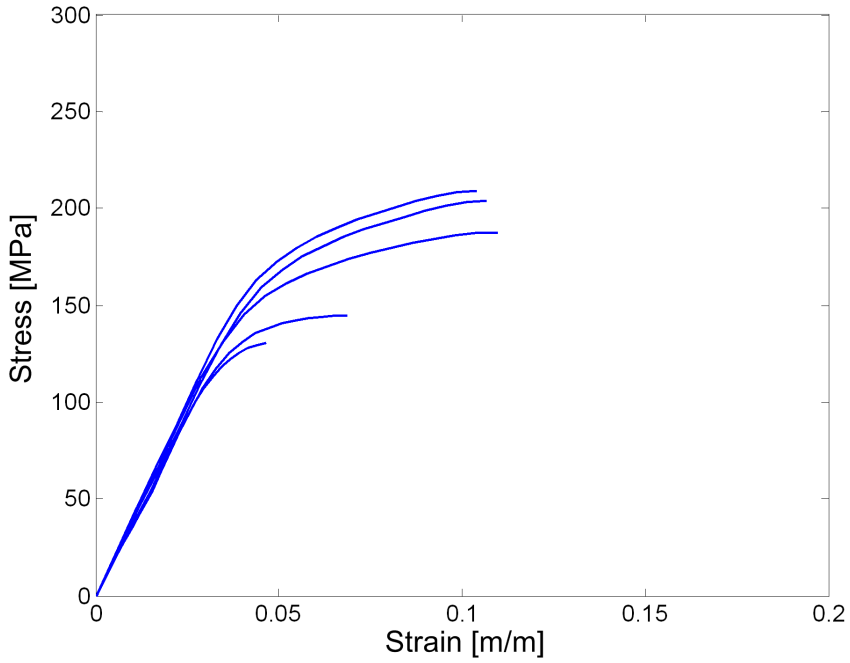

(a) Stress vs. strain

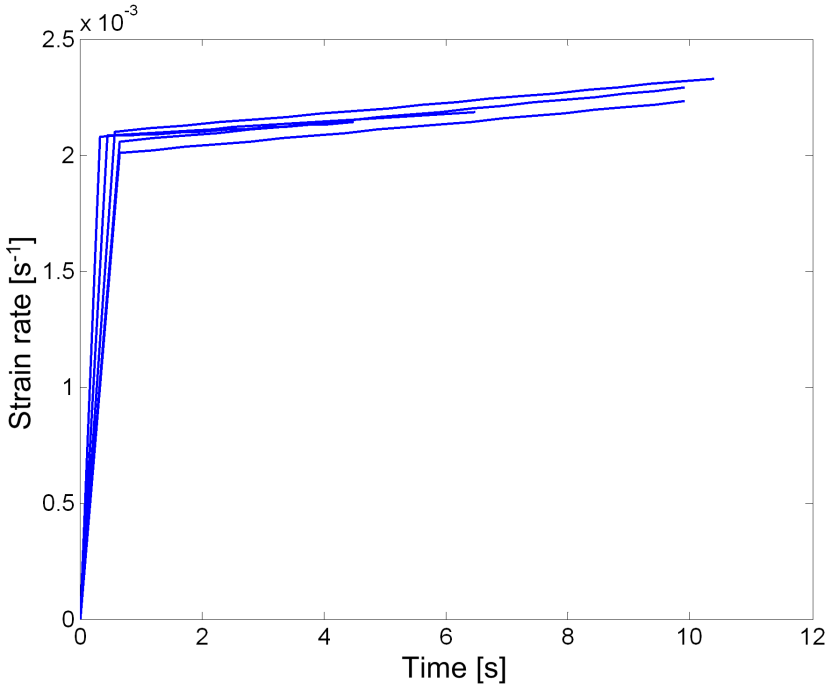

(b) Strain rate vs. time

Figure B.3: Radial bovine cortical bone compression at $\dot{\varepsilon} = 2 \times 10^{-2}\,\mathrm{s}^{-1}$. Ultimate properties for these responses are reported in Table B.3.

Appendix C

Tangential bone compression results

C.1 Ultimate properties of tangential specimens

$\dot{\varepsilon} \approx 10^{-4}\,\mathrm{s}^{-1}$	σ_{ut} [MPa]	ε_{ut} [m/m]
Bone 29	130.23	0.021
Bone 30	103.91	0.019
Bone 31	130.28	0.029
Bone 32	127.24	0.021
Bone 33	115.11	0.021
Average	121.35	0.022

Table C.1: The ultimate properties of tangentially orientated specimens in quasi-static compression at $\dot{\varepsilon} \approx 10^{-4}\,\mathrm{s}^{-1}$. The stress vs. strain and strain rate vs. time histories are presented in Fig.C.1.

$\dot{\varepsilon} \approx 10^{-3}\,\mathrm{s}^{-1}$	σ_{ut} [MPa]	ε_{ut} [m/m]
Bone 29	119.50	0.020
Bone 30	131.28	0.022
Bone 31	130.30	0.043
Bone 32	132.42	0.023
Bone 33	137.38	0.023
Average	130.18	0.026

Table C.2: The ultimate properties of tangentially orientated specimens in quasi-static compression at $\dot{\varepsilon} \approx 10^{-3}\,\mathrm{s}^{-1}$. The stress vs. strain and strain rate vs. time histories are presented in Fig.C.2.

$\dot{\varepsilon} \approx 10^{-2}\,\mathrm{s}^{-1}$	σ_{ut} [MPa]	ε_{ut} [m/m]
Bone 29	160.63	0.027
Bone 30	143.53	0.022
Bone 31	158.18	0.027
Bone 32	149.81	0.024
Bone 33	144.74	0.027
Average	151.38	0.026

Table C.3: The ultimate properties of tangentially orientated specimens in quasi-static compression at $\dot{\varepsilon} \approx 10^{-2}\,\mathrm{s}^{-1}$. The stress vs. strain and strain rate vs. time histories are presented in Fig.C.3.

$\dot{\varepsilon} \approx 3.3 \times 10^{2}\,\mathrm{s}^{-1}$ σ_{ut} [MPa]	ε_{ut} [m/m]	
Bone 29	245.86	0.015
Bone 30	202.48	0.013
Bone 31	205.36	0.017
Bone 33	217.00	0.015
Average	217.67	0.015

Table C.4: The ultimate properties of tangentially orientated specimens in dynamic compression at $\dot{\varepsilon} \approx 3.3 \times 10^{2}\,\mathrm{s}^{-1}$ with a shaped striker. The stress vs. strain and strain rate vs. time histories are presented in Fig.C.4.

C.2 Tangential specimen response histories

C.2.1 Quasi-static compression at $\dot{\varepsilon} = 10^{-4}\,\mathrm{s}^{-1}$

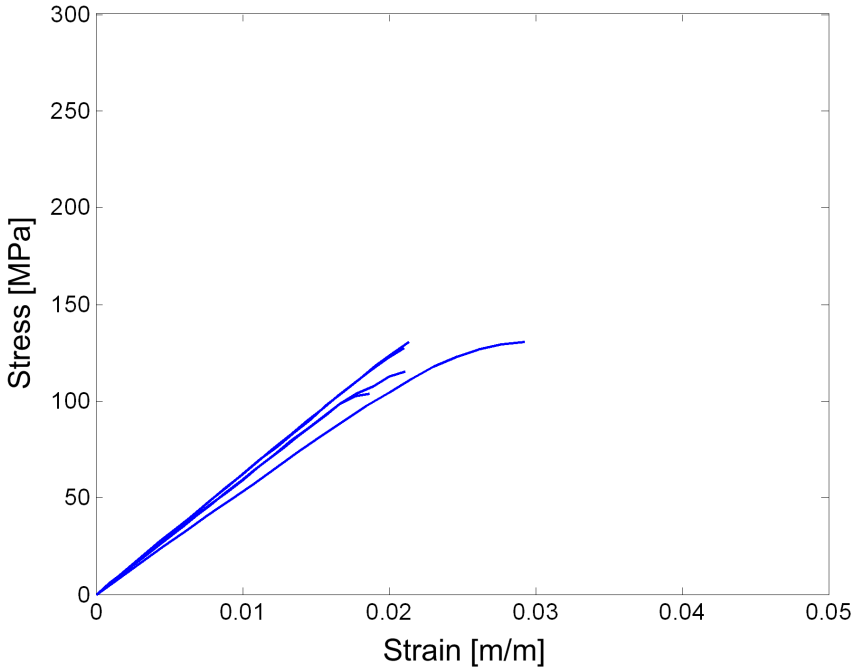

(a) Stress vs. strain

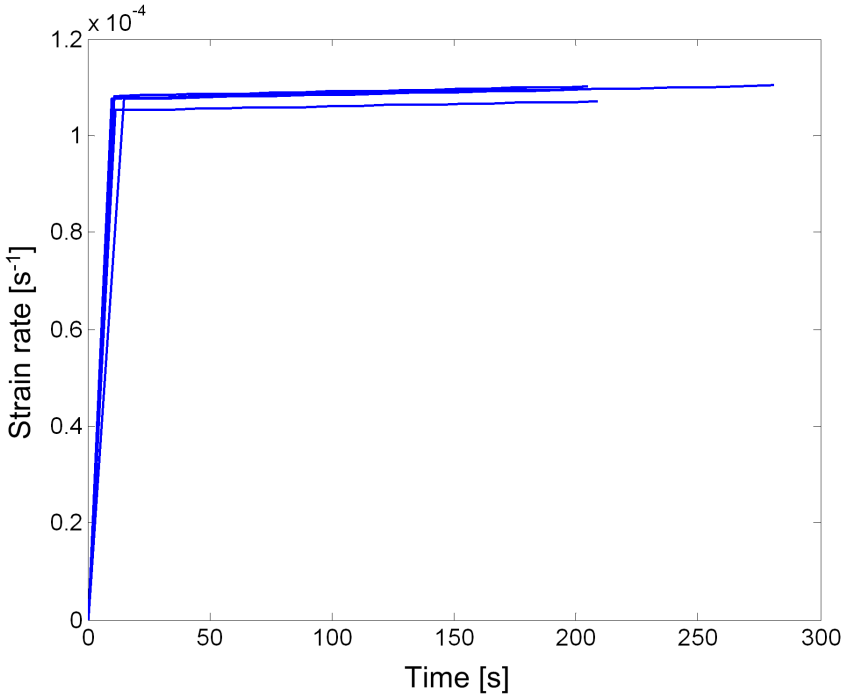

(b) Strain rate vs. time

Figure C.1: Tangential bovine cortical bone compression at $\dot{\varepsilon} = 10^{-4}\,\mathrm{s}^{-1}$. Ultimate properties for these responses are reported in Table C.1.

C.2.2 Quasi-static compression at $\dot{\varepsilon} = 10^{-3}\,\mathrm{s}^{-1}$

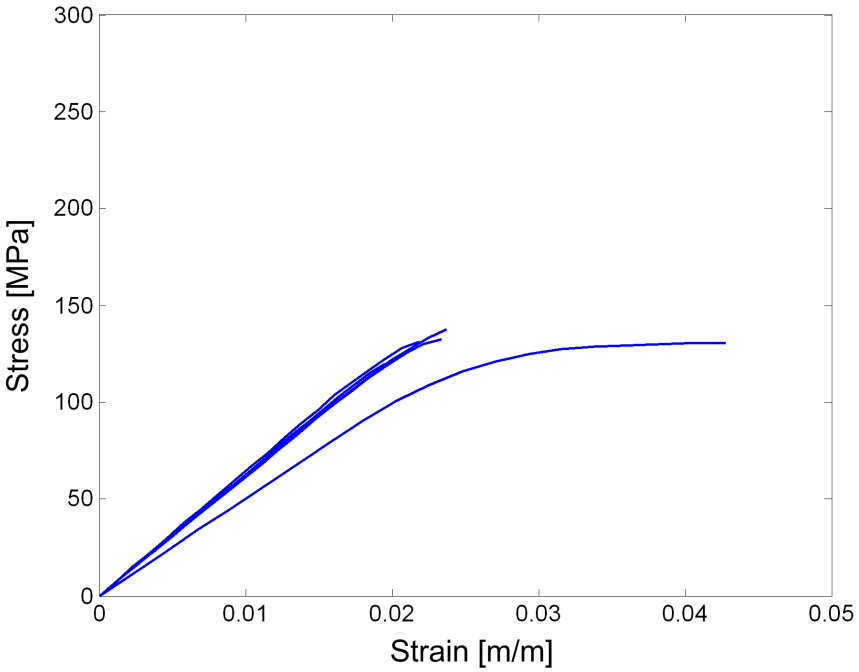

(a) Stress vs. strain

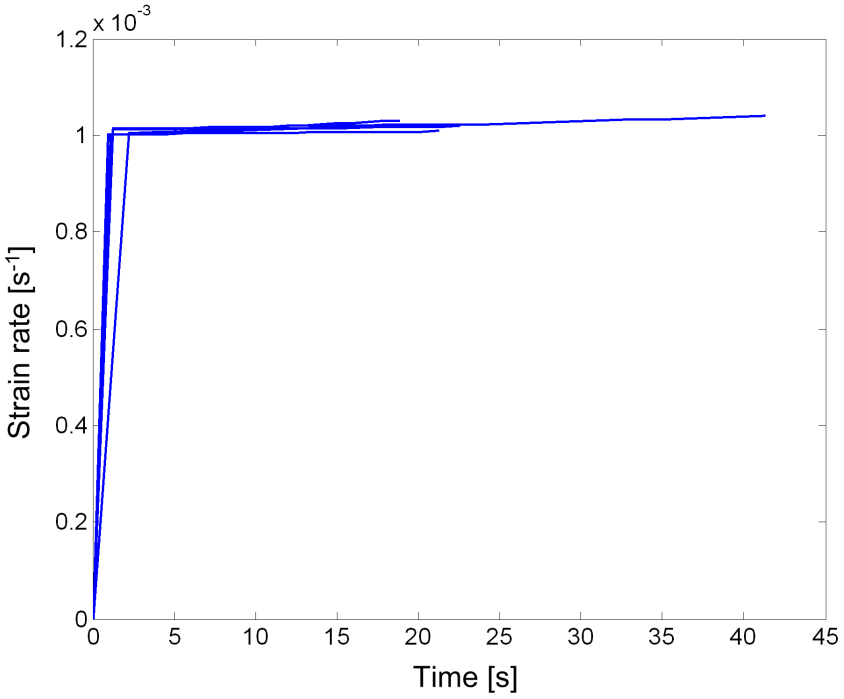

(b) Strain rate vs. time

Figure C.2: Tangential bovine cortical bone compression at $\dot{\varepsilon} = 10^{-3}\,\mathrm{s}^{-1}$. Ultimate properties for these responses are reported in Table C.2.

C.2.3 Quasi-static compression at $\dot{\varepsilon} = 10^{-2}\,\mathrm{s}^{-1}$

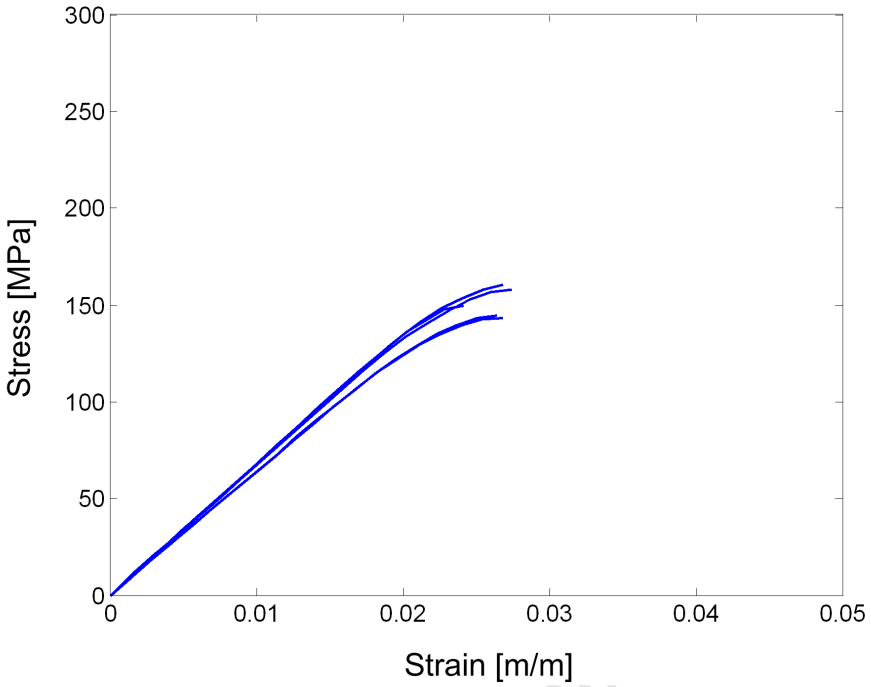

(a) Stress vs. strain

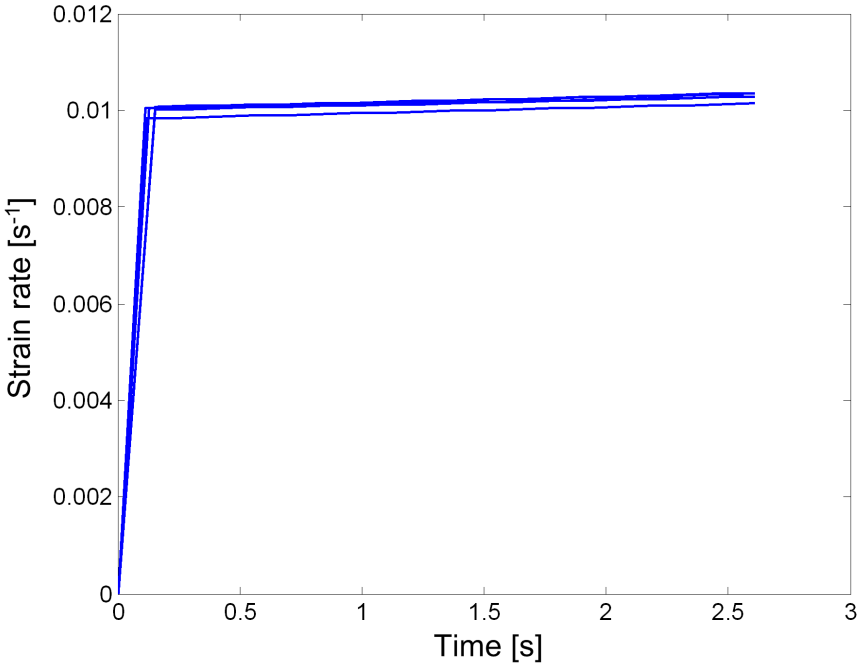

(b) Strain rate vs. time

Figure C.3: Tangential bovine cortical bone compression at $\dot{\varepsilon} = 10^{-2}\,\mathrm{s}^{-1}$. Ultimate properties for these responses are reported in Table C.3.

C.2.4 Dynamic compression at $\dot{\varepsilon} = 3.3 \times 10^2\,\mathrm{s}^{-1}$

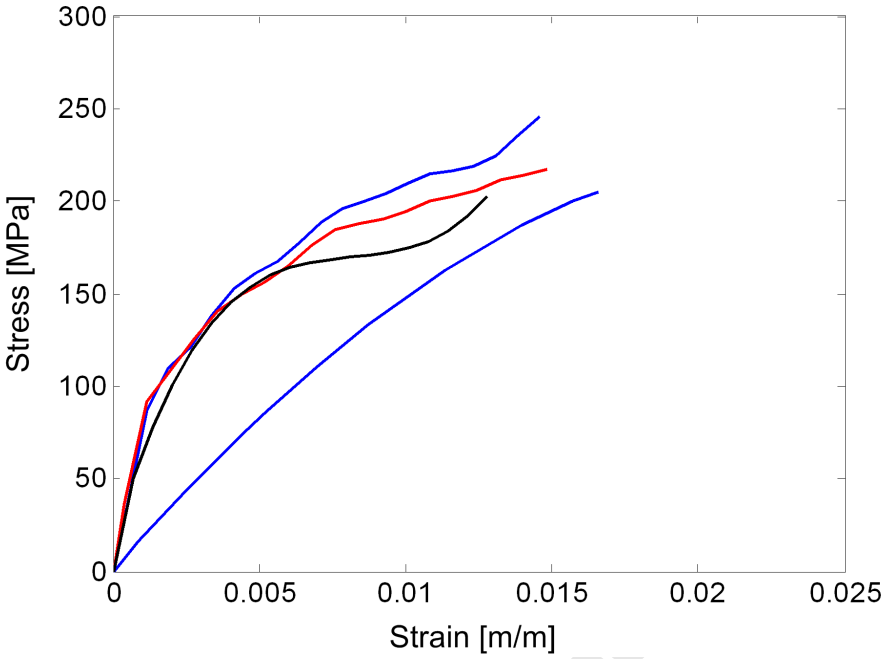

(a) Stress vs. strain

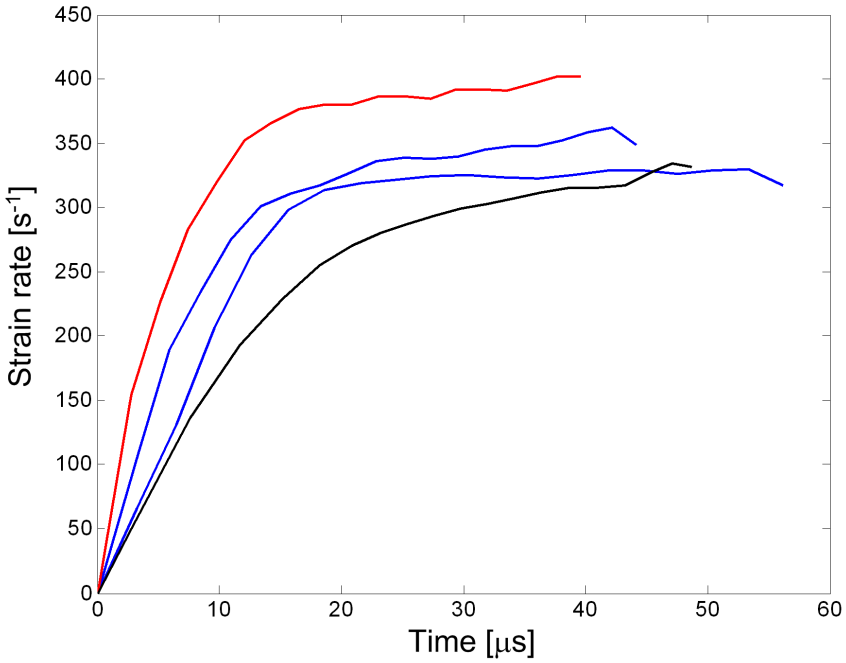

(b) Strain rate vs. time

Figure C.4: Tangential bovine cortical bone compression at $\dot{\varepsilon} = 3 \times 10^2\,\mathrm{s}^{-1}$. Ultimate properties for these responses are reported in Table C.4.

Appendix D

Viscoelastic model parameters

D.1 Maxwell model

Viscoelastic relation

$$\sigma(t) = k_1 \varepsilon(t) + \eta_1 \dot{\varepsilon}(t)$$

Parameters

$k_1 = 4.28\,\text{GPa}$

$\eta_1 = 2.28\,\text{MPa.s}^{-1}$

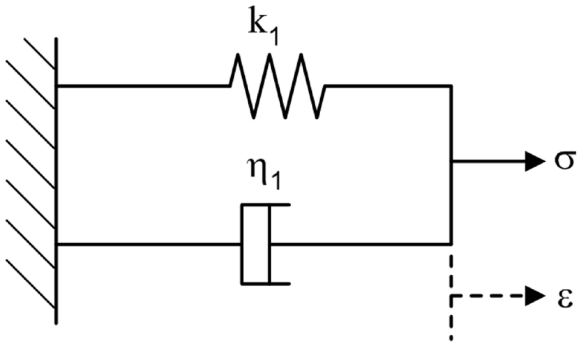

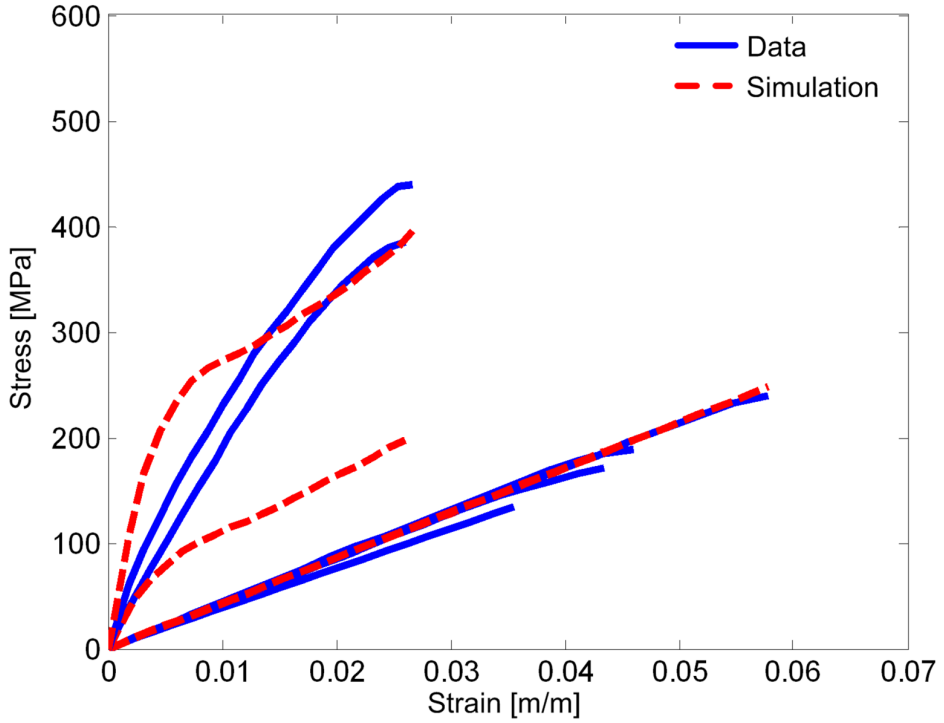

Figure D.1: Parameters for the Maxwell viscoelastic model

D.2 Voigt model

Viscoelastic relation

$$\sigma(t) = k_1\varepsilon(t) + \eta_1\dot{\varepsilon}(t)$$

Parameters

$k_1 = 4.28\,\text{GPa}$

$\eta_1 = 2.28\,\text{MPa.s}^{-1}$

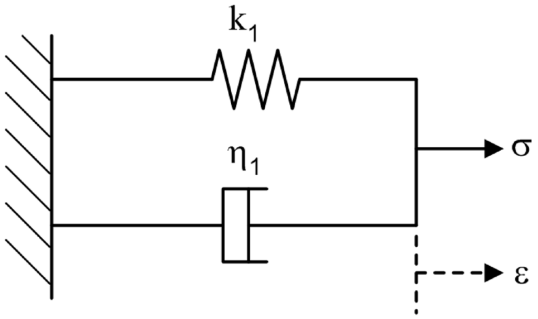

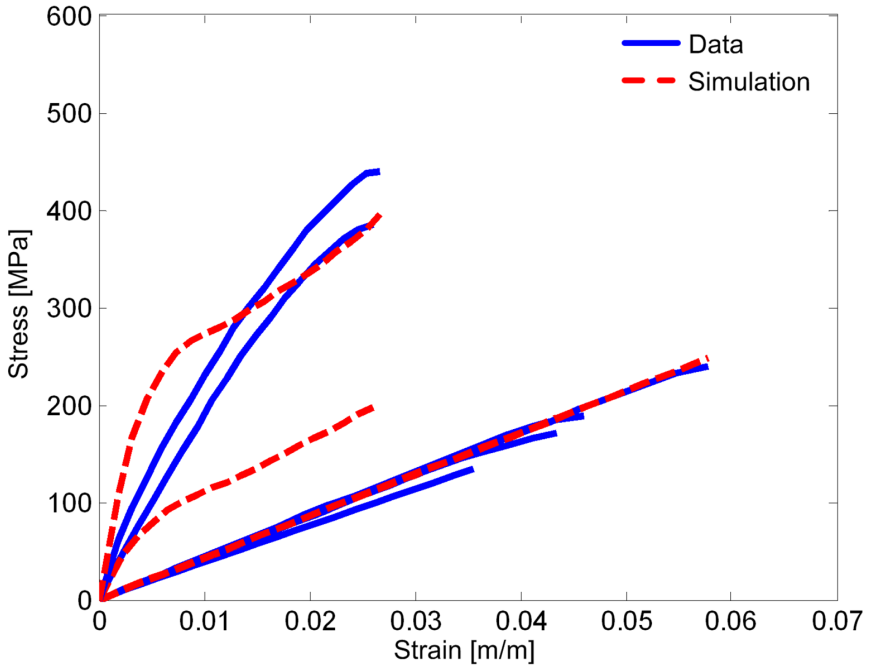

Figure D.2: Parameters for the Voigt viscoelastic model

D.3 Tanabe and Kobayashi model [16] *(DAMAGE INCLUDED)*

Viscoelastic relation

$$\sigma(t) = k_1(\varepsilon(t) - \varepsilon(t)^D) + \eta_1 \left(\frac{\dot{\varepsilon}(t)}{\dot{\varepsilon}_0}\right)^P$$

Parameters

$k_1 = 4.15\,\text{GPa}$
$\eta_1 = 185.38\,\text{MPa.s}^{-1}$
$D = 2.43$
$P = 0.38$

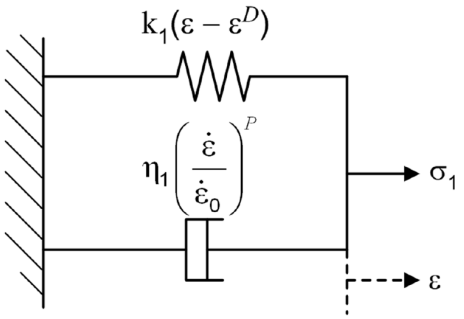

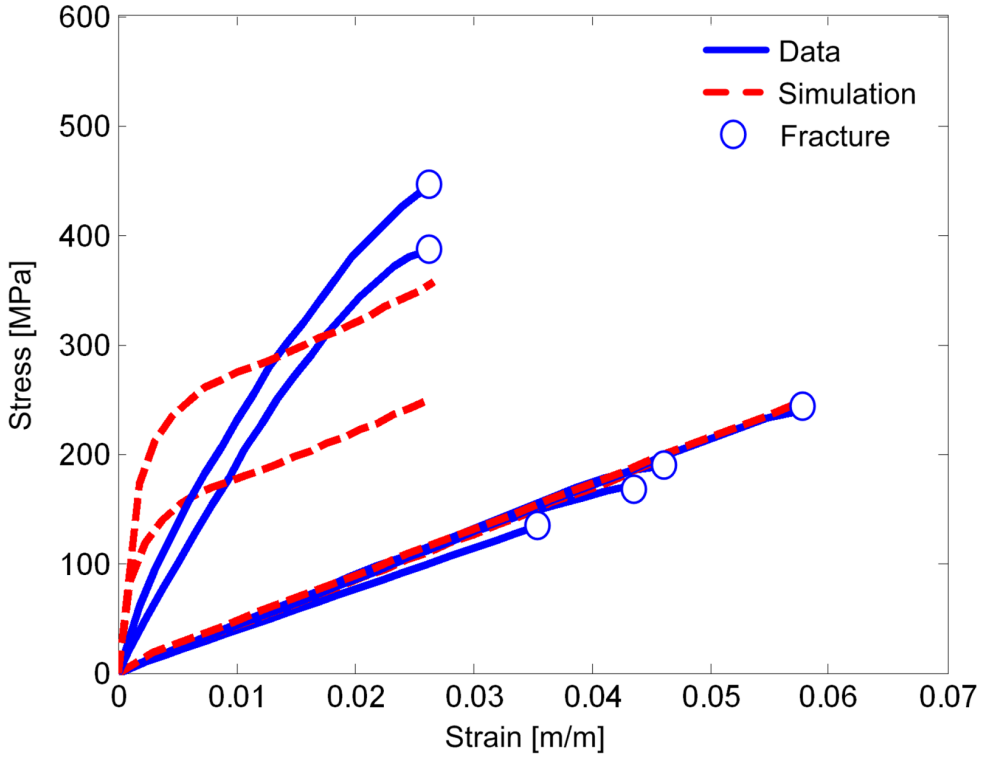

Figure D.3: Parameters for the viscoelastic model by Tanabe and Kobayashi [16]

D.4 Elastic and Maxwell models in parallel

Viscoelastic relation

$$\sigma(t) = k_1\varepsilon(t) + \int_0^t k_2\dot{\varepsilon}(\tau)e^{-\frac{\eta_2}{k_2}(t-\tau)}d\tau$$

Parameters

$k_1 = 4.27\,\text{GPa}$
$k_2 = 20.62\,\text{GPa}$
$\eta_2 = 1.83\,\text{MPa.s}^{-1}$

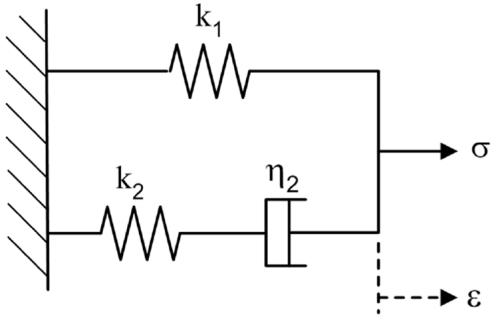

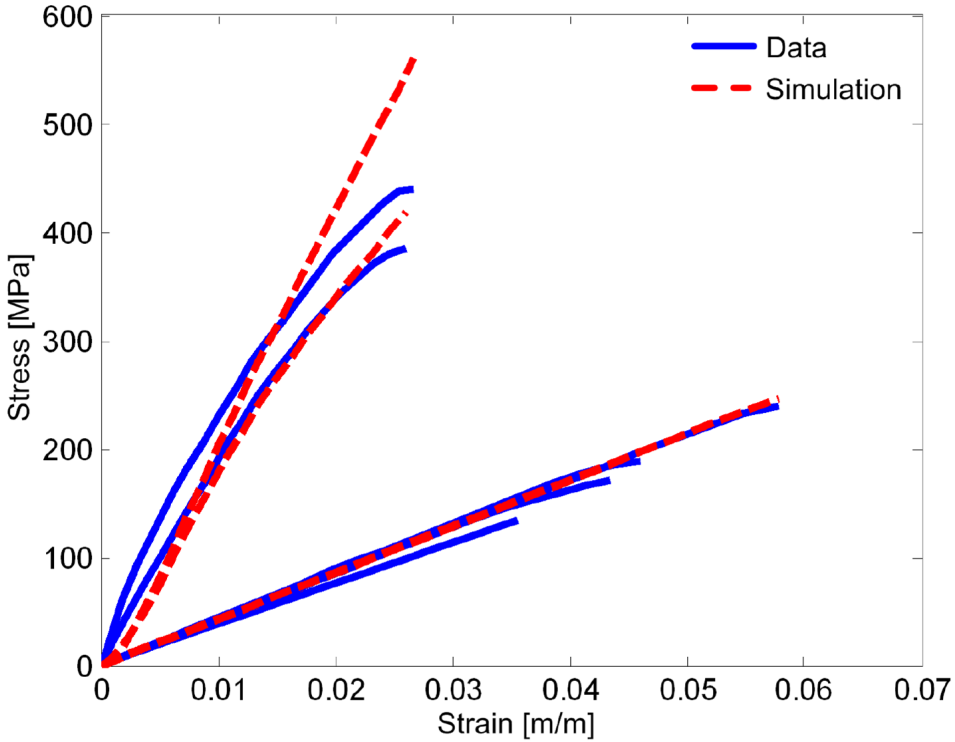

Figure D.4: Parameters for a viscoelastic model which comprises of a Maxwell model in parallel with an elastic model

D.5 Elastic and non-linear Maxwell models in parallel

Viscoelastic relation

$\sigma(t) = k_1\varepsilon(t) + \text{result Eq.6.26}$

Parameters

$k_1 = 4.20\,\text{GPa}$
$k_2 = 21.17\,\text{GPa}$
$\eta_2 = 15.12\,\text{MPa.s}^{-1}$
$Q = 0.53$

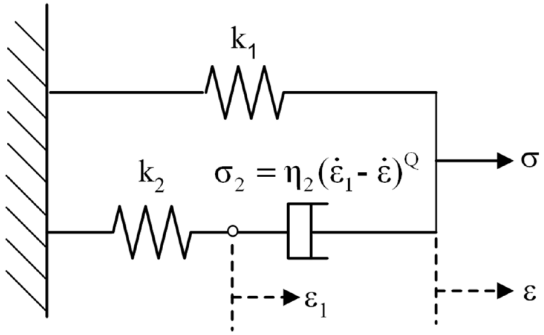

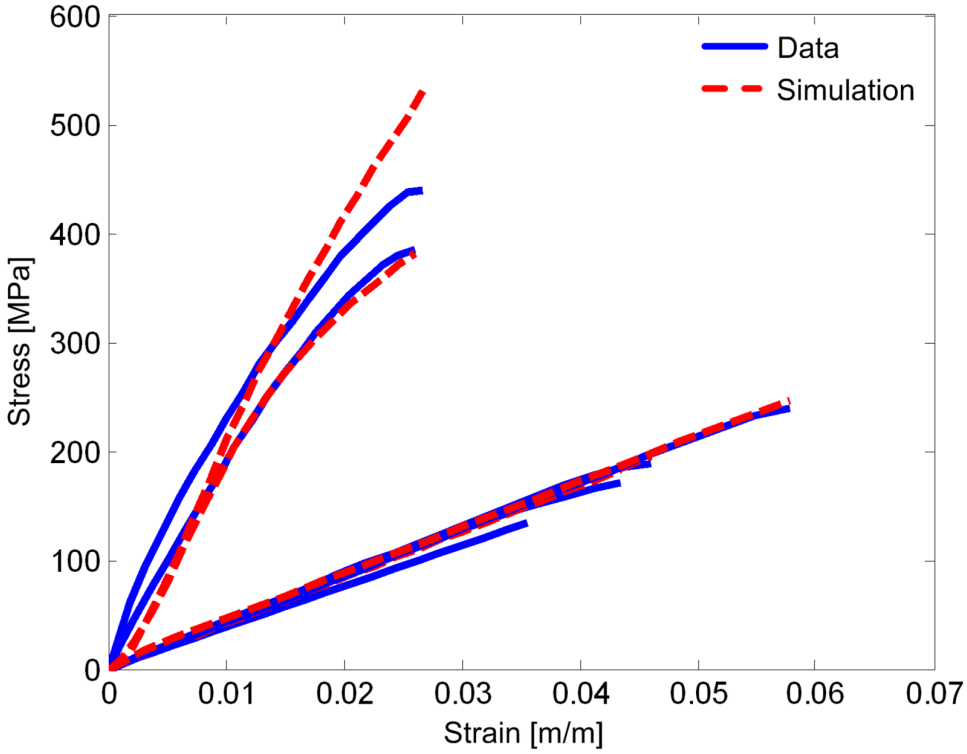

Figure D.5: Parameters for a viscoelastic model which comprises of a non-linear Maxwell model in parallel with an elastic model

D.6 Both non-linear elastic and Maxwell models in parallel *(DAMAGE INCLUDED)*

Viscoelastic relation

$\sigma(t) = k_1(\varepsilon(t) - \varepsilon(t)^D) +$ result Eq.6.26

Parameters

$k_1 = 4.06\,\text{GPa}$
$k_2 = 20.32\,\text{GPa}$
$\eta_2 = 28.91\,\text{MPa.s}^{-1}$
$D = 2.68$
$Q = 0.409$

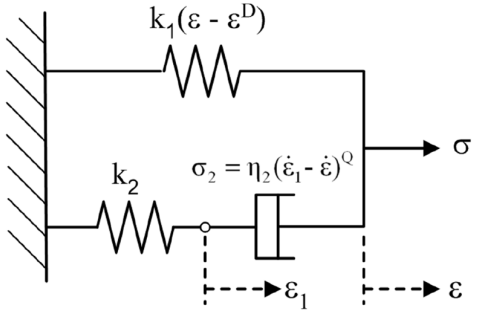

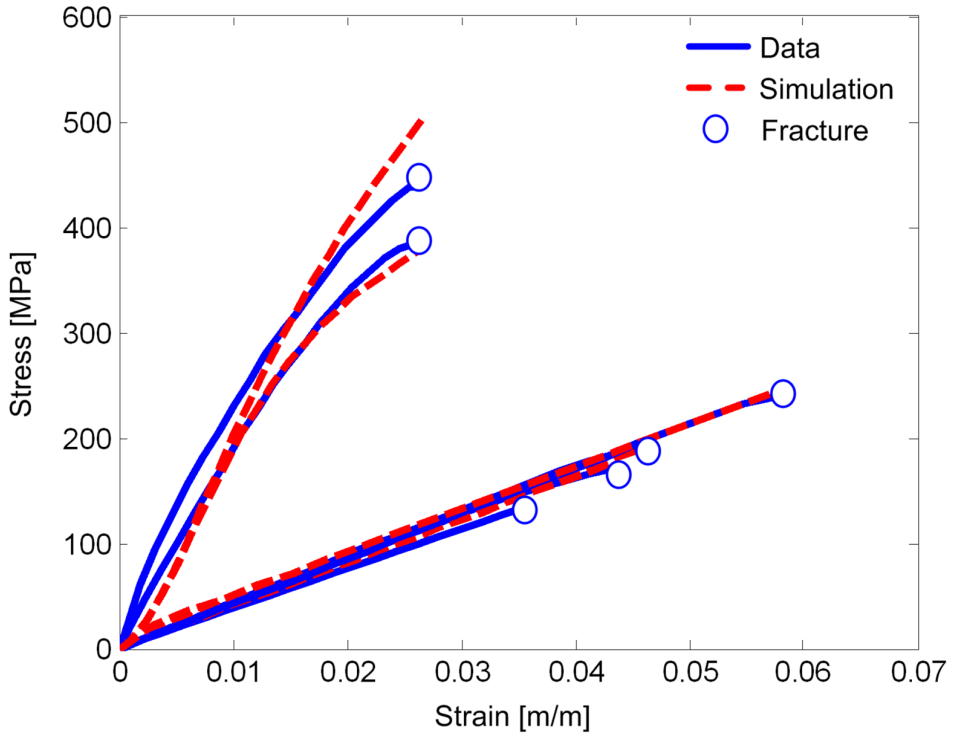

Figure D.6: Parameters for a viscoelastic model which comprises of both non-linear Maxwell and elastic models in parallel

D.7 Maxwell and Voigt models in parallel

Viscoelastic relation

$$\sigma(t) = k_1\varepsilon(t) + \eta_1\dot{\varepsilon}(t) + \int_0^t k_2\dot{\varepsilon}(\tau)e^{-\frac{\eta_2}{k_2}(t-\tau)}d\tau$$

Parameters

$k_1 = 4.25\,\text{GPa}$
$\eta_2 = 0.78\,\text{MPa.s}^{-1}$
$k_2 = 14.04\,\text{GPa}$
$\eta_2 = 14.90\,\text{MPa.s}^{-1}$

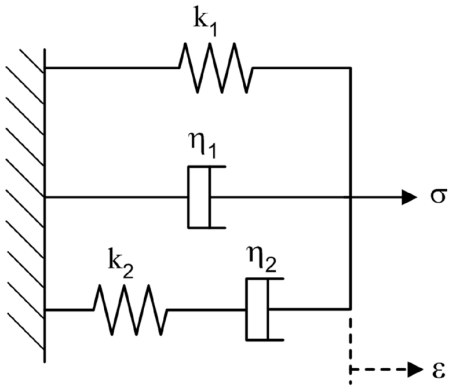

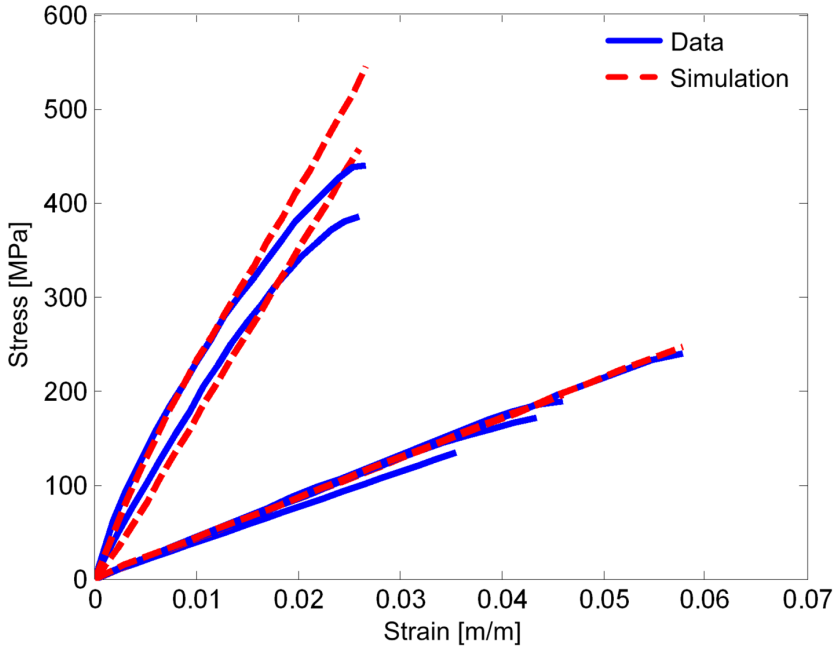

Figure D.7: Parameters for a viscoelastic model which comprises of Maxwell and Voigt models in parallel

D.8 Shim et al. [21] model

Viscoelastic relation

$$\sigma(t) = k_1\varepsilon(t) + \eta_1\dot{\varepsilon}(t)^P + \int_0^t k_2\dot{\varepsilon}(\tau)e^{-\frac{\eta_2}{k_2}(t-\tau)}d\tau$$

Parameters

$k_1 = 4.21\,\text{GPa}$
$\eta_2 = 34.7\,\text{MPa.s}^{-1}$
$k_2 = 13.11\,\text{GPa}$
$\eta_2 = 10.09\,\text{MPa.s}^{-1}$
$P = 0.46$

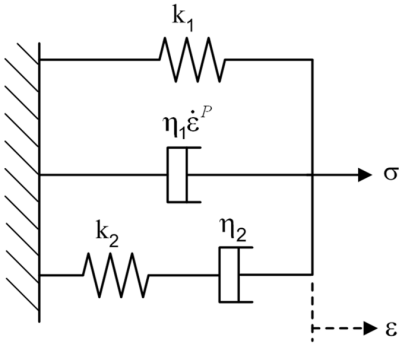

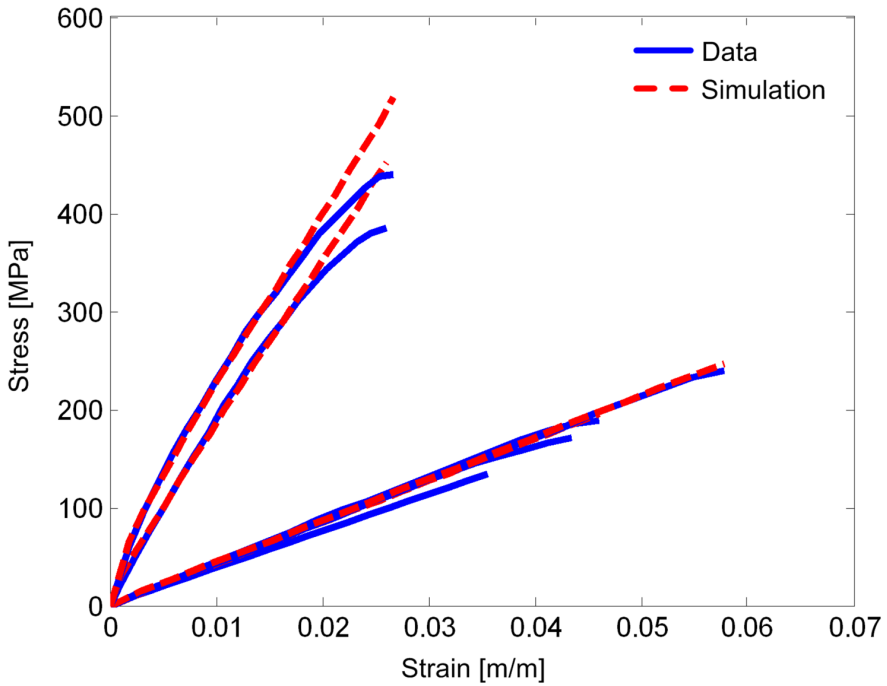

Figure D.8: Parameters for the viscoelastic model by Shim et al. [21]

D.9 Both non-linear Voigt and Maxwell models in parallel *(DAMAGE INCLUDED)*

Viscoelastic relation

$\sigma(t) = k_1\varepsilon(t) + \eta_1\dot{\varepsilon}(t)^P +$ result Eq.6.26

Parameters

$k_1 = 4.04\,\text{GPa}$
$\eta_2 = 77.815\,\text{MPa.s}^{-1}$
$k_2 = 13.06\,\text{GPa}$
$\eta_2 = 21.19\,\text{MPa.s}^{-1}$
$P = 0.33$
$Q = 0.48$

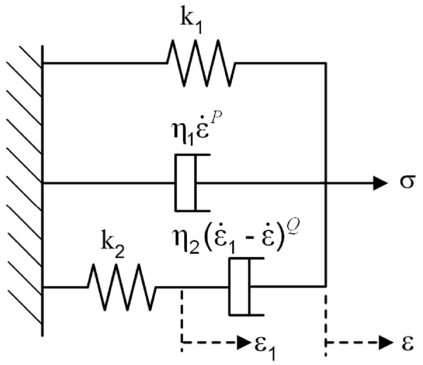

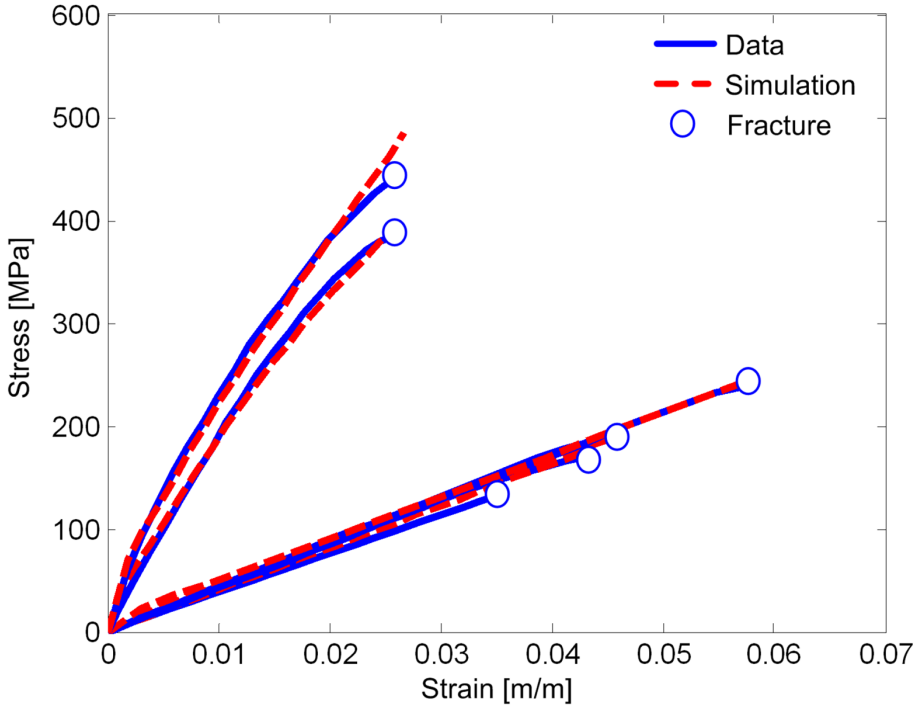

Figure D.9: Parameters for both non-linear Voigt and Maxwell models in parallel

Appendix E

A VUMAT for bovine cortical bone

```
C Bovine cortical bone VUMAT
subroutine vumat(
C Read only -
  1 nblock, ndir, nshr, nstatev, nfieldv, nprops, lanneal,
  2 stepTime, totalTime, dt, cmname, coordMp, charlength,
  3 props, density, strainInc, relSpinInc,
  4 tempOld, stretchOld, defgradOld, fieldOld,
  5 stressOld, stateOld, enerInternOld, enerInelasOld,
  6 tempNew, stretchNew, defgradNew, fieldNew,
C Write only -
  7 stressNew, stateNew, enerInternNew, enerInelasNew )
C
C implicit none
  include 'vaba_param.inc'
C
C Shim viscoelastic model with nonlinear strain rate
C dependency for bovine cortical bone
C
C All arrays dimensioned by (*) are not used in this algorithm
 dimension props(nprops), density(nblock),
  1 coordMp(nblock,*),
  2 charLength(*), strainInc(nblock,ndir+nshr),
  3 relSpinInc(*), tempOld(*),
  4 stretchOld(*), defgradOld(*),
  5 fieldOld(*), stressOld(nblock,ndir+nshr),
  6 stateOld(nblock,nstatev), enerInternOld(nblock),
  7 enerInelasOld(nblock), tempNew(*),
  8 stretchNew(*), defgradNew(*), fieldNew(*),
  9 stressNew(nblock,ndir+nshr), stateNew(nblock,nstatev),
```

```
  1 enerInternNew(*), enerInelasNew(*)
C
      character*80 cmname
C
C Model parameters
      xk1 = props(1)
      eta1  = props(2)
      xk2  = props(3)
      eta2  = props(4)
      P   = props(5)
      v   = props(6)
      alpha = props(7)
      beta  = props(8)
C
C
      do 100 i = 1,nblock
C
C Calculate the strain tensor
      trace = stateOld(i,1) + stateOld(i,2)  + stateOld(i,3) +
     1         strainInc(i,1) + strainInc(i,2) + strainInc(i,3)
      emu1 = 1.0/(1.0+v)
      emu2 = v/(1.0 - 2.0*v)
C
      strain_tensor1 = emu1*(emu2 * trace  + (stateOld(i,1)
     1                 + strainInc(i,1)))
      strain_tensor2 = emu1*(emu2 * trace  + (stateOld(i,2)
     1                 + strainInc(i,2)))
      strain_tensor3 = emu1*(emu2 * trace  + (stateOld(i,3)
     1                 + strainInc(i,3)))
      strain_tensor4 = emu1*(stateOld(i,4) + strainInc(i,4))
      strain_tensor5 = emu1*(stateOld(i,5) + strainInc(i,5))
      strain_tensor6 = emu1*(stateOld(i,6) + strainInc(i,6))
C
C Calculate the strain rate tensor
      tracedot = strainInc(i,1)/dt
     1  + strainInc(i,2)/dt
     2  + strainInc(i,3)/dt
      strain_rate_tensor1 = emu1*(emu2*tracedot + strainInc(i,1)/dt)
      strain_rate_tensor2 = emu1*(emu2*tracedot + strainInc(i,2)/dt)
      strain_rate_tensor3 = emu1*(emu2*tracedot + strainInc(i,3)/dt)
      strain_rate_tensor4 = emu1* strainInc(i,4)/dt
```

```
      strain_rate_tensor5 = emu1* strainInc(i,5)/dt
      strain_rate_tensor6 = emu1* strainInc(i,6)/dt
C
C Calculate the elastic stress increment
      sig1_e = xk1*strain_tensor1
      sig2_e = xk1*strain_tensor2
      sig3_e = xk1*strain_tensor3
      sig4_e = xk1*strain_tensor4
      sig5_e = xk1*strain_tensor5
      sig6_e = xk1*strain_tensor6
C
C Calculate the viscous stress increment
      ratesumsquared = strainInc(i,1)**2.0
     1                + strainInc(i,2)**2.0
     2                + strainInc(i,3)**2.0
     3           + 2.0 * strainInc(i,4)**2.0
     4           + 2.0 * strainInc(i,5)**2.0
     5           + 2.0 * strainInc(i,6)**2.0
      rate_eq = sqrt(ratesumsquared/(1.0+2.0 * v**2.0))/dt
C
      if( rate_eq .gt. 0.0) then
         eq_power = rate_eq**(P - 1.0)
      else
         eq_power = 0.0
      end if
C
      sig1_v = eq_power*eta1*strain_rate_tensor1
      sig2_v = eq_power*eta1*strain_rate_tensor2
      sig3_v = eq_power*eta1*strain_rate_tensor3
      sig4_v = eq_power*eta1*strain_rate_tensor4
      sig5_v = eq_power*eta1*strain_rate_tensor5
      sig6_v = eq_power*eta1*strain_rate_tensor6
C
C Calculate the Maxwell stress increment
C
      a = 1.0 - xk2 * dt / (2.0 * eta2)
      b = xk2 * dt / 2.0
      c = 1.0 + xk2 * dt / (2.0 * eta2)
C
      sig1_m = ( a * stateOld(i,13)
     1    + b * (stateOld(i,7) + strain_rate_tensor1))  / c
```

```
C
    sig2_m = ( a * stateOld(i,14)
  1    + b * (stateOld(i,8) + strain_rate_tensor2))  / c
C
    sig3_m = ( a * stateOld(i,15)
  1    + b * (stateOld(i,9) + strain_rate_tensor3))  / c
C
    sig4_m = ( a * stateOld(i,16)
  1    + b * (stateOld(i,10) + strain_rate_tensor4)) / c
C
    sig5_m = ( a * stateOld(i,17)
  1    + b * (stateOld(i,11) + strain_rate_tensor5)) / c
C
    sig6_m = ( a * stateOld(i,18)
  1    + b * (stateOld(i,12) + strain_rate_tensor6)) / c
C
C
C Total stress is the sum of the elastic viscous and Maxwell stesses
C
    if (totalTime .eq. 0) then
C Define material as purely elastic for ABAQUS first step check
      stressNew(i,1) = (xk1 + xk2)*strainInc(i,1)
      stressNew(i,2) = (xk1 + xk2)*strainInc(i,2)
      stressNew(i,3) = (xk1 + xk2)*strainInc(i,3)
      stressNew(i,4) = (xk1 + xk2)*strainInc(i,4)
      stressNew(i,5) = (xk1 + xk2)*strainInc(i,5)
      stressNew(i,6) = (xk1 + xk2)*strainInc(i,6)
    else
C
      stressNew(i,1) = sig1_e + sig1_v + sig1_m
      stressNew(i,2) = sig2_e + sig2_v + sig2_m
      stressNew(i,3) = sig3_e + sig3_v + sig3_m
      stressNew(i,4) = sig4_e + sig4_v + sig4_m
      stressNew(i,5) = sig5_e + sig5_v + sig5_m
      stressNew(i,6) = sig6_e + sig6_v + sig6_m
  end if
C
C Calculate the failure stress
C
    if( rate_eq .gt. 0.0) then
      sigmaFail = abs(alpha*rate_eq**(beta)*density(i)**2)
```

```
      else
        sigmaFail = abs(alpha*0.0001**(beta)*density(i)**2)
      end if
C
C Calculate the Von Mises stress (distortion of the of the material)
C
      xMises    = abs(sqrt(0.5*
     1           ((stressNew(i,1) - stressNew(i,2))**2.0
     2          + (stressNew(i,2) - stressNew(i,3))**2.0
     3          + (stressNew(i,3) - stressNew(i,1))**2.0)))
      xminrate = 0.0001
      fail = 1.0
C
C UPDATE THE STATE VARIABLES
C
C Strain update
C
      stateNew(i,1) = stateOld(i,1) + strainInc(i,1)
      stateNew(i,2) = stateOld(i,2) + strainInc(i,2)
      stateNew(i,3) = stateOld(i,3) + strainInc(i,3)
      stateNew(i,4) = stateOld(i,4) + strainInc(i,4)
      stateNew(i,5) = stateOld(i,5) + strainInc(i,5)
      stateNew(i,6) = stateOld(i,6) + strainInc(i,6)
C
C Strain rate update
C
      stateNew(i,7)  = strain_rate_tensor1
      stateNew(i,8)  = strain_rate_tensor2
      stateNew(i,9)  = strain_rate_tensor3
      stateNew(i,10) = strain_rate_tensor4
      stateNew(i,11) = strain_rate_tensor5
      stateNew(i,12) = strain_rate_tensor6
C
C Maxwell stress update
C
      stateNew(i,13) = sig1_m
      stateNew(i,14) = sig2_m
      stateNew(i,15) = sig3_m
      stateNew(i,16) = sig4_m
      stateNew(i,17) = sig5_m
      stateNew(i,18) = sig6_m
```

```
C
C Elastic stress update
C
    stateNew(i,19) = sig1_e
    stateNew(i,20) = sig2_e
    stateNew(i,21) = sig3_e
    stateNew(i,22) = sig4_e
    stateNew(i,23) = sig5_e
    stateNew(i,24) = sig6_e
C
C Viscous stress update
C
    stateNew(i,25) = sig1_v
    stateNew(i,26) = sig2_v
    stateNew(i,27) = sig3_v
    stateNew(i,28) = sig4_v
    stateNew(i,29) = sig5_v
    stateNew(i,30) = sig6_v
C
C Non-linear equivalent strain rate update
C
    stateNew(i,31) = eq_power
C
C Establish if element failed and update the element status
C
    if (totaltime .gt. 0) then
      if (xMises .ge. sigmaFail) then
        fail = 0.0
      end if
        stateNew(i,32) = fail
      else
        if ((totalTime + StepTime) .eq. 0) then
          stateNew(i,32) = 1.0
        end if
      end if
C
C Failure stress update
C
    stateNew(i,33) = sigmaFail
C
C Von Mises stress update
```

```
C
    statenew(i,34) = xMises
C
100  continue
C
return
end
```